Wissenschaftliche Mitteilungen

aus dem
Institut für Meteorologie der Universität Leipzig

ISBN **978-3-9814401-6-4**

Meteorologische Arbeiten (XXIII) und Jahresbericht 2017 des Instituts für Meteorologie der Universität Leipzig

Hrsg.: Armin Raabe, Manfred Wendisch

Leipzig 2018

Band 56

Wissenschaftliche Mitteilungen aus dem Institut für Meteorologie der Universität Leipzig Bd. 56 (2018)

Wissenschaftliche Mitteilungen aus dem Institut für Meteorologie der Universität Leipzig, Band 56 (2018)

Wissenschaftliche Mitteilungen aus dem Institut für Meteorologie der Universität Leipzig Bd. 56 (2018)

Ionospheric response during low and high solar activity

Vaishnav, R.[1*], Jacobi, Ch.[1], Berdermann, J.[2], Schmölter, E.[2], Codrescu, M.[3]

[1]Leipzig Institute for Meteorology, Universität Leipzig, Stephanstr. 3, 04103 Leipzig, Germany (rajesh_ishwardas.vaishnav@uni-leipzig.de)
[2]German Aerospace Center, Kalkhorstweg 53, 17235 Neustrelitz, Germany
[3]Space Weather Prediction Centre, National Oceanic and Atmospheric Administration, Boulder, Colorado, USA.

Summary: We analyse solar extreme ultraviolet (EUV) irradiance observed by the Solar EUV Experiment (SEE) onboard the Thermosphere Ionosphere Mesosphere Energetics and Dynamics (TIMED) satellite, and solar proxies (the F10.7 index, and Mg-II index), and compare their variability with the one of the global mean Total Electron Content (GTEC). Cross-wavelet analysis confirms the joint 27 days periodicity in GTEC and solar proxies. We focus on a comparison for solar minimum (2007-2009) and maximum (2013-2015) and find significant differences in the correlation during low and high solar activity years. GTEC is delayed by approximately 1-2 days in comparison to solar proxies during both low and high solar activity at the 27 days solar rotation period. To investigate the dynamics of the delay process, Coupled Thermosphere Ionosphere Plasmasphere electrodynamics model simulations have been performed for low and high solar activity conditions. Preliminary results using cross correlation analysis show an ionospheric delay of 1 day in GTEC with respect to the F10.7 index during low and high solar activity.

Zusammenfassung: Wir analysieren vom Solar Extreme Ultraviolet Experiment (SEE) an Bord des Thermosphere-Ionosphere-Mesosphere Energetics and Dynamics (TIMED) Satelliten gemessene solare EUV-Irradianzen, solare Proxies (den F10.7-Index und denMg-II-Index), und vergleichen deren Variabilität mit derjenigen des global gemittelten Gesamtelektronengehalts (GTEC). Kreuzwaveletanalysen bestätigen eine gemeinsame Variabilität im Periodenbereich der solaren Rotation (27 Tage). Wir vergleichen insbesondere den Zusammenhang während des solaren Minimums (2007-2009) und Maximums (2013-2015), wobei signifikante Unterschiede der Korrelation zwischen solaren und ionosphärischen Parametern auftreten. Es tritt eine Verzögerung der Maxima und Minima von GTEC gegenüber denjenigen der solaren Proxies von einem Tag sowohl im solaren Minimum als auch im solaren Maximum auf.

1. Introduction

The existence of the ionized layer in the atmosphere is due to the incoming solar radiation ranging from X-rays to the extreme ultraviolet (EUV, 0-105 nm). Solar input significantly changes the behavior of the thermosphere/ionosphere system during low and high solar activity, modulated at different time scales including the 11 years solar cycle and the 27 days solar rotation period, as has been shown using various solar proxies (e.g., Jakowski et al., 1991; Liu et al., 2003; Afraimovich et al., 2008; Liu and Chen 2009; Astafyeva et al., 2008; Chen et al., 2015; Patel et al., 2017). Solar EUV

modulations are stronger during high solar activity as compared to low solar activity. The ionosphere region (80-500 km) may be characterized by the total electron content (TEC, given in TEC units (TECU), 1 TECU = 10^{16} electrons/m^2) (e.g., Kane, 1992; Liu et al., 2006). TEC is one of the most important ionospheric parameters, which is frequently used to represent the behavior of the ionosphere. It varies temporally and spatially due to the complex interaction with the solar radiations (e.g., Mukhtarov et al., 2013).

Many researchers have explored possible relations between the solar radiation and the ionosphere (e.g. Jakowski et al., 1991; Afraimovich et al., 2008; Min et al., 2009; Lee et al., 2012; Jacobi et al., 2016). To establish possible relations of solar input and TEC, solar proxies are used as a representative of solar EUV with ionospheric TEC. Solar proxies are not always capable to sufficiently reproduce the EUV variability (Dudok de Wit et al., 2009), but they are often used due to unavailability of the direct EUV measurements. Most commonly used solar proxies are the solar radio flux at 10.7 cm (F10.7 index, given in solar flux units (sfu), 1 sfu = 10^{-22}Wm^{-2} Hz^{-1}) (Tapping, 2013), the Mg-II index (core to wing ratio of MG-II line at 280 nm) (Maruyama, 2010), or the sunspot number (number of active formations) (Wolf, 1856). Direct continuous measurements of EUV from space are available since 2002 from the Solar EUV Experiment (SEE) onboard the Thermosphere-Ionosphere-Mesosphere Energetics and Dynamics (TIMED) satellite (Woods et al., 2000, 2005). However, due to degradation of EUV measuring instruments, solar proxies may be more suitable (BenMoussa et al., 2013), or repeated calibration is necessary.

Several authors have reported an approximately 1-day delay in TEC in comparison to solar indices (Jakowski et al., 1991; Su et al., 1999; Forbes et al., 2000; Liu et al., 2006; Afraimovich et al., 2008; Lee et al., 2012; Jacobi et al., 2016; see also references therein). The dynamics behind the delay observed in the ionospheric TEC with respect to the solar proxies is still an open question. Jakowski et al. (1991) suggested that it might be due to slow diffusion of atomic oxygen, which has a longer lifetime at 180 km altitude, and which is produced via photodissociation of molecular oxygen in the lower thermosphere.

The availability of general circulation models (GCM) gives us the opportunity to explore different atmospheric processes which may play an important role in the modulation of the ionosphere. Some frequently used GCMs are the Thermosphere Ionosphere Electrodynamics General Circulation Model (TIEGCM, Richmond et al., 1992), the Coupled Thermosphere Ionosphere Plasmasphere Electrodynamics (CTIPe, Fuller-Rowell and Rees, 1983**;** Codrescu et al., 2012), and the Global Ionosphere Thermosphere Model (GITM, Ridley et al., 2006). Most of the upper atmospheric models use the F10.7 index, the Mg-II index, or a modified F10.7 index to prescribe the solar variability and initialize the EUV parameterization routine.

It is essential to understand the fundamental behavior of the ionosphere during both low and high solar activity. Therefore, this study is focused on finding the correlation and time delay between global mean TEC (GTEC) and solar proxies during a low solar activity (January 2007 - December 2009) and a high solar activity (January 2013 - December 2015) period. To derive the periodicities in the GTEC and solar parameters, the cross-wavelet method will be utilized. Preliminary results of the CTIPe model to estimate the delay during low and high solar activity will also be presented.

2. Data and model description

2.1. Data sources

We have computed daily GTEC values using global ionospheric maps available from the International GNSS Service (IGS, Hernandez-Pajares et al., 2009) provided by NASA's data archive service (CDDIS, 2017). IGS-TEC maps are available in a latitude/longitude resolution of 2.5°/ 5° with a time resolution of 2 hours. To represent the solar variability, numerous solar proxies are available. We use daily values of F10.7 and the Bremen composite Mg-II index (Snow et al., 2014). The F10.7 index and the TIMED/SEE integrated EUV flux datasets are taken from the LISIRD (DeWolfe et al., 2010) database. Direct EUV measurements are available from the TIMED satellite. The NASA TIMED satellite was launched in 2001 and carries four instruments (GUVI, SABER, SEE and TIDI), orbiting at an altitude of 625 km (Woods et al., 2005). TIMED measures atmospheric density, temperatures, winds, and solar ultraviolet radiation. TIMED/SEE provides solar EUV irradiance measurements since January 22, 2002. The instrument is designed to measure the soft X-rays and EUV/UV radiation from 0.1 to 193 nm with a spectral resolution of 0.1nm. SEE includes two instruments, the EUV grating spectrograph and the XUV (soft x-rays) photometer system (Woods et al., 2000). We have used the daily integrated value of solar irradiance from 5.5 to 105.5 nm.

2.2. CTIPe model description

The CTIPe model is a global, 3-D, time-dependent, nonlinear, physics-based numerical model. It consists of four components, namely (a) a neutral thermosphere model (Fuller-Rowell and Rees, 1980), (b) a mid- and high-latitude ionosphere convection model (Quegan et al., 1982), (c) a plasmasphere and low latitude ionosphere (Millward et al., 1996), and (d) a self-consistent electrodynamics model (Richmond et al., 1992), which run simultaneously and are fully coupled. The thermosphere model solves the equations of momentum, continuity, and energy to calculate global temperature, density, wind components, and atmospheric neutral composition. The numerical solution of the composition equation with the energy and momentum equations describe the transport, turbulence, and diffusion of atomic oxygen, molecular oxygen and nitrogen (Fuller-Rowell and Rees, 1983). The latitude/longitude resolution is 2°/18°.

In the vertical direction, the atmosphere is divided into 15 levels in logarithmic pressure from 1 Pa to $8.73 \cdot 10^{-7}$ Pa with a step of one scale height. The corresponding geometric heights are variable depending on temperature. External inputs like solar UV and EUV, Weimer electric field, TIROS/NOAA auroral precipitation, and tidal forcing are required to drive the model. The F10.7 index is used as input proxy to drive the ionization, photodissociation and heating rates. The lower boundary is characterised by output of the Whole Atmospheric model (WAM, Akmaev, 2011). The F10.7 index is used in an artificial manner as input solar proxy to calculate ionization, heating, and oxygen dissociation processes in the ionosphere. For the simulation, a reference solar spectrum based on the EUV flux model for Aeronomic Calculations (EUVAC) (Richards et al., 1994), driven by variations of input F10.7 is used in the model. More description of CTIPe is available in Codrescu et al. (2008, 2012).

3. Results and discussion

3.1. Variation in TEC and solar EUV proxies

Here we have filtered the datasets using a low pass filter with a cut off period of three months. The filtered datasets have been normalized by subtracting the average value of the respective study period and dividing by the standard deviation. Figure 1 shows the normalized time series of GTEC, daily integrated SEE-EUV flux, F10.7 index, and MG-II index, while the curves are offset by 2 each. Figure 1(a) shows the data during the extended part of solar cycle 23 from 2007 to 2009. During this period solar activity was extremely low, which is also the case for the 27-day amplitudes. In comparison to the low solar activity years, Figure 1(b) shows stronger activity at the 27 days solar rotation period for the years of higher solar activity (2013-2015).

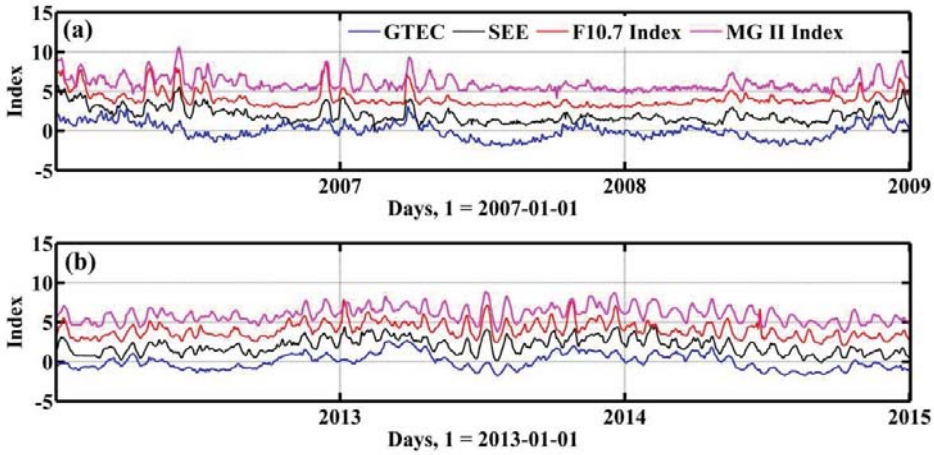

Fig. 1. Temporal variations of normalized datasets of GTEC (blue), SEE-EUV flux (black), F10.7 index (red), and Mg-II index (magenta) during (a) low (2007-2009) and (b) high (2013-2015) solar activity years. The curves are vertically offset by 2 each.

As shown in Figure 2(a), weaker correlation is observed during the low solar activity years between TEC and both the solar proxies in comparison to high solar activity years. During low solar activity years, the F10.7 index shows weaker correlation with the GTEC (Chen et al., 2011). In the correlation analysis during low (high) solar activity cycle, a correlation coefficient of 0.59 (0.77), 0.48 (0.64), and 0.50 (0.70) has been observed between normalized TEC and integrated EUV flux (black), F10.7 index (red), and MG-II index (figure not shown) respectively. The possible reason for the weaker correlation during low solar activity is the tidal forcing from the lower atmosphere, resulting in variability of GTEC (Lee et al., 2012). A strong correlation has been observed during high solar activity years. Mg-II index and SEE EUV flux shows stronger correlation with TEC than the F10.7 index. Jacobi et al. (2016) analyzed GTEC and Solar Dynamic Observatory/Extreme Ultraviolet Variability Experiment (SDO/EVE) integrated EUV flux data from 2011 to 2014 and they found a correlation of about 0.89. In comparison to the F10.7 index and sunspot number, solar EUV flux shows stronger correlation with GPS-TEC during the years 2010 to 2014

(Patel et al., 2017). Furthermore, to estimate the delay in GTEC with respect to solar proxies, the cross-correlation method has been used. In comparison to GTEC, all the solar proxies show a delay of 1-2 days. This means that solar radiation variations take about 1-2 days to influence the ionosphere. Various authors reported a similar ionospheric delay using solar proxies and GTEC (Jakoswki et al., 1991; Lee et al., 2012; Jacobi et al., 2016). According to Jakowski et al. (1991) this is possibly due to slow diffusion of atomic oxygen at 180 km or vertical transport processes.

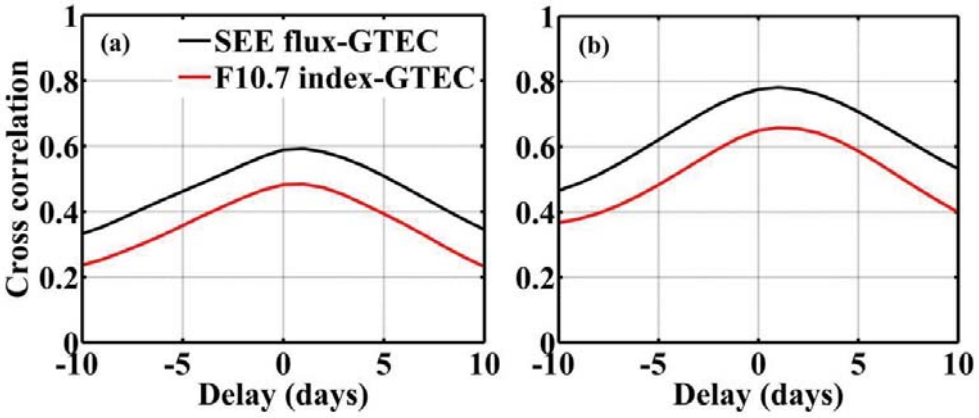

Fig. 2. Cross-correlation of GTEC with the SEE-EUV flux (black) and the F10.7 index (red) during (a) low (2007- 2009) and (b) high (2013-2015) solar activity years. Positive values denote GTEC lagging SEE-EUV or F10.7.

3.2. Wavelet analysis

To further investigate the nature of the relation between oscillations in the solar proxies and GTEC, the cross-wavelet technique has been used (Grinsted et al., 2004). This method indicates common high energy and relative phase between two-time series. Two continuous wavelet transforms using Morlet wavelet as mother function have been constructed.

Figure 3(a-b) shows the cross-wavelet spectra between GTEC with SEE–EUV flux (upper panel) and F10.7 (lower panel) index are during low solar activity years (left) and 3(c-d) during high solar activity years (right). All datasets have been normalized as described in section 3.1. From the figure, it is visible that during low solar activity the cross-wavelet spectra show weak power at the 27 days periodicity. In contrast to low solar activity years, a high energy region is observed at the 27 days periodicity during 2013-2015. All the arrows in the significant region show that GTEC is in phase with SEE and F10.7 index at 27 days periodicity. Thus, from this Figure it can be concluded that solar proxies influence GTEC mainly at the 27 days solar rotation period, which indicates that the solar forcing is strongly affecting the ionospheric activity. Guo et al. (2015) used the cross-wavelet and wavelet coherence methods to estimate the relation between TEC and sunspot numbers during the years 1999 to 2013. They found strong coherence at the solar rotation period, except for the extended solar minima years 2008-2009.

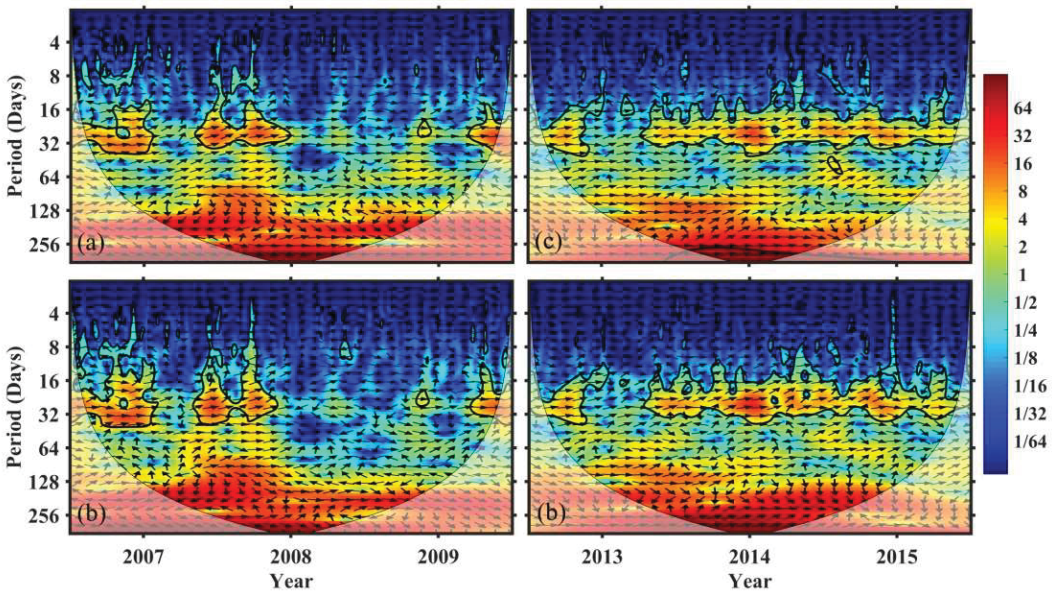

Fig. 3. Upper row: cross-wavelet transform of GTEC with (upper row) SEE-EUV flux and (lower row) F10.7 index during (a-b) low (2007- 2009) and (c-d) high (2013-2015) solar activity years. The cone of influence is shown by a black line. The arrow shows the phase relationship: in-phase pointing right, anti-phase pointing left and down-ward direction means that TEC is leading.

3.3. CTIPe simulated 27 days variation in TEC

The CTIPe model has been used to understand the role of solar EUV radiation in the ionospheric TEC variations. The F10.7 index is used as a model input. During the experiments, the model was run for 30 days by keeping all input parameters constant to attain the diurnally reproducible state and after this spin-up, the input was modified. We have used constant atmospheric conditions for 15 March 2013, and run the model by varying the F10.7 index for the 27 days solar rotation period.

The behavior of the ionosphere varies with solar activity. To understand this concept, we ran the CTIPe model for both low and high solar activity conditions. The F10.7 index was selected for low (70-75 sfu) and high (100-140 sfu) solar activity as shown in Figure 4(a, b), respectively, as a line plot. The simulated zonal mean TEC is shown in Figure 4 as background contour plot. The figure shows the variation in the output TEC with respect to the solar activity. Solar activity controls the ionization process in the ionosphere, which results in increase or decrease of the electron density. The model is capable to simulate the TEC distribution according to input solar activity. The electron density enhancement at low latitudes is due to the fountain effect (Appleton 1946).

As with the data analysis in section 3.1, we utilize the cross-correlation method to estimate the time delay between CTIPe simulated GTEC data and input F10.7 index for low and high solar activity, as shown in Figure 4(c,d). An ionospheric delay of about 1 day in GTEC with respect to the F10.7 index during low and high solar activity years

is observed. Note that in comparison to low solar activity, weaker correlation is observed during high solar activity conditions, which is not supported by the observations. A possible reason is that during solar maximum, EUV varies at different time scales, leading to considerable variability not necessarily directly correlated with TEC, which is not reproduced in our model experiment, where the F10.7 variability was chosen as purely sinusoidal.

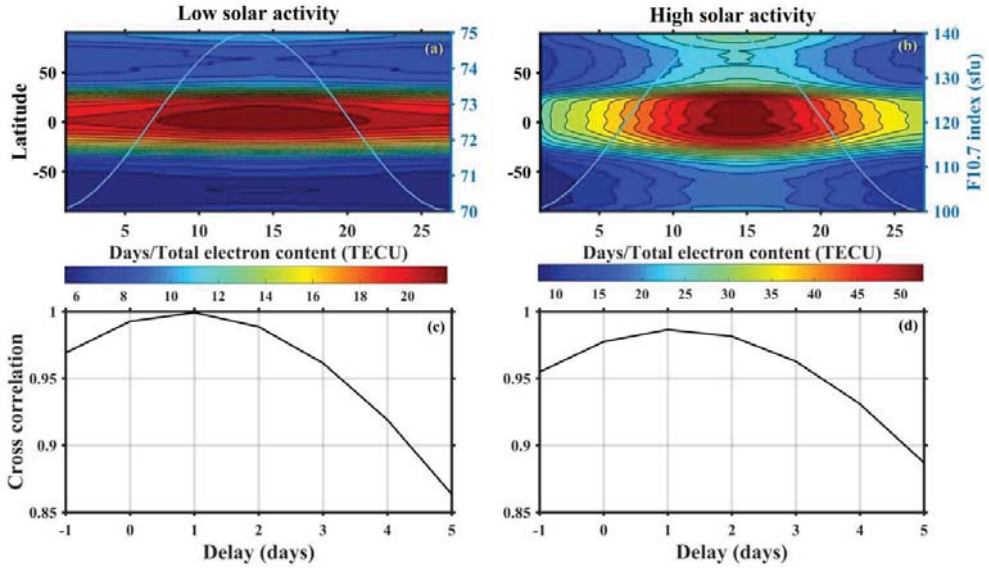

Fig. 4. Upper panel: simulated zonal mean TEC (background contour plot) and input F10.7 index (line plot) for (a) low and (b) high solar activity conditions. Lower panel: corresponding cross-correlation plots between the F10.7 index and modeled GTEC.

4. Summary and Conclusion

We analyzed GTEC and solar proxies datasets to investigate the ionospheric behavior during low (2007-2009) and high (2013-2015) solar activity years. The correlation between GTEC and SEE integrated EUV flux was stronger during high solar activity years than during low solar activity years. Whereas, the F10.7 index results in weaker correlation. An ionospheric delay of about 1 day in GTEC against solar parameters during both low and high solar activity years is observed. As shown by cross-wavelet analysis, EUV flux and F10.7 index show similar characteristics of correlation with GTEC during low and high solar activity years. From this analysis, it is clearly visible that solar radiation is strongly influencing the GTEC at the 27 days solar rotation period.

We have used the CTIPe model to simulate GTEC during low and high solar activity conditions. The experiment was performed using the F10.7 index for low (70-75 sfu) and high (100-140 sfu) solar activity for 15 March 2013 conditions. Preliminary results using cross-correlation analysis show an ionospheric delay of 1 day in GTEC with respect to the F10.7 index during both low and high solar activity. In comparison to low solar activity, a weaker correlation has been observed during high solar activity. In this first approach, we have found that the CTIPe model is able to reproduce the

observed ionospheric delay. In further studies, we will also analyze photodissociation and ionization processes of atomic oxygen, molecular oxygen, and molecular nitrogen to check the validity of the results by Jakowski et al. (1991).

Acknowledgements

IGS TEC maps have been kindly provided via NASA through ftp://cddis.gsfc.nasa.gov/gnss/products/ionex/. Daily F10.7 indices and TIMED/SEE version 3A spectra have been provided by LASP at http://lasp.colorado.edu/lisird/noaa_radio_flux and http://lasp.colorado.edu/lisird/data/timed_see_ssi_l3a, respectively. Mg-II indices have been provided by IUP at www.iup.uni-bremen.de/UVSAT/Datasets/mgii. The study has been supported by Deutsche Forschungsgemeinschaft (DFG) through grant No. JA 836/33-1.

References

Afraimovich, E. L., Astafyeva, E. I., Oinats, A. V., Yasukevich, Yu. V., Zhivetiev, I. V., 2008: Global electron content: a new conception to track solar activity, Ann. Geophys., 26, 335–344, doi:10.5194/angeo-26-335-2008.

Akmaev, R. A., 2011: Whole atmosphere modeling: Connecting terrestrial and space weather, Rev. Geophys., 49, RG4004, doi:10.1029/2011RG000364.

Appleton, E. V., 1946: Two anomalies in the ionosphere, Nature, 157, 691. doi:10.1038/157691a0.

Astafyeva, E.I., Afraimovich, E.L., Oinats, A.V., Yasukevich, Y.V., Zhivetiev, I.V., 2008: Dynamics of global electron content in 1998–2005 derived from global GPS data and IRI modeling, Adv. Space Res., 42(4), 763-769.

BenMoussa, A., S. Gissot, U. Schühle, G. Del Zanna, F. Auchère, et al., 2013: On-orbit degradation of solar instruments, Sol. Phys., 288, 389–434, DOI: 10.1007/s11207-013-0290-z.

CDDIS: GNSS Atmospheric Products, available at: http://cddis.nasa.gov/Data_and_Derived_Products/GNSS/atmospheric_products.html, last access: 29 January, 2017.

Chen, Y., Liu, L., Le, H., Zhang, H., 2015: Discrepant responses of the global electron content to the solar cycle and solar rotation variations of EUV irradiance, Earth, Planets and Space, 67(1), 80.

Chen, Y., Liu, L., Wan, W., 2011: Does the F10.7 index correctly describe solar EUV flux during the deep solar minimum of 2007–2009? J. Geophys. Res., 116, A04304, doi:10.1029/2010JA016301.

Codrescu, M. V., Fuller-Rowell, T. J., Munteanu, V. , Minter, C. F., Millward G. H., 2008: Validation of the coupled thermosphere ionosphere plasmasphere electrodynamics model: CTIPe-Mass Spectrometer Incoherent Scatter temperature comparison, Space Weather, 6, S09005, doi:10.1029/2007SW000364.

Codrescu, M. V., Negrea, C., Fedrizzi, M., Fuller-Rowell, T. J., Dobin, A., Jakowsky, N., Khalsa,H., Matsuo, T., Maruyama, N., 2012: A real-time run of the Coupled Thermosphere Ionosphere Plasmasphere Electrodynamics (CTIPe) model, Space Weather, 10, S02001, doi:10.1029/2011SW000736.

DeWolfe, A. W., Wilson, A., Lindholm, D. M., Pankratz, C. K., Snow, M. A., Woods,T. N., 2010: Solar Irradiance Data Products at the LASP Interactive Solar

Irradiance Datacenter (LISIRD), In AGU Fall255 Meeting 2010, Abstract GC21B-0881.

Dudok de Wit, T., Kretzschmar, M., Lilensten, J., Woods, T., 2009: Finding the best proxies for the solar UV irradiance, Geophys. Res. Lett., 36, L10107, doi:10.1029/2009GL037825.

Forbes, J. M., Palo, S. E., Zhang, X., 2000: Variability of the ionosphere, J. Atmos. Sol-Terr. Phy., 62(8), 685-693.

Fuller-Rowell, T. J. Rees, D., 1980: A three-dimensional time-dependent global model of the thermosphere. J. Atmos. Sci., 37, 2545–2567, doi:10.1175/1520-0469(1980)037<2545:ATDTDG>2.0.CO;2.

Fuller-Rowell, T. J., Rees, D., 1983: Derivation of a conservation equation for mean molecular weight for a two-constituent gas within a three-dimensional, time-dependent model of the thermosphere, Planet. Space 270 sci., 31(10), 1209-1222, doi: 10.1016/0032-0633(83)90112-5.

Grinsted, A., Moore, J. C., Jevrejeva, S., 2004: Application of the cross wavelet transform and wavelet coherence to geophysical time series, Nonlinear proc. Geoph., 11(5/6), 561-566.

Guo J, Li W, Liu X, Kong Q, Zhao C, Guo B., 2015: Temporal-Spatial Variation of Global GPS- Derived Total Electron Content, 1999–2013. PLoS ONE 10(7): e0133378. doi:10.1371/journal.pone.0133378.

Hernandez-Pajares, M., Juan, J. M., Sanz, J., Orus, R., Garcia-Rigo, A., Feltens, J., Komjathy, A., Schaer, S. C., Krankowski, A., 2009: The IGS VTEC maps: a reliable source of ionospheric information since 1998, J. Geod., 83, 263–275.

Jacobi, C., Jakowski, N., Schmidtke, G., Woods, T. N., 2016: Delayed response of the global total electron content to solar EUV variations, Advances in Radio Science: ARS, 14, 175.

Jakowski, N., Fichtelmann, B., Jungstand, A., 1991: Solar activity control of Ionospheric and thermospheric processes, J. Atmos. Terr. Phys., 53, 1125–1130.

Kane, R. P., 1992: Sunspots, solar radio noise, solar EUV and ionospheric foF2, J. Atmos. Terr. Phy., 54(3-4), 463-466.

Lee, C. K., Han, S. C., Bilitza, D., Seo, K. W., 2012: Global characteristics of the correlation and time lag between solar and ionospheric parameters in the 27-day period, J. Atmos. Sol-Terr. Phys., 77, 219-224.

Liu, J. Y., Chen, Y. I., Lin, J. S., 2003: Statistical investigation of the saturation effect in the ionospheric foF2 versus sunspot, solar radio noise, and solar EUV radiation, J. Geophys. Res., 108(A2), 1067, doi:10.1029/2001JA007543.

Liu, L., Chen, Y., 2009: Statistical analysis of solar activity variations of total electron content derived at Jet Propulsion Laboratory from GPS observations, J. Geophys. Res., 114, A10311, doi:10.1029/2009JA014533.

Liu, L., Wan, W., Ning, B., Pirog, O. M., and Kurkin V. I., 2006: Solar activity variations of the ionospheric peak electron density, J. Geophys. Res., 111, A08304, doi:10.1029/2006JA011598.

Maruyama, T., 2010: Solar proxies pertaining to empirical ionospheric total electron content models, J. Geophy. Res., 15, A04306, doi:10.1029/2009JA014890.

Millward, G. H., Moffett, R. J., Quegan, S., Fuller-Rowell, T. J., 1996: A coupled thermosphere-ionosphere-plasmasphere model (CTIP), in Solar-Terrestrial Energy Pro-

gram: Handbook of Ionospheric Models, edited by R. W. Schunk. PP. 239–279, Cent. for Atmos. and Space Sci., Utah State Univ., Logan, Utah.

Min, K., Park, J., Kim, H., Kim, V., Kil, H., Lee, J., Rentz, S., Lühr, H., Paxton, L., 2009: The 27-day modulation of the low-latitude ionosphere during a solar maximum, J. Geophys. Res., 114, A04317, doi:10.1029/2008JA013881.

Mukhtarov, P., Pancheva, D., Andonov, B., Pashova, L., 2013: Global TEC maps based on GNSS data: 1. Empirical background TEC model, J. Geophys. Res., 118, doi:10.1002/jgra.50413.

Patel, N. C., Karia, S. P., Pathak, K.N., 2017: GPS-TEC variation during low to high solar activity period (2010-2014) under the northern crest of Indian equatorial ionization anomaly region, Positioning, 8, 13-35. doi10.4236/pos.2017.82002.

Quegan, S., Bailey, G. J., Moffett, R. J., Heelis, R. A., Fuller-Rowell, T. J., Rees, D., Spiro, R. W., 1982: A theoretical study of the distribution of ionization in the high-latitude ionosphere and the plasmasphere: First results on the mid-latitude trough and the light-ion trough, J. Atmos. Terr. Phys., 44(7), 619–640, doi:10.1016/0021-9169(82)90073-3.

Richards, P. C., Fennelly, J. A., Torr, D. G. 1994: EUVAC: A solar EUV flux model for aeronomic calculations, J. Geophys. Res., 99, 8981–8992, doi:10.1029/94JA00518.

Richmond, A. D., Ridley, E. C., Roble, R. G., 1992: A thermosphere/ionosphere general circulation model with coupled electrodynamics, Geophys. Res. Lett., 19(6), 601–604, doi:10.1029/92GL00401.

Ridley, A.J., Deng, Y., Toth, G., 2006: The global ionosphere–thermosphere model, J. Atmos. Sol. Terr. Phy., 68(8), 839-864.

Snow, M., Weber, M., Machol, J., Viereck, R., Richard, E., 2014: Comparison of Magnesium II core-to-wing ratio observations during solar minimum 23/24, J. Space Weather Space Clim., 4, A04, doi:10.1051/swsc/2014001.

Su, Y. Z., Bailey, G. J., Fukao, S., 1999: Altitude dependencies in the solar activity variations of the ionospheric electron density, J. Geophy. Res., 104(A7), 14879-14891.

Tapping, K. F., 2013: The 10.7 cm solar radio flux (F10.7), Space Weather, 11, 394–406, doi:10.1002/swe.20064.

Wolf, R., 1856: Mittheilungen über die Sonnenflecken, Vierteljahresschrift der Naturforschenden Gesellschaft in Zürich, 1, 151-161.

Woods, T. N., Bailey, S., Eparvier, F., Lawrence, G., Lean, J., McClintock, B., Roble, R., Rottmann, G. J., Solomon, S. C., Tobiska, W. K., White, O. R., 2000: TIMED Solar EUV Experiment, Phys. Chem. Earth, Part C, 25, 393–396, doi:10.1016/S1464-1917(00)00040-4.

Woods, T. N., Eparvier, F., Bailey, S., Chamberlin, P., Lean, J., Rottmann, G. J., Solomon, S. C., Tobiska, W. K., Woodraska, D. L., 2005: Solar EUV Experiment (SEE): Mission overview and first results, J. Geophys. Res., 110, A01312, doi:10.1029/2004JA010765.

6 hr tide seen in sporadic E layers

Jacobi, Ch.[+], Arras, C.[*]

+) Institute for Meteorology, Universität Leipzig, Stephanstr. 3, 04103 Leipzig, E-Mail: jacobi@uni-leipzig.de
**) German Research Centre for Geosciences GFZ, Potsdam*

Summary: The GPS radio occultation technique is used to study sporadic E (E_s) layer plasma irregularities of the Earth's ionosphere on a global scale using COSMIC/FORMOSAT-3 satellite constellation GPS signal-to-noise ratio (SNR) profiles. The maximum deviation from the mean SNR is attributed to the height of the E_s layer. E_s are produced by ion convergence due to vertical wind shear in the presence of a horizontal component of the Earth magnetic field, while the wind shear is provided mainly by solar tides. Indeed, close correlation between E_s and wind shear phases have already been found for the semidiurnal and terdiurnal tidal components. Here, we present the global distribution of quarterdiurnal (QDT) signatures in E_s occurrence rates. We find that, in accordance with upward energy flux, negative vertical phase gradients of QDT E_s signatures are observed. The maximum signal of QDT E_s is found at altitudes above 100 km. In the southern hemisphere, maximum QDT E_s occurrence rates are found in winter and during equinoxes. In the northern hemisphere, however, at altitudes above 100 km strong QDT activity is also visible.

Zusammenfassung: Die GPS-Radiookkultationstechnik wird verwendet, um ionosphärische Plasmairregularitäten in Verbindung mit sporadischen E- (E_s) Schichten auf globaler Skala zu untersuchen. Verwendet werden Signal-Rauschverhältnis- (SNR-) Profile. Die maximale Abweichung vom mittleren SNR wird der Höhe der E_s-Schicht zugeordnet. E_s werden durch Ionenkonvergenz aufgrund von vertikaler Windscherung in Anwesenheit einer horizontalen Komponente des Erdmagnetfeldes hervorgerufen, wobei die Scherung hauptsächlich durch solare Gezeiten verursacht wird. Tatsächlich wurden schon früher deutliche Übereinstimmungen zwischen dem Auftreten von E_s und den Phasen der halb- und dritteltägigen Gezeiten gefunden. Hier stellen wir die globale Verteilung der vierteltägigen (QDT) Signaturen in E_s-Auftretensraten vor. Es zeigt sich dass, in Übereinstimmung mit einem aufwärts gerichteten Energietransport, negative vertikale Phasengradienten der QDT in E_s auftreten. Die maximale Auftretenswahrscheinlichkeit liegt bei Höhen oberhalb von 100 km. Auf der Südhemisphäre fällt das Maximum der QDT in E_s-Auftretensraten in den Winter, während auf der Nordhemisphäre oberhalb von 100 km auch im Sommer starke QDT-Aktivität zu verzeichnen ist.

1. Introduction

The dynamics of the lower thermosphere are strongly influenced by atmospheric waves, including the solar tides with periods of a solar day, and its harmonics. Their wind amplitudes usually maximise around or above 120 km. In these regions, tidal amplitudes are of the order of magnitude of the mean wind. As a result, the solar tides drive the global circulation and more accurate knowledge of their spatial and temporal distribution leads to a better understanding of the wind fields in the lower thermosphere. Shorter period waves often have smaller amplitudes, so that in the past mainly the diurnal tide (DT), the semidiurnal tide (SDT), and also the terdiurnal tide (TDT) have been investigated. The quarterdiurnal tide (QDT), however, although it also forms an integral part of the middle and upper atmosphere dynamics, has attained much less attention, mainly due to its smaller amplitude. While, for example, near the surface the 6 hr-oscillation at times can be a major component e.g. in barographic records (e.g., Warburton and Goodkind, 1977), the amplitude in the mesosphere and lower thermosphere (MLT) is generally substantially smaller than those of the DT, SDT and also of the TDT. Consequently, only few attempts to determine the QDT characteristics from radar or satellite observations have been made so far. Examples of QDT analyses from radar observations have been presented by Smith et al. (2004) and Jacobi et al. (2017), and modelling of the QDT has also been made by Smith et al. (2004).

Earlier than in MLT winds or satellite observations, 6-hr tidal signatures have been observed in lower ionospheric sporadic E (E_s) parameters (Tong and Matthews, 1988; Morton et al., 1993). E_s layers are thin clouds of accumulated plasma, which occur primarily at midlatitudes and maximise during summer. They are generally formed at altitudes between 90 km and 120 km, i.e. in the lower thermosphere and the lower ionospheric E region. According to wind shear theory (Whitehead 1961) the process of E_s formation is an interaction between the Earth's magnetic field, the ion concentration, and the vertical wind shear. Neglecting diffusion, the vertical velocity component of the neutral gas, and the electric force, the vertical ion drift w_I may be written as (see Fytterer et al., 2014):

$$w_I = \frac{r \cdot \cos I}{1 + r^2} U - \frac{\cos I \cdot \sin I}{1 + r^2} V \,, \tag{1}$$

where U and V are the zonal and meridional wind components of the neutral gas, while I is the inclination of the Earth's magnetic field. The parameter $r = \nu/\omega$ describes the ratio of the ion-neutral gas collision frequency ν and the gyro frequency ω given by $\omega = eB_0/m_I$. Here, e is the elementary charge, B_0 is the total intensity of the Earth's magnetic field, and $\underline{m_I}$ is the ion mass. Note that in Eq. (1), in contrast to the usual notations in literature, Cartesian coordinates x, y, and z are used, pointing eastward, northward and upward, respectively. Considering that $r >> 1$ below ~115 km (Bishop and Earle, 2003), the zonal wind component is much more efficient in causing vertical plasma motion than the meridional wind component. Consequently, the second term of Eq. (1) may be neglected in the lower E region, and therefore negative vertical zonal wind shear primarily leads to the formation of E_s. Note that Eq. (1) holds only for magnetic midlatitudes (about 20° - 70°), where electric forces can be neglected.

Assuming that solar tides are the main source of the vertical wind shear, frequently providing larger vertical gradients than the background wind, tide-like structures are expected in E_s occurrence rates. Actually, the SDT and DT are generally accepted to be the major driver of E_s (Mathews, 1998), leading to the reproduction of downward moving tidal signatures e.g. in E_s ionosonde registrations (e.g. Haldoupis et al., 2006). By combining Global Positioning System (GPS) registrations and radar wind measurements, Arras et al. (2009) have shown that E_s occurrence frequencies actually maximize when the zonal wind shear provided by the SDT is negative. More recently, Fytterer et al. (2013, 2014) found a clear correlation between midlatitude radar zonal wind shear and E_s for the 8-hr component also, leading to the conclusion that not only DT and SDT, but TDT as well contributes to E_s formation. However, the 6-hr component has not yet been analysed in detail from GPS radio occultation (RO) observations, which motivates us to search for the QDT signature in Es occurrence rates (OR) derived from RO.

Therefore, in this paper we analyse the quarterdiurnal oscillation seen in E_s, obtained from GPS RO measurements by the FORMOsa SATellite mission-3/Constellation Observing System for Meteorology, Ionosphere and Climate (FORMOSAT-3/COSMIC). The paper is organised as follows. In section 2 the E_s detection is briefly described, while the QDT analysis from E_s OR is described in section 3. In section 4, the global distribution of the OR QDT signature is presented, and section 5 concludes the paper.

2. Analysis of sporadic E from COSMIC/FORMOSAT-3 radio occultations

The FORMOSAT-3/COSMIC constellation consists of six low-Earth orbiting (LEO) microsatellites which orbit the Earth at an initial altitude of ~800 km. The satellites perform RO measurement in both the neutral atmosphere and the ionosphere (Anthes et al., 2008). During an occultation, signals of rising or setting GPS satellites are received by a LEO satellite. While the signals pass Earth's atmosphere they are modified by atmospheric conditions, in particular ionospheric electron density, causing refraction and degradation of the GPS waves. More detailed information on the principles of the RO technique is given by Hajj et al. (2002) and Kursinski et al. (1997).

The method to derive E_s information from RO signals has been described in Arras and Wickert (2017). In brief, for our investigations, we use the Signal-to-Noise ratio (SNR) profiles of the GPS phase measurements. The SNR is very sensitive to height dependent changes in the electron density as they occur within an E_s layer. These vertically small variations in the electron density lead to phase fluctuations of the GPS signal which can be observed as a change of the signal power at the receiver (Hajj et al., 2002).

In order to avoid influences from the different basic signal power values on the further data treatment, every SNR profile is normalized first. In absence of ionospheric disturbances the SNR free-space value is almost constant at altitudes above 35 km. The SNR standard deviation profile is considered to include a disturbance in case it exceeds an empirically found threshold of 0.2. If large standard deviation values are concentrated within an altitude range of less than 10 km, it is assumed that the respective SNR profile includes the signature of an E_s layer. The height where the SNR value has the

strongest deviation from the mean of the SNR profile is assumed to be the altitude of the E_s layer.

Figure 1 shows 2007-2016 mean E_s occurrence rates (OR). OR have been calculated as the number of E_s within a 10° latitude and 10 km height window, divided by the number of RO in the respective latitude window. Figure 1 shows seasonal means for December–February (DJF), March–May (MAM), June–August (JJA) and September–November (SON). Maximum OR are found slightly above 100 km. OR maximise in summer. The summer maximum is more pronounced in the northern hemisphere, which is due to the South Atlantic Anomaly and the weaker magnetic field there, so that southern hemisphere summer OR are smaller than northern hemisphere ones. Near the equator, E_s OR are small, owing to the horizontal magnetic field at the magnetic equator, which does not allow electrons to follow the vertically moving ions, which results in low E_s OR there (e.g. Arras et al., 2008, 2010, 2013; Arras and Wickert, 2017).

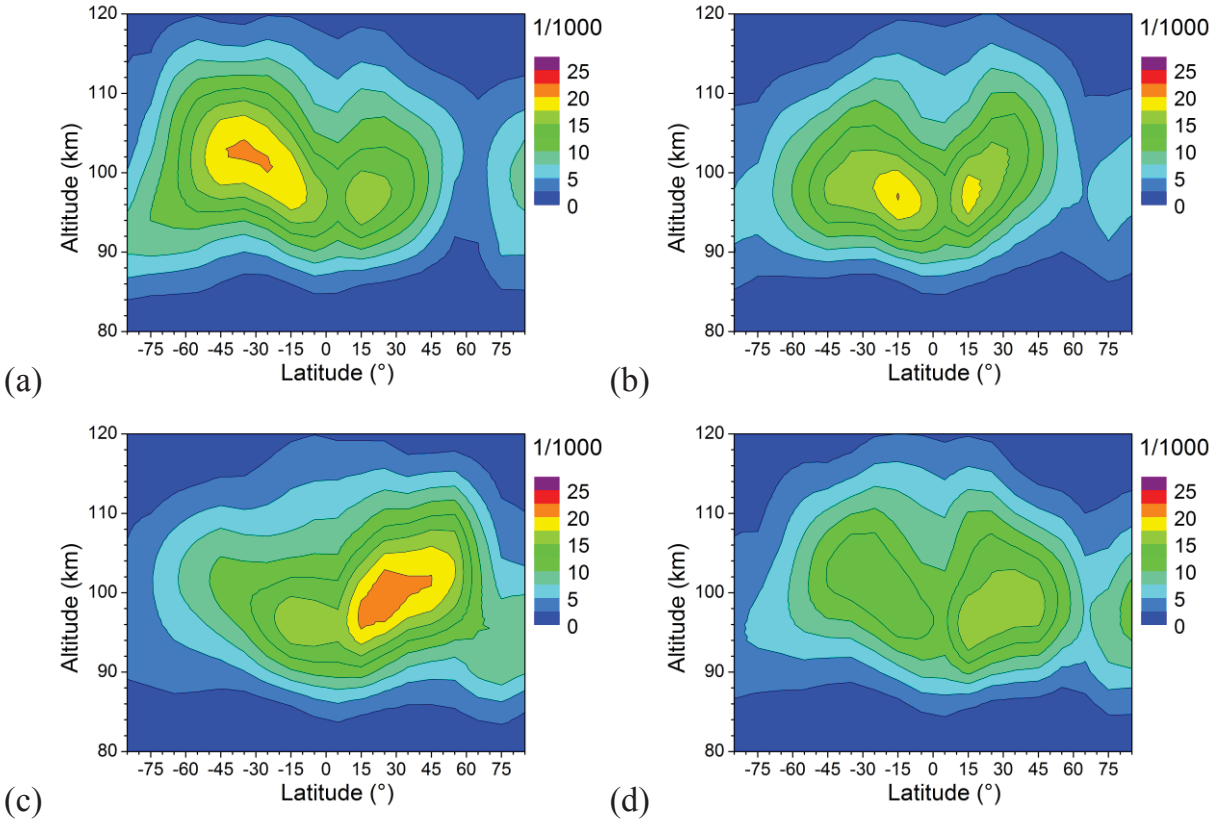

Fig. 1: 2007-2016 mean seasonal mean occurrence rates (a) DJF (b) MAM (c) JJA (d) SON.

3. QDT amplitudes in sporadic E occurrence rates.

In order to analyse the QDT signature in RO E_s, we sampled the detected E_s in a given latitudinal belt and height range according to local time, with a chosen time interval of one hour and a height range of 10 km. As with the global E_s OR, we divided the respective number of E_s by the number of RO in the time and latitude interval under consideration to obtain the OR. As an example, we show in Figure 2 the JJA diurnal

time-height distribution of OR for a latitude of 45 ± 5°N. We note the downward propagation of E_s OR signals, which are dominated by the SDT and, to a lesser degree, by a diurnal variation (see, e.g. Arras et al., 2009). Note that only migrating signatures, which are westward propagating with the sun, are visible in Figure 2 because we did not distinguish between latitudes in our analysis.

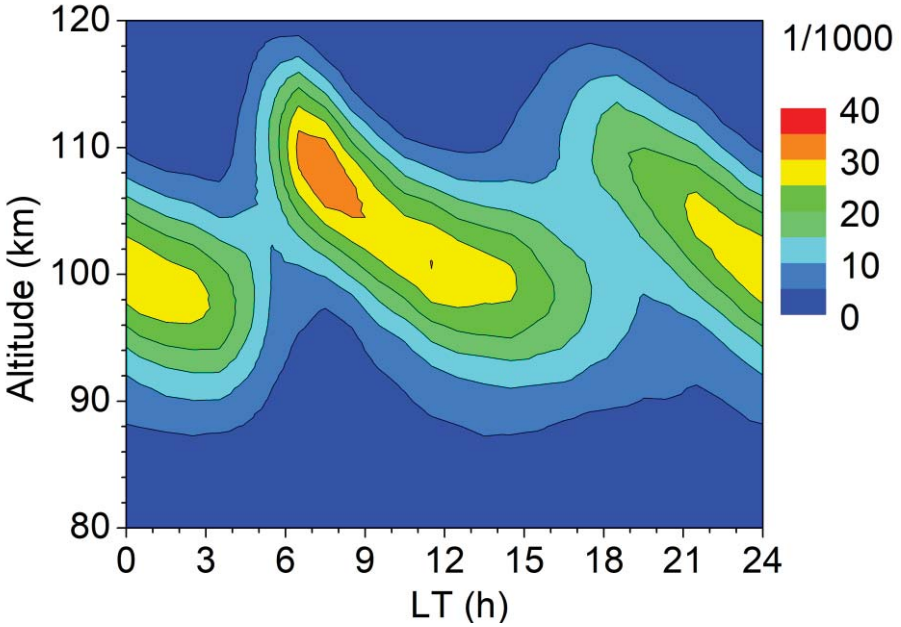

Fig. 2: Diurnal variation of E_s OR at 45 ± 5°N during summer (June-August, JJA). The OR in height gates of 10 km have been sampled, and the data have been attributed to the middle of the respective height interval.

In order to visualise the QDT component in E_s OR, we performed, for each altitude level separately, a multiple least-squares fit and analysed the respective 8-, 12-, and 24-h oscillation, which was then subtracted from the data exemplarily shown in Figure 2. The residual E_s OR for the same season and latitude as in Figure 2 are shown in Figure 3. A clear QDT component is now visible. The QDT phases, i.e. the times of maximum E_s OR for each altitude, are added as squares, while solid symbols denote significant amplitudes according to a t-test. These phases have been obtained from least-squares fitting analyses including the 6, 8, 12-, and 24 hr component. There is a downward phase progression, which is expected for the signature of a wave with upward energy flux.

The least-squares fit analyses of the QDT and the lower harmonics were then performed for each latitude between 85°S and 85°N in steps of 10°, and the results are shown in Figure 4. The amplitudes become small and irregular at low altitudes. Therefore, we present the data from 85 km onwards only. We note maximum amplitudes at midlatitudes with a maximum around 45°. In SON, the main maximum is however found at lower latitudes.

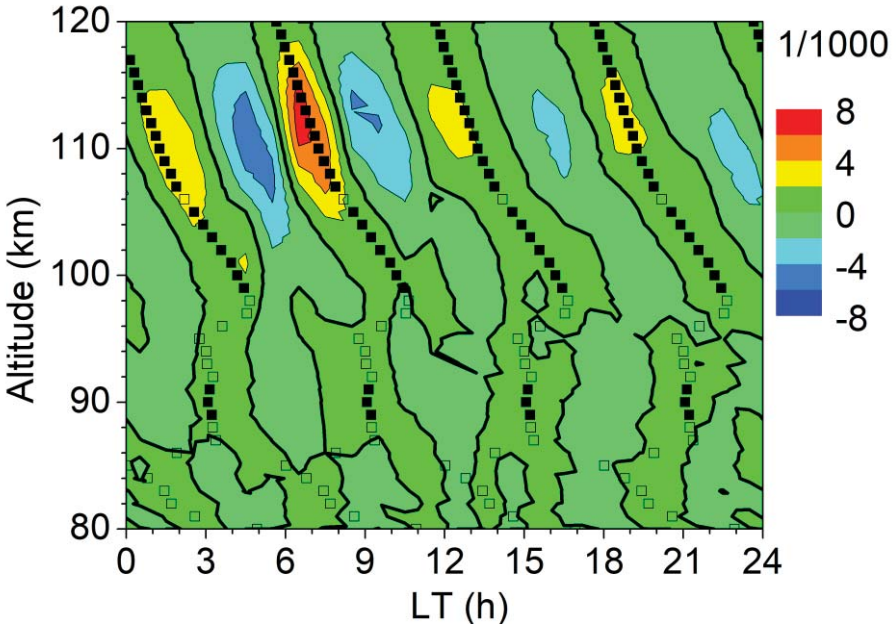

Fig. 3: JJA mean diurnal variation of E_s OR at 45 ± 5°N, after removing the 8, 12, and 24-hr components (contour lines). The QDT phases (times of maximum E_s OR) are added as squares. Solid symbols denote amplitudes significant at the 95% level according to a t-test.

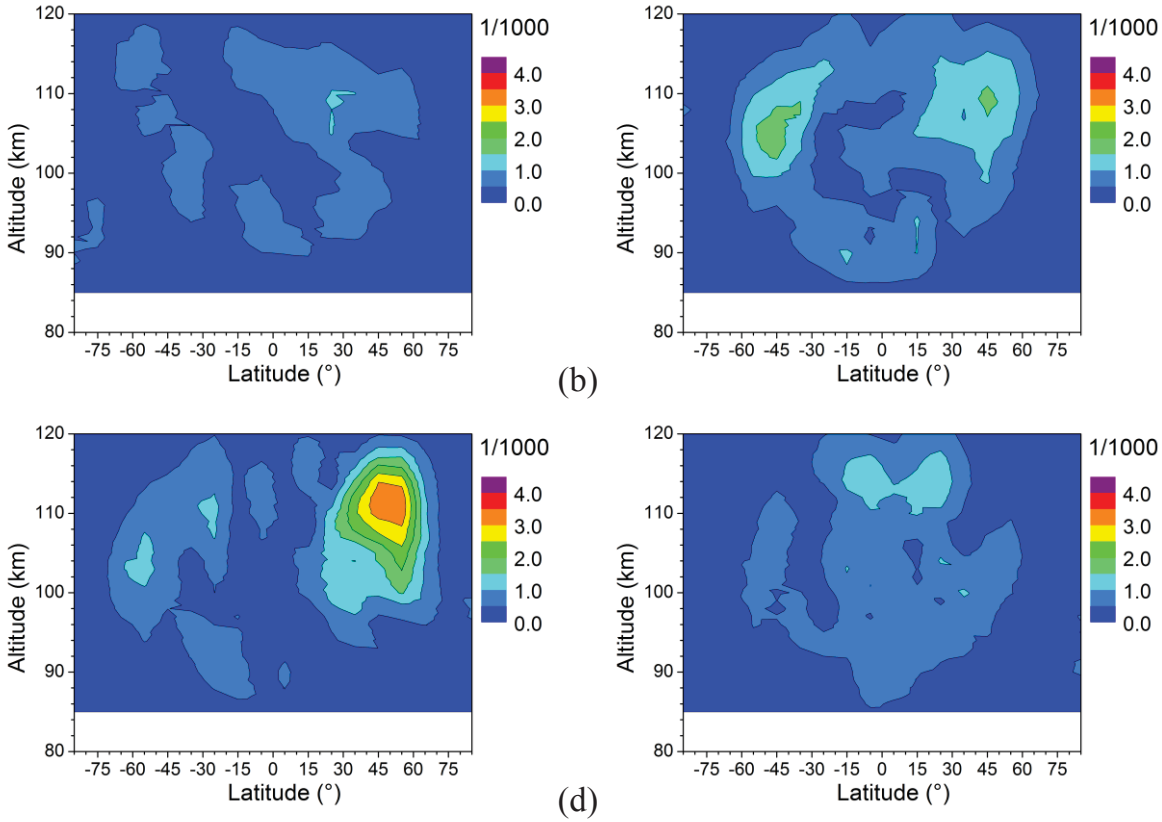

Fig. 4: 2007-2016 mean seasonal mean QDT amplitudes of E_s occurrence rates (a) DJF (b) MAM (c) JJA (d) SON.

4. Global distribution of QDT relative occurrence rate amplitudes

In Figure 3 and Figure 4, large QDT amplitudes are seen at altitudes between approximately 105 and 115 km. However, this does not necessarily reflect the distribution of the underlying tidal wave itself, because the OR amplitudes include both the dynamics, i.e. the 6 hr E_s signature production through QDT wind shear, and the background E_s OR, which is also influenced by background ionization, distribution of meteor rates (Haldoupis et al., 2007), and wind shear through other dynamical parameters. Therefore, to provide a better representation of the QDT, we divided the QDT amplitudes presented in Figure 4 by the background E_s OR shown in Figure 1 to obtain relative amplitudes, similar to the procedure described in Fytterer et al. (2014). These relative values are expected to more directly reflect the effect of the tides. Figure 5 shows the seasonal mean relative QDT amplitudes of E_s RO. The main difference to Figure 4 is that amplitudes in Figure 5 more strongly increase with altitude throughout the height range under investigation, which is more representative for a tide than a maximum at relatively low altitudes.

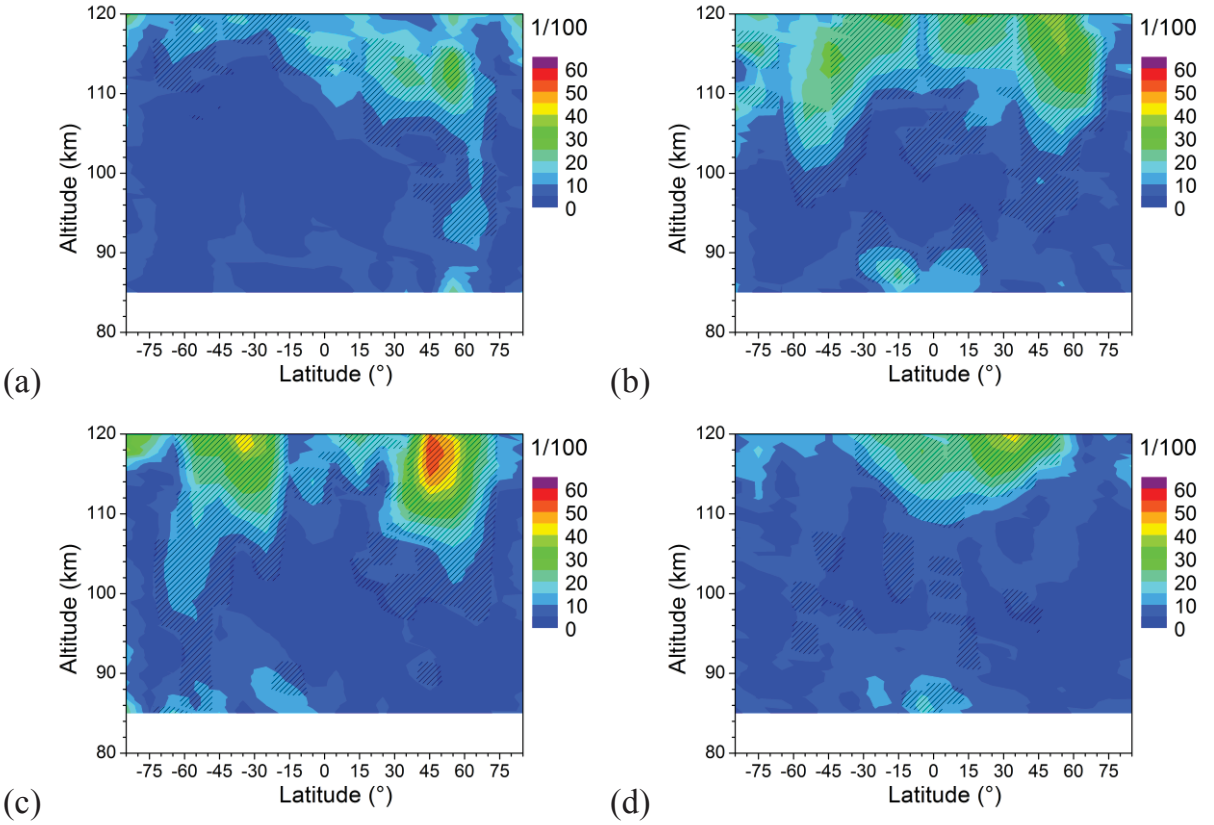

Fig. 5: 2007-2016 mean seasonal mean QDT relative amplitudes of E_s occurrence rates (a) DJF (b) MAM (c) JJA (d) SON. Values that are significant at the 95% according to a t-test are hatched.

The seasonal variation of E_s OR relative QDT amplitudes is shown in Figure 6 for 2 different heights. In contrast to the seasonal means presented above, mean relative amplitudes have been calculated here for each month. The figure shows that maximum relative amplitudes are seen at middle latitudes in both hemispheres, which is consis-

tent with SABER analyses of the QDT in temperature by Liu et al. (2015). At 95 km, there is a tendency for the QDT signature to maximize in the respective winter hemisphere. This has also been modelled by Smith et al. (2004), and is also seen in local radar observations at midlatitudes (Jacobi et al., 2017). At greater altitudes, the winter maxima are still visible. However, there is a strong summer maximum also, which only appears in the northern hemisphere.

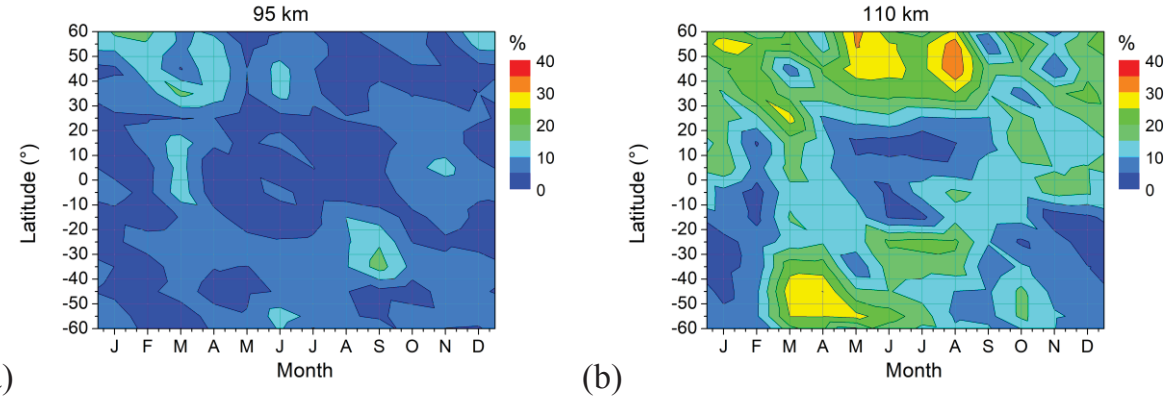

(a) (b)

Fig. 6: Seasonal variation of E_s OR relative QDT amplitudes for 2 heights. The amplitudes base on monthly values from 2007-2016.

5. Conclusions

Analysing E_s OR from FORMOSAT-3/COSMIC GPS RO allows us to show that there is, besides the known DT, SDT and TDT signatures, also a QDT signal in E_s. It shows a downward propagation of the phase, which is consistent with an upward energy flux of the tidal wave responsible for this component of E_s diurnal variability.

The global distribution of relative QDT amplitudes in E_s OR shows some features known for the QDT in neutral atmosphere parameters, in particular a winter maximum, which is well expressed especially in the southern hemisphere, and a summer minimum at southern latitudes. The latter, however, in the northern hemisphere is only seen at altitudes below 100 km, where the amplitudes are generally weak, and at greater heights there is a pronounced summer maximum which has not been reported from radar observations. Future analyses will have to include modelling of the QDT as well as the more detailed comparison of the E_s QDT with observations to shed light on this possible discrepancy.

Acknowledgements

The provision of FORMOSAT-3/COSMIC data by University Corporation for Atmospheric Research is gratefully acknowledged. Ch. Jacobi acknowledges support through the Deutsche Forschungsgemeinschaft (DFG) under grant JA 836/34-1. C. Arras acknowledges support by the DFG Priority Program DynamicEarth, SPP 1788.

6. References

Anthes, R. A., Bernhardt, P. A., Chen, Y., Cucurull, L., Dymond, K. F., Ector, S., Healy, S. B., Ho, S.-P., Hunt, D. C., Kuo, Y.-H., Liu, H., Manning, K., McCormick, C., Meehan, T. K., Randel, W. J., Rocken, C., Schreiner, W. S., Sokolovskiy, S. V., Syndergaard, S., Thompson, D. C., Trenberth, K. E., Wee, T.-K., Yen, N. L., Zhang, Z., 2008: The COSMIC/FORMOSAT-3 mission: early results, Bull. Am. Met. Soc., 89, 313–333, https://doi.org/10.1175/BAMS-89-3-313.

Arras, C., Wickert, J., Beyerle, G., Heise, S., Schmidt, T., Jacobi, Ch., 2008: A global climatology of ionospheric irregularities derived from GPS radio occultation, Geophys. Res. Lett., 35, L14809, https://doi.org/10.1029/2008GL034158.

Arras, C., Jacobi, Ch., Wickert, J., 2009: Semidiurnal tidal signature in sporadic E occurrence rates derived from GPS radio occultation measurements at midlatitudes, Ann. Geophys., 27, 2555–2563, https://doi.org/10.5194/angeo-27-2555-2009.

Arras, C., Wickert, J., Heise, S., Schmidt, T., Jacobi, Ch., 2010: Global sporadic E signatures revealed from multi-satellite radio occultation measurements, Adv. Radio Sci., 8, 225–230, https://doi.org/10.5194/ars-8-225-2010.

Arras, C., Wickert, J., Jacobi, Ch., Beyerle, G., Heise, S., Schmidt, T., 2013: Global sporadic E layer characteristics obtained from GPS radio occultation measurements. In: Lübken, F.-J. (Ed.): Climate and Weather of the Sun-Earth System (CAWSES), Springer, Berlin, 207–222.

Arras, C., Wickert, J., 2017: Estimation of ionospheric sporadic E intensities from GPS radio occultation measurements, J. Atmos. Sol.-Terr. Phys., https://doi.org/10.1016/j.jastp.2017.08.006.

Bishop, R. L., Earle, G. D., 2003: Metallic ion transport associated with midlatitude intermediate layer development, J. Geophys. Res., 108, A11019, https://doi.org/doi:10.1029/2002JA009411.

Fytterer, T., Arras, C., Jacobi, Ch., 2013: Terdiurnal signatures in sporadic E layers at midlatitudes, Adv. Radio Sci., 11, 333–339, https://doi.org/10.5194/ars-11-333-2013.

Fytterer, T., Arras, C., Hoffmann, P., Jacobi, Ch., 2014: Global distribution of the migrating terdiurnal tide seen in sporadic E occurrence frequencies obtained from GPS radio occultations, Earth, Planets and Space, 66:79, https://doi.org/10.1186/1880-5981-66-79.

Hajj, G., Kursinski, E., Romans, L., Bertiger, W., Leroy, S., 2002: A technical description of atmospheric sounding by GPS occultations, J. Atmos. Sol. Terr. Phys. 64, 451–469, https://doi.org/10.1016/S1364-6826(01)00114-6.

Haldoupis, C., Meek, C., Christakis, N., Pancheva, D., Bourdillon, A., 2006: Ionogram height-time-intensity observations of descending sporadic E layers at mid-latitude, J. Atmos. Solar-Terr. Phys., 68, 539–557, https://doi.org/10.1016/j.jastp.2005.03.020.

Haldoupis, C., Pancheva, D., Singer, W., Meek, C., MacDougall, J. 2007: An explanation for the seasonal dependence of midlatitude sporadic E layers. J. Geophys. Res. 112, A06315, https://doi.org/doi:10.1029/2007JA012322.

Jacobi, Ch., Krug, A., Merzlyakov, E., 2017: Radar observations of the quarterdiurnal tide at midlatitudes: Seasonal and long-term variations, J. Atmos. Sol.-Terr. Phys., 163, 70–77, https://doi.org/10.1016/j.jastp.2017.05.014.

Kursinski, E. R., Hajj, G., Hardy, K. R., Schofield, J. T., Linfield, R., 1997: Observing the Earth's atmosphere with radio occultation measurements using the Global Positioning System, J. Geophys. Res., 102, 23429–23465, https://doi.org/10.1029/97JD01569.

Liu, M. H., Xu, J. Y., Yue, J., Jiang, G. Y., 2015: Global structure and seasonal variations of the migrating 6-h tide observed by SABER/TIMED, Science China: Earth Sciences, 58, 1216, https://doi.org/10.1007/s11430-014-5046-6.

Mathews, J. D., 1998: Sporadic E: current views and recent progress, J Atmos, Solar-Terr. Phys. 60, 413–435. https://doi.org/10.1016/S1364-6826(97)00043-6.

Morton, Y. T., Mathews, J. D., Zhou, Q., 1993: Further evidence for a 6-hr tide above Arecibo, J. Atmos. Terr. Phys, 55, 459–465, https://doi.org/10.1016/0021-9169(93)90081-9.

Smith, A. K., Pancheva, D. V., Mitchell, N. J., 2004: Observations and modeling of the 6-hour tide in the upper mesosphere, J. Geophys. Res., 109, D10105, https://doi.org/10.1029/2003JD004421.

Tong, Y., and Mathews, J. D., 1988: An upper E region quarterdiurnal tide at Arecibo? J. Geophys. Res., 93, 10,047–10,051, https://doi.org/10.1029/JA093iA09p10047.

Warburton, R. J., Goodkind, J. M., 1977: The influence of barometric-pressure variations on gravity, Geophys. J. R. Astr. Soc., 48, 281-292, https://doi.org/10.1111/j.1365-246X.1977.tb03672.x.

Whitehead, J., 1961: The formation of the sporadic E layer in the temperate zones, J. Atmos. Terr. Phys., 20, 49–58, https://doi.org/10.1016/0021-9169(61)90097-6

Forcing of the Quarterdiurnal Tide

Ch. Geißler, Ch. Jacobi

Institute for Meteorology, Stephanstr. 3, 04103 Leipzig, E-Mail: christoph.geissler@uni-leipzig.de

Summary: Ensemble calculations for the period from 2000 to 2010 were carried out with the middle and upper atmosphere model (MUAM), and an analysis of the quarterdiurnal tide is performed. The global temporal and latitudinal distributions of the quarterdiurnal tide are modeled with MUAM, and their forcing mechanisms are examined. The quarterdiurnal tides show a similar distribution over the year in the northern and southern hemisphere, with maxima of the amplitude in late winter and spring as well as in autumn. In the latitude-height distribution is also shown that the largest amplitudes of the quarterdiurnal tide are seen at midlatitudes. Due to the decreasing density with height, there is a general increase of the tidal amplitudes with height. The results of the forcing analyses show that direct solar forcing is most important, but also that non-linear forcing and gravity wave interaction with other tides have a non-negligible influence on the quarterdiurnal tide in the middle and upper atmosphere.

Zusammenfassung: Mit dem Modell für die mittlere und obere Atmosphäre MUAM wurden Ensemble-Berechnungen für den Zeitraum 2000 bis 2010 durchgeführt und die vierteltägigen Gezeiten analysiert. Es wird auf die globale zeitliche und räumliche Verteilung der vierteltägigen Gezeiten eingegangen und deren Anregungsmechanismen untersucht. Die vierteltägigen Gezeiten zeigen einen ähnlichen Verlauf über das Jahr auf der Nord- und Südhalbkugel mit Maxima der Amplitude im späten Winter und Frühjahr sowie im Herbst. Ein ähnliches Bild zeigt sich auch für die Verteilung im Breiten-Höhen-Schnitt, wo die größten Amplituden der vierteltätigen Gezeiten in den mittleren Breiten zu finden sind. Aufgrund der abnehmenden Dichte mit der Höhe ist eine allgemeine Zunahme der Amplituden mit der Höhe zu beobachten. Es zeigte sich, dass der direkte solare Antrieb am stärksten ausgeprägt ist, aber auch, dass der nichtlinearer Antrieb und die Interaktion von Schwerewellen mit anderen Gezeiten einen nicht zu vernachlässigenden Einfluss auf die vierteltägigen Gezeiten in der mittleren und oberen Atmosphäre haben.

1. Introduction

Solar tides play an important role for the dynamics of the mesosphere and lower thermosphere (MLT) region. Tides have periods of a solar day and its subharmonics. They emerge mainly through absorption of solar radiation in the troposphere (water vapor) and stratosphere (ozone). The tidal amplitudes increase with height due to a decrease of density and conservation of energy (Chapman and Lindzen, 1970; Andrews et al., 1987). While diurnal, semidiurnal and terdiurnal tide are well understood, for the quarterdiurnal tide (QDT) there is still high research demand. There are some radar measurements available, e.g., at Collm (51°N, 13°E) and Obninsk (55°N, 37°E) as presented by Jacobi et al. (2017) and at Esrange (Smith et al., 2004), where analyses of the QDT had been made. Jacobi et

al. (2017) showed that the QDT at about 90 km has a maximum in zonal wind amplitude in January and during spring (April and May) of up to 3.5 ms^{-1} and in autumn (October and November) with about 3 ms^{-1}. Radar measurement at Esrange (68°N, 21°E) by Smith et al. (2004) show that the zonal wind amplitudes of the 6-hour tide between 85 km and 97 km are large in autumn, winter and early spring. Analyses of the QDT from satellite measurements (SABER) by Azeem et al. (2016) revealed that the QDT amplitudes in temperature increase with height and that there are maxima during the summer months (above 8 K) in the midlatitudes of the northern and southern hemisphere and near the equator. Liu et al. (2015) showed a ten years global distribution of the temperature amplitude of the 6h-tide in SABER measurements. They found that the largest amplitudes (up to 4 K) are seen in the midlatitudes of both hemispheres and at the equator. Liu et al. (2015) showed an increase of amplitude with height between 70 km and 110 km.

It is known from the terdiurnal tide that this tide can also be forced through interaction of other tidal components tide due to non-linear interaction, and due to possible interaction between tides and gravity waves (Beard et al., 1999); Akmaev, 2001; Du and Ward, 2010. Smith et al. (2004) showed in a model study that at 90 km the QDT has a maximum during autumn and winter months in the midlatitudes of the northern and southern hemisphere. They also showed that non-linear effects play an important role for the QDT. In a model run without solar forced 6h-tide they found the remaining non-linear forced tide makes up 50 % of the tide in the standard run (with solar forcing) during summer and one third in winter. Smith et al. (2004) did not look at the interaction between tides and gravity waves.

Generally, investigations of the 6-hr tide and its forcing mechanisms are rare. Therefore, it is necessary to conduct further model studies to see which respective influence solar forcing, gravity wave interaction, and nonlinear tide-tide interaction has on the QDT. It is also important to see if the results of Smith et al. (2004) can be confirmed by the MUAM model, and which forcings play a major role in the non-linear interaction. The remainder of this paper is structured as follows: The first part includes the model description and the used experimental setup. After that the results are presented and in the last part they are discussed.

2. Model Description and Experimental Setup

The middle and upper atmosphere model (MUAM) was used. MUAM is a 3D mechanistic global circulation primitive equation model of the middle atmosphere, which is based on the Cologne Model of the Middle Atmosphere-Leipzig Institute for Meteorology (COMMA-LIM, Fröhlich et al., 2003; Jacobi and Kürschner, 2006). In Pogoreltsev et al. (2007) the more recent version of the MUAM model is described. The model grid reaches from the surface (1000 hPa) up to the lower thermosphere (160 km in log-pressure height) with a vertical resolution of 2.842 km ($h = x \cdot H$ and $H = 7$ km as the scale height). Log-pressure heights are used with $x = ln\,(p_s/p)$ where p as pressure, $p_s = 1000$ hPa as a reference pressure. In the horizontal direction the model has a resolution of 5 × 5.625° and a time step of 225 s in the currently used 56-level version, which is following a Matsuno integration scheme (Matsuno, 1966). In the lower 30 km we nudge monthly mean ERA-Interim reanalyses of zonal mean temperature.

For the model experiments, ensemble runs are performed for 11 years (2000 to 2010). Stationary planetary waves at the lower boundary are not forced here to prevent coupling between stationary planetary waves and tides. The model includes gravity wave, solar, and infrared radiation parameterizations. Likewise, several ionospheric effects are parameterized. The model has a spin-up time of 120 model days. In that time zonal mean heating rates (no tides) form up a background climatology. The following 90 model days heating rates become zonally variable and tides begin to propagate. In the model there are three mechanisms that cause QDTs: solar heating, non-linear interaction between tides, and gravity wave-tidal interactions. Calculation of solar heating is following a Strobel parametrization (Strobel, 1978), which considers heating due to the most important gases like water vapor, carbon dioxide, ozone, oxygen and nitrogen. The carbon dioxide volume mixing ratio is taken from Mauna Loa Observatory data (NOAA ESRL Global Monitoring Division). The carbon dioxide mixing ratio, in the model assumed as horizontally invariable and constant up to 90 km is used in the model. The zonal mean ozone fields are taken from the Stratosphere-troposphere Processes And their Role in Climate project (SPARC; Randel and Wu, 2007) up to 50 km altitude. Non-linear effects can be evoked in the tendency equations of the model (e.g., Jakobs et al., 1986), i.e. in the temperature advection terms and in the zonal and meridional momentum equation terms. A gravity wave parametrization after Lindzen (1981) is used up to the mesosphere, for thermosphere and ionosphere a parametrization after Yigit et al. (2008) is used, which includes ionospheric effects like eddy diffusion. In our model experiment all three forcing processes are included. Carbon dioxide is fixed for the year 2005 (378 ppm for January), and this is also the case for the model ozone field. We performed 11 runs (ensemble) with different lower boundary conditions for the years 2000 to 2010 and calculated the 11-year mean and the standard deviation.

3. Model results

The results of the standard run that includes the solar, non-linear and the gravity wave forcing can be seen in Figure 1. QDT amplitudes of zonal wind (left), meridional wind (middle) and temperature (right) at 101 km altitude are shown for every latitude and month as mean over the 11-years of the ensemble run. Hatched areas show standard deviations larger than 0.1 ms^{-1} for zonal and meridional wind. Maxima of the QDT can be found in the southern and northern midlatitudes, and they reach values of 2 ms^{-1} for zonal and meridional wind amplitudes. Maxima can be seen during spring and autumn on both hemispheres, and also on the northern hemisphere in February and March, in May (only zonal wind), and in October and November. Maxima in the southern hemisphere occur in May, August and September. A second maximum in the zonal wind can be found in November around 50°S. This is the mostly the case at midlatitudes during autumn and winter months. The standard deviation is much stronger in the southern hemisphere because of a larger year-to-year variability. Maxima of the QDT amplitudes in temperature can be seen at midlatitudes in February, March and November in northern hemisphere and in May, August, and September in the southern hemisphere. Hatched areas show standard deviations larger than 0.05 K for temperature. Analogous to the zonal and meridional wind, the largest standard deviation can be seen in autumn and winter for the temperature amplitudes at midlatitudes.

To have a closer look at the tides two months are selected: September and November, to have a maximum at southern and northern hemisphere midlatitudes. The results as height–latitude plot are shown in Figure 2 for the amplitudes of zonal wind (left), meridional wind (middle) and temperature (right). Amplitudes for September (upper row) and November (lower row) are shown. The grey lines denote standard deviation in 0.2 ms^{-1} or 0.2 K, respectively. For September, the largest amplitudes occurs above 120 km at midlatitudes on both hemispheres, but the amplitudes in the southern hemisphere at midlatitudes are much stronger (above 5 ms^{-1}) for wind and temperature. The standard deviation over the northern hemisphere is slightly larger. Above 100 km, a third maximum occurs that can be found near the equator, but it is much smaller than the midlatitude ones.
The largest tides can be seen at midlatitudes. A maximum can be seen, mainly in meridional wind and temperature amplitudes, near the equator at higher altitudes. The same is visible for November, but the amplitude maxima are then seen at midlatitudes of the northern hemisphere. Overall, the amplitudes at midlatitudes of the northern hemisphere are stronger in November than in the midlatitudes of the southern hemisphere in September. Besides, the standard deviation is also considerably higher than in September and reaches up to 25% at midlatitudes of the northern hemisphere for the amplitudes in zonal wind. The different forcing terms of the QDT for September are shown in Fig. 3 and for November in Fig. 4, each scaled by density ($x = exp(-z/2 \cdot H)$). In the first row non-linear zonal wind advection and zonal gravity wave acceleration can be seen, in the second row non-linear meridional wind advection and meridional gravity wave acceleration is shown, in the third row non-linear temperature advection and gravity wave heating is presented, and the fourth row presents non-linear adiabatic heating and direct solar heating.
For September, important forcing terms of the QDT are the direct solar heating and the non-linear meridional wind advection. Forcing from solar heating takes place only below 80 km through water vapor and ozone absorption, and above 120 km due to extreme ultraviolet radiation absorption. The standard deviation (not shown) reaches up to 1×10^{-2} Kd^{-1} for the solar heating in the midlatitudes.

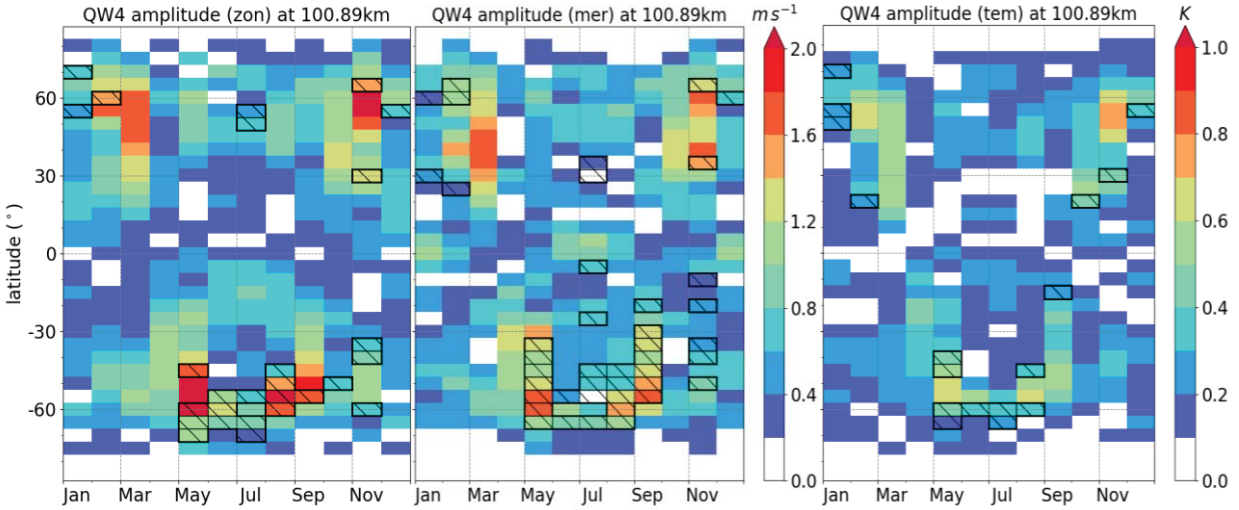

Fig. 1: 11 year mean quarterdiurnal tidal amplitudes of from MUAM simulations for zonal wind (left), meridional wind (mid) and temperature (right) for every month and latitude at 101 km. Hatched areas show months with standard deviation larger than 0.1 ms^{-1} for zonal and meridional wind and larger than 0.05 K for temperature.

Non-linear forcing occurs mainly at low latitudes, with a maximum between 10° and 20° on both hemispheres, up to the lower thermosphere. A secondary role compared with the other forcing terms plays the radiative cooling (not shown here), which can also effect a QDT. The standard deviation (not shown in the plot) is largest for the non-linear forcing of zonal and meridional wind advection in the middle and lower latitudes with up to 1×10^{-4} $ms^{-1}d^{-1}$ and up to 1×10^{-3} Kd^{-1} for temperature advection. Gravity wave forcing below 100 km arises from parameterized gravity waves, and shows largest values for zonal and meridional wind acceleration. Above 100 km the forcing is parameterized using by the Yigit type parametrization and shows maxima at midlatitudes for zonal wind acceleration and also in gravity wave heating above 100 km. The standard deviation of the zonal and meridional gravity wave acceleration has largest values up to 3×10^{-3} $ms^{-1}d^{-1}$ at midlatitudes below 100 km, and up to 3×10^{-2} Kd^{-1} for the gravity wave heating.

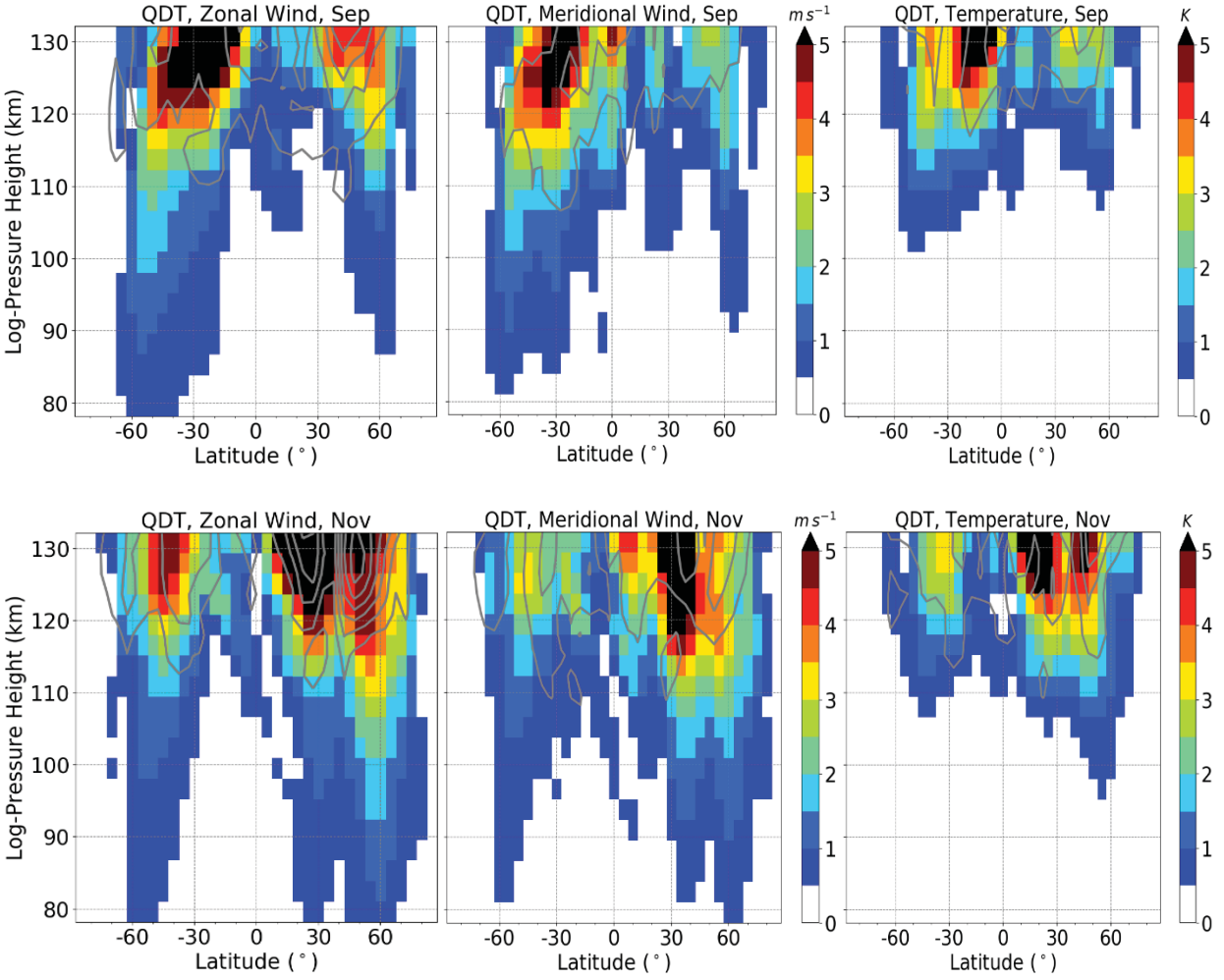

Fig. 2: 11 year mean quarterdiurnal tidal amplitudes of from MUAM simulations (colors) for zonal wind (left), meridional wind (middle) and temperature (right) at upper row for September and lower row for November.

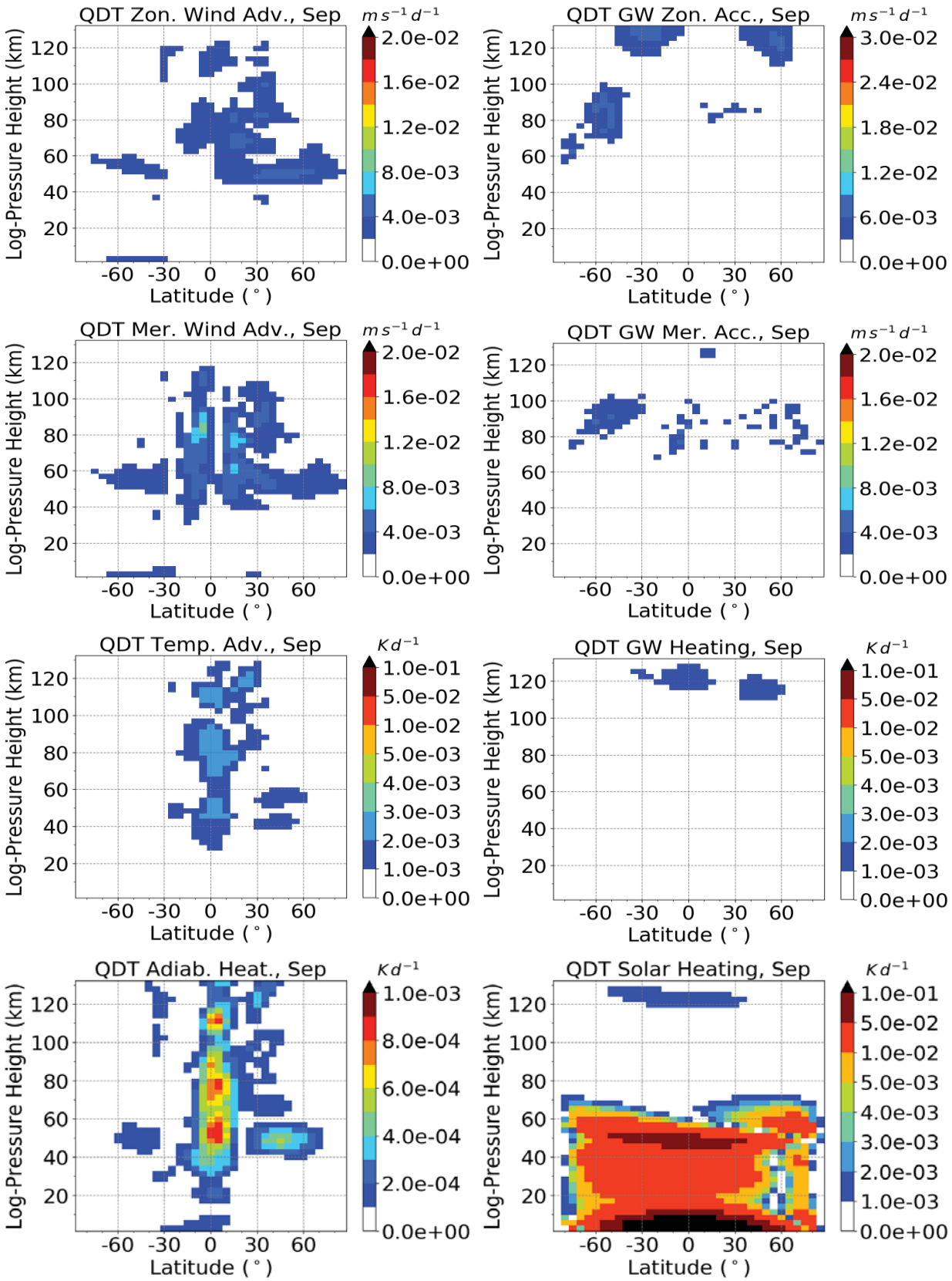

Fig. 3: Quarterdiurnal wavenumber 4 component of forcing terms scaled by density (from left to right) for September: 1st row: a) non-linear zonal wind advection, b) zonal GW acceleration, 2nd a) non-linear meridional wind advection, b) meridional GW acceleration. 3nd row: a) non-linear temperature advection, b) GW heating, 4th row a) non-linear adiabatic heating, b) direct solar heating.

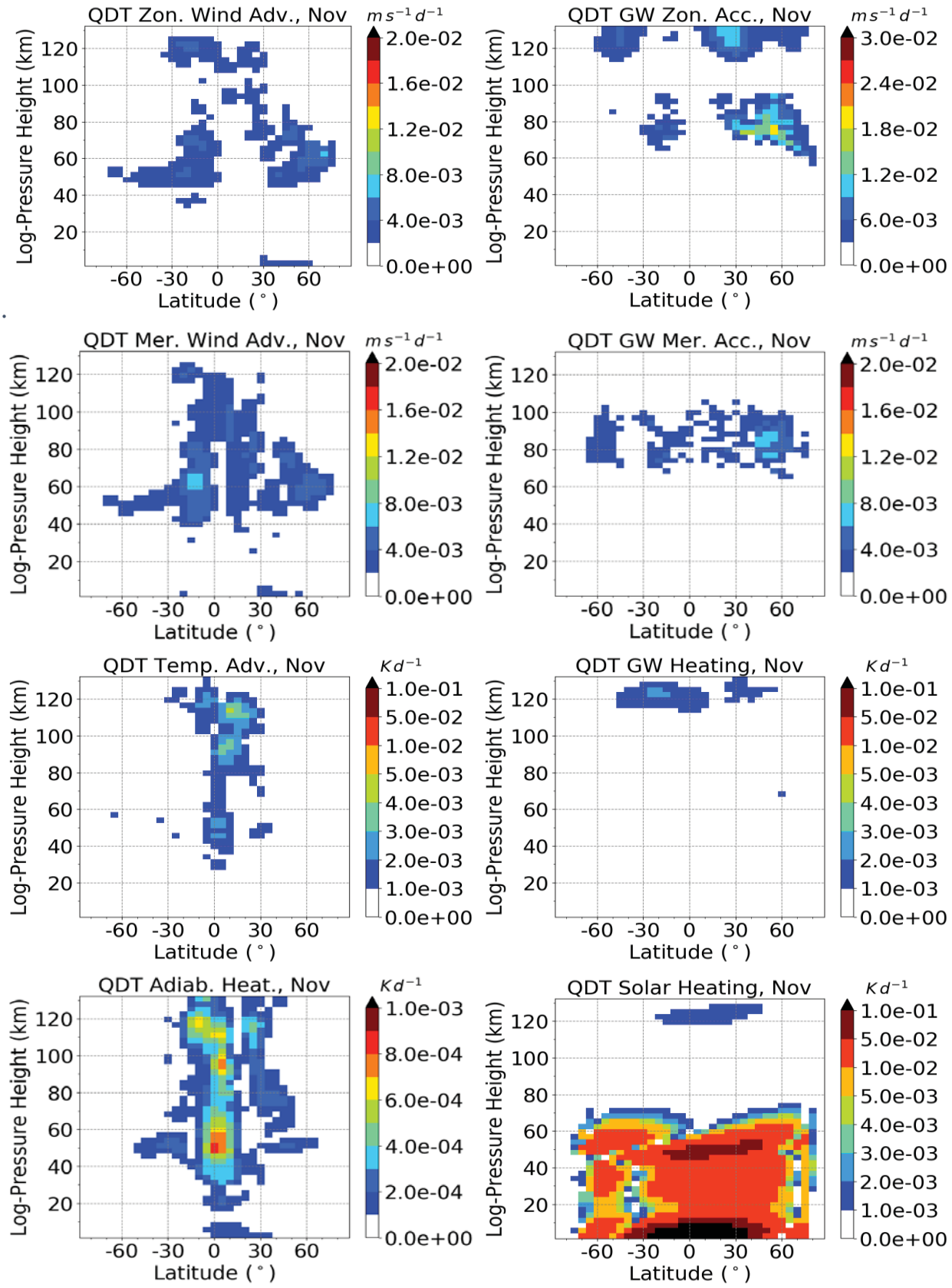

Fig. 4: Same as Fig. 3, but for November.

November (Fig. 4) shows a very similar spatial distribution of the forcing terms and their standard deviations compared to September. Solar heating is the most important forcing in November, but the influence of the gravity wave forcing is larger compared to September. Due to the stronger polar vortex in November the forcing of the gravity wave acceleration of zonal and meridional wind is much stronger in the northern midlatitudes than in September, but there is also a larger standard deviation because of larger year-to-year variability of the strength of polar vortex. The implication of this is that the amplitudes of the QDT must be stronger in November as in September and this can be seen in Fig. 2. In Fig. 3 showed also that the forcings at midlatitudes are larger in the northern hemisphere in November and in November with larger amplitudes in the southern midlatitudes. The weaker third maximum of the amplitudes, which can be seen near the equator in meridional wind and temperature amplitudes of the QDT, is caused from the forcing of non-linear effects like adiabatic heating and temperature advection.

5. Discussion and Conclusion

It could be seen from Figs. 3 and 4 that the direct solar forcing is the most important one for the QDT below 80 km, while non-linear forcing mainly occur at lower and middle latitudes between 20 km and 120 km. Gravity wave forcing plays a role above 80 km at midlatitudes. Smith et al. (2004) also shows that the solar forced QDT is largest. A less important role with much smaller resulting tide plays the non-linear forcing. Smith et al. (2004) indicate that the resulting tides are larger in the winter hemisphere as a consequence of a stronger non-linear forcing. Comparing the results from Fig. 1 with those of Smith et al. (2004) (ROSE model), Liu et al. (2015) (SABER/TIMED data), and Jacobi et al. (2017) (radar data), the amplitudes in the MUAM model are smaller. This could be caused by the lower meridional resolution of the MUAM model, so that the maxima of the QDT are not resolved correctly.

However, the distribution of maxima and minima of the QDT in Fig. 1 is similar than shown tides in other publications. In Smith et al. (2004) and Liu et al. (2015) the amplitudes have a maximum in the midlatitudes in spring and autumn (northern and southern hemisphere), which can also be seen in the MUAM model. The secondary maximum in May (northern hemisphere) and November (southern hemisphere) can be seen in Liu et al. (2015). In comparison with amplitudes from the meteor radar from Collm and Obninsk from Jacobi et al. (2017) for midlatitudes (Collm: 52°N, Obninsk: 55°N) it can be seen for zonal and meridional wind amplitudes that there are maxima in January, April, and November. But in the MUAM model is a time shift of two months in the maxima in late winter and spring. The temperature amplitudes for September and November in Fig. 2 show two larger maxima in the midlatitudes and a smaller one at the equator. This can also be seen in the ten years climatology from Liu et al. (2005), but the QDT amplitudes at 110 km show a stronger maximum at the equator than at northern midlatitude than in the MUAM model. A conclusion derived from the MUAM simulation and the discussion in comparison with other publications is that the direct solar forcing is the most important for the QDT. But monthly and seasonal variations in the strength of the non-linear and gravity wave forcing make these forcings only partially subordinate.

The largest QDT amplitudes can be seen at midlatitudes with maxima in late winter, spring (March and May), and autumn (November). The zonal mean of the amplitudes shows maxima in the midlatitudes and a second (smaller) one at the equator, but these maxima always increases with height up to 130 km. There are some differences in the amplitudes between the MUAM model and radar measurements for the maxima during winter and spring (time shift of one or two months). The height-latitude distribution from the MUAM model and the satellite data from Liu et al. (2015) show good comparison for the temperature amplitude of the QDT in the mesosphere and lower thermosphere.

Acknowledgements

ERA-Interim reanalyzes have been provided by ECMWF through www.ecmwf.int/en/research/climate-reanalysis/era-interim, and have been used in MUAM for assimilation in the troposphere as lower boundary condition. Carbon dioxide data were provided by NOAA: www.esrl.noaa.gov/gmd/ccgg/trends/. SPARC global ozone fields were provided by W.J. Randel (NCAR): ftp://sparc-ftp1.ceda.ac.uk/sparc/ref_clim/randel/o3data/.

References

Akmaev, R.,2001: Seasonal variations of the terdiurnal tide in the mesosphere and lower thermosphere: a modelstudy, Geophys. Res. Let., 28, 3817–3820, doi:10.1029/2001GL013002.

Andrews, D. G., Holton, J. R., and Leovy, C. B., 1987: Middle Atmosphere Dynamics, Academic Press Inc. (London) Ltd.

Azeem, I., Walterscheid. R. L., Crowley, G., Bishop, R. L., and Christensen, A. B., 2016: Observations of the migrating semidiurnal and quaddiurnal tides from the RAIDS/NIRS instrument, J. Geophys. Res. Space Physics, 121, doi:10.1002/2015JA022240.

Beard, A. G., Mitchell, N. J., Williams, P. J. S., and Kunitake, M., 1999: Non-linear interactions between tides and planetary waves resulting in periodic tidal variability, J. Atmos. Sol.-Terr. Phys., 61, 363–376, doi:10.1016/S1364-6826(99)00003-6.

Chapman, S., and Lindzen, R., 1970: Atmospheric tides - thermal and gravitational, p. 200, ix, D. Reidel Publishing Company (Dordrecht, Holland), 1970.

Du, J., and Ward, W., 2010: Terdiurnal tide in the extended Canadian Middle Atmospheric Model (CMAM), J. Geophys. Res., 115, D24, 106, doi:10.1029/2010JD014479.

Fröhlich, K., Pogoreltsev, A., and Jacobi, Ch., 2003: The 48 Layer COMMA-LIM Model: model description, new aspects, and climatology. Rep. Inst. Met. Leipzig 30, 157-185, http://meteo.physgeo.uni-leipzig.de/de/orga/LIM_VIII_HZ_Band_30.pdf.

Jacobi, Ch., and Kürschner, D., 2006: Long-term trends of MLT region winds over Central Europe, Physics and Chemistry of the Earth, Parts A/B/C, 31(1), 16-21, doi:10.1016/j.pce.2005.01.004.

Jacobi, Ch., Lilienthal, F., Geißler, Ch., and Krug, A., 2015: Long-term variability of mid-latitude mesosphere-lower thermosphere winds over Collm (51°N, 13°E), J. Atmos. Sol.-Terr. Phys., 136, 174-186, doi:10.1016/j.jastp.2015.05.006.

Jacobi, C., Krug, A., and Merzlyakov, E., 2017: Radar observations of the quarterdiurnal tide at midlatitudes: Seasonal and long-term variations, J. Atmos. Solar Terr. Phys., 163, 70-77, doi:10.1016/j.jastp.2017.05.014.

Jakobs, H. J., Bischof, M., Ebel, A., and Speth, P., 1986: Simulation of gravity wave effects under solstice conditions using a 3-D circulation model of the middle atmosphere, J. Atmos. Sol.-Terr. Phys., 48, 1203–1223, doi:10.1016/0021-9169(86)90040-1.

Lindzen, R. S., 1981: Turbulence and stress owing to gravity wave and tidal breakdown, J. Geophys. Res.: Oceans, 86, 9707–9714, doi:10.1029/JC086iC10p09707.

Liu, M. H., Xu, J. Y., Yue, J., and Jiang, G. Y., 2015: Global structure and seasonal variations of the migrating 6-h tide observed by SABER/TIMED, Science China: Earth Sciences, 58: 1216–1227, doi:10.1007/s11430-014-5046-6

Matsuno, T., 1966: Quasi-geostrophic motions in the equatorial area, J. Meteor. Soc. Japan, 44, 25-43, doi:10.2151/jmsj1965.44.1_25.

Pogoreltsev, A. I., Vlasov, A. A., Fröhlich, K., Jacobi, C., 2007: Planetary waves in Coupling the lower and upper atmosphere, J. Atmos. Sol.-Terr. Phys., 69, 2083-2101, doi:10.1016/j.jastp.2007.05.014.

Randel, W. J. and Wu, F.: A stratospheric ozone profile data set for 1979–2005, 2007: Variability, trends, and comparisons with column ozone data, J. Geophys. Res.: Atmos., 112, doi:10.1029/2006JD007339, d06313.

Smith, A. K., Pancheva, D. V., and Mitchell, N. J., 2004: Observations and modeling of the 6-hour tide in the upper mesosphere, J. Geophys. Res., 109, D10105, doi:10.1029/2003JD004421.

Strobel, D. F., 1978: Parameterization of the atmospheric heating rate from 15 to 120km due to O_2 and O_3 absorption of solar radiation, J. Geophys. Res.: Oceans, 83, 6225-6230, doi:10.1029/JC083iC12p06225.

Yigit, W., Aylward, A., and Medvedev, A., 2008: Parameterization of the effects of vertically propagating gravity waves for thermosphere general circulation models: Sensitivity study, J. Geophys. Res., 113, D19 106, doi:10.1029/2008JD010135.

Impact of intermittent gravity wave activity on the middle atmospheric circulation during boreal winter

Samtleben N. and Jacobi Ch.

Institute for Meteorology, Universität Leipzig, Stephanstraße 3, 04103 Leipzig, Germany
Email: Nadja.Samtleben@uni-leipzig.de

Summary: Simulations of the circulation in the middle atmosphere during northern winter performed with a nonlinear, mechanistic, global circulation model show that the upper mesospheric jet is greatly overestimated and also the position with respect to latitude and height does not correspond to observations. Apart from that also the winter wind reversal in the mesopause region, evoked by breaking gravity waves (GWs), is located too low around 80 km, but is observed to be usually around 100 km. These discrepancies are planned to be eliminated by modifying the distribution of GW amplitudes driving the GW parameterization. This distribution is currently based on potential GW energy data derived from GPS radio occultation measurements and has to be replaced by a distribution based on momentum flux estimates applying midfrequency approximation. The results show a weaker mesospheric jet more realistically tilted towards lower latitudes with height. Also the meridional circulation extending from the summer to the winter pole decelerates and less GWs are propagating into the mesosphere. By additionally varying the GW amplitudes in magnitude and time, the wind reversal is shifted upwards and the mesospheric jet is slowed down.

Zusammenfassung: Simulationen der Zirkulation der mittleren Atmosphäre während des nordhemisphärischen Winters unter Verwendung eines nicht-linearen mechanistischen globalen Zirkulationsmodells ergaben beim Vergleich mit Messungen, dass der simulierte, mesosphärische Jet stark überschätzt wird und dessen Position von den Beobachtungen abweicht. Die in der Mesopausenregion einsetzende Windumkehr, hervorgerufen durch brechende Schwerewellen, befindet sich in etwa 80 km anstatt in 100 km. Diese Diskrepanzen sollen eliminiert werden. Hierfür wird die Verteilung der Schwerewellenamplituden, die die Schwerewellenparametrisierung innerhalb des Modells antreibt, am oberen Rand der Troposphäre modifiziert. Diese basiert derzeit auf global beobachteten, zonal gemittelten Daten der potentiellen Energie von Schwerewellen abgeleitet aus GPS Radiookkultationsmessungen und soll durch eine auf Impulsflüssen basierende Verteilung ersetzt werden. Das Modellexperiment zeigt, dass der mesosphärische Jet mit der Höhe in Richtung niedriger Breiten geneigt ist und abgebremst wird. Zudem schwächt die Meridionalzirkulation vom Sommer- zum Winterpol leicht ab und weniger Schwerewellen dringen bis in die Mesosphäre vor. Zusätzlich wird durch zeitliche und unterschiedlich starke Variation der Schwerewellenamplitude die Windumkehr verlagert und der mesosphärische Jet abgebremst.

1. Introduction

The dynamics in the middle atmosphere are mainly dominated by the stratospheric and mesospheric jet and also by the impact of atmospheric waves with different spatial and temporal scales. The most important characteristic of atmospheric waves is their ability to transport and deposit energy and momentum from their origin. In particular gravity waves (GWs) distribute energy and momentum throughout the whole atmosphere thereby maintaining the circulation and the thermal structure of the upper atmosphere. They also contribute to turbulence and mixing between all vertical layers. GWs mainly develop in the troposphere [Fritts and Alexander, 2003]. Strongly depending on the phase speed c and the background wind u, GWs are able to propagate into the middle atmosphere. Their amplitude is exponentially increasing with height due to the exponentially decreasing density of the atmosphere. Usually, the GW spectrum is already saturated in the stratosphere which means that GW amplitudes cannot grow anymore and, according to the linear theory, partly break. This effect is the stronger the closer their phase speed c is to the background wind u. If $c=u$, the GW encounters its critical line and cannot propagate anymore. Thus, mainly GWs propagating into the opposite direction than the background wind are frequently observed in the middle atmosphere. Also GWs being faster than the background wind are able to propagate but they are filtered out by the strong mesospheric jet at the latest. For this reason the wind reverses in the mesosphere due to GW breaking, while in the opposite direction to u traveling GWs depositing their momentum [Lindzen, 1981; Holton, 1982].

Due to the huge amount of different trigger mechanisms GWs have a large spatial and temporal variability. They are not distributed homogenously and exhibit a large intermittency which is closely linked to the synoptic conditions, the source of the GWs and the propagation conditions. To capture the irregular global distribution of GWs the momentum flux (MF) is estimated by using satellite data [Ern et al., 2004; Preusse et al., 2006; Fröhlich et al., 2007; Schmidt et al., 2016] as well as the potential energy (E_{pot}), a proxy for GW activity. The potential energy can be derived from GPS radio occultation (RO) density [e.g. Šácha et al., 2015, 2016] or temperature [Ratnam et al., 2004a, b; Schmidt et al., 2016] measurements that are based on radio links between a low-earth orbiting satellite and a GPS satellite. To study specific characteristics like the phase speed, the wavelength, the wavenumber or the temporal development of the GW activity with a certain precision other measurements like lidar [Baumgarten et al., 2015; Witschas et al., 2017], radar [Gavrilov and Fukao, 1999; Oleynikov et al., 2005] or balloon measurements [Hertzog et al., 2012; Plougonven et al., 2012] are performed.

Based on this gained knowledge it is still complicated and extremely computer-time consuming to resolve GWs in global circulation models (GCMs). GWs have horizontal wavelengths of tens to hundreds of kilometers so that most of the GWs are subgrid scale due to the coarse resolution of GCMs. For this reason GWs are mostly parameterized by integrating a GW distribution in the lower part of the atmosphere either based on GW source parameterizations, or on specific functions or observed GW fields [Šácha et al., 2016; Lilienthal et al., 2017], especially from satellite data.

In this paper, we modify the prescribed GW field based on E_{pot} data from GPS RO density measurements [Šácha et al., 2015] by another one based on MF estimates that

have been derived from these E_{pot} field applying midfrequency approximation [Ern et al., 2004]. Also the distribution of small and large GW amplitudes and their temporal sequence are adapted. The aim is to create a more realistic model climatology of the middle atmosphere.

2. MUAM - Model description

MUAM [Pogoreltsev et al., 2007; Jacobi et al., 2015] is a non-linear mechanistic 3D grid point model which is an updated version of the global circulation model COMMA-LIM [Fröhlich et al., 2003a, b; Jacobi et al., 2006]. The model has a horizontal resolution of 5° in latitude and 5.625° in longitude. It has 56 vertical levels up to a logarithmic pressure height of about 160 km with a vertical resolution of 2.842 km and a scale height of H = 7 km. At 1000 hPa, the lower boundary of the model, stationary waves of zonal wavenumbers 1 to 3 are forced, which are extracted from 2000-2010 ERA Interim temperature and geopotential reanalysis data. Up to 30 km the zonal mean model temperature is nudged to zonal mean ERA Interim temperatures to correct the climatology of the troposphere, which is otherwise not included in the model. The model solves the primitive equations in flux form [Jakobs et al., 1986]. It includes parameterizations of solar radiation [Strobel, 1986], infrared cooling [Fomichev, 1998], and GWs. The latter are parameterized with an updated linear scheme [Lindzen, 1981; Jakobs et al., 1986] with multiple breaking levels [Fröhlich et al., 2003a, b; Jacobi et al., 2006]. Once a GW becomes unstable, the amplitude saturates and stops increasing exponentially with height. The MF is simultaneously reduced and the zonal mean flow is accelerated. The GW can have multiple saturation levels until the GW reaches a critical line and the MF becomes equal to zero. GW amplitudes are initialized at an altitude of 10 km as zonal mean with a global average of 1 cms^{-1} for the vertical velocity perturbation. In the standard configuration this value is weighted by a prescribed global GW amplitude distribution based on E_{pot} data obtained from GPS radio occultation measurements [Lilienthal et al., 2017]. At each grid point 48 waves are induced propagating in eight different directions with six different phase speeds.

Fig. 1 shows the zonal (a) and meridional wind (b), the temperature (c), zonal GW flux (d) and acceleration due to breaking GWs (e) in January as a latitude-height plot. The meridional circulation has a maximum of 4 ms^{-1} at about 80 km. This circulation leads to a warming/cooling of the winter/summer mesosphere (Fig. 1c) due to descending/ascending air. The northern hemisphere (NH) mesopause temperature is much higher than on the southern hemisphere (SH). The winter stratosphere is dominated by the polar vortex during polar night. The temperature becomes smaller than 210 K. In the summer stratosphere the temperature increases with height due to absorption of solar radiation by ozone and reaches a maximum of more than 270 K near the stratopause. As a result of the development of the stratospheric low pressure system above the pole on the NH and the increasing pressure and temperature towards lower latitudes, a west wind establishes with a maximum of about 50 ms^{-1} (Fig. 1(a)). Compared to reference climatologies like CIRA-86 [Fleming et al., 1988] or URAP [Swinbank and Ortland, 2003] (see Fig. 7 below) the jet is overestimated by more than 10 ms^{-1}. The mesospheric jet in climatologies is additionally tilted towards lower latitudes with

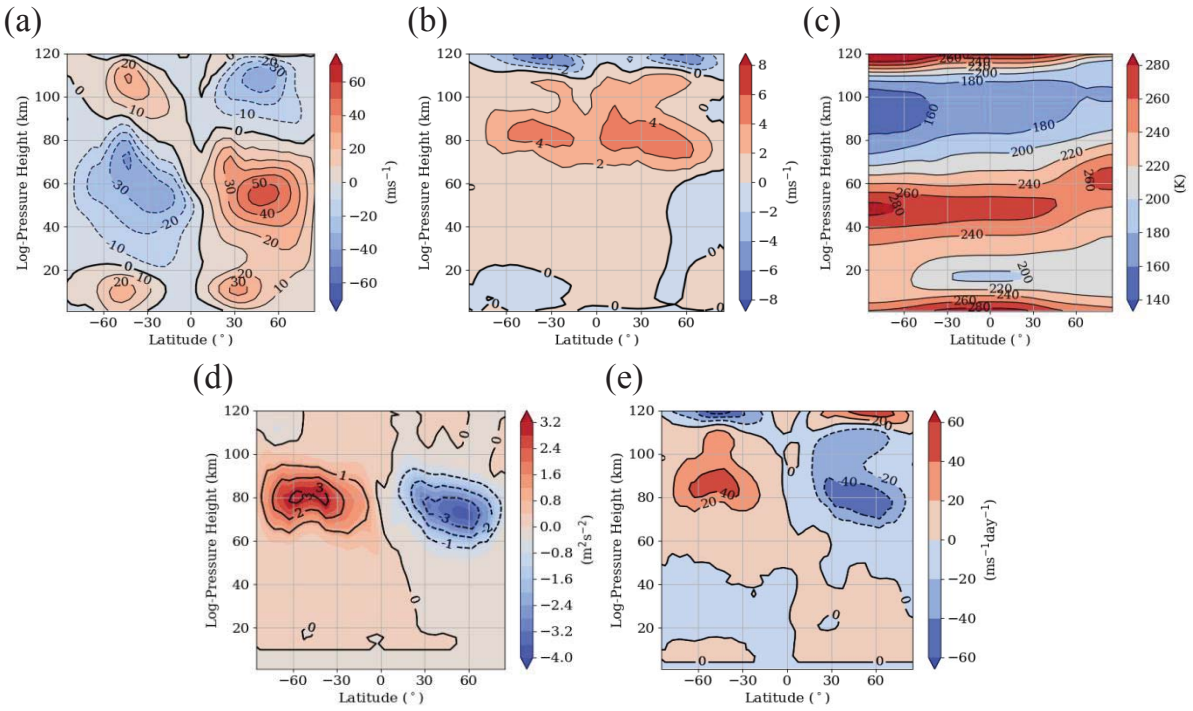

Figure 1: January zonal and monthly mean of the (a) zonal wind [ms^{-1}], (b) meridional wind [ms^{-1}], (c) temperature [K], (d) GW fluxes [m^{2}s^{-2}]and (e) acceleration through breaking GWs [ms^{-1}day^{-1}]. GW parameterization is based on E_{pot} data (standard configuration).

increasing altitude but this cannot be observed in the MUAM standard configuration results. The wind reversal above 80 km is due to breaking GWs. GW fluxes and acceleration due to breaking GWs are shown in Figs. 1(d) and (e).

3. Initialisation of gravity waves in the upper troposphere in MUAM

3.1. Different distributions of gravity wave amplitudes as zonal mean

Instead of using the GW distribution based on the observed E_{pot} data we calculated the MF distribution by applying midfrequency approximation according to Ern et al. [2004]. Therefore, the horizontal momentum flux F_h can be assigned to E_{pot} multiplied with the ratio of the horizontal and vertical wavenumbers k and m [Ern et al., 2004]:

$$F_h = \frac{1}{2}\rho\frac{k}{m}\left(\frac{g}{N}\right)^2\left(\frac{\hat{T}}{T}\right)^2 \qquad \left| \quad E_{pot} = \frac{g^2\hat{T}^2}{2N^2T^2} \right. \tag{1}$$

$$F_h = \rho\frac{k}{m}E_{pot} \tag{2}$$

Here, g is the acceleration due to gravity, N is the buoyancy frequency, ϱ is the density, T is the background temperature and $\hat{T}$ is the deviation of the temperature T. To eliminate the term with the horizontal and vertical wavenumber we are using the dispersion relation valid in the midfrequency approximation (Eq. 3). Following Preusse et al. [2006] we set the ratio of the intrinsic frequency $\hat{\omega}$ and the Coriolis parameter f equal to 3. Thus, we can replace the intrinsic frequency $\hat{\omega}$ by $3f$:

$$\hat{\omega}^2 = \frac{N^2 k^2}{m^2} \quad \left| \quad \frac{\hat{\omega}}{f} = 3 \longleftrightarrow \hat{\omega}^2 = 9 f^2 \right. \tag{3}$$

and obtain a relation of the ratio of the vertical and horizontal wavenumber *m* and *k* to the ratio of *f* and *N*:

$$9 f^2 = \frac{N^2 k^2}{m^2} \longleftrightarrow \frac{k}{m} = \frac{3 f}{N} \tag{4}$$

Combining Eqs. (2) and (4) provides the vertical MF by applying midfrequency approximation:

$$F_h = 3\rho \frac{f}{N} E_{pot} \tag{5}$$

Figure 2 shows the latitudinal distribution of initial vertical wind amplitudes based on E_{pot} (dotted line) and MF (solid line) data with a global mean of 1 cms^{-1}. The standard configuration by using E_{pot} provides higher values in the equatorial region due to convectively generated GWs, which, however, carry low MF and are therefore absent in the new configuration. The maxima in the midlatitudes represent the orographically induced GWs. These amplitudes are larger in the winter hemisphere than in the summer hemisphere. Using MF, the GW amplitudes are a bit larger, which is due to the normalization to the same global average of 1 cms^{-1} in the absence of an equatorial maximum due to $f \to 0$ there.

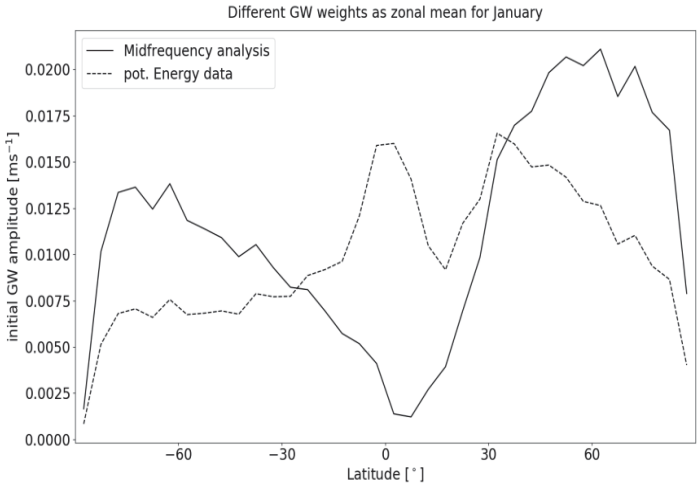

Figure 2: GW vertical wind amplitudes for the simulation based on the GPS RO E_{pot} (dotted line) and MF (solid line) data for January conditions.

3.2. Intermittent gravity wave activity

Hertzog et al. [2012] having performed in situ balloon measurements in the stratosphere for several months and found that the GW MF is unevenly distributed. They observed many GWs with small and only a few ones with large MFs. In the MUAM

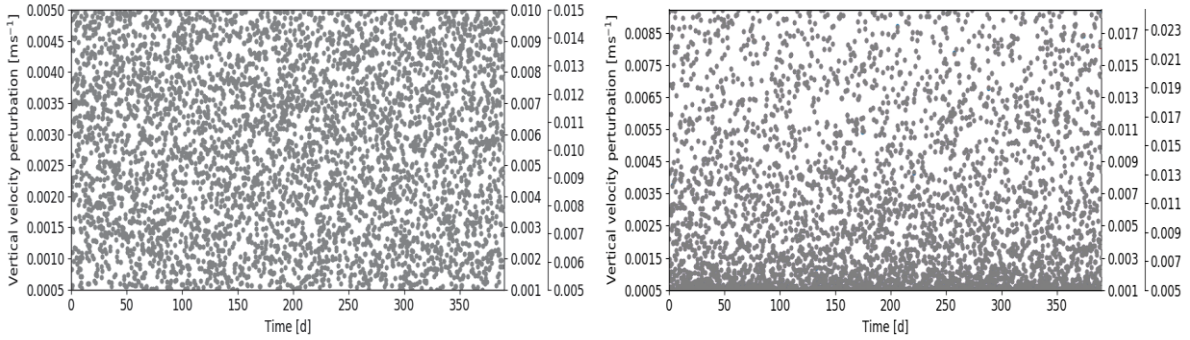

Figure 3: Linear (left) and x³ (right) distribution of the random numbers representing the variation of the vertical velocity perturbation with mean values of 1 cms^{-1}, 0.5 cms^{-1} and 0.275 cms^{-1}.

standard configuration, there is no temporal variation of the GWs excited in the troposphere. To create a more realistic distribution of the MF, based on the results of Hertzog et al. [2012] the GW amplitudes have been multiplied with randomly generated numbers in order to represent their temporal variability. These random numbers are shown in Fig. 3 for a whole simulation. They are distributed either linearly (left) or polynomially (order 3) (right) with mean values of 1 cms^{-1}, 0.55 cms^{-1} and 0.275 cms^{-1}, respectively representing larger or smaller mean amplitudes. The amplitudes for each mean value are based on the same set of random numbers, so that the chronology of large and small amplitudes is the same for each model experiment. For comparison experiments were also performed with the mean value kept constant. The aim is to slow down the mesospheric jet by GWs with larger amplitudes breaking at lower altitudes and to displace the wind reversal upwards by GWs with smaller amplitudes breaking at higher altitudes. Tab. 1 gives an overview of all simulations. The respective short name indicates which GW amplitude distribution was used (EP-potential energy and MF-momentum flux), which vertical velocity perturbation distribution was chosen (C-constant, L-linear and P-polynomial) and the respective minima, maxima and mean values.

Name	Distribution	Minimum (cms^{-1})	Maximum (cms^{-1})	Mean (cms^{-1})
EP-L-C	EP	1	1	1
MF-L-C	MF	1	1	1
MF-M-C	MF	0.55	0.55	0.55
MF-S-C	MF	0.275	0.275	0.275
MF-L-L	MF	0.5	1.5	1
MF-M-L	MF	0.1	1	0.55
MF-S-L	MF	0.05	0.5	0.275
MF-L-P	MF	0.5	2.4	1
MF-M-P	MF	0.1	1.8	0.55
MF-S-P	MF	0.05	0.9	0.275

Table 1: Overview of the model experiments based on E_{pot} data (EP) and on MF calculations (MF) for large (L), medium(M) or small (S) amplitudes and a constant (C), linear (L) and 3rd order polynomial (P) distribution.

4. Results of the simulations with modified gravity wave initialisation

4.1. Potential energy vs. momentum flux based GW distribution

In the first column of Fig. 4 the zonal (Ia) and meridional wind (Ib), the temperature (Ic), the GW flux (Id) and acceleration of the zonal wind due to breaking GWs (Ie) are presented for the MF-L-C1. By comparing Fig. 4(Ia) with Fig. 1(a) it can be seen that the zonal wind has changed. On the SH the mesospheric jet is slightly weaker. This is because GW amplitudes based on the MF distribution are larger on the SH. Thus, more large GWs are generated, which are not able to propagate into the upper mesosphere and thus, break in the stratosphere where they decelerate the mesospheric jet. Due to the small GW amplitudes in the equatorial region (Fig. 2) the wind reversal is lifted from 60 km to 80 km because small GWs are breaking in higher altitudes. As a result the SH mesospheric jet is somewhat shifted towards the NH, which is consistent with observations (see Fig. 7). Also the NH mesospheric jet with 50 ms^{-1} in maximum has changed significantly regarding shape and position. The whole west wind regime is tilted towards lower latitudes with increasing altitude. This also corresponds to observations (Fig. 7 below). However, the strength of the mesospheric jet did not decrease and the wind reversal in the mesosphere dropped from 80 km to 70 km at 50° N as result of the greater inclination of the west wind regime. There are no substantial changes of the meridional wind, except for the equatorial region, where the meridional wind increased above 80 km. The temperature distribution did not change significantly, too. The GW parameters are in good agreement with the zonal wind changes. Due to the displacement of the zero wind line in the equatorial region towards the NH more eastward directed GWs (positive GW flux - Fig. 4(Id)) can propagate and locally maintain the modified zonal wind conditions. The same effect can be observed on the NH. The area of the strongest westward directed GW flux is also tilted towards lower latitudes with increasing height and also preserves the tilt of the zonal wind. The incline can be observed as well in the acceleration through breaking GWs (Fig. 4(Ie)). The strength of the westward directed GW flux and of the acceleration due to GWs on the NH did not change which would be necessary to adjust the strength of the mesospheric jet.

4.2. Modification of the height of the wind reversal and the strength of the stratospheric jet

Figs. 4-6 show the results of the model experiments based on variable vertical velocity perturbations with different mean values and temporal distributions.
Fig. 4 presents the same parameters like in Fig. 1 for the simulations with large amplitudes MF-L-C (column I), MF-L-L (column II) and MF-L-P (column III). By comparing the five parameters of each approach in Fig. 4 no significant changes can be observed. On the NH the mesospheric jet is slightly decreasing with increasing maximum values of the vertical velocity perturbation distribution (from left I(a) to right III(a)). The maximum value of 2.4 cms^{-1} in the MF-L-P simulation generates large GWs breaking early but due to the polynomial distribution they do not occur frequently. Thus, the forcing of large GWs is too weak to significantly decrease the mesospheric jet. Due to the huge amount of small GWs, propagating to higher altitudes, the GW flux is enhanced on the NH. But still these kind of scaling factors are

too small to reduce the intensity of the mesospheric jet and too large to elevate the wind reversal in the mesosphere. Fig. 5 shows the results of the MF-M-C (I), MF-M-L (II) and MF-M-P (III) simulations. In general, the values of the vertical velocity perturbation are smaller than those of the approach in Fig. 4. So, it can be expected that the zonal wind is stronger and the wind reversal even higher. The MF-L-C run

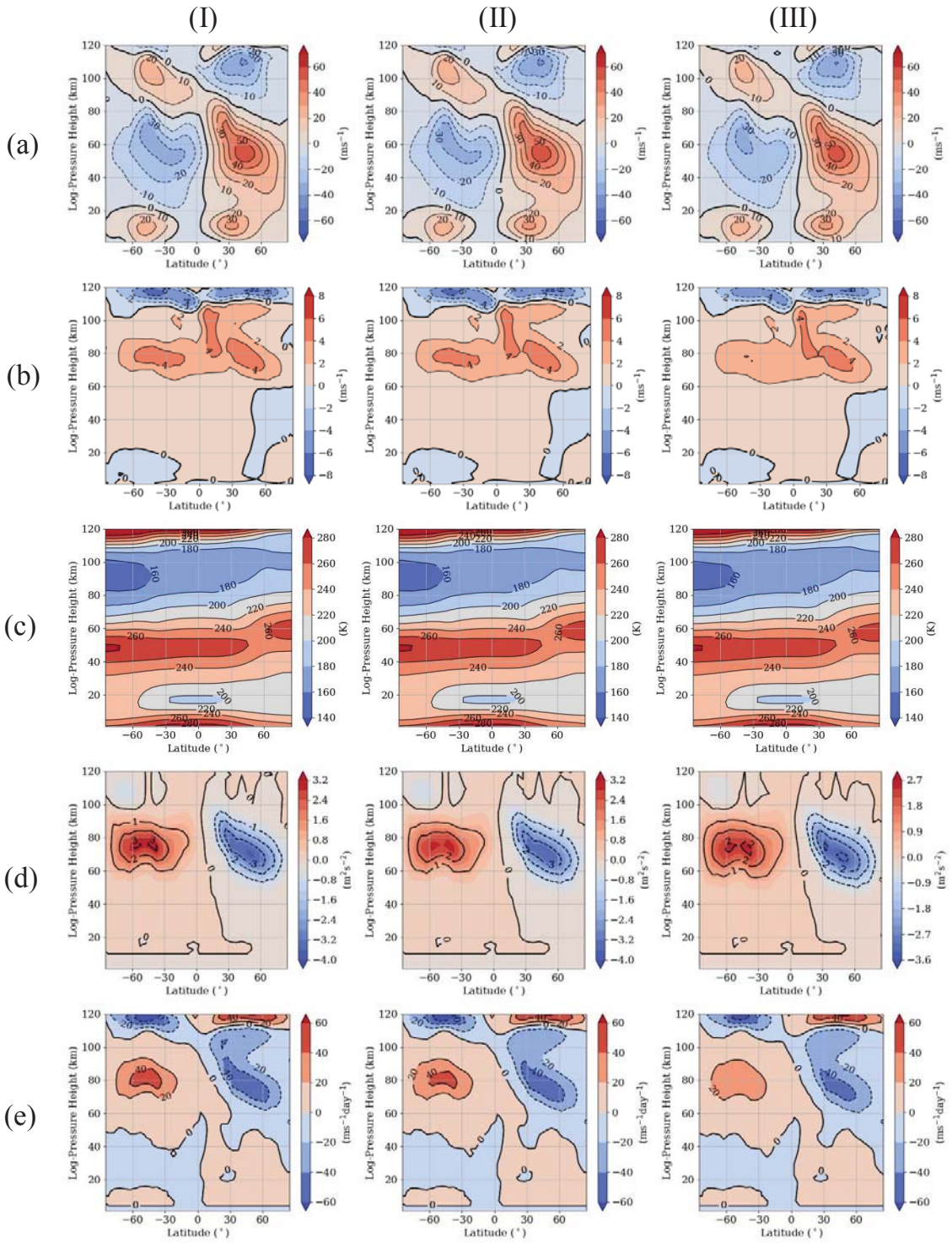

Figure 4: Zonal mean (a) zonal wind, (b) meridional wind, (c) temperature, (d) GW fluxes and (e) acceleration through GWs in the middle atmosphere for the MF-L-C (I) MF-L-L (II) and MF-L-P (III) simulations.

shows a mesospheric jet with 60 ms^{-1} in maximum and a wind reversal shifted by 10 km. The small GWs are able to propagate to higher altitudes where they break and relocate the wind reversal. This can be seen as well in the GW acceleration (Fig. 5 I(e)-III(e)) maximizing in the thermosphere. In this region also the meridional circulation (Fig. 5 I(b)-III(b)) is enhanced. The stratosphere is not affected by these GWs anymore. These effects can be reduced by the larger scaling factors in the polynomial and linear distribution.

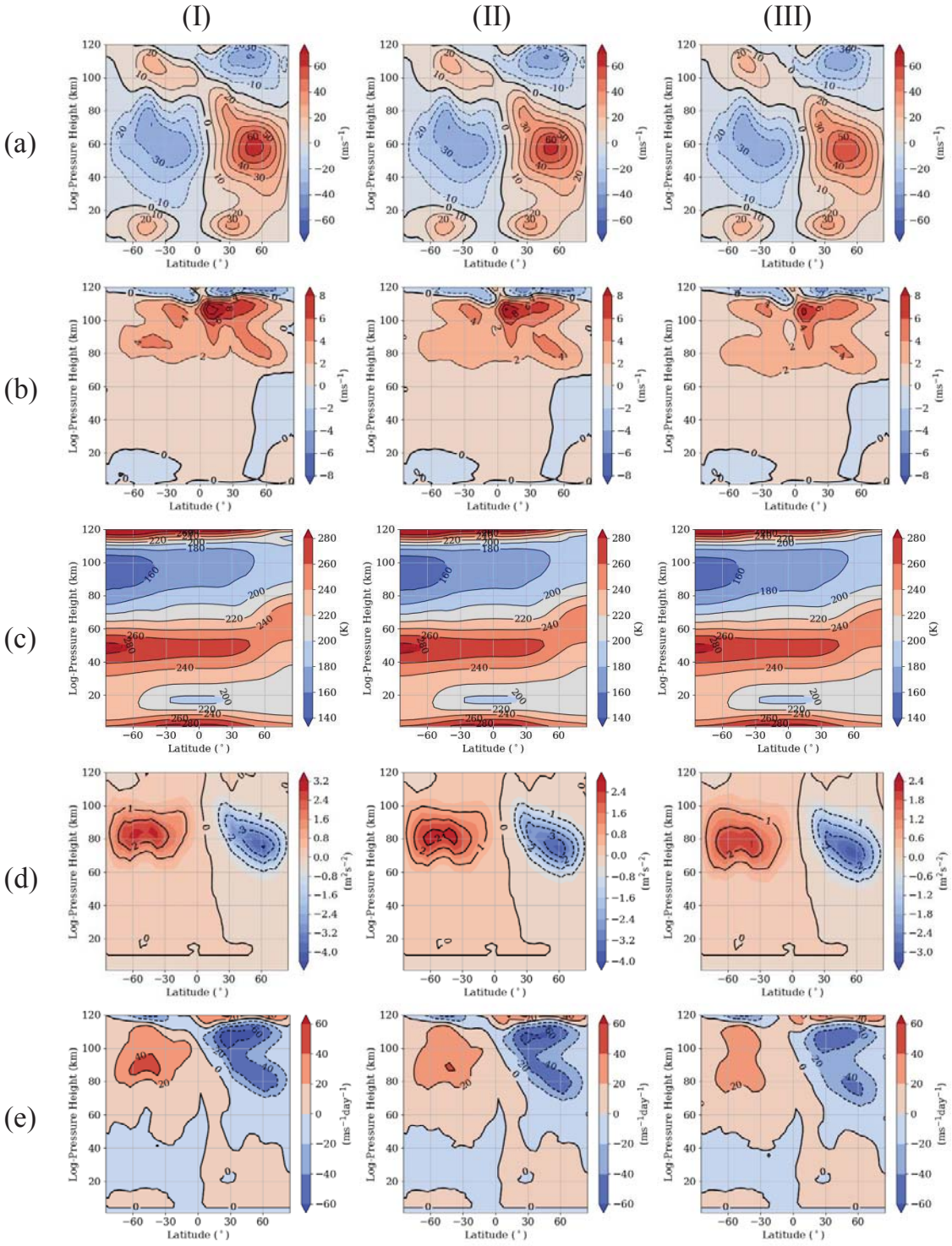

Figure 5: As in Fig. 4, but for the MF-M-C (I) MF-M-L (II) and MF-M-P (III) simulations.

Comparing I(a)-III(a) of Fig.5 shows that the zonal wind is again decreasing from 60 ms^{-1} to 50 ms^{-1} with increasing scaling factor. Also the jet maximum moves towards higher latitudes as in the EP-L-C simulation. But nevertheless, the intensity of the mesospheric jet and the height of the wind reversal are not satisfactorily reproducing observations, so that in the third approach the mean value of the variable vertical velocity perturbation was again reduced to 0.275 cms^{-1}. Results of the MF-S-C (I), MF-S-L (II) and MF-S-P (III) runs are presented in Fig. 6.

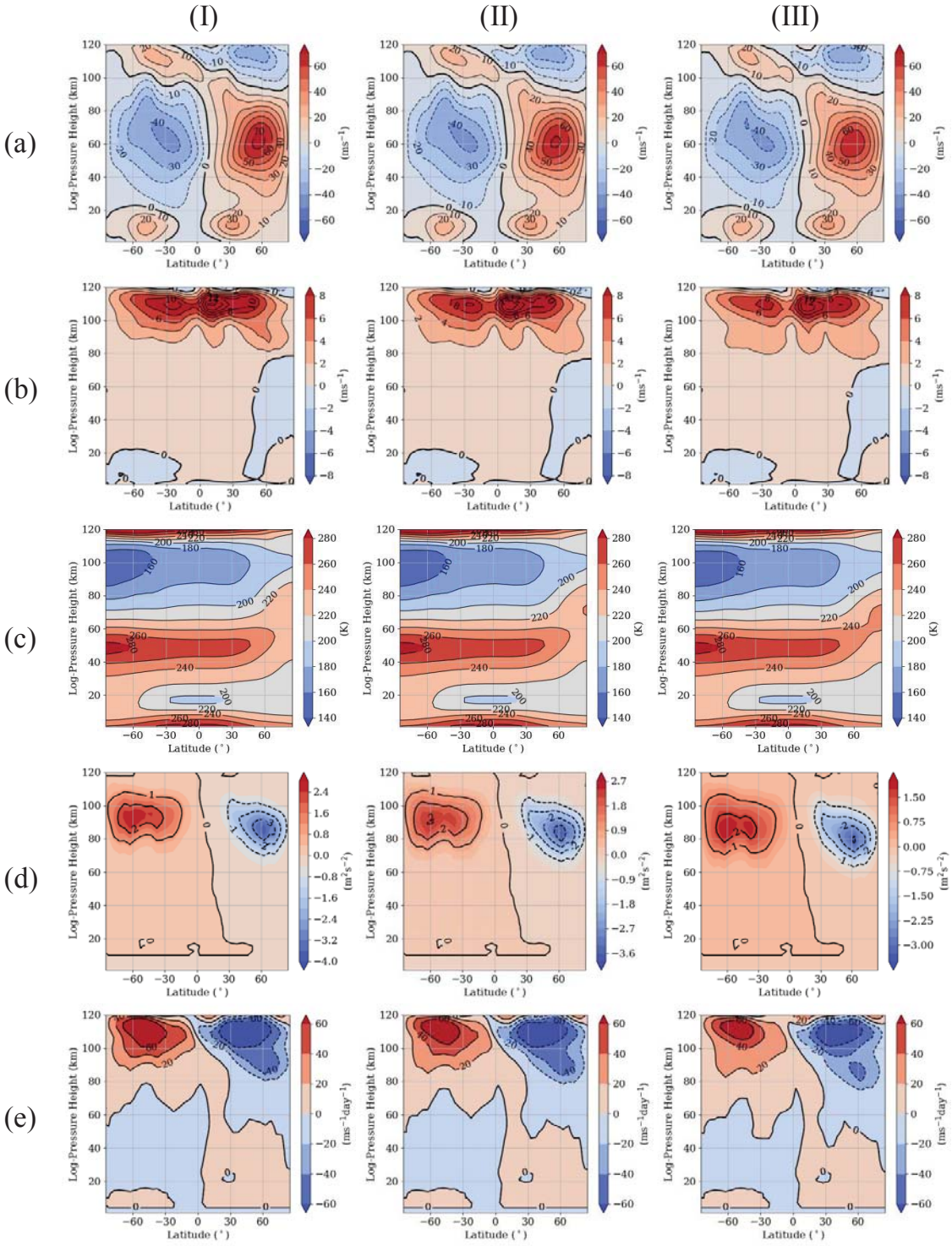

Figure 6: As in Fig. 4, but for the MF-S-C (I) MF-S-L (II) and MF-S-P (III) simulations.

Compared to the other simulations it can be directly seen that the GW flux I(d)-III(d) and the acceleration through GWs I(e)-III(e) are shifted upwards. In Fig. 6 I(a)-III(a) it can be seen that the wind reversal is now located between 90 km and 100 km which is consistent with observations (Fig. 7). But the mesospheric jet is nearly twice as strong as in the observations due to the small GWs breaking at higher altitudes. Also, the generated GWs having larger amplitudes in the linear and polynomial distribution cannot decelerate the mesospheric jet sufficiently strong. The weakest mesospheric jet can be observed in the MF-S-P simulation with a maximum of 60 ms^{-1}. In addition, the meridional circulation (Fig. 6 I(b)-III(b)) with more than 10 ms^{-1} is far too strong so that it leads to a local warming of the thermosphere (Fig. 6 I(c)-III(c)) which is not realistic. Based on these findings even the last approach does not lead to an optimal result.

5. Discussion and conclusions

In this paper we presented a new GW source distribution based on MF distributions by applying midfrequency approximation. The model experiments show that the new GW distribution is leading to a more realistic tilt of the west wind regime in the winter hemisphere towards lower latitudes with increasing height. This final outcome corresponds to the climatology illustrated in Fig. 7. This figure shows the January zonal mean zonal wind obtained from the URAP climatology [Swinbank and Ortland, 2003]. It can be seen that the mesospheric jet reaches a maximum of 40 ms^{-1} and the wind reversal is in an altitude between 90 km and 100 km. Midlatitude radar observations partly show even higher wind reversal altitudes [Jacobi, 2012]. To reproduce these characteristics a variation of large and small GWs was implemented in MUAM to decelerate the mesospheric jet by early breaking GWs with large amplitudes and to displace the wind reversal vertically by later breaking GWs with small amplitudes. A summary of all model experiments with regard to the height of the wind reversal (left) and the strength of the mesospheric jet maximum (right) is shortly summarized in Fig. 8. The height of the wind reversal was calculated for 52.5°N. It shows that the variation of the vertical velocity perturbation with a mean value of 0.275 cms^{-1} may lead to a correct altitude of the wind reversal (MF-S-P) but simultaneously, the intensity of the mesospheric jet cannot be approximately adjusted to the observations. In the reversed case, the experiment (mean of 1 cms^{-1}) may also lead to an acceptable speed of the

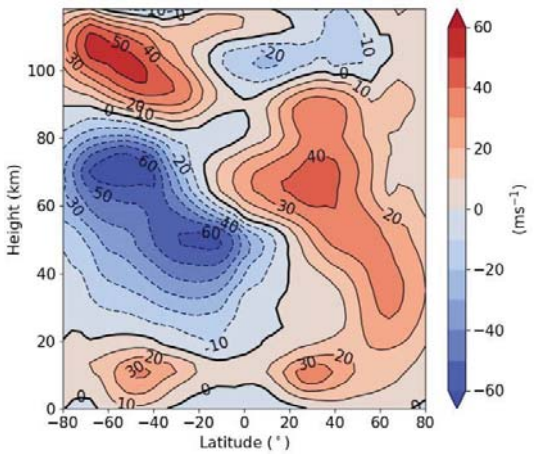

Figure 7: URAP latitude-height plot of the zonal wind [Swinbank and Ortland, 2003].

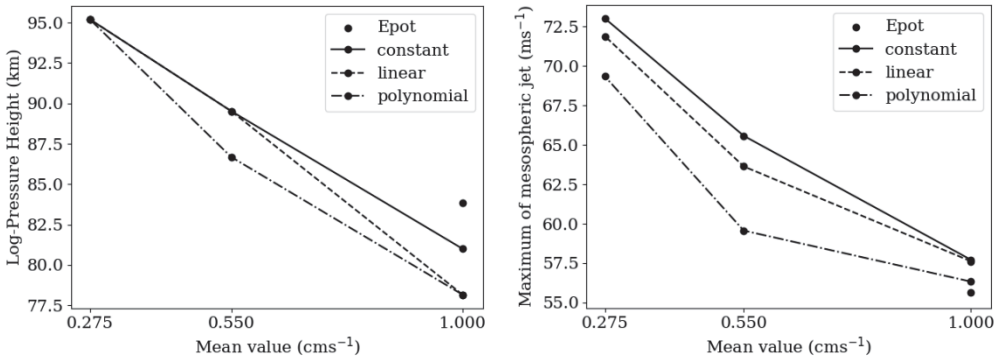

Figure 8: Overview of the height of the wind reversal at 52.5°N (left) and the strength of the mesospheric jet (right) for each simulation.

mesospheric jet (MF-L-P) but simultaneously, the wind reversal drops to lower altitudes. It may be concluded that none of the experiments provided an optimal jet with respect to both wind reversal height and intensity. It may be assumed that a composite of the simulations based on a mean of 1 cms^{-1} (MF-L-C) with a minimum of 0.05 cms^{-1} (MF-S-P) will lead to the optimal result. If this will not be the case, also the phase speed of the GWs has to be modified. Slower GWs are breaking earlier than faster GWs which means that larger GWs with smaller phase speeds are breaking at lower altitudes and may decelerate the mesospheric jet.

Acknowledgements

This study has been supported by Deutsche Forschungsgemeinschaft (DFG) under the grant JA836/32-1. ECMWF reanalysis data are provided by apps.ecmwf.int/datasets/data/. We acknowledge support by P. Šácha, Charles University Prague, for providing GW potential energy distributions.

References

Baumgarten, G., Fiedler, J., Hildebrand, J. and Lübken, F.-J., 2015: Inertia gravity wave in the stratosphere and mesosphere observed by Doppler wind and temperature lidar, Geophys. Res. Lett., 42, 10,929-10,936, https://doi.org/10.1002/2015GL066991.

Ern, M., Preusse, P., Alexander, M. J. and Warner, C. D., 2004: Absolute values of gravity wave momentum flux derived from satellite data, J. Geophys. Res., 109, D20103, https://doi.org/10.1029/2004JD004752.

Fleming, E. L., Chandra, S., Barnett, J. J. and Corney, M., 1990: Zonal mean temperature, pressure, zonal wind and geopotential height as functions of latitude, Adv. Space Res., 10, 12. (12)11-(12)59, https://doi.org/10.1016/0273-1177(90)90386-E.

Fomichev, V. I., Blanchet, J.-P. and Turner, D. S., 1998: Matrix parameterization of the 15 mm CO2 band cooling in the middle and upper atmosphere for variable CO2 concentration, J. Geophys. Res., 103, 11.505–11.528, https://doi.org/10.1029/98JD00799.

Fritts, D. C. and Alexander, M. J., 2003: Gravity wave dynamics and effects in the middle atmosphere, Rev. Geophys., 41, 1003, https://doi.org/10.1029/2001RG000106, 1.

Fröhlich, K., Pogoreltsev, A., Jacobi, Ch., 2003a: The 48-layer COMMA-LIM model, Rep. Inst. Meteorol. Univ. Leipzig, 30, 157-185, http://nbn-resolving.de/urn:nbn:de:bsz:15-qucosa-217766.

Fröhlich, K., Schmidt, T., Ern, M., Preusse, P., de la Torre, A., Wickert, J. and Jacobi, Ch., 2007: The global distribution of gravity wave energy in the lower stratosphere derived from GPS data and gravity wave modelling: attempt and challenges, J. Atmos. Sol.-Terr. Phys., 69, 2238-2248, https://doi.org/10.1016/j.jastp.2007.07.005.

Gavrilov N. and Fukao, S., 1999: The MU radar measurements and modeling of the gravity wave climatology and sources in the atmosphere, Adv. Space Res., 24 ,565-574, https://doi.org/10.1016/S0273-1177(99)00202-1.

Hertzog, A., Alexander, M. J. and Plougonven, R., 2012: On the Intermittency of Gravity Wave Momentum Flux in the Stratosphere. J. Atmos. Sci., 69, 3433–3448, , https://doi.org/10.1175/JAS-D-12-09.1.

Holton, J. R., 1982: The role of gravity wave induced drag and diffusion in the momentum budget of the mesosphere, J. Atmos. Sci., 39, 791-799, https://doi.org/10.1175/1520-0469(1982)039<0791:TROGWI>2.0.CO;2.

Jacobi, Ch., F. Lilienthal, C. Geißler, and A. Krug, 2015: Long-term variability of mid-latitude mesosphere-lower thermosphere winds over Collm (51°N, 13°E), J. Atmos. Sol.-Terr. Phys., 136, B, 174-186, https://doi.org/10.1016/j.jastp.2015.05.006.

Jacobi, Ch., 2012: 6 year mean prevailing winds and tides measured by VHF meteor radar over Collm (51.3°N, 13.0°E), J. Atmos. Sol.-Terr. Phys., 78-79, 8-18, https://doi.org/10.1016/j.jastp.2011.04.010.

Jacobi, Ch., Fröhlich, K. and Pogoreltsev, A., 2006: Quasi two-day-wave modulation of gravity wave flux and consequences for the planetary wave propagation in a simple circulation model, J. Atmos. Sol.-Terr. Phys., 68, 283-292, https://doi.org/10.1016/j.jastp.2005.01.017.

Jakobs, H. J., Bischof, M., Ebel, A., Speth, P., 1986: Simulation of gravity wave effects under solstice conditions using a 3-D circulation model of the middle atmosphere, J. Atmos. Terr. Phys., 48, 1203-1223, , https://doi.org/10.1016/0021-9169(86)90040-1.

Lilienthal, F., Jacobi, Ch., Schmidt, T., de la Torre, A. and Alexander, P., 2017: On the influence of zonal gravity wave distributions on the Southern Hemisphere winter circulation, Ann. Geophys., 35, 785-798, https://doi.org/0.5194/angeo-35-785-2017.

Lindzen, R. S., 1981: Turbulence and stress owing to gravity wave and tidal breakdown, J. Geophys. Res., 86, 9707-9714, https://doi.org/10.1029/JC086iC10p09707.

Oleynikov, A.N., Jacobi, Ch. and Sosnovchick, D.M., 2005: Parameters of internal gravity waves in the mesosphere-lower thermosphere region derived from meteor

radar wind measurements, Ann. Geophys., 23, 3431-3437, https://doi.org/10.5194/angeo-23-3431-2005.

Plougonven, R., Hertzog, A. and Guez, L., 2013: Gravity waves over Antarctica and the Southern Ocean: consistent momentum fluxes in mesoscale simulations and stratospheric balloon observations, Q.J.R. Meteorol. Soc., 139, 101–118, https://doi.org/10.1002/qj.1965.

Pogoreltsev, A. I., Vlasov, A. A., Fröhlich, K., und Jacobi, C., 2007: Planetary waves in coupling the lower and upper atmosphere, J. Atmos. Solar-Terr. Phys., 69, 2083-2101, https://doi.org/10.1016/j.jastp.2007.05.014.

Preusse, P., Ern, M., Eckermann, S. D., Warner, C. D., Picard, R. H., Knieling, P., Krebsbach, M., Russell, J. M., Mlynczak, M. G., Mertens, C. J. and Riese, M., 2006: Tropopause to mesopause gravity waves in August: Measurement and modeling, J. Atmos. Sol.-Terr. Phys., 68, 1730-1751, https://doi.org/10.1016/j.jastp.2005.10.019.

Ratnam, M.V., T. Tsuda, Ch. Jacobi, and Y. Aoyama, 2004a: Enhancement of gravity wave activity observed during a major Southern Hemisphere stratospheric warming by CHAMP/GPS measurements, Geophys. Res. Lett., 31, L16101, https://doi.org/10.1029/2004GL019789.

Ratnam, M.V., Tetzlaff G. and Jacobi, Ch., 2004b: Global and seasonal variations of stratospheric gravity wave activity deduced from the CHAllenging Minisatellite Payload (CHAMP)-GPS Satellite, J. Atmos. Sci., 61, 1610-1620, https://doi.org/10.1175/1520-0469(2004)061<1610:GASVOS>2.0.CO;2.

Šácha, P., Kuchar, A., Jacobi, Ch. and Pišoft, P., 2015: Enhanced internal gravity wave activity and breaking over the Northeastern Pacific / Eastern Asian region, Atmos. Chem. Phys., 15, 13097-13112, https://doi.org/10.5194/acp-15-13097-2015.

Šácha, P., F. Lilienthal, Ch. Jacobi, and P. Pišoft, 2016: Influence of the spatial distribution of gravity wave activity on the middle atmospheric circulation and transport, Atmos. Chem. Phys., 16, 15755-15775, https://doi.org/10.5194/acp-16-15755-2016.

Schmidt, T., P. Alexander, and A. de la Torre, 2016: Stratospheric gravity wave momentum flux from radio occultations, J. Geophys. Res. Atmos., 121, 4443–4467, https://doi.org/10.1002/2015JD024135.

Strobel, D. F., 1986: Parameterization of the atmospheric heating rate from 15 to 120km due to O2 and O3 Absorption of solar radiation, J. Geophys. Res., 83:6225–6230. https://doi.org/10.1029/JC083iC12p06225.

Witschas, B., Rahm, S., Dörnbrack, A., Wagner, J. and Rapp, M., 2017: Airborne Wind Lidar Measurements of Vertical and Horizontal Winds for the Investigation of Orographically Induced Gravity Waves, J. Atmos. Oceanic Technol., 34, 1371–1386, https://doi.org/10.1175/JTECH-D-17-0021.1.

Analyzing Arctic surface temperatures with Self Organizing-Maps: Influence of the maps size

D. Mewes, Ch. Jacobi

Universität Leipzig, Institute for Meteorology, Stephanstr. 3, 04103 Leipzig,
E-Mail: daniel.mewes@uni-leipzig.de

Summary: We use ERA-Interim reanalysis data of 2 meter temperature to perform a pattern analysis of the Arctic temperatures exploiting an artificial neural network called Self Organizing-Map (SOM). The SOM method is used as a cluster analysis tool where the number of clusters has to be specified by the user. The different sized SOMs are analyzed in terms of how the size changes the representation of specific features. The results confirm that the larger the SOM is chosen the larger will be the root mean square error (RMSE) for the given SOM, which is followed by the fact that a larger number of patterns can reproduce more specific features for the temperature.

Zusammenfassung: Wir benutzten das künstliche neuronale Netzwerk Self Organizing-Map (SOM), um eine Musteranalyse von ERA-Interim Reanalysedaten durchzuführen. Es wurden SOMs mit verschiedener Musteranzahl verglichen. Die Ergebnisse zeigen, dass SOMs mit einer größeren Musteranzahl deutlich spezifischere Muster produzieren im Vergleich zu SOMs mit geringen Musteranzahlen. Dies zeigt sich unter anderem in der Betrachtung der mittleren quadratischen Abweichung (RMSE) der Muster zu den zugeordneten ERA Daten.

1 Introduction

Finding specific patterns of meteorological variables is necessary to understand common features that governs the weather and climate of the Earth. One method that can been used to find patterns and to analyze time variation of those patterns is called Self Organizing-Maps. It was developed by Kohonen (1998) and has been used in multiple studies since (e.g. Hewitson and Crane (2002); Cassano et al. (2006); Lynch et al. (2016); McDonald et al. (2016); Ford and Schoof (2017)). The advantage of SOMs compared to empirical orthogonal Eigenfunction analysis is that SOMs are not limited to a linear assumption. The pattern recognition of SOMs seeks to map a user-defined number of patterns to a distribution of input data, while preserving the probability density function of the analyzed data. This means that the SOM method is reproducing patterns in a way that the patterns that are more frequent in the dataset occur more often in a SOM.
As a cluster algorithm, using the SOM method poses the problem to choose the number of patterns that shall be extracted. This number has to be defined *a priori* and may depend on the parameters to be investigated, the general variability of the dynamics, and the sciences questions. In general it can be said that a larger number of patterns result in

a more detailed decomposition of the data. In turn, a small number of patterns gives a broader picture of the meteorological states.
In this report we analyzed the clustering of high-latitude two meter temperature winter fields for differently sized SOMs. In Section 2 we explain the data that has been used and which sizes of SOMs were analyzed. Section 3 will show the results of the different SOMs. The last section 4 will shortly summarize and discuss the results.

2 Data and Method

For this study, synoptic (00, 06, 12, 18 UTC) ERA-Interim (ECMWF, 2017; Dee et al., 2011) two meter temperatures during the 1979-2016 winter seasons were used. The ERA-Interim data are available at a horizontal resolution of approximately 0.7 degrees. For the performed analysis the synoptic values were daily averaged, which lead to a total of 3340 daily temperature fields. The analysis was limited to regions north of 50°N.
To feed the temperature data into the SOM algorithm it is necessary to reshape from an three-dimensional data field (time, latitude, longitude) to a three-dimensional data field where the latitude and longitude dimensions are stacked onto each other. After applying the SOM algorithm, the shape of the latitudes and longitudes as horizontal coordinates is restored. Afterwards each pattern is subtracted by the ERA-Inetrim winter mean temperature in order to obtain the temperature anomalies with respect to the the whole analyzed time frame. Note, that for the structure of evolving patterns it does not matter whether anomalies are directly used in the SOM analysis, or whether the differences from the mean are calculated afterwards. The general process of the SOM method is summarized in Mewes and Jacobi (2017).
SOMs of the size of 3x1, 3x2, 4x3 and 5x4 were analyzed. For all of these test cases the set-up parameters for the SOM where the same: 1000 iterations, learning rate starting at 0.5 and linearly decreasing to 0.001 during the iterative process, and an decrease of the neighbourhood definition from the number of the columns to one during the iteration. To distinguish between patterns of the different SOMs the following notation is introduced: (r,c).(CxR), where r and c denotes the row and column of the pattern as described within one SOM. R and C denotes the maximum number of rows and columns of the specific SOM. For example, the leftmost pattern of the SOM with three patterns will be addressed as (0,0).(3x1). Speaking of a small (large) SOM means that the SOM consists of a small (large) number of patterns.
Further the root mean square error (RMSE) of each pattern of each SOM compared to the corresponding daily data fields was calculated. The RMSE was averaged over all patterns of one SOM. This averaged RMSE is used as a metric to characterize how well a size of a SOM corresponds to the representation of the daily data field. Hereby large values will indicate that the SOM only serves as an overview of the data while small values for the averages RMSE are corresponding to a SOM that can represent single features better.

3 Results

Figure 1 shows the SOM of the two meter temperature with 3 patterns. The pattern (0,0).(3x1) shows a colder than usual central Arctic, Greenland, Bering Strait and East Russia, and a warmer than usual North America and Eurasia. This composite is created

from 1309 days. The lowest temperatures are observed northeast of Svalbard with -4 K and the warmest temperature in central Siberia with +4 K. On the opposite site (0,2).(3x1) of this 3x1 SOM every region is warmer than usual (up to +7 K), for parts of the North Atlantic, North America, and central Siberia (-3 K). Pattern (0,1).(3x1) produces cold Eurasia and North America (-4 K) anomalies and a warmer than usual sector from the North Pacific over the Northwest Passage to Greenland and the west coast of Greenland (+2 K). The last two patterns are each a composite from 1015 days.

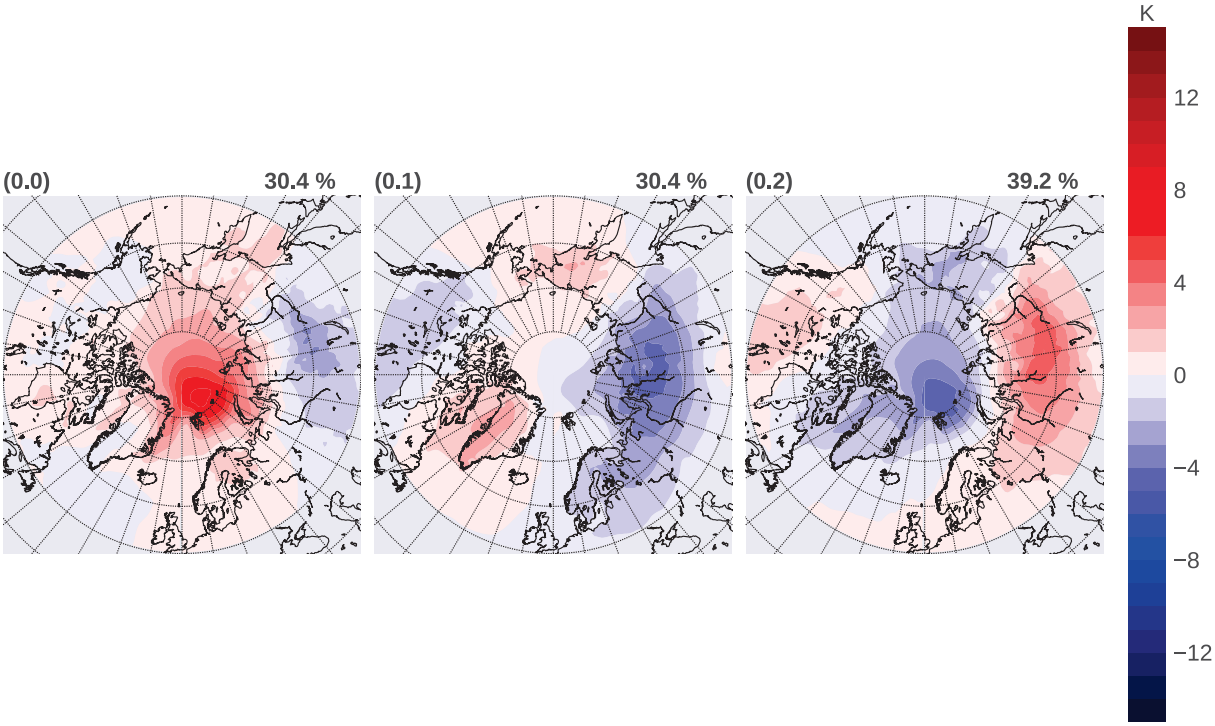

Fig. 1: 3x1 SOM of 2 meter air temperature, from ERA-Interim daily mean data for the winters from 1979/80 to 2015/16; numbers on the upper right show occurrence frequencies in percent. The numbers on the upper left show the number of the node.

For the next comparison the size of the SOM was doubled (see Figure 2). In general, going from three to six patterns creates about three new patterns and 3 patterns that can be related to the patterns from the 3x1 SOM. The range of represented days by each pattern varies from 484 to 701 for this SOM. Pattern (0,0).(3x2) is similar to pattern (0,0).(3x1) of the 3x1 SOM, but with bigger amplitudes of the anomalies (-5 K and +5 K). Similar results are found when comparing (1,1).(3x2) with (0,1).(3x1) and (1,2).(3x2) with (0,2).(3x1). New patterns identified in the 3x2 SOM are (0,1).(3x2), (1,0).(3x2), and (0,2).(3x2). Node (0,2).(3x2) shows an Arctic that is everywhere warmer than usual except for central Greenland. The new pattern (0,1).(3x2) shows a generally warmer situation while having colder regions reaching from East Russia to North Svalbard. Very cold anomalies over North Canada are shown in pattern (1,0).(3x2), which coincides with strong negative anomalies for the region north of the Barents sea and the Kara sea.
The general shape of the patterns in the corners of the following SOMs will be the same.

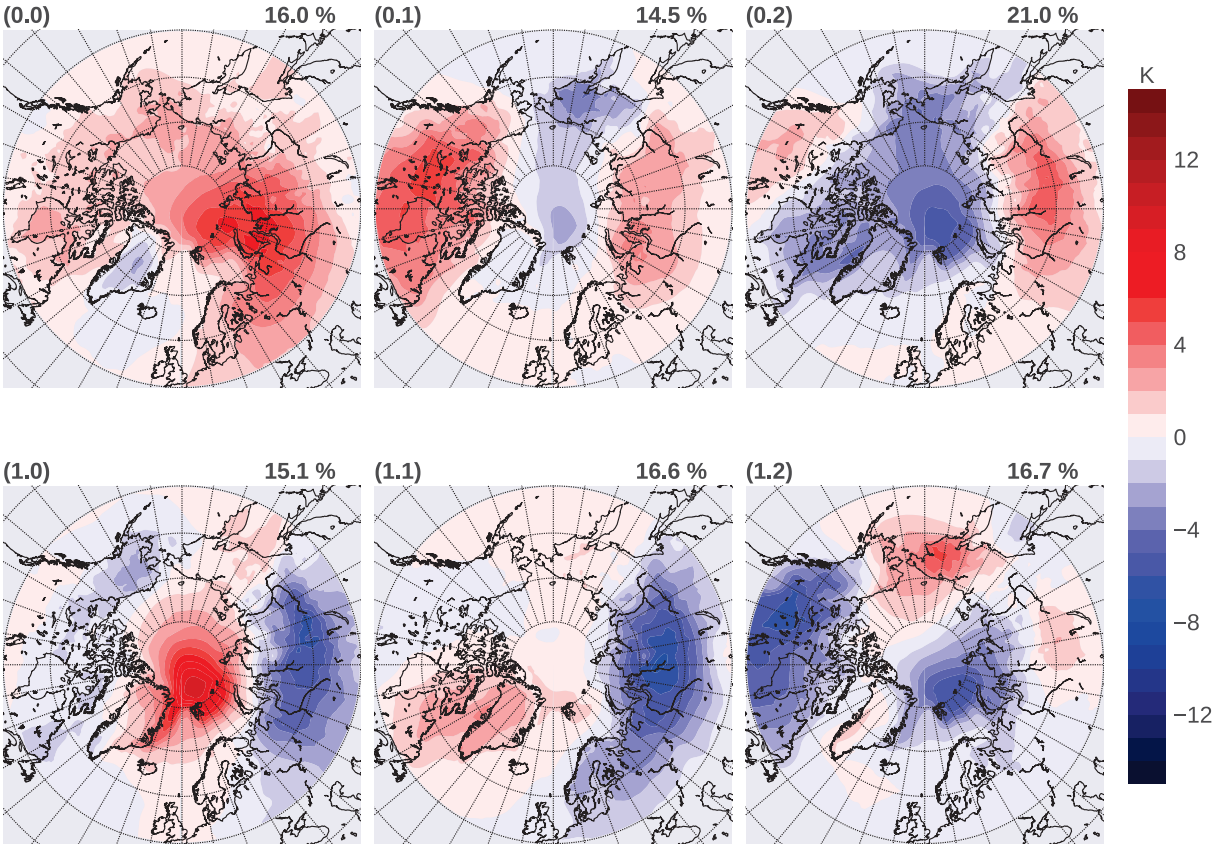

Fig. 2: As in Fig. 1 but for the 3x2 SOM.

For increasing SOM size the differences in the anomalies of the corner patterns are getting larger in space. Figure 3 shows the 2 meter temperature SOM with four by three patterns, which represents a doubling from six to twelve patterns. With this size of SOM each pattern represents about 193 to 337 days. Patterns (0,1).(4x3) and (0,2).(4x3) show that those two patterns might have developed from the pattern (0,1).(3x2). Similar can be seen for the patterns (2,1).(4x3) and (2,2).(4x3) compared to (1,1).(3x2). New patterns can be found in the new introduced row of patterns. Pattern (1,3).(4x3) shows to be very warm overall while having the center of maximal positive anomaly east of Svalbard, while pattern (1,2).(4x3) seems to be the opposite of the corner pattern in the bottom left ((2,0).(4x3) and (1,0).(3x2)). With Pattern (1,1).(4x3) a more neutral pattern has emerged while still having a colder than usual Siberia and central Arctic (-3 K) but slightly warmer North America (-3 K) and a warming of the Barents Sea (2 K). Pattern (1,0).(4x3) appears to combine features from (0,0).(3x2) and (1,0).(3x2).

Figure 4 shows an amount of twenty patterns, which is an increase of eight patterns compared to Figure 3. The amount of days represented by each pattern is in the range of 133 and 197 days. As it was stated above, the patterns in the corners are similar to the other two SOMs shown before. Most changes of patterns occur in the two middle rows compared to the 3x2 SOM. While in pattern (1,1).(4x3) data were clustered so that a warm Barents Sea was present, this pattern completely disappeared in the 5x4 SOM. One comparable new pattern would be (1,2).(5x4) but the warming is extending from the Barents Sea to the Kara Sea and northern Europe. Generally other patterns have emerged that were previously merged into other pattern of the smaller SOMs.

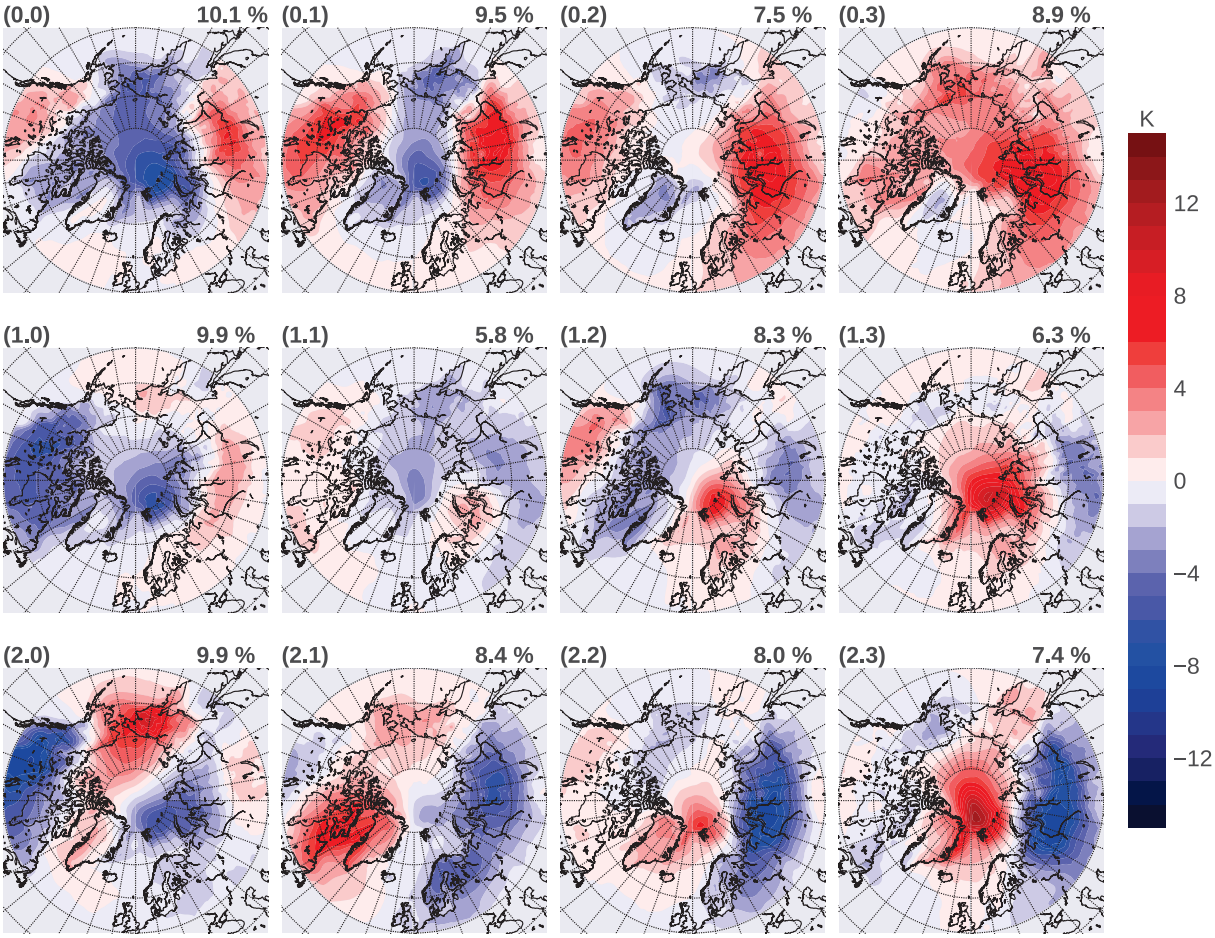

Fig. 3: As in Fig. 1 but for the 4x3 SOM.

Table 1 shows the RMSE in dependence of the number of Patterns (N). In addition to the SOMs shown here two other SOMs were created and analyzed with respect to their RMSE, one with 50 and one with 100 patterns. Generally the results show that with an increasing number of the patterns the mean RMSE is decreasing. Moreover, a linear

Table 1: RMSE depending on the number of patterns (N)

N	Mean RMSE in K
3	4.7164
6	4.5194
12	4.3435
20	4.2188
50	4.0038
100	3.8512

relationship between the RMSE and the logarithm of N has been found. After a linear fit the function for the stated relationship is as follows:

$$RMSE = (-0.566 \pm 0.012)\ \log(N) + 4.967 \pm 0.016$$

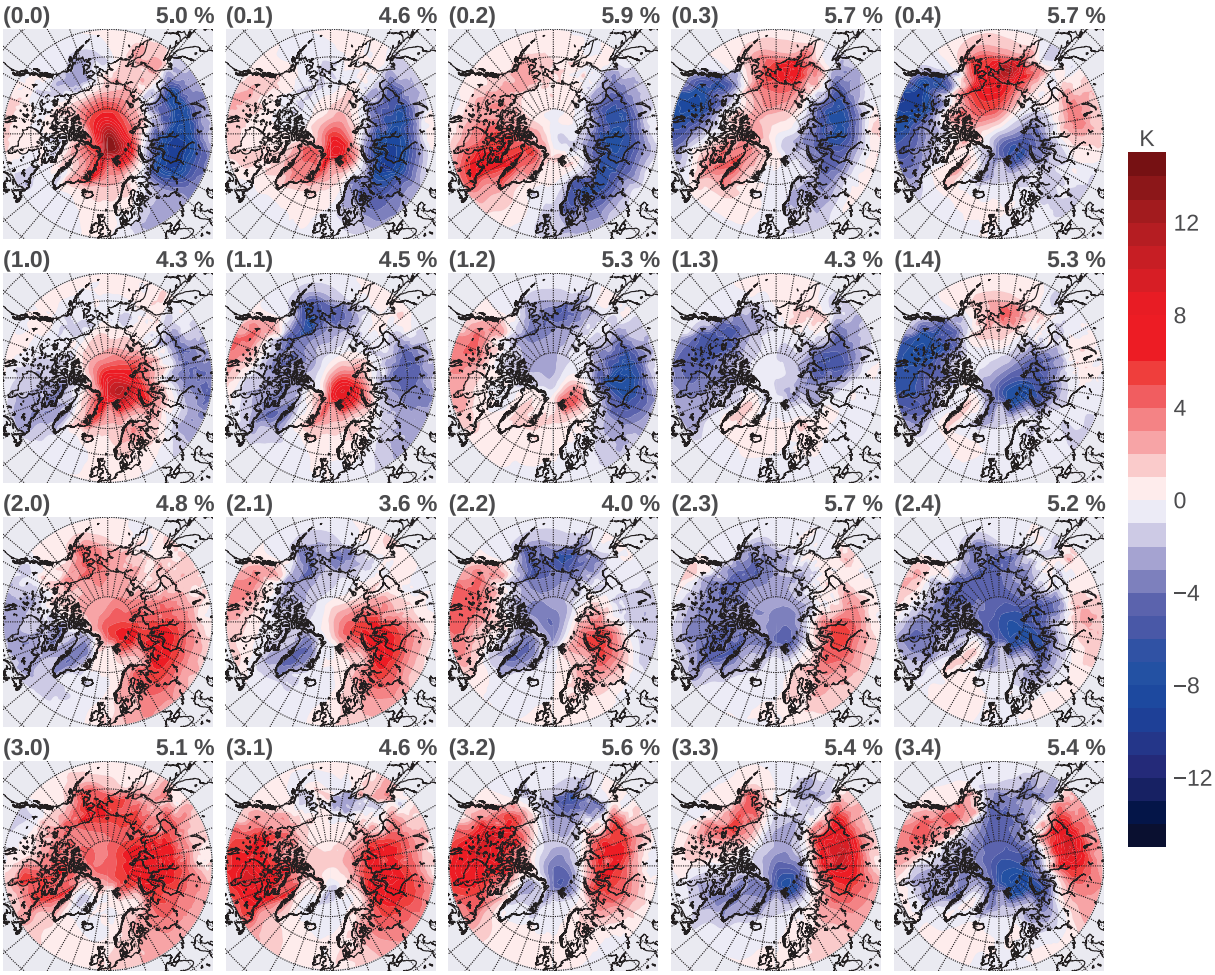

Fig. 4: As in Fig. 1 but for the 5x4 SOM.

This model between RMSE and the number of patterns results into an r^2 of 0.998 and a standard error of 0.0123. This means that an increase by 10 patterns leads to an improvement of the RMSE of 11.38% compared to the starting RMSE.

4 Summary and Discussion

We analyzed the influence of the size of a SOM on the decomposition and clustering of ERA-Interim daily mean 2 meter temperature fields north of 50°N.
It could be shown that increasing the SOM size from 3x2 on, the corner patterns remained structurally the same. This was expected due to the fact that those pattern where mathematically the most different from each other and thus had to been placed far apart from each other according to how the method works. Most new pattern were developing along an added row comparing different sized SOMs. With increasing number of patterns it could be seen that in some cases multiple patterns were evolving at the expense of a single one and these more specific cases of the temperature anomalies could be identified. This also could be seen with respect to the RMSE. With increasing number of patterns, each pattern has to represent a fewer amount of daily data and following this the general error from the pattern to the data connected to it has to decrease. This leads to the conclusion that patterns of larger SOMs can represent specific patterns much better than smaller SOMs. Through this shift of data to different/new patterns they could be partly recognized

from more general patterns of smaller SOMs.
In summary, it can be seen that the choice of the size of the SOM can change the representation of specific patterns dramatically. The general advise for using Self-Organizing Maps for distinguishing meteorological situations would be to create a fairly large SOM (with many patterns) and then re-group distinct patterns with similar meteorological features manually. This will help to understand and control better, which pattern might fit together. Leaving this grouping to the method by just simply using a smaller map size might result into composites of days that might fit mathematically well to each other, but not under a meteorological point of view. This problem occurs due to the fact that the used package to create the SOM works by simply calculating the Euclidean distances between daily fields and the patterns to assign the specific daily fields to a specific pattern.

Acknowledgements

ERA-Interim reanalyses data are provided http://apps.ecmwf.int/datasets/data/interim-full-moda. We gratefully acknowledge the support from the German Research Foundation (Deutsche Forschungsgemeinschaft) within the Transregional Collaborative Research Center (TR 172) “Arctic Amplification: Climate Relevant Atmospheric and Surface Processes, and Feedback Mechanisms (AC)^3.”

References

Cassano, E. N., Lynch, A. H., Cassano, J. J., and Koslow, M. R., 2006: Classification of synoptic patterns in the western Arctic associated with extreme events at Barrow, Alaska, USA, Climate Res., 30, 83–97, doi:10.3354/cr030083.

Dee, D. P., Uppala, S. M., Simmons, A. J., Berrisford, P., Poli, P., Kobayashi, S., Andrae, U., Balmaseda, M. A., Balsamo, G., Bauer, P., Bechtold, P., Beljaars, A. C. M., van de Berg, L., Bidlot, J., Bormann, N., Delsol, C., Dragani, R., Fuentes, M., Geer, A. J., Haimberger, L., Healy, S. B., Hersbach, H., Hólm, E. V., Isaksen, L., Kållberg, P., Köhler, M., Matricardi, M., McNally, A. P., Monge-Sanz, B. M., Morcrette, J.-J., Park, B.-K., Peubey, C., de Rosnay, P., Tavolato, C., Thépaut, J.-N., and Vitart, F., 2011: The ERA-Interim reanalysis: configuration and performance of the data assimilation system, Quart. J. Roy. Meteor. Soc., 137, 553–597, doi:10.1002/qj.828, URL http://dx.doi.org/10.1002/qj.828.

ECMWF: ERA Interim, Daily, URL http://apps.ecmwf.int/dataset/data/interim-full-daily, 2017.

Ford, T. W. and Schoof, J. T., 2017: Characterizing extreme and oppressive heat waves in Illinois, J. Geophys. Res. Atmos., 122, 682–698, doi:10.1002/2016JD025721.

Hewitson, B. and Crane, R., 2002: Self-organizing maps: applications to synoptic climatology, Climate Res., 22, 13–26, doi:10.3352/cr022013.

Kohonen, T., 1998: The self-organizing map, Neurocomputing, 21, 1–6, doi:10.1016/S0925-2312(98)00030-7.

Lynch, A. H., Serreze, M. C., Cassano, E. N., Crawford, A. D., and Stroeve, J., 2016: Linkages between Arctic summer circulation regimes and regional sea ice anomalies, J. Geophys. Res. Atmos., 121, 7868–7880, doi:10.1002/2016JS025164.

McDonald, A. J., Cassano, J. J., Jolly, B., Parsons, S., and Schuddeboom, A., 2016: An automated satellite cloud classification scheme using self-organizing maps: Alternative ISCCP weather states, J. Geophys. Res. Atmos., 121, doi:10.1002/2016JD025199.

Mewes, D. and Jacobi, C., 2017: Variability of horizontal temperature fluxes over the Arctic, Wiss. Mitteil. aus dem Instit. f. Meteorol. der Univ. Leipzig, 55, 51–60, URL http://nbn-resolving.de/urn:nbn:de:bsz:15-qucosa2-167700.

Evolution of deep convective clouds derived from ground-based observations

Kátia Mendes de Barros[+*], Evelyn Jäkel[+], Michael Schäfer[+], Johannes Stapf[+], Manfred Wendisch[+]

[+] *Institut of Meteorology, Stephanstr. 3 04103 Leipzig, *E-Mail: katia.mendes_de_barros@uni-leipzig.de**

Summary: Deep convective clouds (DCCs) play a crucial role in redistributing latent heat, hydrological cycle and in the radiative budget of our climate system. Therefore, their complex evolution processes are in focus of many studies. Changes in the structure of DCCs can delay the onset of precipitation and alter the albedo of clouds. Knowing where in the cloud and under what circumstances the cloud liquid water droplets start to freeze is an important step to improve climate and weather forecast models. The purpose of this planned study is to characterize the impact of aerosol and thermodynamic conditions on the cloud particle growth. Therefore, ground-based cloud side observation of the reflected solar spectral radiation (near infrared) using an imaging spectroradiometer and measurements of the emitted thermal radiation using an infrared camera will be combined. These measurements will be taken at the Amazon Tall Tower Observatory, in the Amazon forest, Brazil. Here, the campaign will be introduced.

Zusammenfassung: Hochreichend konvektive Bewölkung (deep convective clouds, DCCs) spielt eine entscheidende Rolle bei der Umverteilung latenter Wärme, sowie für den Wasserkreislauf und dem Strahlungshaushalt unseres Klimasystems. Aus diesem Grund stehen ihre komplexen Wolkenbildungsprozesse im Fokus vieler Untersuchungen. Veränderungen in der mikrophysikalischen Struktur der DCCs können das Einsetzen der Niederschlagsbildung verzögern. Darüber hinaus verändern sie die Albedo der Wolke. Das Wissen darüber, wo in der Wolke und unter welchen Umständen die Wolkentropfen beginnen zu gefrieren, ist ein wichtiger Schritt zur Verbesserung von Klima- und Wettervorhersagemodellen. Das Ziel der geplanten Untersuchungen besteht in der Charakterisierung des Einflusses von Aerosolpartikeln und thermodynamischer Bedingungen auf den Partikelwachstum und der Phasenumwandlung in Wolken. Hierzu werden bodengebundene Wolkenseitenbeobachtungen der reflektierten solaren Strahlung (nahes infrarot), aufgezeichnet mit Hilfe eines abbildenden Spektrometers, sowie Messungen der emittierten thermischen Strahlung, detektiert mit einer Infrarotkamera, kombiniert. Die entsprechenden Messungen werden am „Amazon Tall Tower

Observatory“ im Amazonas Regenwald in Brasilien durchgeführt. Im folgendem wird die zugehörige Kampagne vorgestellt.

1. Introduction

In general, the evolution of deep convective clouds (DCCs) follows three stages. First, thermal instability is needed for forming cumulus clouds. This very first stage called towering cumulus stage is associated with updrafts. The second stage (mature stage) is identified when there are both water droplets and ice crystals existing simultaneously within the cloud and strong updrafts and downdrafts are observed. The third and last stage, namely dissipating phase, is dominated by downdrafts. Since the cloud is no longer supplied with moisture from updrafts, the cloud soon evaporates.

In general, a DCC in its mature stage consists of three different layers, as can be seen in Fig. 1. Since the temperature decreases with altitude these layers are defined by the cloud particle phase (liquid, mixed-phase, and ice phase). The relation between temperature or height and cloud particle phase depends on the presence of aerosol particles and their ability to act as cloud condensation nuclei (CCN) or ice nuclei (IN).

According to Rosenfeld and Woodley (2003), in a pristine maritime atmosphere, the mixed-phase layer can be positioned in temperatures between -2ºC and -10ºC, with the effective radius of both liquid water droplets and ice crystals between 25 and 33 µm. They also found that for continental and polluted cases, when more aerosols are expected, the same layer is shifted to colder temperatures, between -8ºC and -18ºC and -19ºC to -35ºC, respectively, and with effective radii of the cloud particles between 20 and 33 µm and 14 and 33 µm.

Therefore, for a larger amount of aerosol particles, the cloud will develop higher in the atmosphere. It occurs, because for the same amount of available water vapor, more aerosol particles are present to act as CCN, leading to more, but smaller droplets (Tao et al., 2012). Subsequently, this will delay the onset of precipitation (Albrecht, 1989), since the droplets need more time to get large enough to precipitate, which happens at approximately 14 µm (Rosenfeld and Gutman, 1994).

Furthermore, the change of the structure of DCCs due to changing aerosol properties lead to changing radiative effects of the clouds, known as Twomey effect (Twomey, 1977). It states that a cloud with more and smaller droplets will have a higher albedo than a cloud with fewer larger droplets, leading the amount of solar radiation reflected by the clouds to increase.

To understand the changes on the beginning of the glaciation associated with the mixed-phase layer depth in DCCs due to the aerosol load, this work aims to follow the evolution of DCCs by means of ground-based cloud side observations on a 325 m high tower in the

Amazon forest (Andreae et al., 2015). The method and the main instruments will be introduced in this paper. Similar cloud side observation but from an airborne platform were presented by Jäkel et al. (2017). They used an imaging spectroradiometer installed on a side viewport on the aircraft to estimate the vertical extension of the mixed phase layer in relation to the aerosol load. The advantage of ground-based observations is that complete profiles of one evolving cloud can be observed throughout the three stages while the aircraft measurements presented in Jäkel et al. (2017) reported the vertical distribution of the cloud phase for variable clouds at different stages of evolution.

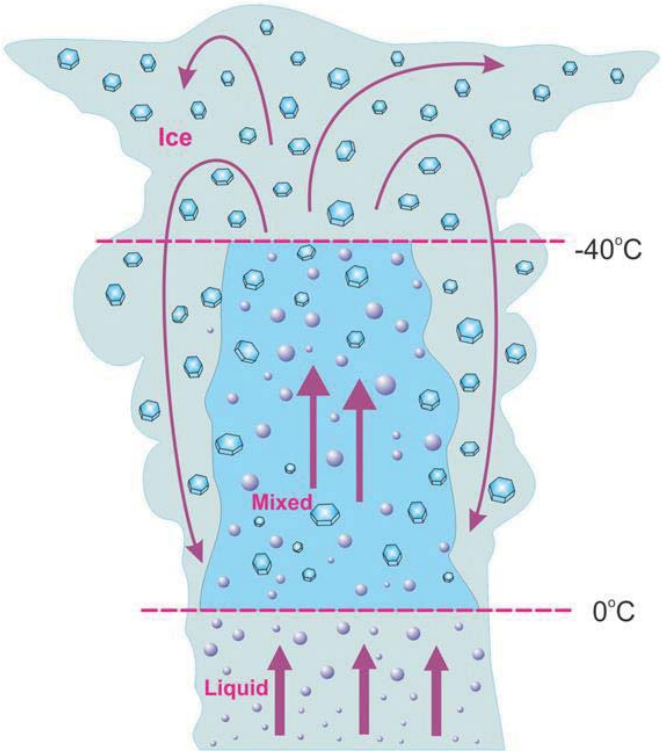

Figure 1: The different layers of the deep convective clouds. From Korolev et al. 2017.

2. Measurements

2.1. Measurement Site

The site chosen for our study was the Amazon Tall Tower Observatory (ATTO, S 02º 08.752', W 59º 00.335', 130 a.s.l.), a 325 meters tall tower, approximately 150 km northeast of Manaus, in the heart of the Amazon forest (Andreae et al., 2015).

In the Amazon, DCCs can be met at any time of the year (Giangrande et al., 2017) because of the high temperatures and abundant amount of water vapor. Due to the fact

that the average temperatures only change by about 2 K throughout the year (Collow et al., 2016) with well-defined dry and wet seasons, the presence of different aerosol conditions needs to be the main driver of the variable DCC formation. Most fires are detected from August to late October in the western region of ATTO. These fire events have a strong impact on the aerosol optical depth (AOD) over ATTO. Back trajectories show that the increase in AOD for the dry season is mainly caused by biomass burning around the ATTO site which is exposed to air masses from easterly and southeasterly regions (Andreae et al., 2015). Best time to measure cloud developments for pristine and polluted situations is between September and October, at the end of the dry season.

2.2. Instruments

To understand the evolution of DCCs and especially the transition from liquid to mixed phase with regard to a different aerosol background, remote sensing observations will be performed at ATTO using the instruments listed in Tab. 1.

The AisaHawk instrument is a hyperspectral sensor, in a form of a line camera, and measures the reflected radiance in the short wave infrared, between 970 and 2500 nm. This line camera will be installed together with an infrared camera Varioscan 3021 ST on a mount which is able to rotate and scan vertically. The infrared camera takes pictures in the wavelength range between 8 and 12 µm. To complement, two GoPro cameras will be used, taking pictures of the sky in similar intervals of time to estimate the distance and the height of the observed clouds.

Table 1: Instruments that will be taken to ATTO and its specifications. RGB stands for the red, green and blue channel.

Instrument	Spectral Coverage	Spatial Coverage	Temporal resolution (Hz)	Measured quantity
AisaHawk	970 to 2500 nm, 254 bands, FWHM = 12 nm	320 pixels for FOV = 17.8°	100	Spectral radiance
Infrared-camera	8 – 12 µm	(30 x 20)° to (5 x 3,3)°, with electro-optical zoom	1.1	Brightness temperature, height of layers
GoPro cameras	RGB	12 megapixels for FOVh = 122.6°, FOVv = 94.4°	0.1	Distance and height of the cloud

2.3 Measurement strategy

The imaging spectrometer, AisaHawk, and the infrared camera will be installed on a mount, on a platform at 150 meters altitude above ground level. Since AisaHawk is a line camera, vertical scans will be performed to measure the entire cloud side. From the reflected radiation measurements on cloud side, the radiances in the wavelength range between 1550 nm and 1700 nm can be used to derive the thermodynamic phase following principles as published in Pilewskie and Twomey (1987) and Jäkel et al. (2013). They defined a phase index from the spectral slope between these two wavelengths which is sensitive to the cloud particle phase due to the difference in the refraction index between liquid water and ice in this spectral range. The additional information of the infrared images, once calibrated with data from radio soundings and modeling outputs, makes possible to calculate the brightness temperature of each of these layers and since the camera provides the zenith angle of the images, it is possible to calculate the height of each of these layers.

To complement, a GoPro camera will be placed at the same platform where the AisaHawk and the infrared camera are mounted. A second GoPro will be placed on another tower, 600 m apart from ATTO (80 meters height). Both GoPros will observe the same direction. The strategy is to use two simultaneously observed pictures of the same cloud from different directions to derive the distance and the height of the clouds in relation to the surface by triangulation (Beekmans et al., 2016).

3. First examples and expected results

Many studies have been held in the Amazon forest in the past years, due to the possibility of studying the atmosphere in both natural and anthropogenic effects (Avissar et al., 2002, Martin et al., 2016, Wendisch et al., 2016). As an example, the ACRIDICON-CHUVA campaign (Aerosol, Cloud, Precipitation, and Radiation Interactions and Dynamics of Convective Cloud Systems - Cloud Processes of the Main Precipitation Systems in Brazil: A Contribution to Cloud Resolving Modeling and to the GPM [Global Precipitation Measurement]; Wendisch et al., 2016) was held in Manaus during September and October of 2014. During ACRIDICON-CHUVA the HALO aircraft (High Altitude and LOng range research aircraft) operated by the German Aerospace Center (Deutsches Luft- und Raumfahrtzentrum, DLR) performed 14 research flights under different aerosols conditions. Using HALO, remote sensing observations of the cloud sides but also in-situ observations of liquid water and ice content, aerosol particles and meteorological conditions were performed.

Braga et al. (2017) used in-situ data to analyze cloud depth and cloud droplet concentration for three clouds under different aerosol scenarios. They found that in a clean atmosphere, the cloud depth was 3000 m and had a maximum droplet concentration

of 400 cm^{-3}, while for polluted and very polluted cases, the instruments measured approximately 6000 m and 700 cm^{-3} and 6500 m and 2000 cm^{-3}, respectively.

In Jäkel et al. (2017), analysis of the cloud side of deep convective clouds in different aerosol scenarios were made. From 16 clouds measured in very polluted scenario, ten contained all three different layers. All of them had its basis higher than 4 km, the mixed-phase layer was first identified at temperatures below -5ºC and the deeper ones achieved cloud top altitudes of 14 km, with temperatures of -60ºC. For moderate aerosol conditions and clean atmosphere, there were not enough measurements to achieve statistical significant results. It is expected that this can be achieved now during the new campaign at ATTO.

Using the infrared camera some field studies were already performed at ATTO in 2017. Fig. 2a shows a picture of a DCC close to the ATTO tower. Fig. 2b illustrates the brightness temperature of the same cloud taken by the infrared camera which is interfered by the atmospheric emission. In the later course of the project this atmospheric contribution will be excluded by radiative transfer simulations following the approach by Stapf (2016). However, also without atmospheric correction, it can be seen that the cloud base is warmer than the top, with a difference of approximately 10 K. Due to the atmospheric masking the true brightness temperature gradient between cloud top and cloud base is expected to be much larger.

Once the distance of the clouds from the GoPro-Images and the height and temperature of the cloud layers from the infrared camera are calculated, using the AisaHawk data will be possible to identify when glaciation will start in the cloud and how it will change during the course of evolution.

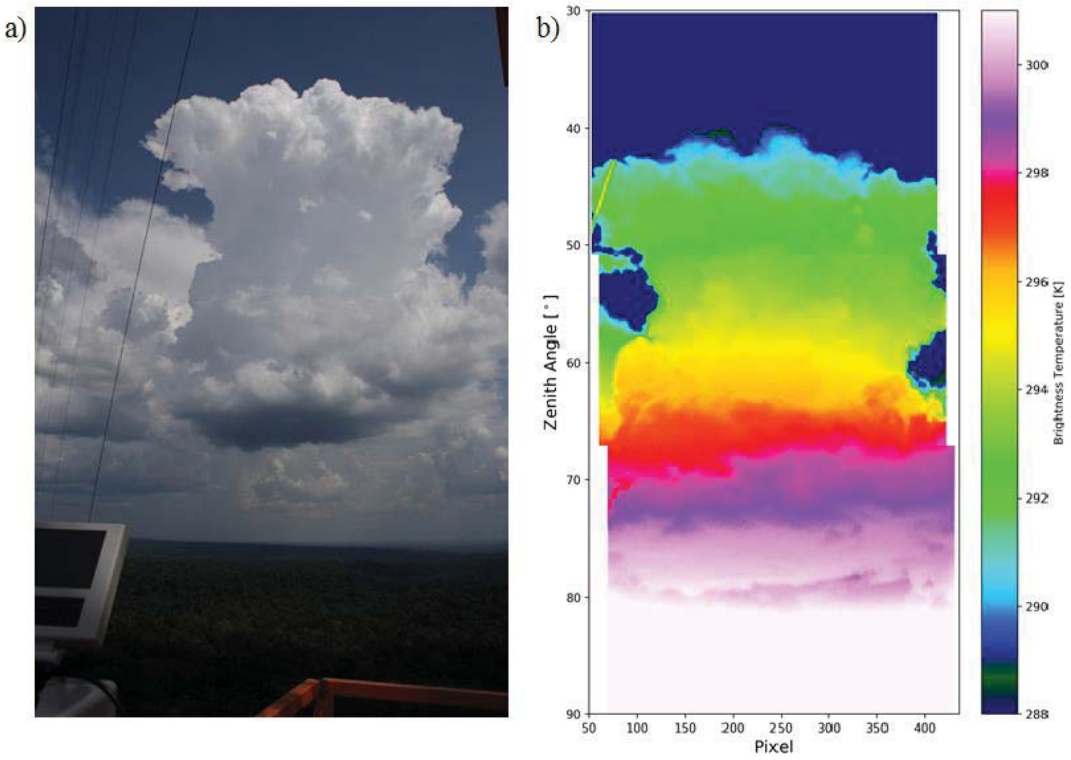

Figure 2: a) Picture and b) infrared image with different brightness temperatures of a deep convective cloud on 2nd November 2017 at 17:36:08 UTC at ATTO.

4. Conclusions and outline

DCCs are still a source of uncertainty for weather prediction and climate models. Several studies were already performed relating aerosol conditions and DCC development, but the results are still inconclusive. This study aims to improve the understanding about cloud development with respect to glaciation by observing the vertical distribution of the thermodynamic phase during all stages of DCC evolution.

Observations of the sides of DCCs with an imaging spectrometer AisaHawk (spectral radiance), an infrared camera (brightness temperature and height of layers) and two GoPros cameras (distance and height of the cloud) will be performed, and once all results are analyzed together, it is expected to identify the altitude and temperature of the three layers of DCCs.

The Amazon Tall Tower Observatory was chosen as the location to collect data due to its atmospheric conditions. An intensive campaign will be performed in September / October 2018, when we expect the transition between low and high aerosol load around ATTO.

5. References

Albrecht, B. A., 1989: Aerosols, Cloud Microphysics, and Fractional Cloudiness, Science, 245, 1227–1230.

Andreae, M. O., and Coauthors, 2015: The Amazon Tall Tower Observatory (ATTO): Overview of pilot measurements on ecosystem ecology, meteorology, trace gases, and aerosols. Atmos. Chem. Phys., 15, 10 723–10 776, doi:10.5194/acp-15-10723-2015.

Avissar, R., Silva Dias, P. L., Silva Dias, M. A. F., Nobre, C. A., 2002: The Large-Scale Biosphere-Atmosphere Experiment in Amazonia (LBA): Insights and future research needs, J. Geophys. Res., 107(D20), 8086, doi:10.1029/2002JD002704.

Beekmans, C., Schneider, J., Läbe, T., Lennefer, M., Stachniss, C., Simmer, C., 2016: Cloud photogrammetry with dense stereo for fisheye cameras. Atmos. Chem. Phys., 16, 14231–14248.

Braga, R. C., Rosenfeld, D., Weigel, R., Jurkat, T., Andreae, M. O., Wendisch, M., Pöschl, U., Voigt, C., Mahnke, C., Borrmann, S., Albrecht, R. I., Molleker, S., Vila, D. A., Machado, L. A. T., Grulich, L., 2017: Further evidence for CCN aerosol concentrations determining the height of warm rain and ice initiation in convective clouds over the Amazon basin. Atmos. Chem. Phys., 17, 14433–14456.

Collow, A. B. M., Miller, M. A., Trabachino, L. C., 2016: Cloudiness over the Amazon rainforest: Meteorology and thermodynamics, J. Geophys. Res. Atmos., 121, 7990–8005, doi:10.1002/2016JD024848.

Giangrande, S. E., Feng, Z., Jensen, M. P., Comstock, J. M., Johnson, K. L., Toto, T., Wang, M., Burleyson, C., Bharadwaj, N., Mei, F., Machado, L. A. T., Manzi, A. O., Xie, S., Tang, S., Silva Dias, M. A. F., Souza, R. A. F., Schumacher, C., Martin, S. T., 2017: Cloud characteristics, thermodynamic controls and radiative impacts during the Observations and Modeling of the Green Ocean Amazon (GoAmazon2014/5) experiment. Atmos. Chem. Phys., 17, 14519–14541.

Jäkel, E., Walter, J., Wendisch, M., 2013: Thermodynamic phase retrieval of convective clouds: impact of sensor viewing geometry and vertical distribution of cloud properties. Atmos. Meas. Tech., 6, 539–547.

Jäkel, E., Wendisch, M., Krisna, T. C., Ewald, F., Kölling, T., Jurkat, T., Voigt, C., Cecchini, M. A., Machado, L. A. T., Afchine, A., Costa, A., Krämer, M., Andreae, M. O., Pöschl, U., Rosenfeld, D., Yuan, T., 2017: Vertical distribution of the phase state of particles in tropical deep-convective clouds as derived from cloud-side reflected solar radiation measurements. Atmos. Chem. Phys. Discuss., doi:10.5194/acp-2017-64.

Korolev, A., McFarquhar, G., Field, P., Franklin, C., Lawson, P., Wang, Z., Williams, E., Abel, S., Axisa, D., Borrmann, S., Crosier, J., Fugal, J., Krämer, M., Lohmann, U., Schlenczek, O., Wendisch, M., 2017: Mixed-Phase clouds: Progress and Challenges. Baumgardner, D., McFarquhar, G., and Heymsfield, A. (Eds.). Chapter 5: Mixed-Phase Clouds: Progress and Challenges. AMS Meteorological Monographs. 58, pp. 5.1-5.50, doi:10.1175/AMSMONOGRAPHS-D-17-0001.1,
http://journals.ametsoc.org/doi/pdf/10.1175/AMSMONOGRAPHS-D-17-0001.1

Martin, S. T., Artaxo, P., Machado, L. A. T., Manzi, A. O., Souza, R. A. F., Schumacher, C., Wang, J., Andreae, M. O., Barbosa, H. M. J., Fan, J., Fisch, G., Goldstein, A. H., Guenther, A., Jimenez, J. L., Pöschl, U., Silva Dias, M. A., Smith, J. N., and Wendisch, M., 2016: Introduction: Observations and Modeling of the Green Ocean Amazon (GoAmazon2014/5), Atmos. Chem. Phys., 16, 4785-4797, https://doi.org/10.5194/acp-16-4785-2016.

Martins, J. V., Marshak, A., Remer, L. A., Rosenfeld, D., Kaufman, Y. J., Fernandez-Borda, R., Koren, I., Correia, A. L., Zubko, V., Artaxo, P., 2011: Remote sensing the vertical profile of cloud droplet effective radius, thermodynamic phase, and temperature. Atmos. Chem. Phys., 11, 9485–9501.

Pilewskie, P. and Twomey, S., 1987: Discrimination of ice from water in clouds by optical remote sensing. Atmos. Res., 21: 113-122.

Rosenfeld, D., Gutman, G., 1994: Retrieving microphysical properties near the tops of potential rain clouds by multispectral analysis of AVHRR data. Atmospheric Research, 34, 259-283.

Rosenfeld, D., and Woodley, W.L., 2003: Closing the 50-year circle: From cloud seeding to space and back to climate change through precipitation physics, Meteor. Monogr., 51, 59-80.

Stapf, J., 2016: Ableitung von Temperaturprofilen aus Infrarot-Kamera Messungen (Master's thesis). Universität Leipzig, 69 p.

Tao, W.-K., Chen, J.-P., Li, Z., Wang, C., Zhang, C., 2012: Impact of aerosols on convective clouds and precipitation, Rev. Geophys., 50, RG2001, doi:10.1029/2011RG000369.

Twomey, S., 1977: The influence of pollution on the shortwave albedo of clouds, J. Atmos. Sci., 34, 1149–1152.

Wendisch, M. et al, 2016: ACRIDICON–CHUVA CAMPAIGN, Studying Tropical Deep Convective Clouds and Precipitation over Amazonia Using the New German Research Aircraft HALO. BAMS, 1885 - 1908.

Water vapor retrieval in the upper troposphere and lower stratosphere using airborne measurements of spectral solar irradiance

Peter Stammer*, Kevin Wolf, André Ehrlich, Manfred Wendisch

*Institut of Meteorology, Stephanstr. 3 04103 Leipzig, *E-Mail: p.stammer@hotmail.com*

Summary

Airborne measurements of the downward spectral solar irradiance were analyzed with differential optical absorption spectroscopy for the integrated water vapor (IWV) in the atmospheric column above the aircraft. The measurements are obtained from two campaigns in 2016, during which the High Altitude and Long Range Research Aircraft (HALO) took measurements of the downward solar irradiance within the upper troposphere and lower stratosphere (UTLS). The feasibility and limitations of the presented method are discussed for the dry conditions, which are typical for the high altitudes of the UTLS and above. Considering the uncertainties encountered in the irradiance measurements and the high sensitivity of the retrieval, the method was unable to provide sound results for the stratosphere, but provided reasonable results in the troposphere.

Zusammenfassung

Flugzeuggetragene Messungen der abwärtsgerichteten spektralen solaren Irradianz wurden mit der Methode der differenziellen optischen Absorptionsspektroskopie auf den integrierten Wasserdampf (IWV) in der Atmosphäre oberhalb des Flugzeuges untersucht. Im Rahmen zweier Messkampagnen im Jahr 2016 führte das High Altitude and Long Range Research Aircraft (HALO) Messungen der spektralen solaren Irradianz in dem Höhenbereich der oberen Troposphäre und unteren Stratosphäre (UTLS) durch. Hier werden das Potential und die Limitierungen eines solchen Verfahrens untersucht, um Wasserdampf in den trockenen Gegebenheiten abzuleiten, die in und oberhalb der UTLS herrschen. Angesichts der Messunsicherheiten und der hohen Sensitivität des Verfahrens, konnten in der Statosphäre nicht aussagekräftige Ergebnisse erreicht werden, aber in der Troposphäre konnte das Verfahren zuverlässige Ergebnisse liefern.

1 Motivation

The amount of water vapor in the upper troposphere and lower stratosphere (UTLS) is significantly lower, compared to tropospheric water vapor, but it has significant impacts on radiative and dynamical processes (Maycock et al., 2013) and therefore influences the earth's climate (Solomon et al., 2010). Additionally, water vapor has an impact on the troposphere-stratosphere exchange and serves as a tracer for investigating the stratosphere (Fueglistaler et al., 2009).

Longterm records of water vapor in the UTLS are scarce in number and often have low temporal or spatial coverage. Measurements of water vapor in high altitudes by in situ observations is challenging due to the low concentrations in the dry stratosphere. There is evidence for a gradual increase of stratospheric water vapor over the past decades, but the responsible processes are not completely understood (Hurst et al., 2011).

Remote sensing by measurements of downward solar radiation were already used by Houghton and Seeley (1960) to quantify the integrated water vapor at high altitudes over England. This water vapor remote sensing generally relies on the principle of differential optical absorption spectroscopy (DOAS). Kindel et al. (2015) discussed an example of the application of DOAS for retrieving water vapor both within a constrained layer in the atmosphere, as well as within the atmospheric column above an aircraft up to the top of the atmosphere (TOA). Their study concluded that the airborne measurements have the ability to probe the mechanisms of stratospheric water vapor transport at a higher vertical and horizontal resolution and higher accuracies than would be possible with balloon or satellite measurements.

In the study presented here, this method was adapted to spectral solar irradiance measurements obtained on board of the research aircraft HALO (High Altitude and Long Range Research Aircraft), which are described in Section 3. In Section 2, the retrieval method is described and characterized by a sensitivity study. Exemplary results are presented in Sections 4-5.

2 Differential optical absorption spectroscopy

2.1 Theory

The retrieval of water vapor by means of differential optical absorption spectroscopy (DOAS) relies on the absorption of solar radiation by atmospheric water vapor. Solar radiation that is incident on the top of the atmosphere (TOA) has an initial spectral irradiance $F_{\lambda,0}$. After propagating through the atmosphere by a certain path length s, the irradiance is reduced to $F_\lambda(s)$ by absorption by water vapor, as described by Lambert-Beer's,

$$F_\lambda(s) = F_{\lambda,0} \cdot exp\left(-\frac{\tau}{\mu}\right) = F_{\lambda,0} \cdot exp\left(-b_{abs}\frac{z}{\mu}\right) = F_{\lambda,0} \cdot exp\left(k \cdot \rho_{wv}\frac{z}{\mu}\right) = F_{\lambda,0} \cdot exp\left(k\frac{IWV}{\mu}\right), \tag{1}$$

when considering the geometry $s = z/\mu$ and $\mu = cos\theta$ being defined as the cosine of the solar zenith angle θ. In equation 1 the optical thickness τ equals the product s and the absorption coefficient b_{abs}. b_{abs} is equal to the product of the mass absorption coefficient k ($m^2\ kg^{-1}$) of water vapor and the absolute humidity ρ_{wv}. ρ_{wv} integrated over s results in the integrated water vapor (IWV), which has the units $kg\ m^{-2}$.

Based on equation 1 the IWV can be derived by the ratio between the irradiance at TOA and at the irradiance at z, at a wavelength λ_{wv} where water vapor absorbs radiation. The strongest water vapor absorption bands in the visible range are centered at 0.82, 0.94 and 1.1 μm. The near-infrared (NIR) has absorption bands centered at 1.37, 1.87 and 2.6 μm. At the higher altitudes of concern for this work the NIR bands are no longer saturated, but are still strong enough that radiation is absorbed sufficiently despite the low IWV amounts. Therefore, the bands at 1.37 and 1.87 μm are both used to infer IWV in the UTLS.

F_0 cannot be measured directly, but is estimated instead by measurements at wavelengths near the water vapor absorption where there is no absorption by water vapor. There are many more processes besides the absorption by the trace gas that contribute to an extinction of radiation, such as Rayleigh scattering or effects in the measuring instrument (Platt and Stutz, 2008). Differential optical absorption spectroscopy solves this problem by observing the difference in the occurring absorption at several wavelengths. While absorption by the trace gas water vapor, the differential absorption, occurs over a narrow band, the rest of the factors that cause extinction generally have spectrally broad structures. The narrow band trace gas absorption can be separated from the broadband extinction. Therefore, broadband extinction is subtracted from F_0, and the resulting $F_0^{'}$ becomes the new intensity spectra of reference, to which the trace gas absorption is compared.

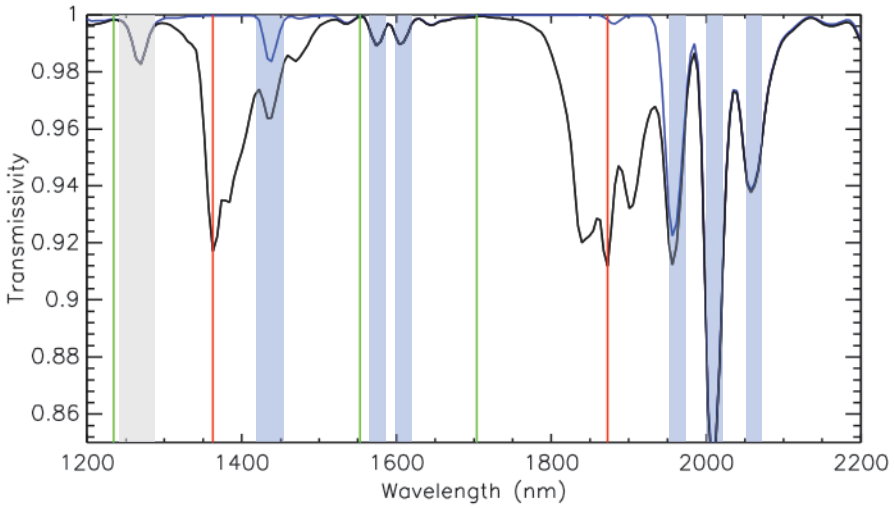

Fig. 1: *Spectral transmissivity of the US standard atmosphere as simulated at an altitude of 10 km for an atmosphere with water vapor (blue line) and without water vapor (black line). Red lines denote center of the two water vapor absorption bands in the NIR (1363 nm and 1873 nm) and the green lines denote minima in water vapor absorption (1235 nm, 1553 nm and 1704 nm) which can be used for scaling because they are close to the respective absorption band. The gray shaded region denotes absorption from O_2, the blue shaded region that of CO_2.*

Figure 1 gives a detailed picture of the water vapor absorption in the NIR. The blue line is the simulated transmittance of a model atmosphere considering all atmospheric gases besides water vapor, while the black line includes water vapor. In the regions where both lines differ, absorption by water vapor is involved. At the centers of both absorption bands, located at 1363 nm and 1873 nm (red lines), practically all molecular absorption is due to water vapor. The green lines denote examples of wavelengths that are close to the bands, at which the atmosphere is practically free of molecular absorption not only from water vapor but from all gases. These are 1235 nm, 1553 nm and 1704 nm.

One of these absorption-free wavelengths is used to scale the spectral irradiance to obtain $F_0^{'}$. Scaling is performed by means of a simple gain of the measurement across all wavelengths, so that the measured irradiance is identical to the TOA irradiance at the scaling wavelength. Performing such a scaling introduces relative irradiances instead of absolute irradiances. The quantity under consideration is now the relative relation between the band center and the scaling wavelength.

2.2 Iterative Retrieval

The downward spectral irradiance is simulated with the version 2.0.2 of the radiative transfer routines libRadtran (Emde et al., 2016). Calculation of radiative transfer in libRadtran is based primarily on the DISORT (DIScrete ORdinate Radiative Transfer solver) code. Simulations are performed for identical conditions for all relevant quantities, being the solar zenith angle, the flight altitude and atmospheric profiles above the aircraft. The simulated irradiance is then compared with the measurement.

The unknown quantity in the simulation is the IWV of the overlying atmospheric column. LibRadtran incorporates several model atmospheres that include, among other quantities, a profile of air temperature and water vapor. Model atmospheres are available for a range of latitudes and seasonal conditions. A profile is chosen according to the setting of the measurement. A custom model atmosphere is created be eliminating water vapor at all levels below the flight altitude. When adjusting the IWV of the simulation, the water vapor profile of the rest of the model atmosphere is scaled to the new IWV value while its shape is maintained.

The IWV is varied so that the simulated irradiance and the scaled measured irradiance within the water vapor absorption band match. Due to scaling both spectra at the wavelength outside the absorption band, this is the same as bringing the relative difference of the irradiance inside and outside the absorption band to unity. The retrieval of water vapor is performed by iteratively adjusting the input IWV of the model. With the measured irradiance $F_{meas}(\lambda_{wv})$ and the simulated irradiance $F_{sim}(\lambda_{wv}, IWV_n)$ the iteration is performed by:

$$IWV_{n+1} = \frac{F_{sim}(\lambda_{wl})}{F_{meas}(\lambda_{wl})} \cdot IWV_n \tag{2}$$

After a sufficiently large amount of iterations the iteration factor becomes close to one and the IWV converges. In the algorithm the iteration was stopped when the difference between the measured and the simulated water vapor absorption was minimized to below a certain threshold. This threshold was set to 0.01 % of the scaled measured irradiance.

2.3 Feasibility of retrieval method

The differences of transmissivity within and outside the water vapor absorption band become lower the higher measurement is made in the atmosphere and the less water vapor is above the aircraft. Therefore, the accuracy of the irradiance measurements needs to be sufficiently high in order to allow a reliable retrieval of IWV. Figure 2 shows the simulated spectral transmissivity at two altitudes (10 km and 15 km) in the model US standard atmosphere. The tropopause in this model atmosphere

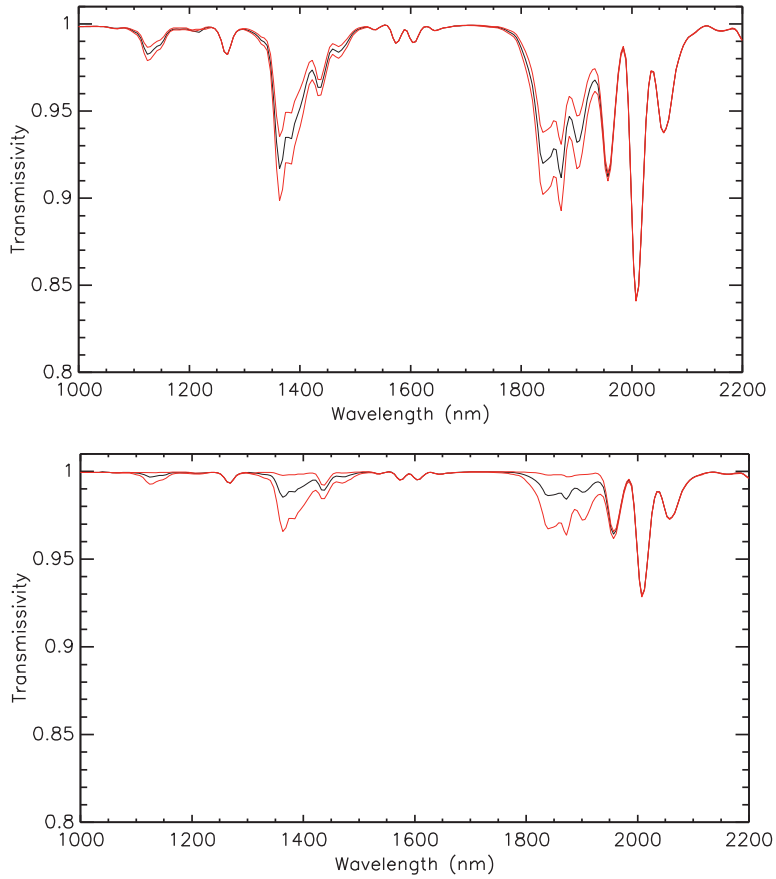

Fig. 2: *Spectral transmissivity (black line) of model US standard atmosphere at 10 km (top) and 15 km (bottom) and with the introduction a measurement uncertainty in the irradiance measurement of ±2% (red lines).*

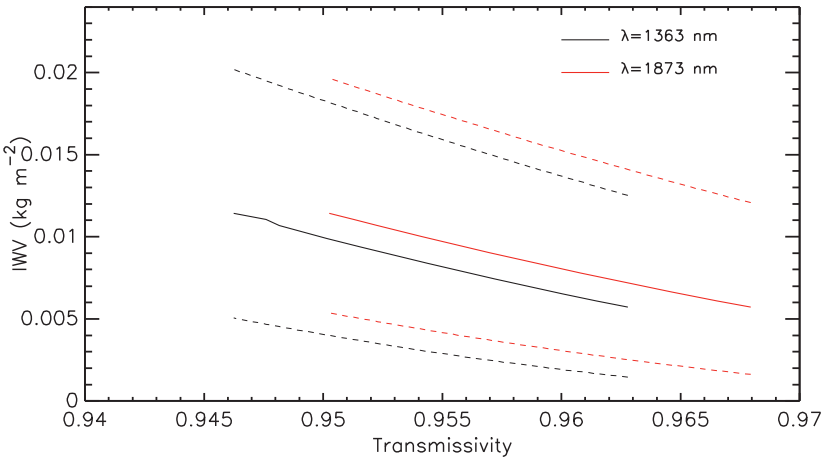

Fig. 3: *Retrieved IWV in dependance of the simulated transmissivity of the atmospheric column from 10 km altitude to the TOA. Dashed lines illustrate the +/-2 % uncertainty of SMART.*

is located at 11 km. There is a large difference in the strength of the water vapor absorption bands between both altitudes. An uncertainty for the measured irradiance of ± 2 % is a good first estimate. The effect of this uncertainty is considered by applying the ± 2 % uncertainty to the original irradiance (as represented by the black plots) and then applying the IWV retrieval to these modified irradiance spectra to deduce modified values for the IWV. These modified values for the IWV then produce new irradiance spectra, that are displayed as the red plots, thus representing the effective uncertainty of the IWV retrieval. The model atmosphere has an IWV of 0.031 mm at 10 km and 0.004 mm at 15 km. At 10 km the IWV uncertainty results in a clear spread within the water vapor absorption bands. At 15 km the IWV is so low that the upper bound in the irradiance measurement leads to a transmissivity spectrum in which water vapor absorption becomes vanishingly small.

In the next scenario a range of IWV values was created with an upper and lower bound, which were oriented towards the values of the stratospheric water vapor found by Hurst et al. (2011). These were 3.0 pmmv and 6.0 pmmv. For this range it was assumed that the water vapor mixing ratio between 10 km and the TOA was constant. Accordingly a range of transmittances in the water vapor bands were simulated at 10 km. Figure 3 displays the retrieved IWV as a function of detected transmissivity at 1363 nm and 1873 nm. The dashed lines display the respective range of the transmission due to the irradiance uncertainty. The change in transmissions over this range of IWV is quite small and would require a precise measurement for the concerning range of stratospheric water vapor. In comparison, uncertainty of the transmission is about as large as the actual variability of IWV. As the transmission is generally high for these low values of IWV even an uncertainty of 2 % for the absolute irradiance causes a large uncertainty in transmissivity. The resulting uncertainty of IWV is very large, between ± 50 % and ± 100 %.

Both the absolute and the relative uncertainty of the IWV retrieval vary, depending on the actual amount of IWV. The absolute uncertainty increases and the relative uncertainty decreases the higher the actual IWV is. The simulations from figure 2 result in an uncertainty of the IWV of +0.008 / -0.011 mm or +27 / -37 % at 10 km and +0.014 / -0.004 or +380 / -100 % on the upper bound at 15 km. When performing calculations in this way and assuming a 2 % uncertainty in the irradiance measurement we find that, in order to obtain an uncertainty of at most 5 % in the IWV one needs an IWV of at least around 1 kg m^{-2}. For comparison, this is the IWV one finds in the US standard atmosphere at an altitude of approximately 6 km. When assuming a spectrometer uncertainty of 0.1 %, as Kindel et al. (2015) applied, an uncertainty of 5 % can be achieved for an IWV as low as 0.05 kg m^{-2}, or at approximately 10 km altitude in the US standard atmosphere.

3 Measurement with HALO

The High Altitude and Long Range Research Aircraft (HALO) is a modified business jet that has been operated as a German research aircraft since 2009. HALO has some advantageous characteristics compared to other research aircraft, having a large payload, long flight ranges and durations and a high flight ceiling. The aircraft's maximum flight altitude is 15 km. Depending on the latitude, HALO can thus reach far into the stratosphere and is well suited for studying the UTLS.

In the past, HALO has carried several instruments that are capable of measuring low water vapor concentrations in the UTLS. In-situ measurements include the Fast In-Situ Stratospheric Hygrometer (FISH) and the Hygrometer for Atmospheric Investigation (HAI) (Rolf et al., 2015). HALO accommodates two nadir looking remote sensing instruments, which are the HALO Microwave Package (HAMP) and the WAter vapor Lidar Experiment in Space (WALES). Details on the instruments can be found in Schnitt et al. (2017) and Grooß et al. (2014). Being a microwave radiometer, HAMP infers the IWV of the column below the aircraft. The lidar instrument WALES infers a vertical profile of the water vapor mixing ratio.

The Next-generation Aircraft Remote-sensing for VALidation studies (NARVAL-II) and the North Atlantic Waveguide and Downstream impact EXperiment (NAWDEX) were two campaigns, that HALO performed in 2016. NARVAL-II took place from June 20 - August 31 and was located near Barbados. NAWDEX took place shortly afterwards from September 12 - October 16. This campaign was focused on the North Atlantic and was based on Iceland. The general cruise altitude during both campaigns was above 8 km and up to approximately 14 to 15 km. With both of these campaigns, measurements are available from the sub-tropics and midlatitude region. Depending on the geographical location the flight ceiling was in the upper troposphere or lower stratosphere.

3.1 Irradiance measurements on HALO

The Spectral Modular Airborne Measurement System (SMART)-Albedometer installed on HALO measures the spectral upward and downward solar irradiance with two optical inlets. These inlets are mounted to the upper and lower fuselage. A third inlet with a narrow field of view measures the upward radiance. The optical inlets are each connected with two grating photodiode array spectrometers by optical fibers. After entering into the spectrometer through a slit, the incoming radiation is spectrally dispersed by a reflective grating and is detected by an array of photo-diodes. Each diode measures a pixel in the spectrum. For a single scan of the spectrum the diodes count photons over an integrated measurement time of 0.5 s. The second spectrometer covers 950-2200 nm with 256 pixels. A description of SMART can by found e.g. in Bierwirth et al. (2009) and Ehrlich et al. (2008).

Another key component of the SMART-Albedometer is an active horizontal stabilization system, which reduces measurement uncertainty from misalignment of the sensors. For proper measurements of $F_\lambda^\downarrow$ the sensor must be aligned with the horizontal plane. Even small deviations from a horizontal alignment can cause significant measurement errors. Even during horizontal flight conditions it is impossible for the airplane to maintain a perfectly stable horizontal position and not experience variability of the pitch or roll angle. With a firm installation of the sensor to the aircraft fuselage an accuracy of ± 5 % or better would not be possible (Wendisch et al., 2001).

In order to solve this problem Wendisch et al. (2001) developed the active stabilization system, which maintains a horizontal alignment of the optical inlets during flight with respect to the earth-fixed coordinate system. A measurement unit determines the aircraft's changes in attitude using an artificial horizon, which it cross-checks with data from a global positioning system (GPS). The measured changes in attitude are then simultaneously compensated by an active horizontal adjustment system. With the active stabilization an accuracy of the sensor's horizontal alignment of better than

$\pm 0.2^\circ$ for pitch and roll angles of up to $\pm 6^\circ$ is obtained. For the measured irradiance the stabilization system thereby ensures an accuracy of better than ± 1 % (Wendisch et al., 2001).

Several components go into the measurement uncertainty of the irradiance. The photodiodes in the spectrometer give off electronic noise, the dark current, by producing a signal even when there is no incoming radiation. The instrument undergoes an absolute calibration in the laboratory for the pixel-wavelength assignment and the absolute irradiance. The spectrometer also undergoes a transfer calibration when it is moved into the field. These three components add to a total measurement uncertainty in the NIR between 8.3 % and 9.4 % (Brückner et al., 2014). The largest fraction of the total uncertainty is on account of the total calibration. When considering the ratio of the irradiance at two different wavelengths, as opposed to the absolute irradiance, the uncertainty of the spectrometer and transfer calibration can be ignored and only the uncertainty of the spectrometer signal remains relevant. Thus the uncertainty in the NIR is reduced to that of the spectrometer noise, with 1.8 % to 2.2 % (Brückner et al., 2014).

3.2 Water vapor retrieval

In theory the retrieval of the IWV is a straightforward process of matching the simulated and measured irradiances at the center of the absorption band. One of several technical limitations is the finite spectral resolution of the measurement. Each of the spectrometer's photodiodes is centered at a specific wavelength. The diode receives radiation not only from the infinitesimal spectral range of this wavelength, but from within a certain spectral interval that lies symmetrically around the center wavelength. Simulated spectra have an arbitrary resolution and consist of infinit points. In order to apply simulations to the measurements, the simulations need to be convoluted with a spectral slit function. This slit function is applied to each point of the simulated irradiance spectrum. It is essentially a Gaussian function with a full width at half maximum (FWHM) that matches that of the measurements pixel.

The FWHM varies throughout the spectrum and between the 1.4 μm and the 1.9 μm band. Choosing an accurate value for the FWHM becomes a trade-off between reproducing the center of an absorption band the most accurately or reproducing an absorption band as a whole the most accurately. The retrieval was performed for a suitable NAWDEX measurement made at 8 km using a range of values for the FWHM. The ideal value for the FWHM was determined from a combination of reducing the standard deviation in the difference between measured and simulated irradiance in the absorption band on the one hand and on the other hand a simple estimation by eyesight.

As the spectrometer has a limited resolution, it must be taken into account, that the spectrometer has no pixel that is centered at the precise location of the absorption band center and instead measures at wavelengths that are close to the center. Choosing the center of the absorption band becomes ambiguous. When looking at the 1363 nm absorption band, one notices a steep drop in absorption when moving along the spectrum away from the maximum. As a result, varying the wavelength in the retrieval slightly can result in differing values of the detected IWV. With that it becomes less clear how to interpret a simulation and a measurement that achieve identical absorption at a central wavelength of one of the absorption bands. Missing the theoretical center of the absorption band with the spectrometer has an effect on the quality of the retrieval. For the 1.4 μm band the center pixel of the measurement is at 1365 nm. Variation of the retrieval wavelength by the two adjacent pixels leads to a variation in retrieved IWV with a standard deviation of $5.5 \cdot 10^{-3}$ mm or approximately 7% of the retrieved IWV. In the case of the 1.9 μm the center pixel is at 1873 nm and variation has a standard deviation of $3 \cdot 10^{-3}$ mm or approximately 5% of the retrieved IWV. The retrieval is relatively sensitive to the FWHM of the slit function. A was to quantify this sensitivity is to observe the degree to which the retrieved IWV changes after changing the FWHM by a small value ($dIWV/dFWHM$.) For the

retrieval at 1365 nm the sensitivity is 0.003 mm/nm or approximately 3 % of the retrieved IWV and at 1873 nm this is 0.0044 mm/nm or 6 %.

A retrieval criteria that seems to be less sensitive to the measurement's finite resolution is to instead use the integral over a broader span of the water vapor absorption band. It would theoretically make sense to detect IWV by the entire spectral range of the absorption band. However, including the wings of the bands, where the water vapor signal becomes smaller, would also allow the noise in the measurement to obtain a greater influence. The integral range chosen for this work was from 1300 nm to 1500 nm for the 1.4 μm absorption band and 1750 nm to 1950 nm for the 1.9 μm absorption band. This is respectively approximately the entire span of the band. In comparing both retrieval methods, the integral method is less sensitive to the slit function. This is understandable, as the integration results in an averaging of the gap between measurement and simulation. The sensitivity $dIWV/dFWHM$ is 0.00019 mm/nm or 0.2 % for the 1.4 μm band and 0.00037 mm/nm or 0.5 % for the 1.9 μm band.

The retrieved values for IWV tend to be lower when retrieving with the 1900 nm band than with the 1400 nm band, both for the integral and for the wavelength method. On average the disagreement between both retrieval bands is smaller for the wavelength method than the integral method. The average deviation of the retrieved IWV between both wavelengths is 0.007 mm throughout the FWHM range of 10.8 - 15.6 nm for integral method versus 0.014 mm for the wavelength method.

The FWHM for the integral retrieval method was set to 15.6 nm for the 1.4 μm band and 10.8 for the 1.9 μm band. For the wavelength method the FWHM was 18.0 nm and 10.8 nm, respectively. With these slit functions the disagreement becomes twice as good for the integral method compared to the wavelength method. The disagreement for the central wavelength makes up 36 % of the mean IWV from both bands versus 19 % for the integral method. In the following the retrieval method of integration of the 1.4 μm band between 1.3 μm and 1.5 μm will be used. This method is less dependent on the FWHM of the slit function being applied to the simulation and shows fairly good agreement between both bands. Also, one can expect the 1.4 μm band to have a better signal-to-noise ratio than the 1.9 μm band, because the solar irradiance under a cloudless sky is stronger at a shorter wavelength within the NIR.

When evaluating a measured irradiance spectrum, first a moving average over three measurement pixels is applied to the measurement. This smooths out some of the high frequency structure in the signal caused by electronic noise and may decrease the uncertainty from pixel registration (Kaufman and Gao, 1992). Scaling of the measurement to the simulation is performed at 1553 nm for the 1.4 μm band or 1704 nm at the 1.9 μm band.

4 Estimation of Retrieval Uncertainty

The uncertainty in the IWV retrieval results from several factors. One of these is the uncertainty concerning the temperature and water vapor profile above the aircraft. Factors from the irradiance measurement itself include the uncertainty of the horizontal alignment of the optical inlets, as well as noise from the spectrometer. Noise sources, as stated by Platt and Stutz (2008) are photon statistics, electronic detector noise in the instrument and further, unexplained, random spectral structures in the signal. A reason for the latter factor can for example be pixel-to-pixel variations in sensitivity.

From the above section the uncertainty of the spectrometer irradiance amounts to ± 2 %. The active stabilization amounts to an uncertainty of ± 1 %. The latter is a conservative estimate and may actually be reduced further because it is the ratio of two irradiances from the same scan being considered for the retrieval and not an absolute irradiance.

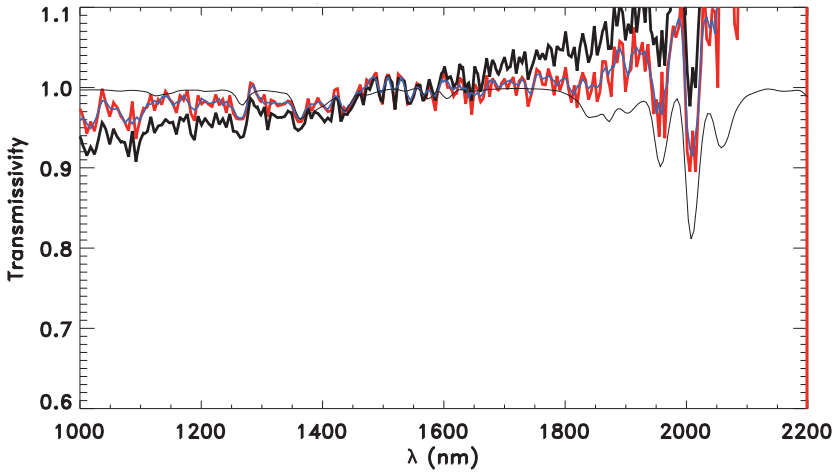

Fig. 4: *Spectral transmissivity measured at 12.3 km during a NAWDEX flight (red) and the spectral transmissivity averaged over 600 spectra (black). The blue plot is the result of a moving average over three pixels of the red plot.*

4.1 Spectral noise

Kindel et al. (2015) achieve an uncertainty for the spectrometer of only 0.1 % after averaging over 5 to 10 minutes of scans, or 300-600 spectra. For the measurements that were available for this work such a reduction in uncertainty was not achieved. The red plot in figure 4 shows an example of the spectral transmissivity from a single measurement taken during a cruise episode at 12.3 km during a NAWDEX flight. After averaging irradiance spectra over five minutes or approximately 600 spectra (black plot) the signal noise remains as high and shows a similar structure as the non-averaged spectrum. There must be a noise component that is due to spectral structures of the instrument.

Figure 5 shows the transmissivity from two scans taken at different altitudes during the NAWDEX campaign. Both spectra are now smoothed with the moving average. The signal noise was investigated using the standard deviation of the dispersion of the measured (red plot) from the theoretical irradiance as given by the simulation (black plot) in the range 1530 to 1700 nm. In this range water vapor has no influence. After applying the running average the standard deviation is reduced from $\sim$2 % to $\sim$1 %. The error bars denote the resulting water vapor uncertainty due to the signal noise.

In the case of the low measurement, where there is a strong water vapor signal, noise uncertainty results in a relative uncertainty in the IWV detection of 10%. For the high measurement this uncertainty in the order of 100 %. This confirms the apparent insight from the plot, which is that at a certain altitude the expected amount of water vapor becomes so low, that the resulting absorption signal becomes too weak to reliably detect.

4.2 Resulting total uncertainty in IWV retrieval

The total uncertainty of the relative irradiance is $\pm$3 %. The resulting uncertainty in the IWV retrieval is obtained by adjusting the measurement by $\pm$3 % and observing the resulting change in retrieved IWV. The absolute and the relative uncertainty of IWV are both not generally constant, but vary with the actual value of IWV. The calculated retrieval uncertainty is generally not symmetrical, which is in line with the physics of Lambert-Beer's law.

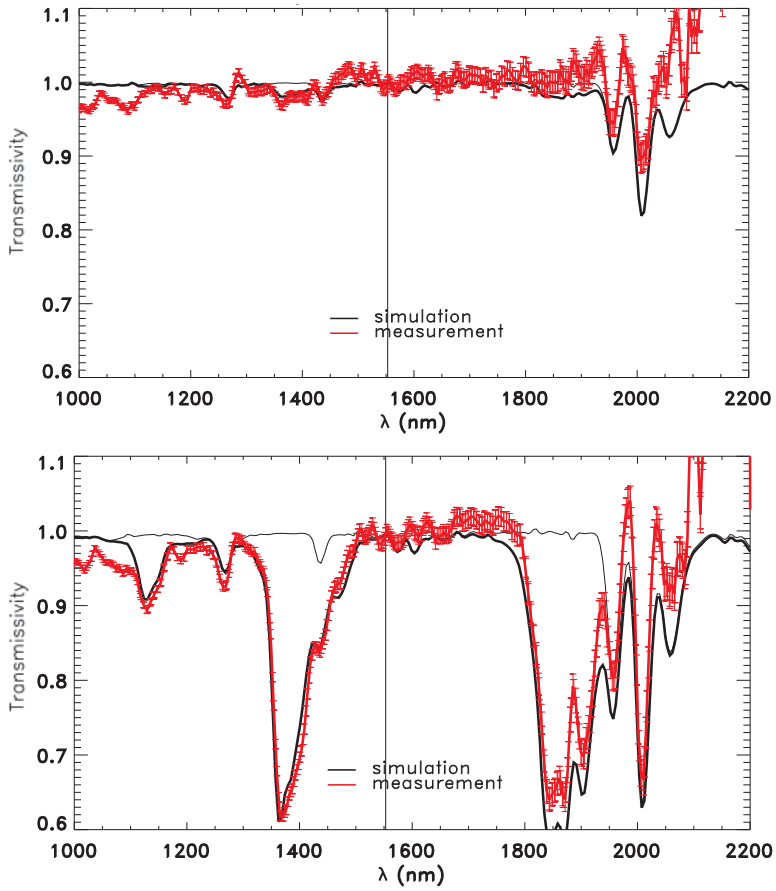

Fig. 5: *Spectral transmissivity measured at 12 km (left) and 7 km (right) and retrieved transmissivity with noise. Vertical line denotes scaling wavelength.*

For the measurement at 7 km from the bottom panel in figure 5 the calculated uncertainty is +0.059/-0.069 kg m^{-2} or +32/-38 %. This measurement was geographically in the North Atlantic and the flight altitude was thus roughly at the tropopause. At 12 km during the same flight the uncertainties grow to +0.049/-0.038 kg m^{-2} or +188/-92 %. This finding underlines the difficulty of the task at hand, because even small uncertainties of the irradiance lead to a large uncertainty in retrieved IWV due to the scarcity in water vapor that one encounters in the UTLS.

5 Results

NAWDEX measurements taken during a cruise segment at 12.3 km on the August 19 show a water vapor signal that is too low compared to the noise to deduce IWV. A model atmosphere for similar conditions (sub-arctic, summer) contains an IWV of 0.006 kg m^{-2} at this altitude. The uncertainty of the retrieval was calculated at +200/-100 %.

Figure 6 shows the time series of the retrieved IWV during a cruise at 9.7 km altitude on the September 21 during NARVAL-II. This is well below the tropopause and in a generally more moist atmosphere. The uncertainty here is +40/-34 %. The model atmosphere for the tropics has an IWV of 0.12 kg m^{-2}.

Another interesting consideration is to construct a vertical profile of the water vapor mixing ration or to retrieve the IWV for a limited layer of the atmosphere from measurements taken during ascent or descent of the aircraft. From the SMART measurements taken during the ascent on the same day

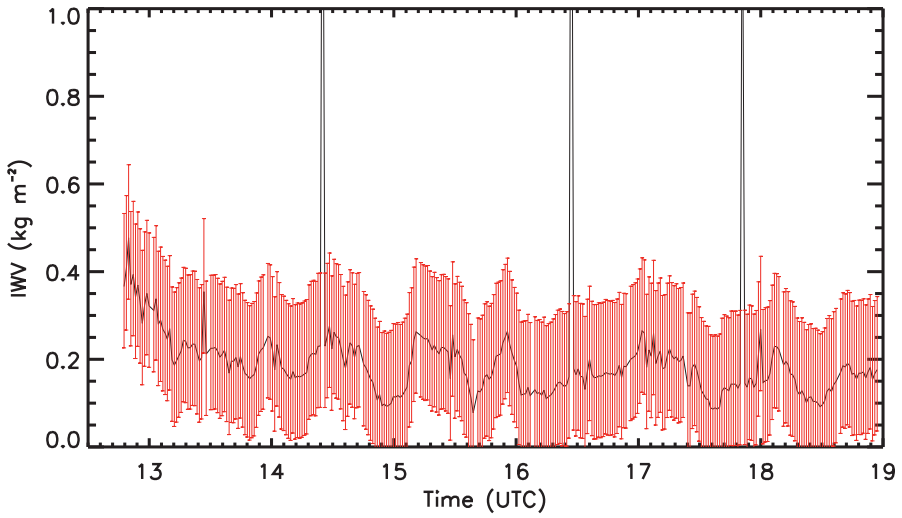

Fig. 6: *Time series of retrieved IWV during cruise at 9.7 km during a NARVAL-II flight with error bars (8:30 to 15:00 local time).*

the retrieved IWV in the layer between 4 km and 9.7 km is 2.43 +0.32/-0.36 kg m^{-2}. This can be compared to 3.21 kg m^{-2} from in-situ measurements of water vapor made on HALO and 2.74 kg m^{-2} from a radio sonde launched at the airport of take-off.

6 Conclusion

A DOAS method for retrieving the IWV from airborne measurements of the spectral solar irradiance has been introduced. The method relies on the water vapor absorption bands located at 1.37 μm and 1.87 μm in the NIR. The potential of thus retrieving the IWV near the UTLS has been analyzed. A sensitivity study showed that, as there is only a weak water vapor signal under such conditions, uncertainties in the radiation measurement lead to a large uncertainty in the retrieval. At 10 km the US standard atmosphere has an IWV of 0.03 kg m^{-2}. When applying an uncertainty of $\pm$2% for the irradiance measurement the resulting uncertainty of the retrieval was found to be +27/-37 %. In order to obtain a retrieval with an uncertainty of better than 5% the highest altitude for performing the retrieval would be 6 km. If, e.g, the uncertainty of the irradiance measurement could be decreased to only 0.1% the retrieval could perform with the same degree of certainty at altitudes of up to 10 km. The water vapor signal in HALO measurements taken in the stratosphere becomes indistinguishable above the signal noise and the stabilization uncertainty. Consideration of these data was limited to lower altitudes. As an example, a time series was created of the IWV at 9.7 km at the Bahamas. The retrieval uncertainty here was +40/-34 %. Also, from the aircraft's ascent after take-off, the IWV was retrieved within a layer between 4 and 9.7 km. The resulting value (2.43 +0.32/-0.36 kg m^{-2}) compared well with onboard in-situ and radiosonde measurements.

References

Bierwirth, E., Wendisch, M., Ehrlich, A., Heese, B., Tesche, M., Althausen, D., Schladitz, A., Müller, D., Otto, S., Trautman, T., Dinter, T., Hoyningen-Huene, W., Kahn, R., 2009: Spectral surface albedo over Morocco and its impact on radiative forcing of Saharan dust, Tellus, 61B, 252-269.

Brückner, M., B. Pospichal, A. Macke, M. Wendisch, 2014: A new multispectral cloud retrieval method for ship-based solar transmissivity measurements, J. Geophys. Res. Atmos., 119, 11,338-11,354.

Ehrlich, A., Bierwirth, E., Wendisch, M., Gayet, J.-F., Mioche, G., Lampert, A., Heintzenberg, J., 2008: Cloud phase identification of Arctic boundary-layer clouds from airborne spectral reflection measurements: test of three approaches, Atmos. Chem. Phys., 8, 7493-7505.

Emde, C., Buras-Schnell, R., Kylling, A., Mayer, B., Gasteiger, J., Hamann, U., Kylling, J., Richter, B., Pause, C., Dowling, T., Bugliaro, L., 2016: The libRadtran software package for radiative transfer calculations (version 2.0.1), Geosci. Model Dev., 9, 1647-1672.

Fueglistaler, S., Dessler, A. E., Dunkerton, T. J., Folkins, I., Fu, Q., Mote, P. W., 2009: Tropical Tropopause Layer, Rev. Geophys., 47, RG1004.

Groß, S., Wirth, M., Schäfler, A., Fix, A., Kaufmann, S., Voigt, C., 2014: Potential of airborne lidar measurements for cirrus cloud studies, Atmos. Meas. Tech., 7, 2745-2755.

Houghton, J. T., Seeley, J. S., 1960: Spectroscopic observations of the water-vapor content of the stratosphere, Quart. J. R. Met. Soc., 86, 358.

Hurst, D. F., Oltmans, S. J., Vömel, H., Rosenlof, K. H., Davis, S. M., Ray, E. R., Hall, E. G., Jordan, A. F., 2011: Stratospheric water vapor trends over Boulder, Colorado: Analysis of the 30 year Boulder record, J. Geophys. Res., 116, D02306.

Kaufman, Y. J., Gao, B.-C., 1992: Remote sensing of water vapor in the near IR from EOS/MODIS, IEEE TGRS, 30, 5.

Kindel, B. C., Pilewskie, P., Schmidt, K. S., Thornberry, T., Rollins, A., Bui, T., 2015: Upper-troposphere and lower-stratosphere water vapor retrievals from the 1400 and 1900 nm water vapor bands, Atmos. Meas. Tech., 8, 1147-1156.

Maycock, A. C., Joshi, M. M., Shine, K. P., Scaife, A. A., 2013: The Circulation Response to Idealized Changes in Stratospheric Water Vapor, Am. Met. Soc., 554-561.

Platt, U., Stutz, J., 2008: Differential Optical Absorption Spectroscopy: Principles and Applications, Springer-Verlag Berlin Heidelberg, p. 138 ff.

Rolf, C., Afchine, A., Bozem, H., Buchholz, B., Ebert, V., Guggenmoser, T., Hoor, P., Konopka, P., Kretschmer, E., Müller, S., Schlager, H., Spelten, N., Sumińska-Ebersoldt, O., Ungermann, J., Zahn, A., Krämer, M., 2015: Transport of Antarctic stratospheric strongly dehydrated air into the troposphere observed during the HALO-ESMVal campaign 2012, Atmos. Chem. Phys., 15, 9143-9158.

Schnitt, S., Orlandi, E., Mech, M., Ehrlich, A., Crewell, S., 2017: Characterization of Water Vapor and Clouds During the Next-Generation Aircraft Remote Sensing for Validation (NARVAL) South Studies, J-STARS, VOL. 10, NO. 7.

Solomon, S., Rosenlof, K. H., Portmann, R. W., Daniel, J. S., Davis, S. M., Sanford, T. J., Plattner, G.-K., 2010: Contributions of stratospheric water vapor changes to decadal variation in the rate of global warming, Science, 327, 1219-1223.

Wendisch, M., Müller, D., Schell, D., Heintzenberg, J., 2001: An airborne spectral albedometer with active horizontal stabilization. J. Atmos. Oceanic Technol.,18, 1856-1866.

Multi-model-analysis of Arctic climate trends

Schubert, Jan *Institut of Meteorology, Stephanstr. 3 04103 Leipzig, E-Mail: janschubert93@web.de*

Summary:
In the last few decades the Arctic has warmed faster than the rest of the globe and exceeds the global-mean warming by a factor of two to three. This phenomena is called Arctic Amplification (Barnes und Polvani, 2015) and was examined by models, reanalysis and observations. To give a comprehensive overview about the current presentation of the Arctic climate and the agreement of climate predictions of different climate models this thesis presents the results of a multi-model trend analysis of Arctic climate parameters. Six CMIP5 models over a period of 41 years (1980 to 2020) are used. The data of the historical simulations (1980-2005) and of the RCP8.5 scenario (2006-2020) are combined. Arctic climate parameters, such as surface temperature, water vapor, sea ice cover, cloud cover and radiation fluxes, are analyzed for their annual and seasonal development over the last four decades as well as for their spatial distribution.

Zusammenfassung:
In den vergangenden Jahrzehnten erwärmte sich die Arktis 2-3 mal schneller als die restliche Erde. Dieses Phänomen wird Arktische Verstärkung genannt (Barnes und Polvani, 2015) und wurde durch Modellssimulationen, Reanalysen und Beobachtungen untersucht. Um einen umfassenden Überblick über die aktuelle Darstellung des arktischen Klimas und die Übereinstimmung von Klimaprognosen verschiedener Klimamodelle zu geben, werden in dieser Arbeit die Ergebnisse einer Multi-Modell-Trendanalyse von arktischen Klimaparametern vorgestellt. Dafür werden sechs CMIP5 Modelle über einen Zeitraum von 41 Jahre (1980-2020) verwendet. Dazu werden Daten der historischen Simulationen (1980-2005) und des RCP8.5 Scenarios kombiniert. Die arktischen Klimaparameter Temperatur, Meereisbedeckung, Wasserdampf, Wolkenbedeckung und Strahlungsflüsse werden auf ihre jährliche und saisonale Entwicklung sowie auf ihre räumliche Verteilung der letzten 40 Jahre untersucht.

1. Introduction

In the past few decades the global temperature has risen [(Hansen et al. (2010)), (Foster und Rahmstorf (2011))]. The human influence to global warming is not deniable. Since the industrial revolution CO_2 and other greenhouse gas emissions continuously increased (Graßl, 1995). Meanwhile the anthropogenic influence is that great, that the bounds of natural variability are exceeded (Karl und Trenberth, 2003). Several studies investigated the global warming with view to the Arctic warming [(Johannessen et al. (2004)), (Hinzman et al. (2005)), (Najafi et al. (2015))]. In the period from 1960 to 2010 the Arctic north of 60°N warmed by 1.5 to 2.5 K in the annual mean (Bengtsson et al., 2013). In the

work of Chylek et al. (2009) temperature records of Arctic meteorological stations (north of 70°N) in a period from 1970-2008 were analyzed. The greatest trend with 0.75 K/41 years occurred in fall and the smallest trend with 0.31 K/41 years in summer.
Since the availability of satellite passive microwave remote sensing data in 1979, the sea ice decline was well documented (Vihma, 2014). Johannessen et al. (2004) examined sea ice data from satellite passive-microwave sensor measurements in a period from 1978-2003. In this period a decrease of 7.4 % of the ice area of the Arctic was found. The trends are largest in September with 14 %/decade and smallest in March with 5 %/decade. The CMIP5 analyze work of Shu et al. (2015) depict decreasing sea ice all over the Arctic with a maximum trend in September with -8.46 %/decade during a period from 1979-2005.
Due to the linkage to temperature the atmospheric water vapor increases in the Arctic (Rinke et al., 2009). Serreze et al. (2012) analyzed the water vapor trends in the Arctic on basis of reanalysis data. Apart from scattered regions the water vapor increases all over the year with maximum in July and September.
Intrieri et al. (2002) showed that the Arctic region was cloudy 85 % of the year. Over most of the year clouds have a warming effect on surface, except summer where they cool the surface (Karlsson und Svensson, 2011). The seasonal analysis of the cloud fraction data of the extended AVHRR (Advanced Very High Resolution Radiometer) Polar Pathfinder data set (APP-x) of Schweiger (2004) resulted in significant decrease of 7.1±4.3 %/decade in winter and increase of 3.4±3.0 %/decade in spring. This is in agreement with the satellite derived results of Wang and Key (2003) showing a cloudier summer and a less cloudy winter.
All of the previous climate parameters have an influence on the radiation budgets on Top of Atmosphere (TOA) and surface (Wang und Key, 2005). Reduced sea ice cover leading to more open ocean and thus to more radiation absorption and storing. Simultaneously less radiation is reflected to the TOA, which affects the radiation budget.
The climate system is a complex system of interacting climate parameters. A special feature of the Arctic regions is the enhanced warming compared to the rest of the globe. This phenomena is called the Arctic Amplification (AA) (Barnes und Polvani, 2015). The AA is well documented by observations [(Screen und Simmonds 2010), (Serreze und Barry 2011)], models [(Screen 2014), (Bintanja et al. 2011)] and reanalysis [(Francis und Vavrus 2012), (Serreze et al. 2009)] in recent years. The warming is contributed of increased greenhouse gases and positive feedbacks involving sea ice, water vapor and clouds[(Stroeve et al. 2012), (Francis und Vavrus 2012)]. The feedbacks are explained by Pithan and Mauritsen (2014).
My master thesis investigates the current state of agreement of presenting Arctic climate parameters and their development in climate change. To give a comprehensive overview trends of surface temperature (T_{sfc}) , sea ice concentration (SIC), water vapor (WV), total cloud cover (TCC), surface (R_{sfc}) and TOA radiation budget (R_{toa}) are analyzed on their spatial and temporal structure using six CMIP5 (5^{th} Coupled Model Intercomparison Project (Taylor et al. 2012)) models. This article summarizes the results of the first part of my thesis.

2. Data and Methods

2.1 CMIP5 global climate models

Tab. 1: Institute and spatial resolution for the six used CMIP5 models

Model	Institute	Spatial Resolution
CanESM2 (Chylek et al., 2011)	**CCCma** Canadian Centre of Climate Modelling and Analysis	2.8125 ° x 2.8125 °
CCSM4 (Gent et al., 2011)	**NCAR** National Center for Atmosperic Research	0.93 ° x 1.25 °
HadGem2-ES (Jones et al., 2011)	**MOHC** Met Office Hadley Centre	1.24 ° x 1.875 °
CM5A-LR (Dufresne et al., 2013)	**IPSL** Institut Pierre Simon Laplace	1.9 ° x 3.75 °
MIROC5 (Watanabe et al., 2010)	**MIROC** Model for Interdisciplinary Research on Climate	1.41 ° x 1.41 °
MPI-ESM-LR (Stevens et al., 2013)	**MPI** Max Planck Institute	1.875 ° x 1.875 °

The latest Climate Model Intercomparison Project [CMIP5, (Taylor et al. (2012))] compares a great number of models from diverse modeling centers which perform simulations under the same sets of initial and boundary conditions. The participating climate models provide an extensive basis for evaluating and comparing an ensemble of climate model projections (Haywood et al., 2014). The CMIP5 includes a variety of climate projections summarized by Taylor et al. (2012). The historical run contains a period of 1850 to 2005 and is forced by observed atmospheric composition changes which reflect both anthropogenic (such as green house gases and anthropogenic aerosols) and natural sources (volcanic influences, solar forcing, aerosols and emissions of short-lived species and their precursors) and, for the first time, including time-evolving land cover (Taylor et al. (2012)). For the period of the 21th century three radiative forcing scenarios are used. They are called “Representative Concentration Pathway” (RCP) and are designed to cover a wide range of possibilities in social and economic development to represent the full width of possible future emission trajectories (Kharin et al., 2013).
In my master thesis the historical simulation from 1980 to 2005 are combined with the RCP8.5 scenario from 2006-2020. The RCP8.5 scenario is the scenario, where the

radiative forcing in 2100 is 8.5 Wm^{-2} in comparison to 1850. This scenario is used, because the global warming follows this scenario at the present moment (Peters et al., 2013). For the thesis six models from CMIP5 were selected, which have the first three realizations of the mentioned climate parameters. Table 1 summarizes the models, their institutes and spatial resolutions.
In my thesis the first three realizations of the climate parameters are used to analyze the inter-model agreement of the natural variability in climate prediction, because natural variability is one of the major sources of uncertainty in climate projections (Deser et al., 2012). For a better comparison, all models are brought to the same spatial and temporal resolution. The new modified data has a spatial resolution of 1.875°x1.875° and a temporal resolution of 492 monthly time steps, corresponding to 41 years. The Arctic is defined here as the area north of 60°N (Bengtsson et al., 2013), for which trend calculations are performed.

2.2 Era-Interim

Era-Interim (Dee et al., 2011) is the latest ECMWF (European Centre of Medium-Range Weather Forecasts) global atmospheric reanalysis data set containing the period from 1979 to present. The Era-Interim reanalysis is consistent of a vertical resolution of about 60 levels with TOA at 0.1 hPa and a spatial resolution of 1° x1° (Berrisford et al.,2009). In this thesis, ERA-Interim data for temperature and sea ice concentration are used to compare them to the results of the CMIP5 models. There it is worth noting, that the sea ice concentration is simulated and not assimilated (Hiraharaet al., 2016).

2.3 Observations

To compare the model results of temporal temperature development against observations temperature data record from NASA GISS (Goddard Institute for Space Studies) is used, spanning a period of 1880 to present with a spatial resolution of 2° x 2° (Hansen et al., 2010).
For comparing the temporal evolution of sea ice concentration, satellite data of the NIMBUS 7 SMMR (Scanning Multichannel Microwave Radiometer) and of DMSP (Defense Meteorological Satellite Program) SSM/I (Special Sensor Microwave/Imager) is used. The data has a spatial resolution of 0.22° x 0.22° and contains data from 1978 to present (Peng et al., 2013). The data can be downloaded at https://nsidc.org/data/g02135.

2.4 Statistical methods

My master thesis focused on linear trends of Arctic climate parameters. Therefore

- Arctic annual mean trends
- spatial seasonal trends in the Arctic region
- Arctic monthly trends

are calculated on basis of monthly data on a uniform t63-grid. The seasons are defined as spring (March-Mai), summer (June-August), fall (September-November) and

winter (December-February). To prove the significance of the trends a Student's t-test (Stone und Ellis, 2006) was applied. For each year and each model a t-value were calculated and is compared with a reference value, depending on degrees of freedom and level of significance. The results of the Arctic, annual mean trends are presented in this article.

3. Results

3.1 Temperature

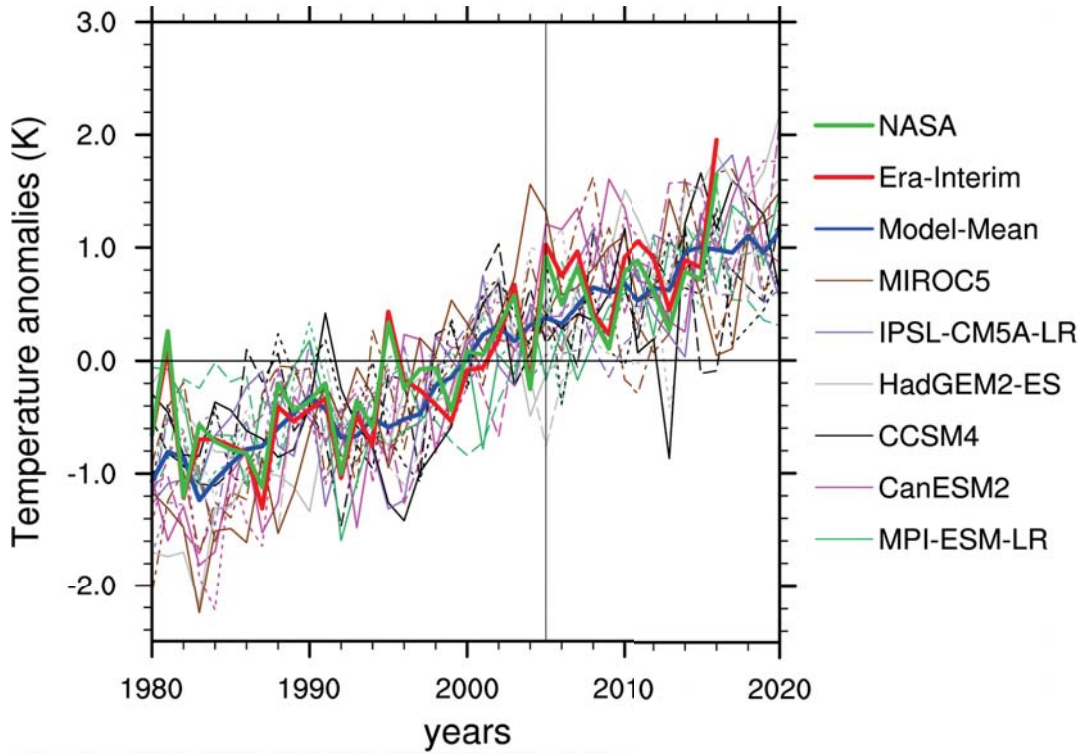

Fig. 1: Annual Arctic T_{sfc} trends from 1980 to 2020 of three ensemble members of the six used models, the multi-model-mean and trends of ERA-Interim and NASA GISS observations from 1980 to 2016

One of the major phenomena concerning the climate change is the amplified T_{sfc} increase in the Arctic compared to the whole globe, called the Arctic Amplification (Serreze und Francis, 2006). Fig. 1 shows the annual trends in the region of the Arctic for the six used models and their first three realizations, the multi-model-mean, the ERA-Interim data and GISS (Goddard Institute for Space Studies) observations from NASA.
Overall a good agreement between models, reanalysis and observations can be seen. They all show a clear positive trend over the period of 41 years. Until the year 2000 the majority of the model ensembles shows deviations smaller than the mean of 1980-2016 and after the year 2000 almost only positive T_{sfc} anomalies can be observed. The greatest trend is shown by the first realization of HadGEM2-ES with 3.79 K/41 years and the smallest trend of 1.66 K/41 years is obtained from the third realization of CCSM4. The

models simulate a mean T_{sfc} increase from 264.29±0.72 K to 266.51±0.75 K which corresponds to a trend of 2.39±0.6 K/41 years. The small uncertainty of the multi-model-mean illustrates the good agreement of the models T_{sfc} prediction. The trends of the multi-model-mean and of all ensemble members are significantly different from zero at 90 % significance level. The ERA-Interim data show a T_{sfc} increase of 2.17 K/37 years and the NASA GISS data an increase of 1.85 K/37 years. Their two curves show similar variabilities, while the multi-model-mean underestimates this natural variability. Comparing the trends of the multi-model-mean, the ERA-Interim and the NASA GISS, the multi-model-mean calculates the greatest trend.

3.2 Sea ice

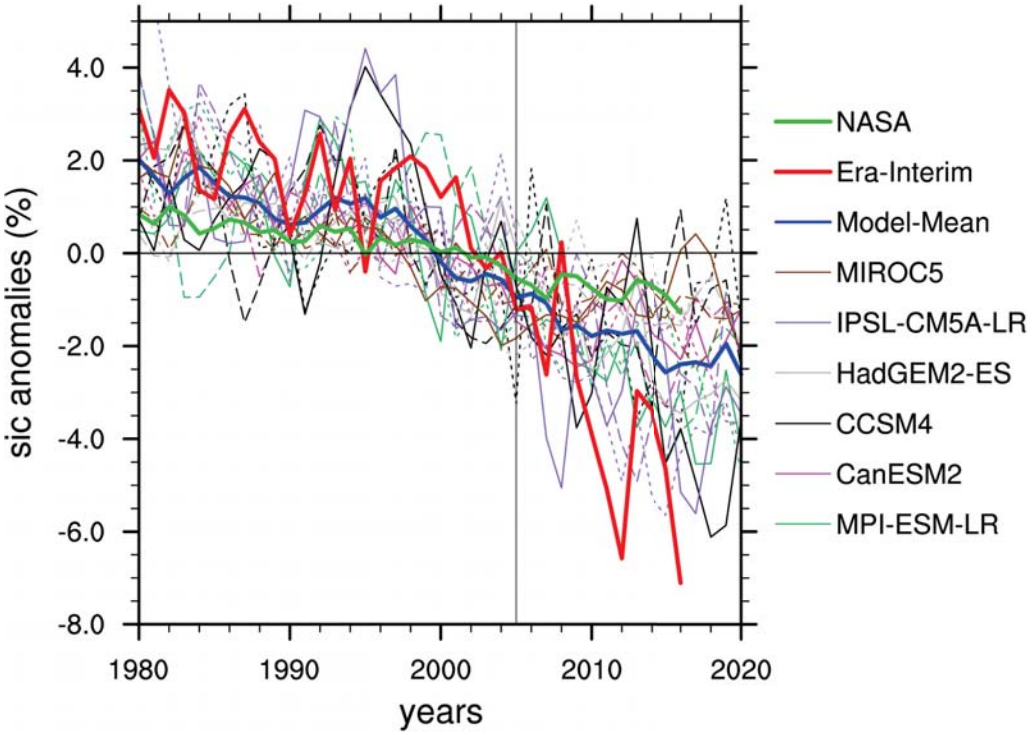

Fig. 2: Annual Arctic sea ice concentration trends from 1980 to 2020 of the first three ensemble members of the six used models, the multi-model-mean and trends of ERA-Interim and NASA observations from 1980 to 2016

The sea ice decrease is a clear consequence of the Arctic Amplification in recent years. Figure 2 shows the annual SIC anomalies in reference to the mean from 1980 to 2016 for the 18 ensemble members of the six models, ERA-Interim reanalysis and NASA observations. All data sets show a clear decreasing trend of Arctic sea ice. The greatest trend is -9.27 %/41 years by the third realization of CM5A-LR and the smallest is -2.51 %/41 years by the third realization of HadGEM2-ES. The models simulate a mean decrease of SIC from 26.05±10.33 % to 22.78±9.55 % ($8.91 \times 10^6 \pm 3.53 \times 10^6$ km² to $7.79 \times 10^6 \pm 3.26 \times 10^6$ km²), which corresponds to a trend of -4.90±1.79 %/41 years. This uncertainty is small compared to the uncertainties in the individual seasons. The trends of

all ensemble members and of the multi-model-mean are significant at 90 % significance level.
The simulated SIC from ERA-Interim decreases from 1980 to 2016 from 51.38 % to 41.17 %. The Era-Interim reanalysis shows a trend of -8.31 % in the considered 37 years, about twice as high as the multi-model-mean trend. The NASA observations are much more in agreement with the multi-model-mean. The observations show a trend of -3.62 %/37 years. Comparing the three datasets the trend of the observations is the smallest. This result conflicts with the results of Stroeve et al. (2007) who described the observed trends as three-times larger than the multi-model-mean. One possible reason for the difference might be the used data. Stroeve et al. (2007) used CMIP3 data, while in this thesis CMIP5 models were used.

3.3 Water vapor

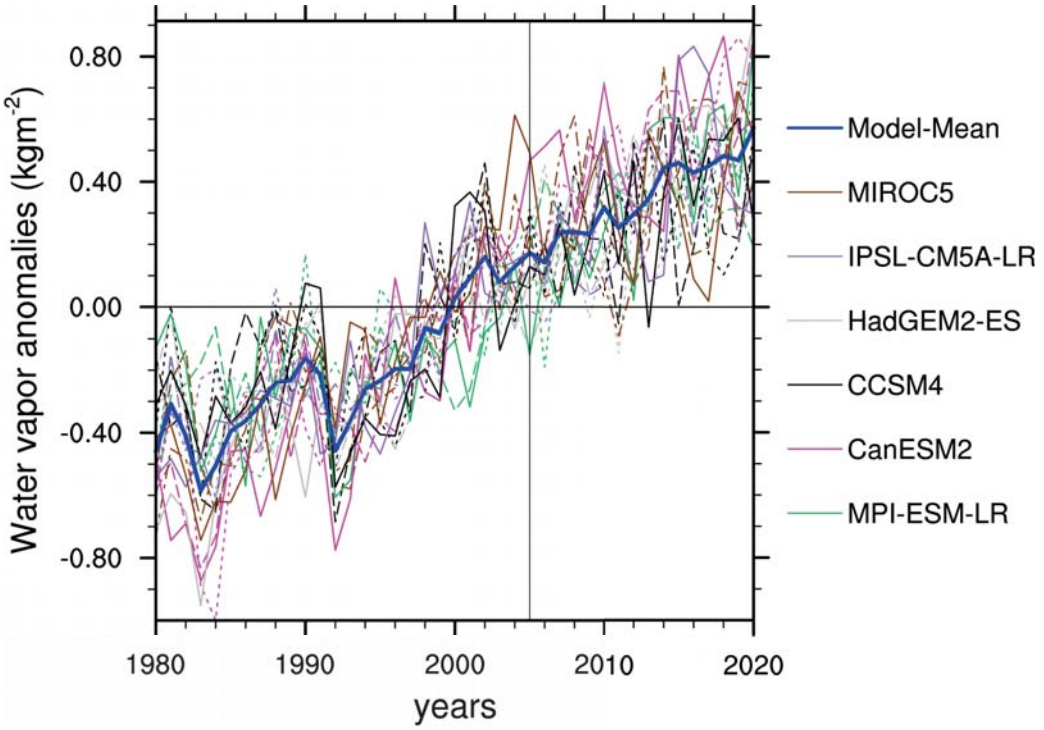

Fig. 3: Annual Arctic WV trends from 1980 to 2020 of the first three ensemble members of the six used models and the multi-model-mean

In a warming climate, the WV content is constantly rising, because of its dependency on T_{sfc}. This relation is described by the Clausius-Clapeyron equation (Holton und Hakim, 2012). After integration this equation one can see that the vapor pressure increases exponentially with T_{sfc}. As a result warm air can hold more WV than cold air. Therefore WV content increases with rising T_{sfc}. A clear positive trend in all model realizations is visible. Furthermore the trends of all realizations are significantly different from zero at 90 % significance level. The smallest trend is 0.79 kgm^{-2}/41 years shown by the third realization of CCSM4 and the greatest is 1.17 kgm^{-2}/41 years shown by the first

realization of MIROC5. The multi-model-mean shows an increase from 7.76±0.48 to 8.79±0.48 kgm^{-2} which results in a trend of 1.10±0.21 kgm^{-2}/41 years. The low uncertainty of the multi-model-mean shows the good agreement between the models and compared to the other climate parameters WV has the best accuracy.

3.4 Total cloud cover

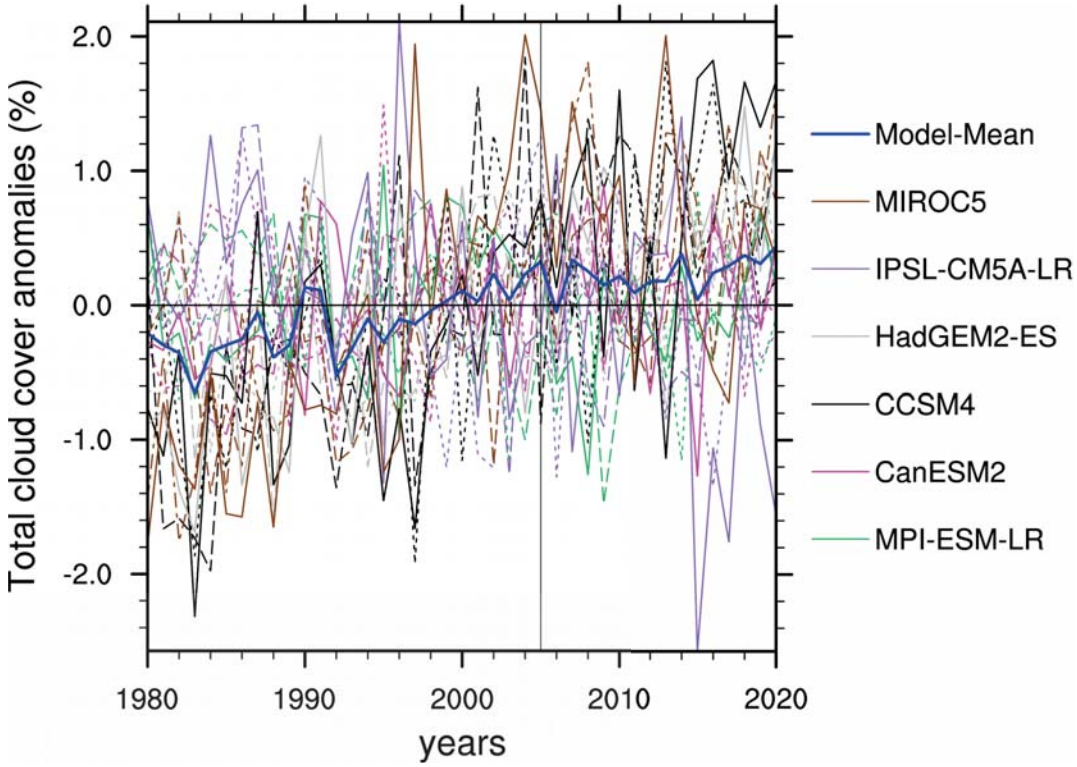

Fig. 4: Annual Arctic TCC trends from 1980 to 2020 of the first three ensemble members of the six used models and the multi-model-mean

Cloud representation is one of the major uncertainties in climate models (Bonyund Dufresne, 2005). Fig. 4 shows the temporal development of the annual TCC. A great spread between the ensemble trends is obvious. The anomalies of the ensemble members are varying strongly over the 41 years. The greatest trend is calculated by the second realization of CCSM4 with +2.53 %/41 years. The highest negative trend is shown by the first realization of CM5A-LR with -1.34 %/41 years. Four of the 18 model ensembles show a negative TCC trend, three from the CM5A-LR and one of the MPI-ESM-LR. The trends of the first and third realization of the MPI-ESM-LR, the third realization of the CanESM2 and the second realization of the IPSL are not significantly different from zero at 90 % significance level. Hence those trends are randomly created and only trends greater (smaller) than 0.41 (-0.41) %/41 years are statistically significant. Due to the great inter-model spread only a slight positive increase from 65.18±10.75 % to 65.83±10.11 % is simulated by the multi-model-mean resulting in a trend of 0.78±1.18 %/41 years. Despite the great uncertainty the trend is significantly different from zero.

3.5 Surface netto radiation flux

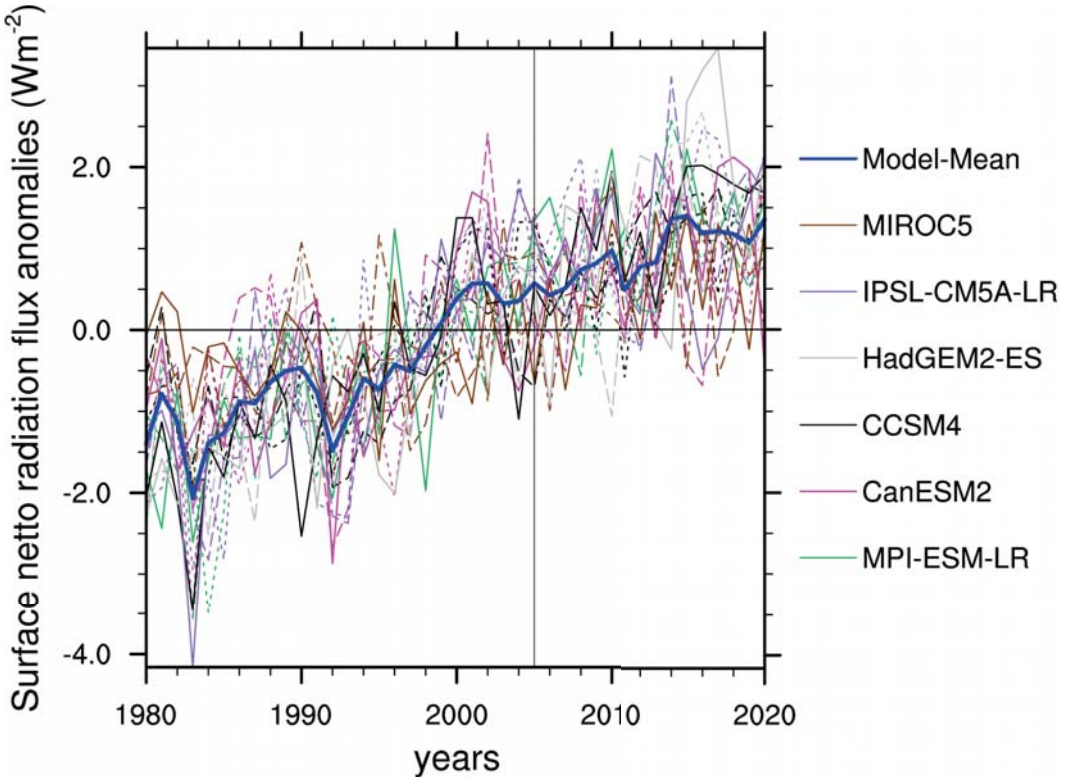

Fig. 5: Annual Arctic surface radiation trends from 1980 to 2020 of the first three ensemble members of the six used models and the multi-model-mean

The R_{sfc} is defined as: $R=SW^{\downarrow} - SW^{\uparrow} + LW^{\downarrow} - LW^{\uparrow}$
The netto flux is therefore the difference between the shortwave and longwave radiation netto fluxes. The components of the shortwave radiation netto flux are the incident solar radiation reaching the surface $SW^{\downarrow}$ and the reflected shortwave radiation $SW^{\uparrow}$. The longwave radiation budget consists of the atmospheric back radiation $LW^{\downarrow}$ and the surface outgoing radiation $LW^{\uparrow}$. The longwave radiation fluxes are calculated by the Stefan-Boltzmann-law via $R_{lw}=\sigma T^4$. The greater the atmospheric T_{sfc} is, the greater the fluxes of longwave radiation get. The trends of all model ensembles are significantly different from zero at 90 % significance level. The plotted anomalies are negative until 1999 and thereafter positive. This development (change from negative to positive in 1999/2000) is similar to those of WV (Fig. 3) and T_{sfc} (Fig. 1). Therefore a certain relation exist between those parameters, which is explained in my master thesis in section 3.2. The model trends are in the range of +1.41 Wm^{-2}/41 years by the first realization of MIROC5 to +4.28 Wm^{-2}/41 years by the first realization of HadGEM2-ES. The multi-model-mean R_{sfc} increases from 18.98±3.04 to 21.73±3.15 Wm^{-2} which results in a trend of +3.06±0.84 Wm^{-2}/41 years. All ensemble members show a positive trend of the R_{sfc}. The contributions of the different radiation fluxes to the trend of the multi-model-mean are shown in table 2.

Due to a positive R_{sfc} more energy is stored in the surface, even though less incident shortwave radiation (-1.23±2.26 Wm^{-2}/41 years) reaches the surface.

Tab. 2: Composition of the Arctic R_{sfc} trend in Wm^{-2}/41 years. The sign of the components in the line header describes the direction of the flux. Positive is directed to the surface

Δ	$+SW^{\downarrow}$	$-SW^{\uparrow}$	$+LW^{\downarrow}$	$+LW^{\downarrow}$
+3.06±0.84	-1.23±2.26	-3.73±2.84	+10.42±1.83	9.87±2.13

3.6 TOA netto radiation flux

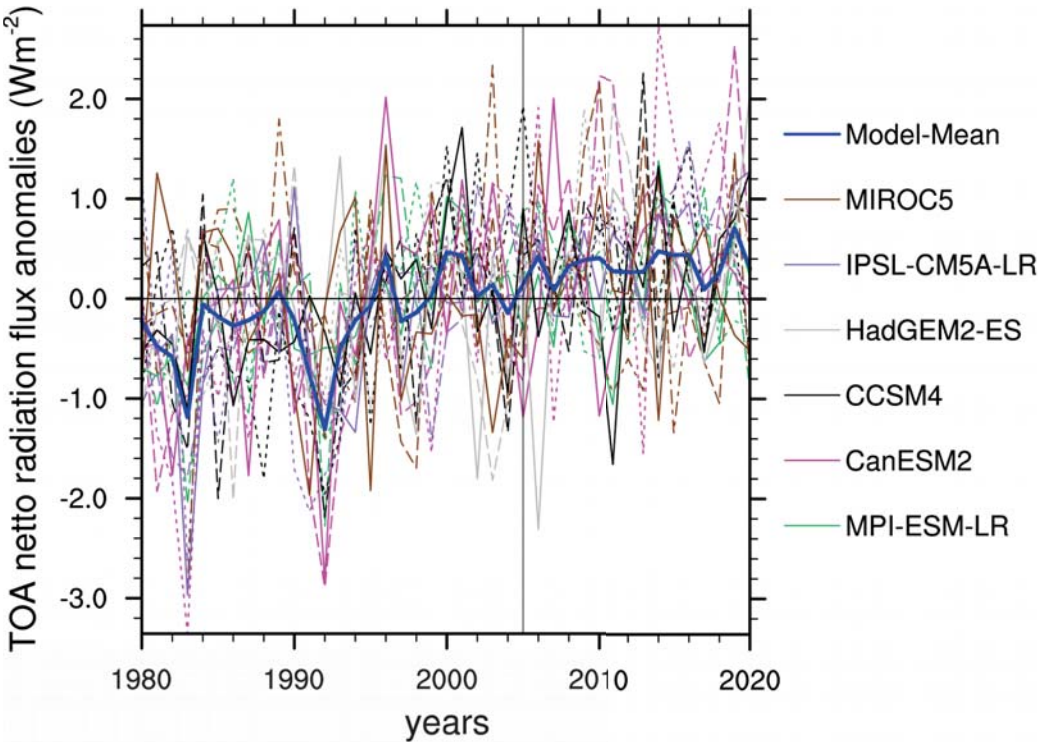

Fig. 6: Annual Arctic TOA radiation trends from 1980 to 2020 of the first three ensemble members of the six used models and the multi-model-mean

The R_{toa} is defined as the difference of the shortwave and longwave radiation budget at TOA: $R=SW^{\downarrow}-SW^{\uparrow}-LW^{\uparrow}$.

The shortwave radiation budget comprises the incident $SW^{\downarrow}$ and the reflected solar radiation $SW^{\uparrow}$.

The reflected part is divided into the shortwave radiation flux reflected by the surface and by clouds and the atmosphere. The longwave radiation budget only consists of the outgoing longwave radiation $LW^{\uparrow}$ since no incident longwave radiation is present. The representation of the R_{toa} is dominated by large fluctuations all over the considered period, because shortwave radiation uncertainties originating from TCC uncertainties dominate

over longwave radiation contributions. Thus the multi-model-mean shows only a small positive trend and is only half as great as the trend on the surface. The greatest trend is +2.47 Wm^{-2}/41 years presented by the third realization of CanESM2 and the smallest trend is 0.08 Wm^{-2}/41 years by the third realization of MIROC5. The trends of the third realization of the MPI, the first and second realization of HadGEM2-ES and all realizations of MIROC5 are not significant at 90 % significance level. Therefore, one third of the used model ensembles are unreliable. Those uncertain-ties have a large influence on the precision of the multi-model-mean. The mean shows a significant trend of +1.27±0.69 Wm^{-2}/41 years. The uncertainty is half as great as the trend itself.
The components of the TOA multi-model-mean radiation trend are shown in Table 3. A positive TOA radiation trend means less energy leaves the atmosphere. Therefore more energy is stored in the Arctic climate system. On the basis of almost constant incident radiation (only a change of 0.03±0.006 Wm^{-2}/41 years) the R_{toa} trend is dominated by the outgoing shortwave and longwave radiation trends. In the annual mean less shortwave radiation leaves the atmosphere (-3.66±1.56 Wm^{-2}/41 years). Consequently more energy is stored due to reduced sea ice.

Tab. 3: Components of the Arctic R_{toa} trend in Wm^{-2}/41 years

Δ	$+SW^{\downarrow}$	$-SW^{\uparrow}$	$-LW^{\uparrow}$
+1.27±0.69	+0.03±0.006	-3.66±1.56	+2.42±0.70

4. Conclusion and Outlook

Climate parameters such as T_{sfc}, SIC, WV, TCC, R_{sfc} and R_{toa} are investigated for the Arctic, here defined as the region north of 60°N. In my master thesis a multi-model-analysis based on six CMIP5 models was made to give a comprehensive overview about the current Arctic climate modeling. In this article only the annual, temporal development is analyzed.

In the Arctic, annual mean T_{sfc} increases continuously over the mentioned 41 years. Furthermore the simulated T_{sfc} development is in good agreement with observational records. As a results of increasing temperature the SIC steady decreases. Although the multi-model trends are significantly different from zero they are partly of great uncertainty. Beside T_{sfc} WV has the best inter-model agreement and also continuously increasing due to the linkage to the temperature.
For the TCC, the inter-model spread is greater than the multi-model mean trend itself. The great uncertainty of this parameter propagates onto estimates of the shortwave netto radiation flux, leading to increased uncertainties also in R_{sfc} and R_{toa}.
In the annual mean, both net radiation fluxes increase showing that more energy is reaching the surface as well as leaving the atmosphere. However the R_{sfc} increases more than R_{toa} which means that more heat is stored in the atmospheric column.
Beside the aforementioned Arctic, annual trends seasonal, spatial trends and multi-year monthly trends are analyzed in my master thesis.

In future studies the exact contribution of clouds to the netto radiation fluxes should be investigated, by examining the cloud radiative effect. This might help to differentiate the components of the radiation fluxes of TOA and surface. Furthermore the representation of TCC and SIC in the climate models must be improved. This would contribute to a better representation of the current and future Arctic climate.
An extensive comparison of the multi-model trends with observational and reanalysis data, in the annual Arctic mean as well as in the seasonal spatial distribution, would help to evaluate the accuracy of the presented climate parameters.

References

Barnes and Polvani, 2015: Barnes, Elizabeth A and Polvani, Lorenzo M, CMIP5 projections of Arctic amplification, of the North American/North Atlantic circulation, and of their relationship, 2015

Hansen et al. (2010): Hansen, James and Ruedy, Reto and Sato, Mki and Lo, Ken, Global surface temperature change, 2010

Foster und Rahmstorf (2011): Foster, Grant and Rahmstorf, Stefan, Global temperature evolution 1979-2010, 2011

Graßl, 1995: Graßl, Hartmut, Der veränderte Energiehaushalt der Erde: Globale und regionale Klimaänderung durch den Menschen, 1995

Karl und Trenberth, 2003: Artymiak, Jacek, LibreOffice Calc Functions and Formulas Tips, 2011

Johannessen et al. (2004): Artymiak, Jacek, LibreOffice Calc Functions and Formulas Tips, 2011

Hinzman et al. (2005): Hinzman, Larry D and Bettez, Neil D and Bolton, W Robert and Chapin, F Stuart and Dyurgerov, Mark B and Fastie, Chris L and Griffith, Brad and Hollister, Robert D and Hope, Allen and Huntington, Henry P and others, Evidence and implications of recent climate change in northern Alaska and other arctic regions, 2005

Najafi et al. (2015): Najafi, Mohammad Reza and Zwiers, Francis W and Gillett, Nathan P, Attribution of Arctic temperature change to greenhouse-gas and aerosol influences, 2015

Bengtsson et al., 2013: Bengtsson, Lennart and Hodges, Kevin I and Koumoutsaris, Symeon and Zahn, Matthias and Berrisford, Paul, The changing energy balance of the polar regions in a warmer climate, 2013

Vihma, 2014: Vihma, Timo, Effects of Arctic sea ice decline on weather and climate: a review, 2014

Rinke et al., 2009: Rinke, Annette and Melsheimer, C and Dethloff, Klaus and Heygster, G, Arctic total water vapor: comparison of regional climate simulations with observations, and simulated decadal trends, 2009

Karlsson und Svensson, 2011: Karlsson, Johannes and Svensson, Gunilla, The simulation of Arctic clouds and their influence on the winter surface temperature in present-day climate in the CMIP3 multi-model dataset, 2011

Wang und Key, 2005: Wang, Xuanji and Key, Jeffrey R, Arctic surface, cloud, and radiation properties based on the AVHRR Polar Pathfinder dataset. Part II: Recent trends, 2005

Screen und Simmonds 2010: Screen, James A and Simmonds, Ian, The central role of diminishing sea ice in recent Arctic temperature amplification, 2010

Serreze und Barry 2011: Serreze, Mark C and Barry, Roger G, Processes and impacts of Arctic amplification: A research synthesis, 2011

Screen 2014: Screen, James A, Arctic amplification decreases temperature variance in northern mid-to high-latitudes, 2014

Bintanja et al. 2011: Bintanja, R and Graversen, RG and Hazeleger, W, Arctic winter warming amplified by the thermal inversion and consequent low infrared cooling to space, 2011

Francis und Vavrus 2012: Francis, Jennifer A and Vavrus, Stephen J, Evidence linking Arctic amplification to extreme weather in mid-latitudes, 2012

Serreze et al. 2009: Serreze, MC and Barrett, AP and Stroeve, JC and Kindig, DN and Holland, MM, The emergence of surface-based Arctic amplification, 2009

Stroeve et al. 2012: Stroeve, Julienne C and Serreze, Mark C and Holland, Marika M and Kay, Jennifer E and Malanik, James and Barrett, Andrew P, The Arctic’s rapidly shrinking sea ice cover: a research synthesis, 2012

Taylor et al. 2012: Taylor, Karl E and Stouffer, Ronald J and Meehl, Gerald A, An overview of CMIP5 and the experiment design, 2012

Chylek et al., 2011: Chylek, P and Li, J and Dubey, MK and Wang, M and Lesins, G, Observed and model simulated 20th century Arctic temperature variability: Canadian earth system model CanESM2, 2011

Gent et al., 2011: Gent, Peter R and Danabasoglu, Gokhan and Donner, Leo J and Holland, Marika M and Hunke, Elizabeth C and Jayne, Steve R and Lawrence, David M and Neale, Richard B and Rasch, Philip J and Vertenstein, Mariana and others, The community climate system model version 4, 2011

Jones et al., 2011: Jones, CDea and Hughes, JK and Bellouin, Nicolas and Hardiman, SC and Jones, GS and Knight, Jeff and Liddicoat, Spencer and O'Connor, FM and Andres, Robert Joseph and Bell, Christopher and others, The HadGEM2-ES implementation of CMIP5 centennial simulations, 2011

Dufresne et al., 2013: Dufresne, J-L and Foujols, M-A and Denvil, Sébastien and Caubel, Arnaud and Marti, Olivier and Aumont, Olivier and Balkanski, Yves and Bekki, Slimane and Bellenger,

Hugo and Benshila, Rachid and others, Climate change projections using the IPSL-CM5 Earth System Model: from CMIP3 to CMIP5, 2013

Watanabe et al., 2010: Watanabe, Masahiro and Suzuki, Tatsuo and O'ishi, Ryouta and Komuro, Yoshiki and Watanabe, Shingo and Emori, Seita and Takemura, Toshihiko and Chikira, Minoru and Ogura, Tomoo and Sekiguchi, Miho and others, Improved climate simulation by MIROC5: mean states, variability, and climate sensitivity, 2010

Stevens et al., 2013: Stevens, Bjorn and Giorgetta, Marco and Esch, Monika and Mauritsen, Thorsten and Crueger, Traute and Rast, Sebastian and Salzmann, Marc and Schmidt, Hauke and Bader, Jürgen and Block, Karoline and others, Atmospheric component of the MPI-M Earth System Model: ECHAM6, 2013

Taylor et al. (2012): Taylor, Karl E and Stouffer, Ronald J and Meehl, Gerald A, An overview of CMIP5 and the experiment design, 2012

Haywood et al., 2014: Haywood, Jim M and Jones, Andy and Jones, Gareth S, The impact of volcanic eruptions in the period 2000--2013 on global mean temperature trends evaluated in the HadGEM2-ES climate model, 2014

Kharin et al., 2013: Kharin, Viatcheslav V and Zwiers, FW and Zhang, Xuebin and Wehner, Michael, Changes in temperature and precipitation extremes in the CMIP5 ensemble, 2013

Peters et al., 2013: Peters, Glen P and Andrew, Robbie M and Boden, Tom and Canadell, Josep G and Ciais, Philippe and Le Quéré, Corinne and Marland, Gregg and Raupach, Michael R and Wilson, Charlie, The challenge to keep global warming below 2° C, 2013

Deser et al., 2012: Deser, Clara and Knutti, Reto and Solomon, Susan and Phillips, Adam S, Communication of the role of natural variability in future North American climate, 2012

Dee et al., 2011: Dee, DP and Uppala, SM and Simmons, AJ and Berrisford, Paul and Poli, P and Kobayashi, S and Andrae, U and Balmaseda, MA and Balsamo, G and Bauer, P and others, The ERA-Interim reanalysis: Configuration and performance of the data assimilation system, 2011

Berrisford et al.,2009: Berrisford, Paul and Dee, DPKF and Fielding, Keith and Fuentes, Manuel and Kallberg, P and Kobayashi, Shinya and Uppala, Sakari, The ERA-interim archive, 2009

Hiraharaet al., 2016: Hirahara, Shoji and Balmaseda, Magdalena Alonso and de Boisseson, Eric and Hersbach, Hans, 26 Sea Surface Temperature and Sea Ice Concentration for ERA5, 2016

Lawrimore et al. (2011): Lawrimore, Jay H and Menne, Matthew J and Gleason, Byron E and Williams, Claude N and Wuertz, David B and Vose, Russell S and Rennie, Jared, An overview of the Global Historical Climatology Network monthly mean temperature data set, version 3, 2011

Huang et al. (2015): Huang, Boyin and Banzon, Viva F and Freeman, Eric and Lawrimore, Jay and Liu, Wei and Peterson, Thomas C and Smith, Thomas M and Thorne, Peter W and Woodruff, Scott D and Zhang, Huai-Min, Extended reconstructed sea surface temperature version 4 (ERSST. v4). Part I: upgrades and intercomparisons, 2015

Turner et al. (2004): Turner, John and Colwell, Steve R and Marshall, Gareth J and Lachlan-Cope, Tom A and Carleton, Andrew M and Jones, Phil D and Lagun, Victor and Reid, Phil A and Iagovkina, Svetlana, The SCAR READER project: toward a high-quality database of mean Antarctic meteorological observations, 2004

Hansen et al., 2010: Hansen, James and Ruedy, Reto and Sato, Mki and Lo, Ken, Global surface temperature change, 2010

Peng et al., 2013: Peng, G and Meier, WN and Scott, DJ and Savoie, MH, A long-term and reproducible passive microwave sea ice concentration data record for climate studies and monitoring, 2013

Stone und Ellis, 2006: Stone, D and Ellis, Jon, Evaluation of Means for small samples - The t-test, 2006

Serreze und Francis, 2006: Serreze, Mark C and Barrett, Andrew P and Stroeve, Julienne, Recent changes in tropospheric water vapor over the Arctic as assessed from radiosondes and atmospheric reanalyses, 2012

Holton und Hakim, 2012: Holton, James R and Hakim, Gregory J, An introduction to dynamic meteorology, 2012

Bonyund Dufresne, 2005: Bony, Sandrine and Dufresne, Jean-Louis, Marine boundary layer clouds at the heart of tropical cloud feedback uncertainties in climate models, 2005

Wissenschaftliche Mitteilungen aus dem Institut für Meteorologie der Universität Leipzig Bd. 56 (2018)

Dynamik der atmosphärischen Grenzschicht über der Stadt – erste Ergebnisse der Wind-LIDAR-Messungen am Leipziger Institut für Meteorologie

Lochmann, M.* und Raabe, A.[+]

**) Institut für Meteorologie, Stephanstraße 3, 04103 Leipzig, E-Mail: moritz.lochmann@uni-leipzig.de*

[+]) Institut für Meteorologie, Stephanstraße 3, 04103 Leipzig, E-Mail: raabe@uni-leipzig.de

Zusammenfassung: Seit 2015 gibt es Doppler-LIDAR-Messungen der Windgeschwindigkeit über Leipzig. Diese Messungen werden zum einen vom HALO Photonics Streamline Doppler-LIDAR am Leipziger Institut für Troposphärenforschung (TROPOS) sowie vom Leosphere Windcube 8 Doppler-LIDAR am Leipziger Institut für Meteorologie (LIM) aufgenommen. In dieser Arbeit werden insbesondere die Daten des Windcubes bezüglich der horizontalen Windgeschwindigkeit, der Windrichtung und der Turbulenzintensität bis in eine Höhe von ca. 500 m ausgewertet. Der Vergleich mit dem HALO Photonics Streamline Doppler-LIDAR zeigt gute Korrelationen zwischen beiden Geräten.
Die Ergebnisse beinhalten unter anderem eine gute Übereinstimmung mit der Ekman-Theorie. Auch die erhöhte Rauhigkeit der Stadtfläche gegenüber dem ländlichen Raum wird in der Auswertung deutlich. Es wurde ein Verfahren getestet, das es erlaubt, den turbulenten Diffusionskoeffizienten und die aerodynamische Rauhigkeitslänge aus den Messwerten abzuleiten und erste Abschätzungen dieser Größen vorzunehmen. Diese Arbeit legt nahe, den Einsatz der Fernerkundungsmessung zur Bestimmung der urbanen Grenzschichtdynamik fortzusetzen und wenn möglich zu erweitern.

Abstract: Since 2015 Doppler-LIDAR measurements above Leipzig are available. The Leibniz Institute for Tropospheric Research (TROPOS) operates a HALO Photonics Streamline Doppler-LIDAR while the Institute of Meteorology Leipzig uses a Leosphere Windcube 8 Doppler-LIDAR. In this study mainly meausrements of the Windcube for horizontal wind velocity, wind direction and turbulence intensity below 500 m are evaluated. The comparison to the HALO Photonics Streamline LIDAR shows good correlations between both devices.
Among others, the results include good agreements with the Ekman theory. Additionally the increased roughness of the city surface compared to rural areas becomes apparent. A way to determine characteristic quantities like the turbulent diffusion coefficient and the aerodynamic roughness length is described and initial estimations were conducted. This study suggests to continue and if possible expand such remote sensing measurements for analyses of urban boundary layer dynamics.

1 Einleitung

Das Windfeld ist ein bedeutender Bestandteil der Grenzschichtmeteorologie und dessen genaue Erfassung und Beschreibung von großem Wert für Grenzschichtmodelle. Über viele Jahre wurde die bodennahe Fernerkundung von RADAR-Windprofilern dominiert, die Frequenzen vom L-Band bis zum VHF-Band nutzen und Windprofile ab ca. 500 m Höhe mit einer zeitlichen Auflösung von 30 min zur Verfügung stellen (Päschke et al., 2015). Seit einigen Jahren werden kompakte Doppler-LIDAR-Geräte in der Fernerkundung eingesetzt, die schon ab unter 100 m Messwerte liefern. Für diese bodennaheren Messungen ist die Nachfrage von der Windenergieindustrie groß, aber auch der wissenschaftliche Einsatz zur Grenzschichterkundung wird getestet. Besonders in urbanen Gebieten liefert das Doppler-LIDAR Messwerte aus Höhen, die vorher nicht erreicht werden konnten. Die hohe zeitliche und räumliche Auflösung, der geräuscharme und platzsparende Betrieb sowie die hohe Zuverlässigkeit der Messwerte sind gute Argumente für die Fernerkundung der urbanen Grenzschicht mit einem Doppler-LIDAR.

2 Das Windcube-8 Doppler-LIDAR

Der Leosphere Windcube 8 ist ein bodengebundenes, gepulstes Doppler-LIDAR mit einer Reichweite von 500 m. Alle 6 bis 7 Sekunden werden Laserpulse um 15° von der Senkrechten geneigt in eine Himmelsrichtung ausgesendet und die entsprechende Radialgeschwindigkeit gemessen. Nach Analyse der Dopplerverschiebung $\Delta f = 2\frac{v_r}{\lambda}$ kann die Partikelgeschwindigkeit in Strahlrichtung v_r bestimmt werden. Man benötigt Messungen in 3 Himmelsrichtungen, um den kompletten Windvektor in der Streuhöhe zu bestimmen. Das bedeutet, dass ungefähr alle 18 Sekunden ein unabhängiger Windvektor errechnet wird.
Die zeitliche Länge des Laserpulses ergibt, multipliziert mit der Lichtgeschwindigkeit und unter Berücksichtigung der Neigung von der Senkrechten, die physikalische Länge des Pulses, über die das Signal gemittelt wird. Im Fall des Windcubes entspricht das einer vertikalen Mittelung über 20 m. Der Geschwindigkeitsmesswert ist also immer ein Mittelwert über den Zeitraum, den das Gerät benötigt, um in drei Richtungen zu messen (ungefähr 12 bis 15 Sekunden), sowie über die durch die Neigung des Lasers in die vier Himmelsrichtungen aufgespannte Fläche in der Messhöhe. Bedingt durch dieses Messverfahren ist also jeder Messwert ein Mittel aus einem umgekehrten Pyramidenstumpfvolumen über dem Messstandort. Je höher das Messniveau, desto höher ist auch das Messvolumen (vgl. Abb. 1). Die Messhöhe wird aus der Laufzeit des Signals in der Atmosphäre abgeleitet.

3 Validierung der Messwerte

Im Rahmen der Melpitz Column 2015, einer Aerosolmesskampagne im Norden Sachsens nahe Torgau, operierte der Windcube zum ersten Mal unter Normalbedingungen. Um die Güte der Messdaten des Windcubes zu überprüfen, werden sie mit Messwerten des HALO Photonics Streamline Doppler-LIDARs des Instituts für Troposphärenforschung Leipzig (TROPOS) verglichen. Beide Geräte operierten in der Zeit vom 01.07.2015 bis zum 05.07.2015 gleichzeitig bei Melpitz. Im Vergleich mit diesem bereits etabliertem Messgerät (u.a. in Bühl et al., 2015; Lane et al., 2013) lässt sich die Zuverlässigkeit des Windcubes abschätzen. Tabelle 1 zeigt die angewendeten technischen Parameter der Messgeräte. Einige Unterschiede der beiden Geräte sollten für die Verhältnismäßigkeit des Vergleichs berücksichtigt werden. Zuerst, dass die betrachteten Messwerte des Streamline-LIDARs Momentaufnahmen sind und nicht, wie die Werte des Windcubes, 15-minütige Mittelwerte. Desweiteren unterscheidet sich die Mittelungslänge. Der Laserpuls des Streamline-LIDARs ist etwas länger, wodurch die vertikale Mittellungslänge

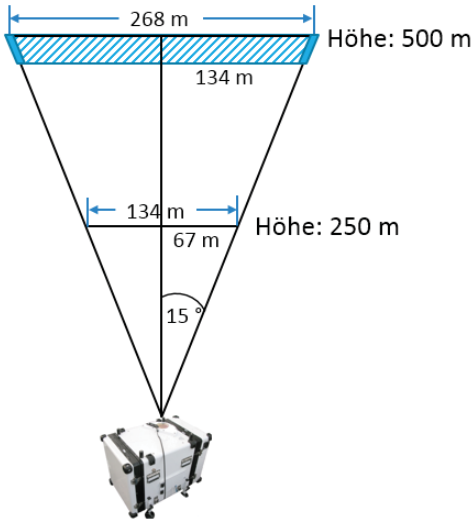

Abbildung 1: Schematische Darstellung des Messvolumens des Windcubes

auf ungefähr 34 m steigt. Verglichen werden zwei Messniveaus die ungefähr auf gleicher Höhe liegen. Die zu vergleichenden Messniveaus befinden sich etwa in 100 m (102 m Tropos-LIDAR) und 200 m (204 m Tropos-LIDAR). Als Vergleichszeitraum wurde der 02.07.2015 0:00 Uhr bis zum 03.07.2015 0:00 Uhr gewählt, da an den anderen aufgrund der Hitze tagsüber Messwerte des Windcubes fehlen.

Tabelle 1: Technische Parameter beider Messgeräte

	Leosphere Windcube 8 (LIM)	HALO Photonics Streamline (TROPOS)
Wellenlänge	1,54 μm	1,5 μm
Pulslänge	75 ns	160 ns
Vert. Mittelungsintervall	20 m	33,9 m
Öffnungswinkel	15°	45°
Erstes Messniveau	40 m	33,9 m
Höchstes Messniveau	500 m	2000 m
Anzahl Messniveaus	25	200
Anzahl gemittelter Pulse	9000	7500
Teleskopfokus	250 m	1500 m
Integrationszeit	1,5 s	2 s

Im Folgenden findet sich eine kurze Gegenüberstellung der Messungen beider Messgeräte. Die Korrelation der Windgeschwindigkeitsmessung (siehe Abb. 2) ist in den zwei Höhen gut, wobei sie in 200 m Höhe etwas besser ist. Dieser Grad der Übereinstimmung ist zufriedenstellend, weil in Anbetracht der technischen Unterschiede bessere Übereinstimmungen nicht möglich sind. Die Korrelation der Windrichtungsmessung (siehe Abb.3) ist auch in 200 m Höhe etwas besser als in 100 m Höhe, jedoch nicht zufriedenstellend. Gerade tagsüber sind die Abweichungen der Windrichtung zwischen beiden Geräten sehr deutlich, was auf thermisch induzierte Turbulenz und Grenzschichtdurchmischung zurückzuführen ist. Gerade in diesen turbulenten Situationen bemerkt man die Unterschiede zwischen Momentaufnahme und Mittelungsmessung. Um thermische Turbulenz zu vermeiden, wurde die Auswertung auf Messwerte der Nachtstunden (0 bis 6 Uhr UTC sowie 18 bis 0 Uhr UTC) reduziert (siehe Abb. 4). Eliminiert man die turbulenten Tageswerte, ist die Übereinstimmung deutlich besser und, im Rahmen der unvermeidlichen

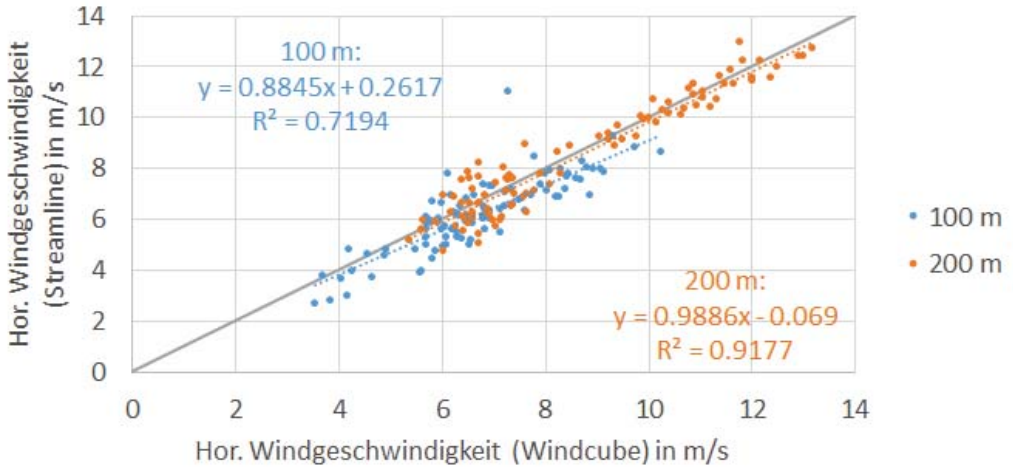

Abbildung 2: Korrelation der Geschwindigkeitsmessung, gepunktet: lineare Trendlinie, grau: 1:1-Gerade

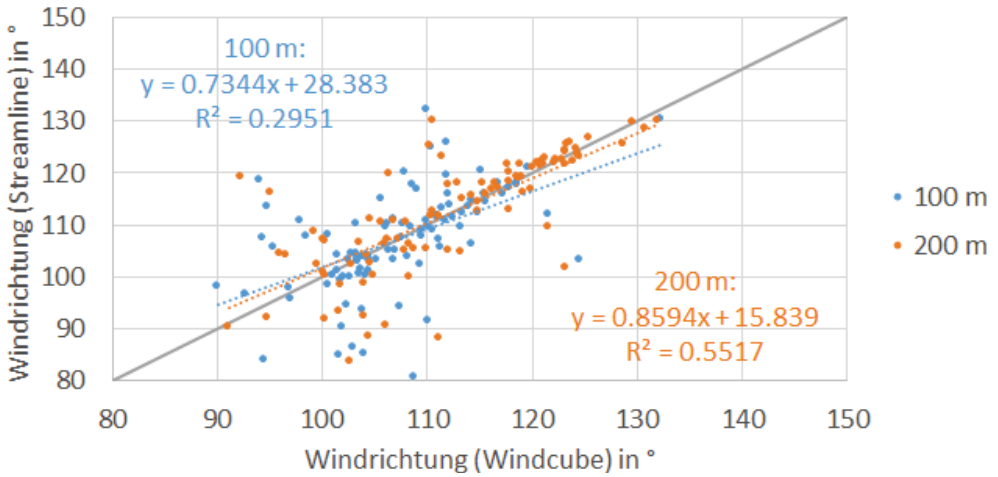

Abbildung 3: Korrelation der Windrichtungsmessung, gepunktet: lineare Trendlinie, grau: 1:1-Gerade

technischen Unterschiede zwischen beiden Geräten, ebenfalls zufriedenstellend.
Generell ist die Korrelation der Messwerte beider Geräte sehr gut, einen deutlichen Einbruch erleidet sie jedoch bei der Windrichtung tagsüber. Kleinere Abweichungen zwischen beiden Geräten sind erwartungsgemäß vorhanden, wobei in der Messhöhe 200 m die Übereinstimmungen besser sind als in 100 m Höhe.

4 Messstandort in Leipzig

Der Standort des Windcubes ist die Terasse des LIM (51°20'01"N 12°23'18"E). Dafür wurden in der Auswertung 10 m auf die geräteinternen Messhöhen addiert, um etwa die reale Höhe über Grund zu erhalten. Das LIM befindet sich ungefähr 1 km südöstlich des Leipziger Stadtzentrums. Vorherrschend ist in der Regel eine südwestliche Anströmung, obwohl die örtliche Bebauung in der Nähe des Messplatzes bodennah eine vom klimatischen Mittel abweichende Häufung südöstlicher Winde bewirkt. Diese häufiger registrierten Windrichtungen aus Südost verlieren sich jedoch mit der Höhe (siehe dazu Abb. 5).

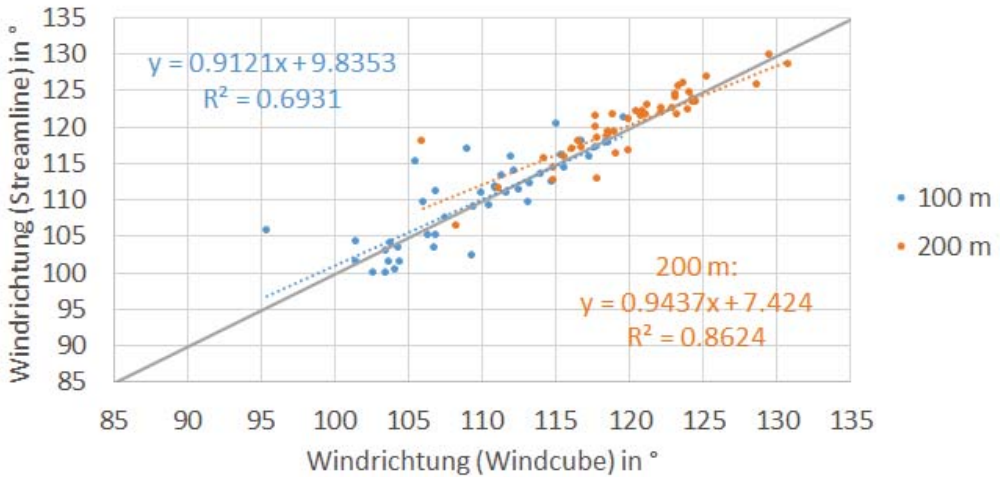

Abbildung 4: Korrelation der Windrichtungsmessung nachts (0 Uhr UTC - 6 Uhr UTC; 18 Uhr UTC - 0 Uhr UTC), gepunktet: lineare Trendlinie, grau: 1:1-Gerade

4.1 Die Ekman-Spirale

Die Ekman-Spirale beschreibt die durch Reibungs- und Corioliskraft bestimmte Ablenkung des geostrophischen Windes in Bodennähe. Diese Drehung der Windrichtung lässt sich auch in den Messwerten des Windcubes beobachten. Dazu wurden die Windrichtungen über das Jahr 2016 gemittelt. Für jede der 25 Messhöhen wurde eine Windrichtungsverteilung erstellt. Sie sollen an dieser Stelle aber nur exemplarisch abgebildet werden (Abb. 5). Man erkennt klar eine Winddrehung von Südwestwinden am Boden auf Westwind in 510 m Höhe (mit Anteilen WSW und WNW). Außerdem ist der in 24 m Höhe häufig auftretende Ostwind mit zunehmender Höhe immer weniger zu erkennen.

4.2 Der Turbulente Diffusionskoeffzient

Die physikalische Definition der Ekman-Spirale lässt sich aus den Navier-Stokes-Gleichungen unter Voraussetzung stationärer Verhältnisse und horizontaler Homogenität von Grundstrom und turbulenten Größen herleiten (Herleitung nach Etling, 2008). Aus dieser Herleitung erhält man neben Termen für die beiden horizontalen Windkomponenten (siehe Gl.1 & Gl.2) eine Integrationskonstante $D = \sqrt{2\frac{K_m}{f}}$ mit dem Coriolisparameter f. D hat die Einheit Meter (m), weshalb D auch als Ekman-Länge bezeichnet wird.

$$\bar{u}(z) = \bar{u_g}\left[1 - exp\left(-\frac{z}{D}\right)cos\left(\frac{z}{D}\right)\right] - \bar{v_g}exp\left(-\frac{z}{D}\right)sin\left(\frac{z}{D}\right) \quad (1)$$

$$\bar{v}(z) = \bar{v_g}\left[1 - exp\left(-\frac{z}{D}\right)cos\left(\frac{z}{D}\right)\right] + \bar{u_g}exp\left(-\frac{z}{D}\right)sin\left(\frac{z}{D}\right) \quad (2)$$

Sind der turbulente Diffusionskoeffizient K_m und die geostrophischen Windkomponenten bekannt, kann damit das Windprofil in die Prandtl-Schicht hinein bis in die Nähe des Bodens bestimmt werden. Andersherum ist es möglich, mit dem Windprofil und den geostrophischen Windkomponenten den turbulenten Diffusionskoeffizienten zu bestimmen. Der turbulente Diffusionskoeffizient ist ein Maß für die Reichweite und Intensität der turbulenten Diffusion.
Im Rahmen dieser Arbeit ist es von Interesse, ob aus den Windcubemessungen ein solcher Diffusionskoeffizient bestimmt werden kann. Dazu wird die Annahme getroffen, dass die Windgeschwindigkeit in der obersten Messhöhe der geostrophischen Windgeschwindigkeit entspricht. Da K_m in der Realität nicht höhenkonstant ist, wird der Messbereich in drei Abschnitte unter-

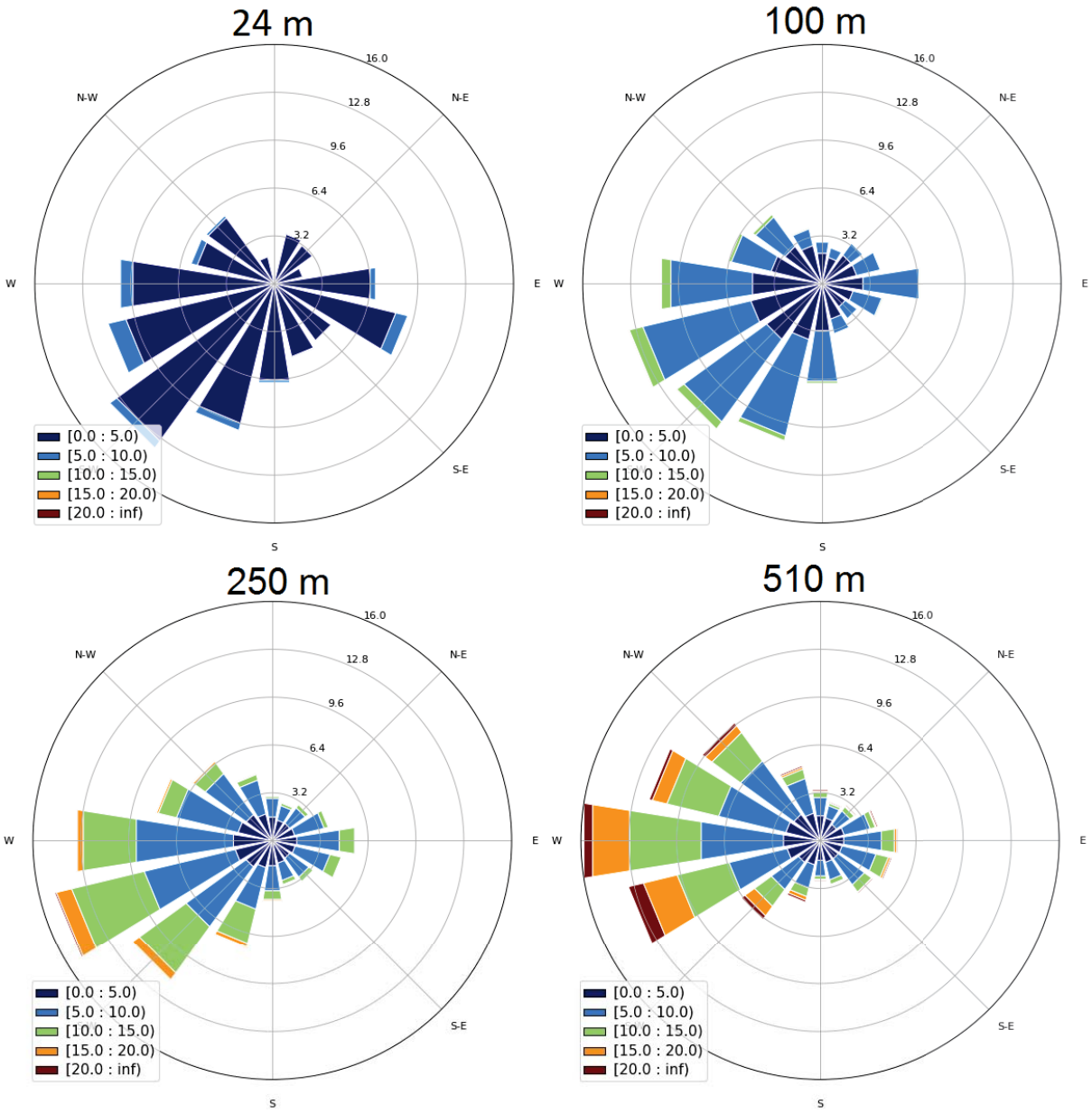

Abbildung 5: Relative Häufigkeit der Windrichtung und Windgeschwindigkeit am LIM in 24 m Höhe (oben links), 100 m Höhe (o.r.), 250 m Höhe (u.l.) und 510 m Höhe (u.r.) im Jahr 2016

teilt, in denen unabhängig voneinander ein passendes K_m bestimmt wird. Diese drei Abschnitte sind wie folgt: Abschnitt 1 – 50 m bis 150 m über Grund, Abschnitt 2 – 150 m bis 310 m über Grund, Abschnitt 3 – 310 m bis 510 m über Grund. Der unterste Bereich umfasst die kleinste Höhendifferenz, weil dort zum einen mehr Messpunkte sind und zum anderen dieser am stärksten von der Stadtfläche beeinflusst werden sollte. Im obersten Bereich befinden sich die am weitesten voneinander entfernten Messpunkte und der geringste Einfluss des Bodens, deshalb ist die Höhendifferenz dort größer.

Das gemessene Windprofil wird mit einem least-squares-fit an die Windkomponenten aus den Gleichungen 1 und 2 angepasst. Ausgewählt wurde dazu ein mittleres Windprofil über alle vollständigen Windprofile des Messdatensatzes (von September 2015 bis einschließlich Oktober 2017), die in 250 m Höhe über Grund eine Windgeschwindigkeit von 5-7 m/s und eine Windrichtung von 225-270° (SW-W) aufweisen. Abbildung 6 zeigt beispielhaft diese Ekman-Anpassung. Insgesamt wurden damit 1804 10-Minuten-Mittelwerte als Beispielprofil gemittelt.

Die errechneten Ekman *u*- und *v*-Werte liegen im Bereich der Standardabweichung der tatsächlichen Profile beider Windkomponenten. Die Werte für die daraus resultierenden Diffusionskoeffizienten liegen zwischen 1 m^2/s in der bodennächsten Schicht und 2 m^2/s in der obersten Schicht (siehe Tab. 2). Das bedeutet, dass die Durchmischung nach oben zunimmt, was mit der Theorie übereinstimmt (Oke, 1988).

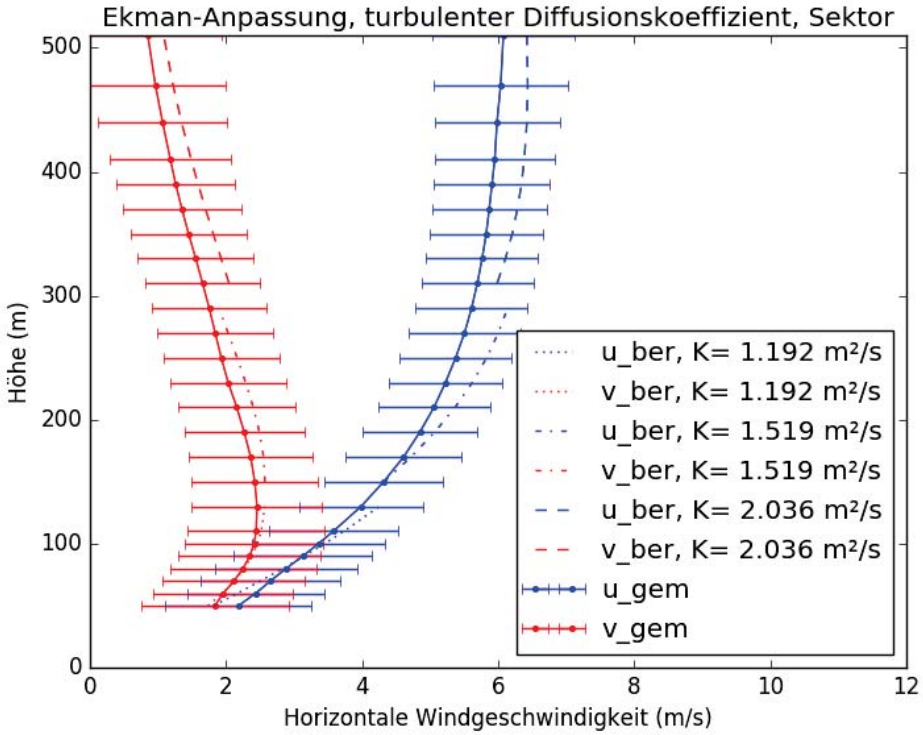

Abbildung 6: Ekman-Anpassung des Windsektors 225–270° mit Standardabweichung

Tabelle 2: Turbulenter Diffusionskoeffizient

Höhe (m)	Turbulenter Diffusionskoeffizient (m^2/s)
50-150	1,192
150-310	1,519
310-510	2,036

In ähnlicher Weise ist es möglich eine Analyse der turbulenten Diffusionskoeffizienten für andere Windrichtungssektoren, andere Windgeschwindigkeitsintervalle, bestimmte Wetterlagen und Schichtungsverhältnisse vorzunehmen.

4.3 Die aerodynamische Rauhigkeitslänge

Die aerodynamische Rauhigkeitslänge z_0 beschreibt physikalisch die Höhe über dem Erdboden, in der die Windgeschwindigkeit gleich Null ist. Für die Rauhigkeitslänge gibt es in zahlreichen Standardwerken (u.a. in Stull, 1988) Richtwerte für verschiedene Oberflächenklassen, die sich mehr oder wenig einig sind. Die World Meteorological Organization (WMO) hat folgende Terrainklassen und entsprechende Rauhigkeitslängen vorgeschlagen:

Tabelle 3: Oberflächenklassen und zugehörige Rauhigkeitslängen z_0, Quelle: nach WMO (2008)

Klassenindex	Kurze Oberflächenbeschreibung	z_0 (m)
1	Offene See, mind. 5 km vom Land entfernt	0,0002
2	Watt, Schnee; ohne Vegetation, ohne Hindernisse	0,005
3	Offenes, flaches Gelände; Gras mit wenigen, einzelnen Hindernissen	0,03
4	Niedrige Felder, gelegentlich mit größeren Hindernissen	0,1
5	Hohe Felder, verstreute Hindernisse	0,25
6	Parks, Gesträuch, mehrere Hindernisse	0,5
7	regelmäßige hohe Hindernisse (Vorstadt, Wald)	1,0
8	Stadtzentrum mit Hochhäusern und mehrstöckigen Gebäuden	≥ 2

Der Standort in Leipzig sollte demnach eine Rauhigkeitslänge von etwa einem Meter haben (in Tabelle 3 – Klasse 7: regelmäßige, hohe Hindernisse (Vorstadt)), eventuell etwas weniger, weil sich der Standort nicht homogen aus hohen Hindernissen zusammensetzt. Da mittlerweile Windmessungen aus verschiedenen Höhen aus über zwei Jahren vorliegen, lassen sich daraus Werte für z_0 bestimmen.
Allerdings gibt es zwei Einschränkungen. Zuerst gilt das logarithmische Windprofil nur in der bodennahen Prandtl-Schicht (bis ca. 60-100 m über dem Erdboden). In der Prandtl-Schicht wächst die Windgeschwindigkeit bis auf Werte von 70-80 % der reibungsfreien Strömung, während erst in der darüber liegenden Ekmanschicht nahezu die gesamte Winddrehung in Richtung des geostrophischen Windes stattfindet (DWD Wetterlexikon[1]). In diesen hier zu betrachtenden untersten 100 m gibt es sechs Messniveaus, das unterste davon allerdings erst in 50 m Höhe über dem Erdboden. Ein beträchtlicher Teil des logarithmischen Windprofils liegt somit unterhalb des Messausschnitts. Wenn die Prandtl-Schicht und damit das logarithmische Windprofil bis in (bestenfalls) 100 m Höhe reicht, wird davon nur die obere Hälfte erfasst. Ist die Prandtl-Schicht flacher, wird sogar ein noch geringerer Anteil gemessen. Nichtsdestotrotz sollte die Prandtl-Schicht gerade in den Sommer- und Frühlingsmonaten die 100 m ausfüllen und damit zuverlässige Messwerte liefern.
Das zweite Problem ist, dass das logarithmische Windgesetz nach Gleichung 3 nur für eine neutrale Atmosphäre gilt. Da die Messwerte hier nicht nach der Stabilität differenziert sind, fließen in die Berechnungen von z_0 auch Windprofile unter stabilen und labilen Bedingungen mit ein.
Zur Bestimmung von z_0 wird ein linearer Fit auf die halblogarithmisch aufgetragenen Messwerte gelegt. Wenn man im logarithmischen Windgesetz den Logarithmus $ln(z/z_0)$ in eine Differenz umschreibt:

$$U(z) = \frac{u_*}{\kappa} \cdot ln(z) - \frac{u_*}{\kappa} \cdot ln(z_0) \tag{3}$$

ist für die lineare Regression

$$Y_i = m \cdot x_i + b \tag{4}$$

$U(z)$ die Zielgröße Y, $ln(z)$ ist die Einflussgröße x, $\frac{u_*}{\kappa}$ ist der Anstieg m und $-\frac{u_*}{\kappa} \cdot ln(z_0)$ ist der Schnittpunkt mit der y-Achse b. b und m sind dabei die linearen Parameter, die man aus der linearen Regression für ein Windprofil erhält. Die Schubspannungsgeschwindigkeit u_* und die von Karman-Konstante $\kappa = 0,4$ sind konstant und z_0 ist es per Definition auch.

[1] https://www.dwd.de/DE/service/lexikon/Functions/glossar.html?lv2=101996h&lv3=102070, besucht am 25.01.2018

Nach den Gleichungen 3 und 4 gilt für die beiden linearen Parameter:

$$m = \frac{u_*}{\kappa} \tag{5}$$

$$b = -\frac{u_*}{\kappa} \cdot ln(z_0) = -m \cdot ln(z_0) \tag{6}$$

Mit $\kappa = 0,4$ und dem Anstieg kann man auf u_* schließen. Außerdem ist z_0 mit den linearen Parametern b und $m = \frac{u_*}{\kappa}$ aus der linearen Regression die einzige Unbekannte in Gleichung 6. Stellt man nach z_0 um, erhält man:

$$z_0 = exp\left(-\frac{b}{m}\right) \tag{7}$$

In diesen Zusammenhang müssen nur noch die aus der linearen Regression erhaltenen Parameter eingesetzt werden, um z_0 zu bestimmen. Aus den Monatsmittelwerten von Tages- (6 Uhr UTC bis 18 Uhr UTC) und Nachtwerten (18 Uhr UTC bis 6 Uhr UTC) wurden für jeden Monat die Rauhigkeitslängen bestimmt. Wie erwartet fällt auf, dass die Nachtwerte in jedem Monat deutlich unter dem erwarteten Wert $z_0 \approx$1 m liegen. Ebenso liegen die Werte der Wintermonate unter dem erwarteten Wert. Nur die Rauhigkeitslängen weniger Monate stimmen etwa mit der Vermutung überein (siehe Tabelle 4).

Tabelle 4: Rauhigkeitslänge z_0 aus Monatsmittelwerten für Tageswerte der Sommermonate

Monat	Rauhigkeitslänge z_0 (m)	Monat	Rauhigkeitslänge z_0 (m)
Aug 15	1,594	Sep 16	0,345
Sep 15	0,495	Apr 17	0,428
Apr 16	1,117	Mai 17	0,210
Mai 16	0,711	Jun 17	0,622
Jun 16	1,287	Jul 17	1,249
Jul 16	1,483	Aug 17	1,054
Aug 16	1,629	Sep 17	0,358

Werte ab ungefähr 0,5 m werden nach den Literaturwerten (u.a. WMO, 2008) als plausibel für den Standort eingeschätzt. Da Leipzig generell nicht viele sehr hohe Gebäude besitzt und auch die weitere Umgebung des Messstandorts bis auf wenige Ausnahmen nur vier- bis fünfstöckige Gebäude aufweist, sollte der Rauhigkeitswert am LIM unter Klasse 8 mit $z_{0,Kl.8} \geq$2 m (vgl. Tab. 3) liegen. Diese werden von den Messwerten auch nicht überschritten.
Damit sind es die Sommermonate (2016: April bis August; 2017: Juni bis August), in denen z_0 ungefähr auf dem erwarteten Niveau liegt. Ursache dafür ist wahrscheinlich die Höhe der Prandtl-Schicht. Im Winter und nachts verhindert die sich häufig einstellende stabile Schichtung eine Ausprägung der Prandtl-Schicht-Verhältnisse bis in die hier erreichten Messhöhen über 50 m. Im Sommer ist die turbulente, gut durchmischte Bodenschicht stärker ausgeprägt, weshalb man auch mit den Messwerten aus Höhen im Messbereich des Windcubes z_0 bestimmen kann.
Natürlich sollte der z_0-Wert der Stadt sich mit der Jahreszeit nicht groß ändern, jahreszeitliche Abhängigkeit könnte nur durch den Vegetationszyklus verursacht werden. Außerdem könnte die Windrichtung und damit der Teil der Stadt, den die Luftmasse vor der Messung am LIM überströmt, einen Einfluss auf die Höhe der Rauhigkeitslänge am LIM haben. Drew et al. (2013) zeigt allerdings, dass für Messungen mitten in London die mittleren Windprofile für Stark-

windsituationen aus verschiedenen Windrichtungen ähnlich sind, obwohl ein Unterschied in der Oberflächenbeschaffenheit der verschiedenen Stadtviertel vorhanden ist. Um einen repräsentativeren Wert für z_0 zu bestimmen, werden die Tageswerte aus zwei abgeschlossenen Jahren des Messzeitraumes (August 2015 bis Juli 2017) gemittelt, sodass sich ein Wert $\bar{z}_{0,alleWerte}$= 0,51 m für die Rauhigkeitslänge ergibt. Dort fließen allerdings auch die Monate mit ein, in denen die Prandtl-Schicht vermutlich nicht durch den Messbereich abgebildet werden konnte und die nach den Literaturwerten (z.B. WMO, 2008) für die Stadt als „unplausibel“ bezeichnet werden. Lässt man diese Werte (mit $z_0 \leq$ 0,5 m) aus der Mittelwertbildung weg, erhält man einen zweiten Wert $\bar{z}_{0,plaus.Werte}$= 1,21 m. Beide Ergebnisse liegen in dem Intervall, was Literaturquellen für die Stadt vorschlagen (etwa 0,5 m$\leq z_0 \leq$2 m). Um herauszufinden, welcher Wert näher an der Realität liegt, würde es sich anbieten eine ausführliche Kategorisierung der gemessenen Windprofile nach Stabilität, Windrichtungssektoren und unter Einbeziehung der 24 m Windgeschwindigkeit aus den Messungen des LIM durchzuführen. Weitere Messpunkte unter 50 m Höhe wären wünschenswert, da die Messungen des Windcubes allein nicht ausreichend sind, um z.B. im Winter die Prandtl-Schicht abzubilden.

4.4 Die Turbulenzintensität

Eine Größe zur Quantifizierung der Wirbelhaftigkeit einer Luftmasse ist die Turbulenzintensität TI (z.B. Emeis et al., 2007). Sie beschreibt das Verhältnis aus Standardabweichung σ_U zu mittlerer Windgeschwindigkeit $U(z)$:

$$TI = \frac{\sigma_U}{U(z)} \tag{8}$$

Analog dazu wird hier ein Turbulenzmaß $\widetilde{TI}$ definiert, welches aus den Werten des Standardmittelungszeitraums von 10 min abgeleitet wurde. In den Mittelwert und die Standardabweichung fließen demnach für einen Messzeitraum von 10 min etwa 90 Einzelmessungen ein. Es ist noch eine offene Frage, ob in stark turbulenten Situationen tagsüber der 10-minütige Mittelwind tatsächlich ein repräsentativer Wert für den Zeitraum ist, oder kürzere Mittelungszeiträume gewählt werden müssen, um durch systematische Schwankungen hervorgerufene Windänderungen zu eliminieren und nur zufällige Abweichungen zu betrachten. Außerdem ist noch nicht endgültig geklärt, welcher Anteil der 10-minütigen Standardabweichung eventuell auf eine Ungenauigkeit des Geräts zurückzuführen ist. Die hier beschriebenen Ausführungen zur Turbulenz sind mit diesen Hinweisen zu betrachten.
In der Regel wird Turbulenz durch mechanische Einflüsse, wie Gebäude oder hohe Bäume, oder durch thermische Einflüsse (differentielle Oberflächenerwärmung und anschließende thermische Konvektion durch Sonneneinstrahlung) erzeugt. Turbulenz durch mechanische Einflüsse ist allein durch den hohen Bebauungsgrad im Stadtgebiet immer vorhanden, sobald etwas Wind weht. Der thermische Aspekt unterliegt jedoch einem Tagesgang. Besonders an Strahlungstagen ist die thermisch induzierte Turbulenz sehr ausgeprägt und kann auch anhand der Windcubemessungen gezeigt werden. Der 14.06.2017 war ein Sommertag, der nicht übermäßig heiß war, aber mit viel Einstrahlung und geringer horizontaler Windgeschwindigkeit in 24 m. Tagsüber sollte sich also bodennah Turbulenz entwickeln und sich nach und nach in höhere Schichten ausbreiten.
Abbildung 7 zeigt $\widetilde{TI}$ im Tagesgang. In den ersten Stunden des Tages erkennt man bodennah leicht erhöhte Werte bis ungefähr 150 m Höhe. Darüber ist $\widetilde{TI}$ niedriger mit Werten unter 15 %. Diese Situation ist noch ohne thermisch induzierte Turbulenz. Typische Werte der Turbulenzintensität in 100-200 m Höhe über Land liegen zwischen 10 und 20 % (nach Barthelmie et al.,

2007). Um ca. 3 Uhr UTC (4:54 Uhr MESZ) war Sonnenaufgang. Danach dauert es noch etwas, bis sich die Stadtoberfläche erwärmt hat und sich tatsächlich thermische Turbulenz am Boden entwickelt. Ab ungefähr 5 Uhr UTC sieht man den Bereich erhöhter Turbulenz (rote Werte) anwachsen bis um etwa 7 Uhr UTC die gesamten unteren 500 m der atmosphärischen Grenzschicht durch hohe $\widetilde{TI}$-Werte ausgezeichnet werden. Das bedeutet es dauert an diesem strahlungsreichen Sommertag etwa 4 Stunden nach Sonnenaufgang, bis die turbulente Bodenschicht bis in 500 m angewachsen ist.

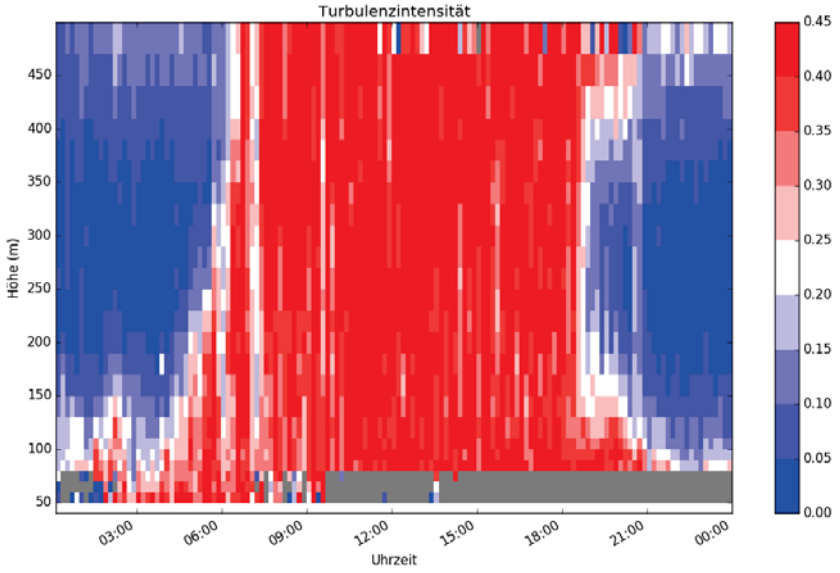

Abbildung 7: Turbulenzintensität im Tagesgang, 14.06.2017, Uhrzeit (UTC)

5 Zusammenfassung und Ausblick

Die mit dem Windcube im Zentrum von Leipzig seit 2015 durchgeführten Messungen liefern Angaben zum Windvektor zwischen 50 m und 510 m über Grund. Hier wird die Eignung der Messdaten zur Betrachtung von anerkannten Aussagen zur Struktur des Windfeldes über einer Stadt geprüft. Wünschenswert sind belastbare Aussagen für eine turbulente Atmosphäre über der Stadt, unter anderem zur höhenveränderlichen Struktur der Windgeschwindigkeit im Bereich der Ekman- und Prandtl-Schicht. Physikalische Größen wie der turbulente Diffusionskoeffizient K_m oder die aerodynamische Rauhigkeitslänge z_0, deren Größenangaben sich oft nur auf Aussagen aus der Literatur stützen, können so durch konkrete Messungen plausibilisiert werden. Hier werden Wege aufgezeigt, wie das umfangreiche Datenmaterial aufgearbeitet werden kann.

1. Es gelingt sehr gut, eine Winddrehung mit der Höhe nachzuweisen, die qualitativ und quantitativ mit der Ekman-Theorie übereinstimmt. Während am Boden die Hauptwindrichtung Südwest ist, dreht diese bis in 510 m Höhe um etwa 45° im Uhrzeigersinn. Außerdem wurden mithilfe der zonalen und meridionalen Windkomponenten und der Ekman-Theorie der turbulente Diffusionskoeffizient K_m für einen bestimmten Windsektor in drei verschiedenen Höhenstufen bestimmt. Die Durchmischung nimmt für das Beispiel nach oben hin zu. Naheliegend sind weitere Untersuchungen des Diffusionskoeffizienten zu anderen Windrichtungen und anderen Geschwindigkeitsintervallen. Allerdings ist auch eine Abhängigkeit von Wetterlage und Stabilität denkbar.

2. Es gestaltete sich äußerst schwierig, für Leipzig einen charakteristischen z_0-Wert zu bestimmen, da die Messungen erst in 50 m Höhe beginnen. Gerade im Winter und nachts ist die Prandtl-Schicht im Mittel nicht ausgeprägt genug, um mit dem Windcube eine aerodynamische Rauhigkeitslänge zuverlässig zu bestimmen. Die ermittelten Werte wären zwar mit den ohnehin meist sehr grob gefassten Literaturangaben vereinbar, für die Bestimmung der Rauhigkeitslänge in Zukunft ist es jedoch unabdingbar, die 24 m-Messwerte des LIM mit in das Windprofil zu integrieren. Das resultiert in einer notwendigen Verlängerung des Windprofils in die bodennahe Schicht. Außerdem gilt das logarithmische Windprofil in seiner hier angewandten Form nur für neutrale Schichtungen.

3. Die Daten eignen sich, um den Tagesgang der Turbulenz über der Stadt zu zeigen. Die Ergebnisse stimmen insofern mit den Erwartungen überein, dass $\widetilde{TI}$ nach Sonnenaufgang in Bodennähe zunimmt und der Bereich größerer Turbulenz sich rasch über den gesamten Messbereich ausbreitet. Tagsüber bleibt $\widetilde{TI}$ konstant hoch. Am Abend sinkt der Bereich größerer Turbulenzintensität wieder ab und nachts erstreckt er sich nur noch auf bodennahe Schichten bis etwa 100–150 m.

Dies sind Ansätze, um das Verständnis für das urbane Windprofil und speziell für das Windprofil über Leipzig weiter zu verbessern. Damit ebnet diese Arbeit den Weg zur noch spezielleren Auswertung einzelner Punkte. Gerade die charakteristischen Turbulenzgrößen bilden eine wichtige Stütze für Modelle, die immer wieder auf Parametrisierungen verschiedener Art zurückgreifen müssen. Diese Arbeit zeigt, wie umfangreich die Windcube-Messwerte zu interpretieren sind und weist Wege auf, mit den Daten die gesuchten Größen zu bestimmen.

6 Danksagung

Besonderer Dank gilt Dr. Johannes Bühl vom Leibniz Institut für Troposphärenforschung (TROPOS) für die Bereitstellung der Streamline-LIDAR-Daten, die den ersten Vergleich beider Messgeräte ermöglicht haben.

7 Literaturverzeichnis

Barthelmie, R. J., Frandsen, S. T., Nielsen, M. N., Pryor, S. C., Rethore, P.-E., Jørgensen, H. E., 2007, Modelling and measurements of power losses and turbulence intensity in wind turbine wakes at middelgrunden offshore wind farm, Wind Energy, Bd. 10(6), S. 517–528.

Bühl, J., Leinweber, R., Görsdorf, U., Radenz, M., Ansmann, A., Lehmann, V., 2015, Combined vertical-velocity observations with Doppler lidar, cloud radar and wind profiler, Atmospheric Measurement Techniques, Bd. 8(8), S. 3527-3536

Drew, D. R., Barlow, J. F., Lane, S. E., 2013, Observations of wind speed profiles over greater london, UK, using a doppler lidar, Journal of Wind Engineering and Industrial Aerodynamics, Bd. 121, S. 98–105

Emeis, S., Baumann-Stanzer, K., Piringer, M., Kallistratova, M., Kouznetsov, R., Yushkov, V., 2007, Wind and turbulence in the urban boundary layer analysis from acoustic remote sensing data and fit to analytical relations, Meteorologische Zeitschrift, Bd. 16(4), S. 393-406.

Lane, S.E., Barlow, J.F., Wood, C.R., 2013, An assessment of a three-beam Doppler lidar wind profiling method for use in urban areas, Journal of Wind Engineering and Industrial Aerodynamics, Bd. 119, S. 53-59

Päschke, E., Leinweber, R., Lehmann, V., 2015, An assessment of the performance of a 1.5 micrometer doppler lidar for operational vertical wind profiling based on a 1-year trial, Atmospheric Measurement Techniques, Bd. 8(6), S. 2251-2266

Oke, T.R., 1988, Boundary Layer Climates, Routledge

Stull, R.B., 1988, An introduction to boundary layer meteorology, Springer

World Meterological Organization, 2008, Guide to Meteorological Instruments and Methods of Observation

Forschungsbericht 2017
Bearbeitete Forschungsprojekte

Institut für Meteorologie

Direktor Prof. Dr. M. Wendisch

Allgemeine Meteorologie; Manfred Wendisch
AG Atmosphärische Strahlung

Flugzeuggetragene und bodengebundene Messungen von Albedo, BRDF und Schneeeigenschaften in der Antarktis und deren Kopplung zur Verbesserung prognostischer Schneemodelle

Coupling of airborne and in situ ground based measurements of surface albedo, BRDF and snow properties in Antarctica to improve prognostic snow models

Schlagworte: Antarktis, Schnee, Albedo, flugzeuggetragene Messungen, atmosphärische Strahlung

Projektleiter: M. Wendisch (m.wendisch@uni-leipzig.de)
Projektmitarbeiter: T. Carlsen (tim.carlsen@uni-leipzig.de), A. Ehrlich (a.ehrlich@uni-leipzig.de)

Projektbeginn: 2013
Projektende: 2017

Beschreibung

Im Rahmen des Projekts werden die zeitliche und räumliche Variabilität von Oberflächenalbedo, bidirektionaler Reflektivität BRDF und Schneeeigenschaften in der Antarktis untersucht. Das Hauptziel dieses Vorhabens ist eine Verbesserung von prognostischen Schneemodellen und von Parametrisierungen der Schneealbedo, wie sie derzeit in regionalen und globalen Klimamodellen verwendet werden. Diese Parametrisierungen werden in Abhängigkeit von Schneekorngröße, Schneeoberflächenrauigkeit und atmosphärischen Parametern formuliert. Um dieses Ziel zu erreichen, werden bodengebundene in situ Messungen (zeitliche Variabilität) und flugzeuggetragene Fernerkundungsmessungen (räumliche Variabilität) miteinander kombiniert. Die vom Flugzeug erhobenen Daten umfassen die spektrale Bodenalbedo, BRDF, Bodenrauigkeit und Schneekorngröße. Die dazu benötigten Fernerkundungsverfahren werden im Rahmen des Projekts verbessert bzw. entwickelt. Die gleichen Größen werden auf dem antarktischen Plateau mittels bodengebundener Messungen an der Kohnen Station erhoben werden. Die bodengebundenen Daten decken dabei die zeitliche Variabilität von Schnee- und Atmosphäreneigenschaften ab, was es ermöglicht, prognostische Schneemodelle zu validieren und zu verbessern, die an ein Strahlungstransfermodel angekoppelt sind. Durch die Einbindung von Messdaten in die Modelle und einem anschließenden Vergleich zwischen simulierter und gemessener Schneealbedo sowie durch Sensitivitätsstudien werden Parametrisierungen der Schneealbedo, wie sie in Strahlungs- und Klimamodellen verwendet werden, validiert und verbessert. Diese Erkenntnisse werden dazu dienen, Unsicherheiten in Vorhersagen der zukünftigen Klimaänderung in der Antarktis zu reduzieren.

Description

We propose to investigate the temporal and spatial variability of surface albedo, bidirectional reflectivity BRDF and snow properties in Antarctica. The overall goal of the project is to improve prognostic snow models and parameterizations of snow albedo used in regional and global climate models. The parameterizations will be formulated in dependence on snow grain size, snow surface roughness and atmospheric parameters. To achieve this goal we will couple ground based in situ (temporal variability) and airborne remote sensing measurements (spatial variability). Airborne data will include spectral surface albedo, BRDF, surface roughness and snow grain size. Corresponding remote sensing retrieval algorithms will be improved and developed in the project. The same quantities will be measured in situ on the Antarctic plateau by ground based instruments installed at Kohnen Station. The ground based measurements covering the temporal variability of snow and atmospheric properties will allow validating and improving prognostic snow models coupled to a radiative transfer code. By implementing measurement data in the models and comparing simulated and measured snow albedo and by sensitivity studies, snow albedo parameterizations for use in radiative transfer and climate models will be validated and improved. This will reduce uncertainties in predicting future climate change in Antartica.
Weiterführung: nein

Mittelgeber: Uni Leipzig, DFG WE 1900/29-1

Koordination des Schwerpunktprogramms 1294 "Atmosphären- und Erdsystemforschung mit dem Forschungsflugzeug HALO (High Altitude and Long Range Research Aircraft)"
HALO coordination project

Schlagworte: flugzeuggetragene Forschung

Projektleiter: M. Wendisch (m.wendisch@uni-leipzig.de)
Professor Dr. Joachim Curtius, Goethe-Universität Frankfurt am Main, Institut für Atmosphäre und Umwelt
Dr.-Ing. Mirko Scheinert, Technische Universität Dresden, Institut für Planetare Geodäsie

Projektmitarbeiter: Gunda Nitzsche, Jörg Schmidt

Projektbeginn: 2010
Projektende: 2019

Beschreibung
Das Projekt dient vornehmlich der Kooperation und der Kommunikation unter den Einzelprojekten des Schwerpunktprogramms. Im Rahmen des Projekts werden ein jährliches Statusseminar sowie jährliche Themen-Workshops geplant und durchgeführt. Die drei Koordinatoren vertreten den SPP gegenüber der DFG, dem Wissenschaftlichen Lenkungsausschuss von HALO (WLA), dem HALO Projektteam des Deutschen Zentrums für Luft- und Raumfahrt (DLR) und nach außen. Das Koordinatoren-Team betreibt Maßnahmen zur Nachwuchs- und Gleichstellungsförderung. Zentrale Initiativen wie gemeinsame Sammelveröffentlichungen in einem Sonderband oder die Durchführung von Sitzungen zu Themenschwerpunkten ("special sessions") bei internationalen Konferenzen sowie der Internetauftritt des SPP werden im Rahmen dieses Projekts koordiniert und durchgeführt.

Description

funds for the central coordination of SPP 1294 HALO are requested within this proposal. The project serves most of all the promotion of cooperation and communication among the individual scientific projects of the SPP. An annual status seminar as well as topical workshops are organized and conducted within this project. The coordinators represent the SPP via the DFG, the scientific steering committee of HALO (WLA), the HALO project team of the German Aerospace Center (DLR) and the public. The funds for measures to promote gender equality are managed and measures for training of young researchers are coordinated. Within the project special sessions at international conferences or publication of special issues are initiated. An SPP web page is set up and maintained. To support the coordinators in conducting these tasks, staffing for a half-time position of a scientific administrator is applied for.

Weiterführung: ja

Mittelgeber: DFG WE 1900/24-1

EUFAR2 - European Facility for Airborne Research in Environmental and Geo-sciences

Schlagworte: flugzeuggetragene Forschung

Projektleiter: M. Wendisch (m.wendisch@uni-leipzig.de)
Projektmitarbeiter:

Projektbeginn: 2014
Projektende: 2018

Beschreibung (Deutsch- Pflicht; <2000 Zeichen)
Im Rahmen dieses Projektes werden die Expert Working Groups koordiniert. Workshops werden organisiert, und ein Buch wurde geschrieben:
Wendisch, M., and J.-L. Brenguier (Eds.), 2013: Airborne Measurements for Environmental Research: Methods and Instruments. Wiley-VCH Verlag GmbH & Co. KGaA, Weinheim, Germany. ISBN: 978-3-527-40996-9. 655 pp., doi:10.1002/9783527653218.

Description
Within the project Expert Working Groups were coordinated. Workshops were organized with the aim to publish a book reviewing airborne atmospheric measurement methods.
Weiterführung: ja

Mittelgeber: EU

Flugzeuggetragene spektrale solare Strahlungsmessungen während ACRIDICON zur Untersuchung hochreichender Konvektion und Validierung satellitengetragener Fernerkundungssysteme.
Airborne spectral solar radiation measurements during ACRIDICON to investigate deep convection and validate space borne remote sensing.

Schlagworte: flugzeuggetragene Fernerkundung, Satellitenvalidierung, hochreichende Konvektion.

Projektleiter: M. Wendisch (m.wendisch@uni-leipzig.de)

Projektmitarbeiter: Trismono Candra Krisna

Projektbeginn: 2014
Projektende: 2018

Beschreibung
Innerhalb des ACRIDICON Projektes wurden flugzeuggetragene solare Strahlungsmessungen an Bord des Forschungsflugzeuges HALO durchgeführt. Die Messungen fanden in Brasilien im tropischen Regenwald statt und hatten das Ziel hochreichende konvektive Bewölkung zu untersuchen. Die spektralen Messungen sollen für zwei Ziele verwendet werden. In einem ersten Schritt sollen kalibrierte Strahldichtemessungen des SMART-Albedometers genutzt werden, um die Genauigkeit von Satellitenmessungen zu quantifizieren. Im zweiten Schritt werden die Daten verwendet, um Wolkeneigenschaften abzuleiten. Ein Vergleich der Ergebnisse mit den vom Satelliten abgeleiteten Wolkenparametern soll dazu dienen, die Unsicherheiten in den Satellitenmessungen zu bestimmen. Die Möglichkeiten zur Verbesserung der Ableitungsalgorithmen durch die Nutzung der vollen spektralen Information soll untersucht werden. Die abgeleiteten Wolkenparameter sollen über statistische Verfahren genutzt werden, um den Strahlungseinfluss der Wolken im Verlaufe ihres Lebenszyklus zu verfolgen.

Weiterführung: ja

Mittelgeber: DAAD
****

Einfluss der Eisphase auf den Strahlungsantrieb von Wolken: Messungen und Representation in numerischen Wettervorhersagemodellen
Influence of ice phase on radiative forcing of clouds: Observations and representation in numerical weather prediction models

Schlagworte: flugzeuggetragene Messungen, Wolken, Strahlungsantrieb, Eisphase

Projektleiter: M. Wendisch (m.wendisch@uni-leipzig.de)

Projektmitarbeiter: Kevin Wolf

Projektbeginn: 2016
Projektende: 2019

Beschreibung
Methoden der flugzeuggetragenen passiven Fernerkundung mit Hilfe spektraler, solarer und reflektierter Strahldichten werden zur Ableitung der thermodynamischen Phase, der optischen Dicke und des Partikeleffektivradius von Wolken während der HALO Missionen NARVAL-II und NAWDEX angewendet. Insbesondere werden die horizontalen und vertikalen Verteilungen der thermodynamischen Phasen in unterschiedlichen Wolkentypen untersucht. Die Kombination mit anderen HALO-Fernerkundungsinstrumenten einschließlich Radar und Mikrowellensensoren ist geplant. Gleichzeitige Messungen der Wolkenalbedo werden durchgeführt und zur Analyse der

Abhängigkeit des Strahlungsantriebs von Wolken-makrophysikalischen und mikrophysikalischen Eigenschaften verwendet. Auf der Basis von breitbandigen und spektralen Strahlungsgrößen dient die gemessene spektrale Wolkenalbedo zur Bewertung von Ergebnissen des ECMWF Integrated Forecast System (IFS). In mehreren Schritten werden 1D und 3D Strahlungstransfermodelle zusammen mit Beobachtungen verwendet, um die Unsicherheiten in der ECMWF-Vorhersage zu identifizieren. Unsicherheiten in Bezug auf das Strahlungsschema und die simulierten Wolkeneigenschaften werden separiert.

Description
The airborne passive solar remote sensing of spectral reflected radiance will be applied to derive cloud thermodynamic phase, optical thickness, and particle effective radius during the HALO Missions NARVAL-II and NAWDEX. In particular, cloud thermodynamic phase and its horizontal and vertical distribution in different cloud types will be investigated. Combination with other remote sensing instruments of HALO including active radar and passive microwave sensors is planned. Simultaneous measurements of cloud top albedo will be derived and used to analyse the dependence of cloud radiative forcing on cloud macrophysical and microphysical properties. Measured spectral cloud top albedo will be employed to evaluate the ECMWF Integrated Forecast System (IFS) on the basis of broadband and spectral radiative quantities. In different steps, 1D and 3D radiative transfer models will be utilized in combination with the observations to identify and quantify uncertainties in IFS forecasts and analysis fields. Uncertainties due to the radiations scheme and simulated cloud properties will be separated.

Weiterführung: ja

Mittelgeber: DFG, SPP 1294

Hochaufgelöste Messungen von Turbulenz, Wolkenmikrophysik, und Strahlungsabkühlungsraten in der Einmischungszwischenschicht von marinen Stratocumulus-Wolken.
High resolved measurements of turbulence, cloud microphysical properties and radiative cooling rates in the entrainment zone of marine strato cumulus.

Schlagworte: hubschraubergetragene Messungen, Stratocumulus, Energiebilanz, Strahlungsabkühlung.

Projektleiter: M. Wendisch (m.wendisch@uni-leipzig.de)
Dr. Holger Siebert, Leibniz-Institut für Troposphärenforschung e.V. (TROPOS)

Projektmitarbeiter: Felix Lauermann

Projektbeginn: 2015
Projektende: 2018

Beschreibung
Obwohl bisher schon viele Fortschritte im allgemeinen Verständnis von Mischungs- und Strahlungsprozessen in Stratocumulus (Sc) gemacht wurden, verursachen wolkenbedingte Rückkopplungseffekte von Sc Wolken erhebliche Unsicherheiten in Klimaprojektionen. Diese Probleme werden teilweise verursacht durch eine unrealistische Beschreibung der feinskaligen

Mischungsprozesse, die hauptsächlich am Oberrand der Wolken stattfinden. Die Strahlungs-Abkühlung am Wolkenoberrand ist eng mit dynamischen und turbulenten Wolkenprozessen verbunden. Abkühlung am Oberrand der Wolken verursacht ein Absinken. Diese Vertikalbewegungen bedingen Turbulenzen wodurch trockene und warme Umgebungsluft in die Wolke eingemischt wird, so dass sich die damit verbundene Verdunstungsabkühlung erhöht. Zur Untersuchung dieser Vorgänge schlagen wir folgende wesentlichen Projektziele vor: (a) die Verbesserung des Verständnisses der feinskaligen Struktur der Einmischungsinversionszwischenschicht (entrainment interface layer, EIL), (b) die Quantifizierung des Einflusses der EIL auf die Einmischung trockener und warmer Umgebungsluft in Sc Wolken, (c) die Bewertung der Rolle von Strahlungserwärmungs- und Abkühlungsraten bei Einmischungsprozessen in Sc Wolken. Um diese Ziele erreichen zu können, werden Beobachtungen mit den zwei kombinierten, hubschraubergetragenen Messsystemen ACTOS (Airborne Cloud Turbulence Observation System) und SMART--HELIOS (Spectral Modular Airborne Radiation measurement sysTem) vorgeschlagen. Die Messungen finden auf den Azoren statt. Beide Messsysteme werden durch einen langsam fliegenden Hubschrauber getragen. Das kombinierte Messsysteme-Paket ermöglicht in-situ Messungen von dynamischen, thermodynamischen, Wolken-mikrophysikalischen und Strahlungsparametern mit hoher örtlicher Auflösung (überwiegend im cm-Bereich). Kein anderes Messsystem weltweit erreicht diese hohe Auflösung, die allerdings unabdingbar ist für die Erreichung der Projektziele ist. Dies trifft insbesondere auf die Vermessung der Vorgänge in der EIL zu, welche meist eine vertikale Dicke von nur 10 m aufweist.

Weiterführung: ja

Mittelgeber: DFG, WE 1900/33-1

STRATOCLIM - Stratospheric and upper tropospheric processes for better climate predictions

Schlagworte: flugzeuggetragene Forschung

Projektleiter: M. Wendisch (m.wendisch@uni-leipzig.de)
Projektmitarbeiter:

Projektbeginn: 2013
Projektende: 2018

Beschreibung (Deutsch- Pflicht; <2000 Zeichen)
STRATOCLIM wird verlässlichere Vorhersagen von Klimaänderungen und stratosphärischer Ozonverteilung erreichen, durch eine Verbesserung des Systemverständnisses von wichtigen Prozessen in der oberen Troposphäre und unteren Stratosphäre. Unsere Gruppe ist mit Modellberechnungen zur Bestimmung von Erwärmungs- und Abkühlungsraten in der Tropopausenregion beteiligt.

Description
StratoClim will produce more reliable projections of climate change and stratospheric ozone by a better understanding and improved representation of key processes in the Upper Troposphere and Stratosphere (UTS). This will be achieved by an integrated approach bridging observations from

dedicated field activities, process modelling on all scales, and global modelling with a suite of chemistry climate models (CCMs) and Earth system models (ESMs). At present, complex interactions and feedbacks are inadequately represented in global models with respect to natural and anthropogenic emissions of greenhouse gases, aerosol precursors and other important trace gases, the atmospheric dynamics affecting transport into and through the UTS, and chemical and microphysical processes governing the chemistry and the radiative properties of the UTS. StratoClim will (a) improve the understanding of the microphysical, chemical and dynamical processes that determine the composition of the UTS, such as the formation, loss and redistribution of aerosol, ozone and water vapour, and how these processes will be affected by climate change; (b) implement these processes and fully include the interactive feedback from UTS ozone and aerosol on surface climate in CCMs and ESMs. Through StratoClim new measurements will be obtained in key regions:

(1) in a tropical campaign with a high altitude research aircraft carrying an innovative and comprehensive payload,
(2) by a new tropical station for unprecedented ground and sonde measurements, and
(3) through newly developed satellite data products.

The improved climate models will be used to make more robust and accurate predictions of surface climate and stratospheric ozone, both with a view to the protection of life on Earth. Socioeconomic implications will be assessed and policy relevant information will be communicated to policy makers and the public through a dedicated office for communication, stakeholder contact and international co-operation.

Weiterführung: ja

Mittelgeber: EU

SFB/Transregio 172 „Arktische Verstärkung“
Zentrale Dienstleistungen, Verwaltung und Koordinierung (Z01)
Central services, administration and coordination (Z01)

Schlagworte: Arktis.

Projektleiter:
M. Wendisch (m.wendisch@uni-leipzig.de)
Prof. Dr. Susanne Crewell, Universität zu Köln, Institut für Geophysik und Meteorologie
Prof. Dr. Justus Notholt, Universität Bremen, Institut für Umweltphysik

Projektmitarbeiter: Dr. Marlen Brückner

Projektbeginn: 2016
Projektende: 2019

Beschreibung (Deutsch- Pflicht; <2000 Zeichen)
Innerhalb des TR 172 Antrages werden Mittel für die zentrale Koordinierung beantragt. Dieses Teilprojekt dient dazu, die Kooperationen und Kommunikation im Verbund unter den einzelnen wissenschaftlichen Projekten und Clustern zu fördern. Aus diesem Grund werden monatliche

Videokonferenzen, halbjährliche Meetings, jährliche wissenschaftliche Konferenzen, als auch spezielle Workshops organisiert und durchgeführt. Die Mittel für Gleichstellungsmaßnahmen werden dazu verwendet um junge Wissenschaftler/innen in Zusammenarbeit mit lokalen Graduiertenschulen zu trainieren. Die internationale Präsenz des TR 172 wird etabliert. Eine Internetseite wird erstellt und implementiert. Die logistische Organisation und wissenschaftliche Planung von intensiven Messkampagnen innerhalb des TR 172 werden durch das Projekt Z01 unterstützt. Öffentlichkeitsarbeit zwischen den verschiedenen Partnern wird organisiert und koordiniert.

Description
Funds for the central coordination of TR 172 are requested within this proposal. The project serves the promotion of cooperation and communication among the individual scientific projects and clusters. Monthly video conferences, biannual general assemblies, annual scientific conferences, as well as topical workshops will be organized and conducted. The funds for measures to promote gender equality are managed the training of young researchers is coordinated, in collaboration with local graduate schools. The international visibility of TR 172 will be fostered. A web page will be set up and maintained. The logistic organization and scientific planning of the extensive observational campaigns within TR 172 will be supported by project Z01. Public outreach activities will be organized and coordinated between the different partners.

Weiterführung: ja

Mittelgeber: DFG, TRR 172

SFB/Transregio 172 „Arktische Verstärkung“
Fesselballongetragene Messungen des Energiebudgets in der wolkenbedeckten Zentralarktis (A02)
Tethered balloon-borne energy budget measurements in the cloudy central Arctic (A02)

Schlagworte: Arktis, ballongetragene Messungen, Energiebilanz, Strahlungsabkühlung.

Projektleiter: M. Wendisch (m.wendisch@uni-leipzig.de)
Dr. Holger Siebert, Leibniz-Institut für Troposphärenforschung e.V. (TROPOS)

Projektmitarbeiter: Matthias Gottschalk

Projektbeginn: 2016
Projektende: 2019

Beschreibung
Während der Forschungsfahrt von FS Polarstern im Frühsommer (Mai bis Juni) 2017 werden Fesselballon-getragene Messungen von einer Eisschollenstation analysiert. Atmosphärische Vertikalprofile (bis zu einem Kilometer Höhe) der turbulenten Energieflüsse (sensible und latente Wärme), Strahlungsenergieflüsse und turbulente Impulserhaltung werden gemessen. Die Beobachtungen werden den Einfluss von makrophysikalischen (Wolkenbasishöhe, Temperatur, geometrische Dicke, Wolkenbedeckung) und mikrophysikalischen (effektiver Tropfenradius) Eigenschaften von arktischen tiefen Wolken auf (i) die Profile der Flüsse, (ii) den entsprechenden

Strahlungsantrieb und (iii) die damit verbundenen netto Erwärmung/Abkühlung der bodennahen Lufttemperatur untersuchen.

Description
Tethered balloon-borne measurements from an ice-floe camp during the cruise of RV Polarstern in early summer (May to June) 2017 will be analysed. Atmospheric vertical profiles (up to one-kilometer altitude) of turbulent energy fluxes (sensible and latent heat), radiative energy fluxes, and turbulent fluxes of momentum will be measured. The observations will investigate the influence of macrophysical (cloud base height and temperature and geometric thickness, cloud cover) and microphysical (effective radius) properties of Arctic low--level clouds on (i) the profiles of fluxes, (ii) the respective radiative forcing, and (iii) the related net warming/cooling of the near-surface air temperature.

Weiterführung: ja

Mittelgeber: DFG, TRR 172

SFB/Transregio 172 „Arktische Verstärkung“
Einfluss von tiefen Wolken auf die arktische atmosphärische Grenzschichtturbulenz und -Strahlung (A03)
Impact of low-level clouds on Arctic atmospheric boundary layer turbulence and radiation (A03)

Schlagworte: Arktis, flugzeuggetragene Messungen, Energiebilanz, Strahlungsabkühlung.

Projektleiter: M. Wendisch (m.wendisch@uni-leipzig.de)
Dr. Christof Lüpkes, Alfred-Wegener-Institut Helmholtz-Zentrum für Polar- und Meeresforschung

Projektmitarbeiter: Johannes Stapf

Projektbeginn: 2016
Projektende: 2019

Beschreibung (Deutsch- Pflicht; <2000 Zeichen)
Vertikalprofile von Strahlungsenergie- und Turbulenzenergieflüssen sowie Impulserhaltung werden untersucht durch (i) Verwendung vorheriger Schiffs- und Flugzeugkampagnen und (ii) durch die Analyse neuer Messungen von zwei geplanten Flugzeugkampagnen über dem Arktischen Ozean. Die beiden neuen Kampagnen beziehen die AWI Forschungsflugzeuge Polar 5 & 6 ein, um die vertikalen Flussprofile als Funktion von Wolken- und Meereisbedeckung unter verschiedenen synoptischen Bedingungen zu messen. Die Flugzeugbeobachtungen sind für Mai/Juni 2017 und März 2019 geplant und decken somit Zeiträume starker (Spätwinter) und schwacher (Frühsommer) arktischer Verstärkung ab.

Description
Tethered balloon-borne measurements from an ice-floe camp during the cruise of RV Polarstern in early summer (May to June) 2017 will be analysed. Atmospheric vertical profiles (up to one-kilometer altitude) of turbulent energy fluxes (sensible and latent heat), radiative energy fluxes, and turbulent fluxes of momentum will be measured. The observations will investigate the influence of macrophysical (cloud base height and temperature and geometric thickness, cloud

cover) and microphysical (effective radius) properties of Arctic low--level clouds on (i) the profiles of fluxes, (ii) the respective radiative forcing, and (iii) the related net warming/cooling of the near-surface air temperature.

Weiterführung: ja

Mittelgeber: DFG, TRR 172

SFB/Transregio 172 „Arktische Verstärkung“
Einfluss von Bodenheterogenität auf den Strahlungsantrieb und Ableitung von Aerosol- und Wolkeneigenschaften in der Arktis (C01)
Influence of surface heterogeneity on radiative forcing and retrieval of aerosol and cloud properties in the Arctic (C01)

Schlagworte: Arktis, flugzeuggetragene Messungen, Eis- und Schneealbedo, BRDF

Projektleiter: M. Wendisch (m.wendisch@uni-leipzig.de)
Dr. Georg Heygster , Universität Bremen, Institut für Umweltphysik (IUP)

Projektmitarbeiter: Dr. Evelyn Jäkel
Projektbeginn: 2016
Projektende: 2019

Beschreibung
Für die Arktis ist ein diskontinuierlicher Albedo Unterschied zwischen hoch reflektierenden Schnee/Eisoberfächen und meist stark absorbierenden Meeresoberflächen typisch. In diesem Teilprojekt wird quantifiziert, inwiefern diese Heterogenität der Reflektionseigenschaften der Erdoberfläche (i) den Strahlungsantrieb von Wolken (Erwärmung/Abkühlung) und (ii) die Fernerkundungsprodukte von Wolken und Aerosolpartikeln beeinflussen. Aus diesem Grund werden flugzeuggetragene Messungen und Strahlungstransfermodellierungen vorgeschlagen.

Description
In the Arctic, a discontinuous albedo contrast between highly reflecting snow/ice and mostly absorbing sea surfaces is typical. In this project it will be quantified how these affect (i) the radiative forcing of clouds (warming/cooling), and (ii) the remote sensing products of clouds and aerosol particles. For this purpose, airborne measurements and Radiative Transfer modelling studies are proposed.

Weiterführung: ja

Mittelgeber: DFG, TRR 172

SFB/Transregio 172 „Arktische Verstärkung“
Charakterisierung von arktischen Mischphasenwolken durch flugzeuggetragene in-situ Messungen und Fernerkundung (B03)
Characterization of Arctic mixed-phase clouds by airborne in-situ measurements and remote sensing (B03)

Schlagworte: Arktis, flugzeuggetragene Messungen, Mischphasenwolken.

Projektleiter: Dr. André Ehrlich (a.ehrlich@uni-leipzig.de)
Professor Dr. Susanne Crewell, Universität zu Köln, Institut für Geophysik und Meteorologie
Professor Dr. Andreas Macke, Leibniz-Institut für Troposphärenforschung e.V. (TROPOS)

Projektmitarbeiter: Elena Ruiz
Projektbeginn: 2016

Projektende: 2019

Beschreibung
Dieses Teilprojekt schlägt neuartige Beobachtungsstrategien für arktische Wolken vor durch Kombination von flugzeuggetragenen Fernerkundungsmethoden mit in-situ mikrophysikalischen Messungen von Wolken- und Aerosoleigenschaften. Unter der Verwendung von zwei nebeneinanderfliegenden Flugzeugen (Polar 5 & 6) wird es möglich sein die mikrophysikalischen Partikeleigenschaften innerhalb von Wolken gleichzeitig durch in-situ Sensoren zu messen. Ebenfalls werden die vertikale Säule und deren Strahlungseinfluss mittels Fernerkundungsmessungen oberhalb von Wolken gemessen. Beide Kampagnen werden im Sommer 2017 (ACLOUD, Svalbard) und Frühling 2019 (AFLUX, Svalbard und Grönland) durchgeführt, um typische arktische Grenzschichtwolken als Teil der hauptsächlichen experimentellen Aktivitäten innerhalb des TR 172 zu untersuchen.

Description
The project proposes novel observation strategies for Arctic clouds by combining airborne remote sensing with in-situ microphysical measurements of cloud and aerosol properties. Using two identical collocated aircraft, Polar 5 and 6, it will be possible to simultaneously measure the microphysical particle characteristics within clouds by in-situ sensors and probe the vertical column and radiative impact from remote sensing measurements above clouds. Two campaigns will be performed in summer 2017 (ACLOUD, Svalbard) and spring 2019 (AFLUX, Svalbard and Greenland) to investigate typical Arctic boundary layer clouds as part of the major experimental activities of the TR 172.

Weiterführung: ja

Mittelgeber: DFG, TRR 172

SFB/Transregio 172 „Arktische Verstärkung“
Wechselwirkungen von Schnee auf Meereis mit atmosphärischen Bestandteilen inklusive Ruß (C02)
Interactions of snow on sea ice with atmospheric constituents including black carbon (C02)

Schlagworte: Arktis, flugzeuggetragene Messungen, Black Carbon, Eis und Schneealbedo

Projektleiter: Dr. André Ehrlich (a.ehrlich@uni-leipzig.de)
Dr. Rüdiger Gerdes, Alfred-Wegener-Institut Helmholtz-Zentrum für Polar- und Meeresforschung

Projektmitarbeiter: Tobias Donth

Projektbeginn: 2016
Projektende: 2019

Beschreibung
Gleichzeitige Beobachtungen von atmosphärischem Ruß und Rußpartikeln in Schnee- und Bodeneigenschaften sind selten. Daher wird dieses Teilprojekt flugzeug- und bodengebundene Beobachtungen von Aerosolen und Rußkonzentrationen kombinieren, sowie optische Schneeeigenschaften und deren Rückkopplungsmechanismen in der arktischen Region untersuchen. In-situ Messungen von atmosphärischen Rußpartikeln (boden- und flugzeuggetragen) in Verbindung mit Rußpartikeln in Schneeproben und Fernerkundungsbeobachtungen von Schneeeigenschaften werden zusammengefügt.

Description
Concurrent observations of atmospheric Black Carbon (BC), and BC in snow and surface properties are rare. Hence, this project will combine airborne and ground-based observations of aerosols and BC concentrations and snow optical properties to investigate their feedback mechanisms in Arctic regions. In-situ measurements of atmospheric BC (ground-based and airborne) along with sampling of BC in snow and remote sensing observations of snow properties will be merged.

Weiterführung: ja

Mittelgeber: DFG, TRR 172

Entwicklung von tropischer hochreichender Konvektion abgeleitet aus bodengebundenen abbildenden Spektroradiometermessungen
Evolution of tropical deep-convective clouds derived from ground-based imaging spectroradiometer measurements

Schlagworte: Konvektive Wolken, atmosphärische Strahlung, bodengebundene Fernerkundung

Projektleiter: M. Wendisch (m.wendisch@uni-leipzig.de)
Projektmitarbeiter: Kátia Mendes de Barro (katia.mendes_de_barros@uni-leipzig.de)

Projektbeginn: 2017
Projektende: 2020

Beschreibung
Im Rahmen des Projekts soll aus bodengebundenen Wolkenseitenmessungen der reflektierten Strahlung mittels eines abbildenden Spektrometersystems von tropischer hochreichender Konvektion auf das Vertikalprofil der mikrophysikalischen Eigenschaften der Wolke geschlossen werden. Damit soll die vertikale Entwicklung von hochreichender Konvektion, die eine wesentliche klimarelevante Rolle spielt, unter Berücksichtigung des Einflusses von Aerosolpartikeln und von thermodynamischen Bedingungen auf das Tropfenwachstum charakterisiert werden. Die geplanten Messungen sollen auf einem 320 m hohen Messturm (ATTO: Amazonian Tall Tower Observatory), der kürzlich im brasilianischen Regenwald errichtet wurde, stattfinden. ATTO ist mit Messgeräten ausgestattet, die meteorologische, chemische und

Aerosolparameter liefern. Die Messregion bietet ideale Beobachtungsbedingungen mit klar definierten Jahreszeiten (Regen- und Trockenzeit), täglicher Konvektion und variablen Aerosolbedingungen. Aus den Messungen eines neuen abbildenden Spektrometersystems, SPIRAS (SPectral Imaging Radiation System) sollen Vertikalprofile der thermodynamischen Phase und der Partikelgröße mit hoher zeitlicher und räumlicher Auflösung und mit Hilfe von adaptierten Verfahren unter Verwendung von dreidimensionalen Strahlungstransportsimulationen abgeleitet werden. Damit sollen vertikale Bereiche, die das Tropfenwachstum beschreiben (Diffusion, Koaleszenz, Mischphasenbereich und Vereisung), identifiziert werden. Zusätzliche Messungen einer Infrarotkamera und eines scannenden Depolarisations-Lidars werden für die Höhen- und Temperaturbestimmung der beobachteten Wolkenelemente herangezogen. Zusätzlich werden die Polarisationsmessungen des Lidars zur Bestimmung der thermodynamischen Phase verwendet, um den wichtigen Phasenübergang zu identifizieren. Mit Hilfe der gewonnenen Daten werden außerdem Annahmen (Effektivradius als konservative Wolkeneigenschaft) wie sie von Ableitungsverfahren zur Bestimmung von mikrophysikalischen Wolkenprofilen aus Satellitenmessungen gemacht werden, überprüft.

Description
Specifically the project will derive the vertical profile of microphysical properties of tropical deep-convective clouds (DCC) from ground-based measurements of reflected radiation from cloud sides by an imaging spectroradiometer system. This general objective is to characterize the vertical evolution of DCCs, which play an important role in the Earths climate system. The evolution will be studied with respect to the impact of aerosol and thermodynamic conditions on the cloud particle growth. The planned measurements will be performed on the new Amazonian Tall Tower Observatory (ATTO), of 320 m height situated in the Amazon Basin near the equator. ATTO is equipped with instruments to measure micrometeorological and atmospheric chemical variables, as well as aerosol properties. It provides ideal observation conditions with clear seasons (wet and dry season), and daily occurrence of DCCs in a highly variable environment with respect to concentrations and types of aerosol particles. The new imaging spectroradiometer system, SPIRAS (SPectral Imaging Radiation System), will be used to derive vertical profiles of thermodynamic phase and cloud effective radius with high temporal and spatial resolution by means of adapted methods based on three-dimensional radiative transfer simulations. In this way vertical zones characterizing the droplet growth (diffusion, coalescence, mixed-phase, and glaciation) will be identified. Auxiliary measurements by an infrared camera and a scanning depolarization Lidar will be used to estimate the height and the temperature of the observed cloud element. Additionally, polarization measurements by Lidar will support the retrieval of the thermodynamic phase which is important to identify the phase transition. By means of the data obtained we will validate assumptions (effective particle radius as conservative cloud property) of retrieval methods for satellite-based observations to derive microphysical profiles.

Weiterführung: ja

Mittelgeber: DFG WE 1900/34-1
****

Theoretische Meteorologie; Johannes Quaas
AG Wolken und globales Klima

STRATOCLIM Quantifizierung von Aerosol-Wolken-Klima-Effekten für Wolkenregime

Quantifying Aerosol-Cloud-Climate Effects by Regime

Schlagworte: Aerosol, Wolken, Klimawandel, Strahlungsantrieb

Projektleiter:
Koordinator: Johannes Quaas, Universität Leipzig (johannes.quaas@uni-leipzig.de)

Projektmitarbeiter:
Claudia Unglaub (unglaub@rz.uni-leipzig.de)
Karoline Block (karoline.block@uni-leipzig.de)

Projektbeginn: 2011
Projektende: 2017

Beschreibung
Ziel von QUAERERE ist die verlässliche Quantifizierung des Strahlungsantriebs von anthropogenen Aerosolen durch ihren Effekt auf Wolken. Aufbauend auf früheren Arbeiten sollen hierzu Satellitendaten verschiedener Instrumente kombiniert und in einem statistischen Ansatz ausgewertet werden. Die Aerosol-Informationen für diese Studie stammen dabei nicht direkt aus Satellitendaten, sondern in wesentlich verbesserter Qualität aus der Reanalyse des MACC-II-Projetks. Die statistische Analyse soll für einzelne Wolken-Aerosol-Regime durchgeführt werden. Neben dieser beobachtungsbasierten Abschätzung sollen Simulationen mit dem regionalen Aerosol-Klima-Modell COSMO-MUSCAT (in Zusammenarbeit mit dem Leibniz-Institut für Troposphärenforschung) durchgeführt werden, die in Sensitivitätsstudien mit abgeschalteten anthropogenen Emissionen dazu dienen können, in den statistischen Korrelationen aus den Satellitendaten Kausalzusammenhänge nachzuweisen. Schließlich soll in Simulationen mit dem globalen Aerosol-Klima-Modell ECHAM6-HAM2 eine globale Abschätzung erzielt werden, die konsistent ist mit der beobachtungsgestützten Abschätzung.

Weiterführung: nein

Mittelgeber: Europäischer Forschungsrat (ERC) Starting Grant
****

Marine Stratocumulus Cloud Cover and Climate

Schlagworte: Stratokumulus, Aerosol-Wolken-Wechselwirkungen

Projektleiter: Koordinator: Tom Goren (tom.goren@uni-leipzig.de)

Projektmitarbeiter: Dr. Tom Goren (tom.goren@uni-leipzig.de)

Projektbeginn: 2016
Projektende: 2018

Beschreibung

Das Projekt untersucht anhand von Satellitendaten und globalen Modellen den Einfluss anthropogener Aerosol-Emissionen auf marine Grenzschichtwolken. Dabei soll insbesondere untersucht werden, ob das Aufbrechen der geschlossenen Wolkendecken in verschmutzten Luftmassen später erfolgt als ohne anthropogenes Aerosol.

Weiterführung: ja

Mittelgeber: EU Horizon 2020 Marie Skłodowska-Curie Individual Fellowship.

****

Learning about cloud brightening under risk and uncertainty: Investigation of feasibility, traceability, Incentives and de-centralised governance of limited-area climate engineering (LEAC-II)

Schlagworte: Klima-Engineering, Klimawandel, Wolken impfen

Projektleiter:
Koordinator: Johannes Quaas, Universität Leipzig (johannes.quaas@uni-leipzig.de)

Projektmitarbeiter: Dr. Dipu Sudhakar (dipu.sudhakar@uni-leipzig.de)

Projektbeginn: 2016
Projektende: 2019

Beschreibung
Im Rahmen des Schwerpunktprojekts „Climate engineering – risks, challenges, opportunitites?“ der Deutschen Forschungsgemeinschaft untersucht das Projekt „LEAC-II“ in Zusammenarbeit mit dem Fachbereich Umweltökonomie an der Universität Kiel, inwiefern eine Beeinflussung des Klimas auf regionaler Skala machbar wäre. Dabei wird untersucht, ob etwa durch technische Änderung von Wolkeneigenschaften lokal Hitzewellen abgemildert werden könnten und inwiefern die Änderung des Klimas in einer Region Auswirkungen auf benachbarte Regionen hat.

Weiterführung: ja

Mittelgeber: Deutsche Forschungsgemeinschaft (DFG) SPP 1689

****

Forcing in the long-wave spectrum due to aerosol-cloud interactions: satellite and climate modelling vs. HALO (FLASH)

Schlagworte: Eiswolken, Eiswolken-Aerosol-Wechselwirkungen, Strahlungsantrieb, HALO

Projektleiter:
Koordinator: Johannes Quaas, Universität Leipzig (johannes.quaas@uni-leipzig.de)

Projektmitarbeiter:
Dr. Johannes Mülmenstädt (johannes.muelmenstaedt@uni-leipzig.de)

Projektbeginn: 2016
Projektende: 2019

Beschreibung
In der Arbeitsgruppe wurden neue Satellitendaten für die Eiskristallkonzentration entwickelt. Diese sollen im Projekt FLASH mit Hilfe von HALO-In-situ-Beobachtungen evaluiert werden. Dabei soll unter anderem zusammen mit dem DLR-Institut für Physik der Atmosphäre das Satellitenprodukt für kombinierte Radar-Lidar-Retrieval mit Daten der luftgetragenen Instrumente verglichen werden; daneben sollen die Satellitenprodukte mit in-situ-Beobachtungen evaluiert werden.

Weiterführung: ja

Mittelgeber: Deutsche Forschungsgemeinschaft (DFG) SPP 1294

****

Copernicus Atmospheric Monitoring Service 74 - Radiative Forcings

Schlagworte: Aerosol-Strahlungsantrieb, Reanalyse, Aerosol-Wolken-Wechselwirkungen

Projektleiter:
Koordinator: Nicolas Bellouin, Universität Reading (n.bellouin@reading.ac.uk)
J. Quaas (johannes.quaas@uni-leipzig.de)

Projektmitarbeiter: Dr. Johannes Mülmenstädt (johannes.muelmenstaedt@uni-leipzig.de)

Projektbeginn: 2016
Projektende: 2019

Beschreibung
Ziel dieses Services des COPERNICUS Atmospheric Monitoring Service ist die Bereitstellung einer Diagnostik für den anthropogenen Strahlungsantrieb durch verschiedene Mechanismen auf Basis der Reanalyse der Atmosphärenzusammensetzung. Beitrag der Uni Leipzig ist hierbei der Strahlungsantrieb durch Aerosol-Wolken-Wechselwirkungen.

Weiterführung: ja

Mittelgeber: Europäische Union, COPERNICUS-Programm, COPERNICUS Atmospheric Monitoring Service (Subcontractor der Uni Reading)

****

Theoretische Meteorologie
AG Wolken und globales Klima

Modelling aerosols and aerosol-cloud interactions in the Arctic (D02)

Schlagworte: Arktischer Klimawandel, Aerosol-Wolken-Wechselwirkungen, Modellierung

Projektleiter:
Koordinator: Johannes Quaas, Universität Leipzig (johannes.quaas@uni-leipzig.de)

Projektmitarbeiter:
Jan Kretzschmar (jan.kretzschmar@uni-leipzig.de)

Projektbeginn: 2016
Projektende: 2019

Beschreibung
In diesem Beitrag zum SFB/Transregio (AC)³ soll mit Hilfe von globaler Modellierung in Kombination mit verschiedenen Beobachtungen der Einfluss anthropogener Aerosole auf den arktischen Klimawandel untersucht werden. In Kooperation mit dem Leibniz-Institut für Troposphärenforschung liegt hierbei der Schwerpunkt auf dem Meridionaltransport der Aerosole (TROPOS) und der Wechselwirkung von Aerosol mit Wolken (LIM).

Weiterführung: ja

Mittelgeber: Deutsche Forschungsgemeinschaft (DFG) TRR 172 (AC)³

****

Assessment of Arctic feedback processes in climate models (E01)

Schlagworte: Arktischer Klimawandel, Feedbacks, Modellierung

Projektleiter:
Koordinator: Johannes Quaas, Universität Leipzig (johannes.quaas@uni-leipzig.de)

Projektmitarbeiterin:
Karoline Block (karoline.block@uni-leipzig.de)

Projektbeginn: 2016
Projektende: 2019

Beschreibung
In diesem Beitrag zum SFB/Transregio (AC)³ sollen mit Hilfe von globaler Modellierung in Kombination mit verschiedenen Beobachtungen die verschiedenen Klima-Feedback-Mechanismen quantifiziert und in den Klimamodellen evaluiert werden. Spezielles Augenmerk ist hierbei in Kooperation mit der Uni Köln auf dem Wolken-Feedback.

Weiterführung: ja

Mittelgeber: Deutsche Forschungsgemeinschaft (DFG) TRR 172 (AC)³

****

Aerosol-cloud-rainfall interactions over emission source regions

Schlagworte: Aerosol-Wolken-Niederschlagswechselwirkungen, Solar dimming

Projektleiter:
Koordinator: Dr. Ribu Cherian, Universität Leipzig (ribu.cherian@uni-leipzig.de)

Projektmitarbeiter: Dr. Ribu Cherian (ribu.cherian@uni-leipzig.de)

Projektbeginn: 2017
Projektende: 2020

Beschreibung
Aerosol-Wolken-Wechselwirkungen stellen einen der wesentlichen Unsicherheitsfaktoren bei Verständnis und Quantifizierung der geographischen Verteilung von Wolken- und Niederschlagseigenschaften, aber auch des Strahlungsantriebs des globalen Klimawandels dar. Die grundlegende Idee des Projekts ist es, regional unterschiedliche Trends in anthropogenenen Emissionen von Aerosolen zu nutzen, um deren Einfluss auf Trends in Wolken-, Niederschlags- und Strahlungsgrößen zu bestimmen. Hierzu sollen verschiedene Szenarien in Multi-Klimamodell-Ensembles ("historische" Simulationen mit allen Strahlungsantrieben und "Aerosol"-Simulationen mit allen Antrieben außer anthropogenem Aerosol) analysiert werden und mit Beobachtungsdaten verglichen werden. Konkret werden vier Fragen untersucht:
(i) Welche Beziehung besteht zwischen regionalen Trends in Aerosolemissionen und Wolken-Strahlungs-Effekten? - Diese Studien analysieren Simulationen aus dem Multi-Modell-Ensemble.
(ii) Wie erfolgreich reproduzieren die Modelle beobachtete Trends? Hier werden die Klimamodelle mit Beobachtungsdaten verglichen.
(iii) Welchen Einfluss haben Emissionstrends für Aerosole und resultierende Strahlungsantriebe auf die atmosphärische Zirkulation? Simulationen mit dem Aerosol-Klima-Modell ECHAM6-HAM2 sollen für drei Zeitscheiben durchgeführt und analysiert werden.
(iv) Welche Rolle spielen Emissionstrends für Änderungen in Extremniederschlägen in Südost-Asien? - Mit speziellen Simulationen sollen die verschiedenen Hypothesen getestet werden.

Weiterführung: ja

Mittelgeber: Deutsche Forschungsgemeinschaft (DFG) (Eigene Stelle)
****

Hochatmosphäre, Christoph Jacobi
Upper Atmosphere

Untersuchung der Anregungsmechanismen der 8-stündigen solaren Gezeiten in der mittleren Atmosphäre
Analysis of forcing mechanisms of the terdiurnal tide in the middle atmosphere

Schlagworte: Mittlere Atmosphäre, Gezeiten, Wellen

Projektleiter:
Prof. Dr. Christoph Jacobi (jacobi @ rz.uni-leipzig.de)

Projektmitarbeiter:
F. Lilienthal

Projektbeginn: 1.1.2014
Projektende: 1.9.2018

Beschreibung
Ein nichtlineares mechanistisches Zirkulationsmodell der mittleren Atmosphäre wird verwendet, um die Anregungsmechanismen der 8-stündigen Gezeiten in der mittleren Atmosphäre zu untersuchen. Das verwendete Modell MUAM (Middle and Upper Atmosphere Model) verfügt über Strahlungsroutinen zur selbstkonsistenten Anregung von Gezeiten. Zur Analyse der Gezeitenanregung werden im Modell die potenziellen Anregungsmechanismen einzeln und gemeinsam abgeschaltet. Die zu untersuchenden Anregungsmechanismen sind einerseits die direkte Anregung durch die 8-stündige Komponente im Strahlungsantrieb und andererseits die nichtlineare Wechselwirkung der ganz- und halbtägigen Gezeiten, repräsentiert in den Advektionstermen der Bewegungsgleichungen. Durch Vergleich mit Referenzläufen mit vollständiger Gezeitenanregung wird es möglich sein, die Anteile der jeweiligen Anregungsmechanismen am gesamten Wellenantrieb zu bestimmen. Die Arbeiten werden komplettiert durch Analyse von Radar- und Satellitendaten.

Weiterführung: ja

Mittelgeber: Deutsche Forschungsgemeinschaft (DFG JA 836/30-1)
****

Analyse globaler Felder
Analysis of global fields

Schlagworte: Quasi 2-jährige Schwingung, planetare Wellen, Polarwirbel

Projektleiter:
Prof. Dr. Christoph Jacobi (jacobi @ rz.uni-leipzig.de)

Projektmitarbeiter:
-

Projektbeginn: 1.9.2016
Projektende: 31.8.2017

Beschreibung
Innerhalb des Projekts sollen dynamische und chemische Parameter der Troposphäre und Stratosphäre anhand von Reanalysedaten untersucht werden. Dabei sollen einerseits die Verteilungen meteorologischer Größen in Abhängigkeit der äquatorialen stratosphärischen quasi 2-jährigen Schwingung (QBO) untersucht werden, andererseits ein Schwerpunkt auf den arktischen Polarwirbel gelegt werden um dessen Tiefe und Dauer in Abhängigkeit planetarer Wellenaktivität zu untersuchen. Diese Arbeiten sollen mehr Einsicht in die dynamischen

Zusammenhänge der unteren und mittleren Atmosphäre ermöglichen. Die Arbeiten werden innerhalb zweier Masterarbeiten an der Russischen Staatlichen Hydrometeorogischen Universität (RSHU), Abteilung Meteorologische Vorhersagen, St. Petersburg, durchgeführt. Das Projekt umfasst weiterhin je einen einmonatigen Besuch der Stipendiatinnen in Leipzig.

Weiterführung: nein

Mittelgeber: DAAD (Leonhard Euler, 57290950)

****

Dynamik der mittleren Atmosphäre (RSHU)

Dynamics of the middle atmosphere (RSHU)

Schlagworte: Mittlere Atmosphäre, Reanalyse, empirische Modelle

Projektleiter:
Prof. Dr. Christoph Jacobi (jacobi @ rz.uni-leipzig.de)

Projektmitarbeiter:
-

Projektbeginn: 1.9.2017
Projektende: 31.8.2018

Beschreibung
Innerhalb des Projekts sollen globale Daten empirischer Modelle und meteorologischer Reanalysen, als auch regionale Radardaten umfassend untersucht werden. Dabei sollen globale Reanalyse-Datensätze verwendet werden, um empirische Modelle des Windes der mittleren Atmosphäre zu validieren. Die Arbeiten werden innerhalb einer Masterarbeit an der Russischen Staatlichen Hydrometeorogischen Universität (RSHU), Abteilung Meteorologische Vorhersagen, St. Petersburg, durchgeführt. Das Projekt umfasst weiterhin einen einmonatigen Besuch einer Stipendiatin in Leipzig.

Weiterführung: ja

Mittelgeber: DAAD (Leonhard Euler, 57375423)

****

Large-scale dynamical impacts on regional Arctic climate change
Der Einfluss großräumiger Dynamik auf regionale arktische Klimaänderungen

Schlagworte: Arktische Verstärkung, Klimavariabilität

Projektleiter:
Prof. Dr. Christoph Jacobi (jacobi @ rz.uni-leipzig.de), Prof. Dr. Johannes Quaas (johannes.quaas @ uni-leipzig.de)

Projektmitarbeiter: Daniel Mewes

Projektbeginn: 1.1.2016
Projektende: 31.12.2019

Beschreibung
Das Projekt umfasst die Wechselwirkung zwischen der variablen großskaligen Zirkulation und regionalen arktischen Klimaänderungen und der Diagnose der arktischen Verstärkung auf regionaler Skala als Reaktion auf Variationen großskaliger Zirkulation in der Vergangenheit sowie in Klimaszenarien zukünftigen Klimwandels. Es werden hierzu Reanalysedaten und CMIP5-Modellergebnisse herangezogen. Die Kopplung von Troposphäre und Stratosphäre als wichtiger Bestandteil der Variabilität der polaren Atmosphäre wird auch mit numerischen Simulationen untersucht.

Weiterführung: ja

Mittelgeber: Deutsche Forschungsgemeinschaft, SFB-Transregio 172

Effeke lokalen Schwerewellenantriebs auf die mittlere Atmosphäre
Middle atmosphere effects of localized gravity wave forcing (MATELO)

Schlagworte: Schwerewellen, mittlere Atmosphäre, residuelle Zirkulation, Globale Navigationssatellitensysteme, planetare Wellen

Projektleiter:
Prof. Dr. Christoph Jacobi (jacobi @ rz.uni-leipzig.de)

Projektmitarbeiter:
N. Samtleben

Projektbeginn: 1.1.2017
Projektende: 31.12.2019

Beschreibung
Das Projekt beinhaltet eine Studie der Auswirkungen einer begrenzten Region erhöhter atmosphärischer interner Schwerewellenaktivität und Schwerewellenrechens auf die mittlere Atmosphäre. Die Charakteristik solch einer Region, ihre räumlich und zeitliche Variabilität und Verbindung zu anderen Klimaparametern wird anhand von GPS Radiookkultationsanalysen untersucht. Es werden Algorithmen zur dreidimensionalen Analyse der Wellenreibung und der Brewer-Dobson-Zirkulation (BDC) verwendet; als Datengrundlage dienen Simulationen mit einem mechanistischen Zirkulationsmodell der mittleren Atmosphäre und Reanalysedaten. Die dreidimensionaler Variabilität der BDC und die Rolle lokalisierter erhöhte Schwerewellenaktivität wird so untersucht. Weiterhin wird die Anregung und folgende Ausbreitung planetarer Wellen durch eine Region erhöhter Schwerewellenaktivität untersucht. Die Auswirkungen auf die Polarregionen (mittlere Zirkulation, Präkonditionierung, winterliche Stratosphärenerwärmungen) und auf die äquatoriale Stratosphäre (Einfluss auf Tropopausenbrüche und Stratosphäre-

Troposphäre-Austausch) werden untersucht. Weiterhin wird der Einfluss lokalisierten Schwerewellenbrechens auf die mittlere Zirkulation der Mesosphäre analysiert, insbesondere im Hinblick auf stationäre Wellen, und ihre Variabilität. Das Projekt ist eine Kooperation zwischen dem LIM und dem Department Atmosphärenphysik, Karls-Universität Prag.

Weiterführung: ja

Mittelgeber: Deutsche Forschungsgemeinschaft (DFG JA 836/32-1)

6-stündige Gezeiten in den mittleren Atmosphäre (QuarTA)
Quarterdiurnal tide in the middle atmosphere (QuarTA)

Schlagworte: mittlere Atmosphäre; Gezeiten; Ionosphäre

Projektleiter:
Prof. Dr. Christoph Jacobi (jacobi @ rz.uni-leipzig.de)

Projektmitarbeiter:
C. Geißler

Projektbeginn: 1.2.2017
Projektende: 31.1.2020

Beschreibung
Die Dynamik der Mesosphäre und unteren Thermosphäre wird zu großen Teilen von solaren Gezeiten dominiert. Eine davon ist die 6-stündige Gezeit (quarterdiurnal tide, QDT), die unter anderem in sporadischen E-Schichten und mit Hilfe von Radar- und Satellitenmessungen beobachtet wurde. Während allerdings die ganztägigen, halbtägigen, und auch 8-stündigen Gezeiten vergleichsweise gut dokumentiert und untersucht sind, sind Beobachtungen und Analysen der - weniger starken aber nichtsdestoweniger als ein Bestandteil der dynamischen Prozesse in ihrer Gesamtheit zu sehenden - 6-stündigen Komponente bislang selten. Um diese Lücke zu schließen, werden innerhalb des QuarTA-Projekts die 6-stündigen Gezeiten und ihre Antriebsmechanismen im Detail untersucht. Die Klimatologie der Gezeiten wir mit Hilfe von Meteorradarwindmessungen, vor allem der Langzeitreihe in Collm, ergänzt durch weitere Radarmessungen, erstellt. Die globale Verteilung der Gezeitenamplituden wird mit Hilfe von Ionosonden- und GPS-Radiookkultationsmessungen sporadischer E-Schichten untersucht, und die Beobachtungen in Verbindung mit Windscherungen aus Radarmessungen und numerischen Simulationen interpretiert. Um Einblick in die hauptsächlichen Anregungsmechanismen der 6-stündigen Gezeiten zu erhalten, wird ein nichtlineares mechanistisches Zirkulationsmodell, welches auch die Anregung durch Absorption solarer Strahlung enthält, verwendet. Hierbei wird, einzeln und in Kombination, die Anregung der 6-stündigen Gezeit durch Absorption solarer Strahlung und durch nichtlineare Wechselwirkung von Gezeiten in den Simulationen ausgeschaltet, so dass die Hauptantriebsquelle erkennbar wird. Innerhalb des QuarTA-Projekts wird daher, durch die Kombination von Beobachtungen und Modellsimulationen, ein vertiefter Einblick in die Klimatologie und die Anregung der 6-stündigen Gezeiten ermöglicht, der bislang noch nicht in ausreichendem Maße gegeben ist.

Weiterführung: ja

Mittelgeber: Deutsche Forschungsgemeinschaft (DFG JA 836/34-1)

Verzögerte Antwort der Ionosphäre auf Variationen des solaren EUV (DRIVAR)
Delayed response of the ionosphere to solar EUV variability (DRIVAR)

Schlagworte: Ionosphäre, solare Variabilität

Projektleiter:
Prof. Dr. Christoph Jacobi (jacobi @ rz.uni-leipzig.de)

Projektmitarbeiter:
R. Vaishnav

Projektbeginn: 1.5.2017
Projektende: 30.4.2020

Beschreibung

Weiterführung: ja

Mittelgeber: Deutsche Forschungsgemeinschaft (DFG JA 836/33-1)

Allgemeine Meteorologie
AG Akustik
Acoustics

Lärm- und Feldlagerschutz der Bundeswehr
Noise protection of Bundeswehr

Schlagworte: Lärmschutz, Schallklima

Projektleiter:
Dr. A. Raabe (raabe@uni-leipzig.de)

Projektmitarbeiter:
Dipl. Met. Michael Wilsdorf (mwils@uni-leipzig.de)

Projektbeginn: 01.06.2017
Projektende: 31.05.2018

Beschreibung
Die Bewertung von Schallimmissionen, deren Quellen sich in großen Entfernungen (bis zu 15km), aber auch in der näheren Umgebung (weniger als 5km) von Truppenübungsplätzen, oder auch Feldlagern der Bundeswehr befinden, ist ohne Berücksichtigung der aktuellen Wettersituation

nicht möglich. Das heißt, dass die Ausbreitung akustischer Signale über mehrere Kilometer Entfernung wesentlich von der Temperatur- und Windvektorverteilung in dem Teil der Atmosphäre abhängen, durch den sich die Schallwellen ausbreiten. Die bisherige Vorgehensweise bei der Beachtung atmosphärischer Verhältnisse im Zusammenhang mit Schallimmissionen basiert im Wesentlichen auf der Verwendung von Radiosondendaten. Ihr Nachteil besteht darin, dass meist nur wenige Radiosondenaufstiege am Tag (meist 2x) durchgeführt werden und (weltweit) sich nur wenige Stationen über ein riesiges Gebiet verteilen. Deshalb wird der Frage nachgegangen ob Wetter-Modelldaten die Radiosondendaten auf eine solche Weise ersetzen können, dass die auf Basis der Modelldaten abgeleiteten Aussagen bezogen auf die Schallimmissionsverhältnisse weitgehend identisch bleiben.

Weiterführung: Ja

Mittelgeber: BMVg,AGeoBw; M/U2CD/CA277/CA647

Allgemeine Meteorologie

Analyse zur Beziehung zwischen Regenmengenprognose und Regenmengenbeobachtung
Analysis of the relationship between rainfall forecast and rainfall observation

Dr. A. Raabe (raabe@uni-leipzig.de), MSC Johanna Redelstein

Die Schutzmaßnahmen bei Starkregenereignissen, die durch die Landestalsperrenverwaltung Sachsen (LTV) eingeleitet werden, z.B. Talsperrenvorentlastungen, basieren auf den Starkregen- bzw. Niederschlagswarnungen des Deutschen Wetterdienstes (DWD).
In der Öffentlichkeit werden solche Schutzmaßnahmen immer hinterfragt.
Die gefühlte öffentliche Meinung ist, dass die Maßnahmen oft nur unzureichend den erhaltenen Informationen entsprechen oder zu spät eingeleitet wurden.
In diesem Zusammenhang fällt auf, dass es derzeit keine explizite Untersuchung (Für das Gebiet von Sachsen) gibt, die eine Beziehung zwischen den zu einem Vorwarnzeitpunkt verfügbaren meteorologischen Daten (Beobachtung / Prognose) und den daraus folgenden DWD-Warnungen auf der einen Seite und die darauf folgenden wasserwirtschaftlichen Maßnahmen darstellt.
Hier wird der Frage nachgegangen: Wie stellt sich die Korrelation zwischen den tatsächlichen Beobachtungen / Reanalysedaten RADOLAN und den durch DWD an die LTV übergeben Regenmengenprognosen (auf Basis von Quantilen) dar.
Ziel ist es auch für diese Aussagenkombinationen einen Vorhersagezeitpunkt zu ermitteln, der optimal für die wasserwirtschaftliche Entscheidungen ist.

The protective measures of heavy rainfall events initiated by the Landestalsperrenverwaltung Sachsen (LTV), are based on the heavy rainfall and precipitation warnings of the German Weather Service (DWD). In public, such protective measures are always questioned.
Here, the quality of the rainfall forecast is compared with rainfall observations depending on the forecast period. The statements then refer to the territory of the Ore Mountains

Weiterführung: Nein

Finanzierung: Landestalsperrenverwaltung Sachsen LIM-LTV-2321-01217

Fakultät für Physik und Geowissenschaften

Institut für Meteorologie, Stephanstr. 3, 04103 Leipzig

Forschungsbericht 2017

3. Weitere Angaben

3.1 KOOPERATION

Instituto de Pesquisa da Amazônia (INPA), Instituto de Pesquisas Espaciais (INPE), Sao Paulo, Brasilien "Aerosol, Cloud, Precipitation, and Radiation Interactions and Dynamics of Convective Cloud Systems (ACRIDICON)"

Staatliche Russische Hydrometeorologische Universität, St. Petersburg, Prof. Alexander Pogoreltsev: Projekte „Analyse globaler Felder" und „Dynamik der mittleren Atmosphäre (RSHU)"

Universidad Austral, Buenos Aires, Argentinien, Prof. Alejandro de la Torre: „Atmospheric Gravity Waves: Observations and Modeling" (BMBF 01DN14001)

University of Colorado at Boulder, CIRES, Dr. Ostashev; "Acoustic tomography of the atmosphere at the Boulder Atmospheric Observatory"

University of Basilicata, Potenza, Italien, P. di Girolamo: "Kalibration von Raman-Lidar-Wasserdampfprofilen mittels Mikrowellenradiometer"

Universität Innsbruck, Österreich: „Temperaturprofile in einem Alpental aus Mikrowellenradiometer-Beobachtungen"

University of Reading, UK, A. Illingworth: "COST-Aktion TOPROF"

MeteoSchweiz, Payerne, Schweiz, A. Haefele: "Kombinierte Temperatur- und Feuchteprofile mit Mikrowellenradiometer und Raman-Lidar"

University of Reading, N. Bellouin und K. Shine, COPERNICUS-Projekt

CICERO Oslo, G. Myhre: COPERNIUS

University of Leeds, P. Forster, K. Carslaw, COPERNICUS

LMD/CNRS Paris, O. Boucher, COPERNICUS

Hebrew University of Jerusalem, D. Rosenfeld: ACPC initiative

University of Oxford, P. Stier: gemeinsamer Workshop

3.2 GREMIUM MITGLIEDSCHAFT

Prof. Dr. Manfred Wendisch:

- Mitglied des Wissenschaftlichen Beirats des Leibniz-Instituts für Troposphärenforschung (TROPOS) Leipzig, seit 2012 stellvertretender Vorsitzender.
- Ordentliches Mitglied der Sächsischen Akademie der Wissenschaften
- Mitglied des Präsidiums der Sächsischen Akademie der Wissenschaften
- Mitglied im Vorstand der Meteorologischen Gesellschaft, Sektion Mitteldeutschland
- Gewähltes Mitglied im IRC (Internationale Strahlungskommission) innerhalb von IAMAS
- Koordinator Expert Working Groups innerhalb von EUFAR (European Facility for Airborne Research)
- Mitglied des „User Group Selection Panel" (UGSP) innerhalb von EUFAR
- Koordinator des DFG-SPP (Schwerpunktprogramm) 1294 zu HALO (High Altitude and Long Range Research Aircraft), gemeinsam mit Prof. J. Curtius (Uni Frankfurt am Main) und Mirko Scheinert (TU Dresden)
- Vize-Sprecher der „Leibniz-Graduate School on Clouds, Aerosols, and Radiation (LGS-CAR)"
- Mitglied des Gutachtergremiums für Atmosphärenwissenschaften der Finnländischen Akademie der Wissenschaften
- Mitglied des Wissenschaftlichen Beirats des Deutschen Wetterdienstes (DWD)
- Mitglied des Programmrates „Hans-Ertel-Zentrum für Wetterforschung (HErZ)" des DWD

- Stellvertretender Vorsitzender des wissenschaftlichen Lenkungsausschusses (WLA) für HALO (High Altitude and Long Range Research Aircraft)
- Sprecher des Sonderforschungsbereiches SFB-Transregio 172: "Arktische Verstärkung: Klimarelevante Atmosphären- und Oberflächenprozesse, und Rückkopplungsmechanismen (AC)[3]"
- Koordinator des YOPP (Year of Polar Prediction) Task Teams zu Flugzeuggetragenen Messplattformen
- Mitglied des Steuerungskommittees für MOSAiC (**M**ultidisciplinary drifting **O**bservatory for the **S**tudy of **A**rcti**c** **C**limate), Team Koordinator für Flugzeugoperation
- Mitglied DFG-Senatskommission für Erdsystemforschung

Prof. Dr. Johannes Quaas:
- Co-chair, Aerosols, Clouds, Precipitation and Climate (gemeinsame Aktivität des IGBP/iLEAPS und WCRP/GEWEX; Mitglied des wissenschaftlichen Lenkungsausschusses seit 2010; Co-Chair seit 2013)
- Mitglied der International Commission on Clouds and Precipitation (IAMAS-ICCP), 2008-2016
- Mitglied des Leibniz-Instituts für Troposphärenforschung e.V. (TROPOS)
- Mitglied des Wissenschaftlichen Beirats des Leibniz-Instituts für Troposphärenforschung (TROPOS)

Prof. Dr. Christoph Jacobi:

Mitglied im Vorstand der Meteorologischen Gesellschaft, Sektion Mitteldeutschland
-Stellv. Leiter der Division II „Aeronomic Phenomena" der IAGA
-Leiter der Arbeitsgruppe II-D der IAGA: „External Forcing of the Middle Atmosphere"
-Vorsitzender der Mitgliederversammlung des TROPOS

Dr. A. Raabe:
-Vorsitzender der Deutschen Meteorologischen Gesellschaft e.V., Sektion Mitteldeutschland
-Mitglied Sektorkomitee Erneuerbare Energien bei Deutsche Akkreditierungsstelle (DAkkS) des BMWiuT,

Dr. M. Salzmann
-Annales Geophysicae Co-Editor

3.3 Mitgliedschaften in Redaktionskollegien, Herausgebergremien

Prof. Dr. Manfred Wendisch:
Atmos. Meas. Tech. Co-Editor
Meteorologische Zeitschrift Co-Editor
Herausgeber: Wiss. Mitt. Inst. f. Meteorol. Univ. Leipzig

Prof. Dr. Christoph Jacobi:
Annales Geophysicae Editor-in-Chief
Mitteilungen der DMG Mitglied Redaktionsteam

Prof. Dr. Johannes Quaas
Atmos. Chem. Phys. Co-Editor

Dr. A. Raabe:
Herausgeber: Wiss. Mitt. Inst. f. Meteorol. Univ. Leipzig
Koordinator DMG e.V. Meteorologische Zeitschrift

3.4 VERANSTALTUNEN

Workshop "Aerosols, clouds, precipitation and climate" (Funding from W. E. Heraeus foundation), Bad Honnef, 2. - 6. April 2017
Workshop "Liability and regulation of climate engineering", Funded by Priority Programme "Climate engineering - risks, challenges, opportunities?", Kiel, 16. - 18. Oktober 2017
Session "Radar-driven Advances in Understanding and Modeling Clouds and Precipitation", AGU Fall meeting, New Orleans, USA, 11. - 15. Dezember 2017

Publikationen LIM 2017

Autor_Name	Vorname	weitere Autoren	Titel	ID, DOI Publikationsort
Araújo	Luciana	.M. Lima, Ch. Jacobi, P.P. Batista	Quasi-biennial oscillation signatures in the diurnal tidal winds over Cachoeira Paulista, Brazil	https://doi.org/10.1016/j.jastp.2017.02.001 J. Atmos. Sol.-Terr. Phys., 155, 71-78
Bony	Sandrine	B. Stevens, F. Ament, S. Bigorre, P. Chazette, S. Crewell, J. Delanoë, K. Emanuel, D. Farrell, C. Flamant, S. Gross, L. Hirsch, J. Karstensen, B. Mayer, L. Nuijens, J. H. Ruppert Jr., I. Sandu, P. Siebesma, S. Speich, F. Szczap, J. Totems, R. Vogel, M. Wendisch, and M. Wirth	EUREC4A: A Field Campaign to Elucidate the Couplings Between Clouds, Convection and Circulation	doi:10.1007/s10712-017-9428-0 Surv. Geophys., 1573-0956 (2017)
Braga	Ramon	D. Rosenfeld, R. Weigel, T. Jurkat, M. Andreae, M. Wendisch, M. Pöhlker, T. Klimach, U. Pöschl, C. Pöhlker, C. Voigt, C. Mahnke, S. Borrmann, R. Albrecht, S. Molleker, D. Vila, L. Machado, and P. Artaxo	Comparing parameterized versus measured microphysical properties of tropical convective cloud bases during the ACRIDICON–CHUVA campaign	doi:10.5194/acp-17-7365-2017 Atmos. Chem. Phys., 17 (2017), 7365-7386
Braga	Ramon	Rosenfeld, D., Weigel, R., Jurkat, T., Andreae, M. O., Wendisch, M., Pöschl, U., Voigt, C., Mahnke, C., Borrmann, S., Albrecht, R. I., Molleker, S., Vila, D. A., Machado, L. A. T., and Grulich, L.	Further evidence for CCN aerosol concentrations determining the height of warm rain and ice initiation in convective clouds over the Amazon basin	doi:10.5194/acp-17-14433-2017 Atmos. Chem. Phys., 17 (2017), 14433-14456
Bühl	Johannes	S. Alexander, S. Crewell, A. Heymsfield, H. Kalesse, A. Khain, M. Maahn, K. Van Tricht, and M. Wendisch	Ice Formation and Evolution in Clouds and Precipitation: Measurement and Modeling Challenges. Chapter 10: Remote Sensing.	doi:10.1175/AMSMONOGRAPHS-D-16-0015.1 Meteorological Monographs, 58 (2017), 10.1–10.21

Carlsen	Tim	Birnbaum, G., Ehrlich, A., Freitag, J., Heygster, G., Istomina, L., Kipfstuhl, S., Orsi, A., Schäfer, M., and, M. Wendisch	Comparison of different methods to retrieve optical-equivalent snow grain size in central Antarctica	doi:10.5194/tc-11-2727-2017 The Cryosphere, 11 (2017), 2727-2741
Cecchini	M. A.	Machado, L. A. T., Wendisch, M., Costa, A., Krämer, M., Andreae, M. O., Afchine, A., Albrecht, R. I., Artaxo, P., Borrmann, S., Fütterer, D., Klimach, T., Mahnke, C., Martin, S. T., Minikin, A., Molleker, S., Pardo, L. H., Pöhlker, C., Pöhlker, M. L., Pöschl, U., Rosenfeld, D., and Weinzierl, B.	Illustration of microphysical processes in Amazonian deep convective clouds in the gamma phase space: introduction and potential applications	doi:10.5194/acp-17-14727-2017 Atmos. Chem. Phys., 17 (2017), 14727-14746
Cecchini	M. A.	L. A. T. Machado, M. O. Andreae, S. T. Martin, R. I. Albrecht, P. Artaxo, H. M. J. Barbosa, S. Borrmann, D. Fütterer, T. Jurkat, C. Mahnke, A. Minikin, S. Molleker, M. L. Pöhlker, U. Pöschl, D. Rosenfeld, C. Voigt, B. Weinzierl, and M. Wendisch	Sensitivities of Amazonian clouds to aerosols and updraft speed	doi:10.5194/acp-17-10037-2017 Atmos. Chem. Phys. , 17 (2017), 10037-10050
Cherian	Ribu	J. Quaas, M. Salzmann, and L. Tomassini	Black carbon indirect radiative effects in a climate model	10.1080/16000889.2017.1369342 Tellus, 69, 1369342
Costa	Anja	Meyer, J., Afchine, A., Luebke, A., Günther, G., Dorsey, J. R., Gallagher, M. W., Ehrlich, A., Wendisch, M., Baumgardner, D., Wex, H., and Krämer, M.	Classification of Arctic, midlatitude and tropical clouds in the mixed-phase temperature regime	doi:10.5194/acp-17-12219-2017 Atmos. Chem. Phys., 17 (2017), 12219-12238
Dipu	Sudhakar	J. Quaas, R. Wolke, J. Stoll, A. Muhlbauer, M. Salzmann, B. Heinold, and Ina Tegen	Implementation of aerosol–cloud interactions in the regional atmosphere-aerosol model COSMO-MUSCAT and evaluation using satellite data	10.5194/gmd-10-2231-2017 Geosci. Model Devel., 10, 2231-2246
Ehrlich	André	Bierwirth, E., Istomina, L., and Wendisch, M.	Combined retrieval of Arctic liquid water cloud and surface snow properties using airborne spectral solar remote sensing	doi:10.5194/amt-10-3215-2017 Atmos. Meas. Tech., 10 (2017), 3215-3230
Gryspeerdt,	Edward	J. Quaas, S. Ferrachat, A. Gettelman, S. Ghan, U. Lohmann, H. Morrison, D. Neubauer, D. G. Partridge, P. Stier, T. Takemura, Hailong Wang, M. Wang, and K. Zhang	Constraining the instantaneous aerosol influence on cloud albedo	10.1073/pnas.1617765114 Proc. Nat. Acad. Sci. USA, 119, 4899-4904

Heinze	Rieke	A. Dipankar, C. Carbajal Henken, C. Moseley, O. Sourdeval, S. Trömel, X. Xie, P. Adamidis, F. Ament, H. Baars, C. Barthlott, A. Behrendt, U. Blahak, S. Bley, Slavko Brdar, M. Brueck, Susanne Crewell, H. Deneke, P. Di Girolamo, R. Evaristo, J. Fischer, C. Frank, P. Friederichs, T. Göcke, K. Gorges, L. Hande, M. Hanke, A. Hansen, H.-C. Hege, C. Hoose, T. Jahns, N. Kalthoff, D. Klocke, S. Kneifel, P. Knippertz, A. Kuhn, T. Laar, Andreas Macke, V. Maurer, B. Mayer, C. I. Meyer, S. K. Muppa, R. A. J. Neggers, E. Orlandi, F. Pantillon, B. Pospichal, N. Röber, L. Scheck, A. Seifert, P. Seifert, F. Senf, P. Siligam, C. Simmer, S. Steinke, B. Stevens, K. Wapler, M. Weniger, V. Wulfmeyer, G. Zängl, D. Zhang, and J. Quaas	Large-eddy simulations over Germany using ICON: A comprehensive evaluation	10.1002/qj.2947 Quart. J. Roy. Meteorol. Soc., 143, 69-100
Heyn	Irene	K. Block, J. Mülmenstädt, Edward Gryspeerdt, P. Kühne, M. Salzmann, and J. Quaas	Assessment of simulated aerosol effective radiative forcings in the terrestrial spectrum	10.1002/2016GL071975 Geophys. Res. Lett., 44, 1001-1007
Heyn	Irene	M. Salzmann, J. Quaas, and J. Mülmenstädt	Effects of diabatic and adiabatic processes on relative humidity in a GCM, and relationship between mid-tropospheric vertical wind and cloud-forming and cloud-dissipating processes	10.1080/16000870.2016.1272753 Tellus, 69, 1272753
Holstein	Peter	A. Raabe, N. Bader, A. Tharandt, M. Barth, H.-J. Münch	Energetische Probleme und akustische Verfahren	In B. Weller, S. Horn Hrsg., Denkmal und Energie – 2017, Springer Vieweg, 189-199
Jacobi	Christoph	T. Ermakova, D. Mewes, A.I. Pogoreltsev	El Niño influence on the mesosphere/lower thermosphere circulation at midlatitudes as seen by a VHF meteor radar at Collm (51.3°N, 13°E)	https://doi.org/10.5194/ars-15-199-2017 Adv. Radio Sci., 15, 199-206

Jacobi	Christoph	A. Krug, E. Merzlyakov	Radar observations of the quarterdiurnal tide at midlatitudes: Seasonal and long-term variations	https://doi.org/10.1016/j.jastp.2017.05.014 J. Atmos. Sol.-Terr. Phys. , 163, 70-77
Jäkel	Evelyn	Wendisch, M., Krisna, T. C., Ewald, F., Kölling, T., Jurkat, T., Voigt, C., Cecchini, M. A., Machado, L. A. T., Afchine, A., Costa, A., Krämer, M., Andreae, M. O., Pöschl, U., Rosenfeld, D., and Yuan, T.	Vertical distribution of the particle phase in tropical deep convective clouds as derived from cloud-side reflected solar radiation measurements	doi:10.5194/acp-17-9049-2017 Atmos. Chem. Phys., 17 (2017), 9049-9066
Jing,	Xianwen,	K. Suzuki, H. Guo, D Goto, Tomoo Ogura, Tsuyoshi Koshiro, and J. Mülmenstädt	A multimodel study on warm precipitation biases in global models compared to satellite observations	10.1002/2017JD027310 J. Geophys. Res., 122, 11806--11824
Klingebiel	Marcus	Ehrlich, A., Finger, F., Röschenthaler, T., Jakirlic, S., Voigt, M., Müller, S., Maser, R., Wendisch, M., Hoor, P., Spichtinger, P., and Borrmann, S.	A tandem approach for collocated measurements of microphysical and radiative cirrus properties	doi:10.5194/amt-10-3485-2017 Atmos. Meas. Tech., 10 (2017), 3485-3498
Korolev	Alexander	G. McFarquhar, P.R. Field, C. Franklin, P. Lawson, Z. Wang, E. Williams, S.J. Abel, D. Axisa, S. Borrmann, J. Crosier, J. Fugal, M. Krämer, U. Lohmann, O. Schlenczek, and M. Wendisch	Ice Formation and Evolution in Clouds and Precipitation: Measurement and Modeling Challenges. Chapter 5: Mixed-phase clouds: progress and challenges.	doi:10.1175/AMSMONOGRAPHS-D-17-0001.1 Meteorological Monographs, 58 (2017), 5.1-5.50
Kretzschmar	Jan	M. Salzmann, J. Mülmenstädt, O. Boucher, and J. Quaas	Comment on ``Rethinking the lower bound on aerosol radiative forcing"	10.1175/JCLI-D-16-0668.1 J. Climate, 30, 6579-6584
Li	Li	Zheng, X., Li, Z., Dubovik, O., Chen, X. and Wendisch, M	Studying aerosol light scattering based on aspect ratio distribution observed by fluorescence microscope	doi:10.1364/OE.25.00A813 Opt. Express., 25 (2017), A813-A823
Lilienthal	Friederike	Ch. Jacobi, T. Schmidt, A. de la Torre, P. Alexander	On the influence of zonal gravity wave distributions on the Southern Hemisphere winter circulation	https://doi.org/:0.5194/angeo-35-785-2017 Ann. Geophys., 35, 785-798

Martin	S. T.	P. Artaxo, L. Machado, A.O. Manzi, R. A. F. Souza, C. Schumacher, J. Wang, T. Biscaro, J. Brito, A. Calheiros, K. Jardine, A. Medeiros, B. Portela, S. de Sá, K. Adachi, A.C. Aiken, R. Albrecht, L. Alexander, M.O. Andreae, H.M.J. Barbosa, P. Buseck, D. Chand, J.M. Comstock, D.A. Day, M. Dubey, J. Fan, J. Fast, G. Fisch, E. Fortner, S. Giangrande, M. Gilles, A.H. Goldstein, A. Guenther, J. Hubbe, M. Jensen, J.L. Jimenez, F.N. Keutsch, S. Kim, C. Kuang, A. Laskin, K. McKinney, F. Mei, M. Miller, R. Nascimento, T. Pauliquevis, M. Pekour, J. Peres, T. Petäjä, C. Pöhlker, U. Pöschl, L. Rizzo, B. Schmid, J.E. Shilling, M.A. Silva Dias, J.N. Smith, J.M. Tomlinson, J. Tóta, and M. Wendisch, and U. Schlink	The Green Ocean Amazon Experiment (GoAmazon2014/5) Observes pollution affecting gases, aerosols, clouds, and rainfall over the rain forest	doi:10.1175/BAMS-D-15-00221.1. Bull. Am. Meteorol. Soc., 98 (2017), 981-997
McCormack	John	K. Hoppel, D. Kuhl, R. de Wit, G. Stober, P. Espy, N. Baker, P. Brown, D. Fritts, C. Jacobi, D. Janches, N. Mitchell, B. Ruston, S. Swadley, K. Viner, T. Whitcomb, R. Hibbins	Comparison of mesospheric winds from a high-altitude meteorological analysis system and meteor radar observations during the boreal winters of 2009–2010 and 2012–2013	https://doi.org/10.1016/j.jastp.2016.12.007 J. Atmos. Sol.-Terr. Phys., 154, 132-166
Myhre	Gunnar	W. Aas, R. Cherian, W. Collins, G. Faluvegi, M. Flanner, P. Forster, Ø. Hodnebrog, Z. Klimont, J. Mülmenstädt, C. Lund Myhre, D. Olivié, M. Prather, J. Quaas, B. H. Samset, J. L. Schnell, M. Schulz, D. Shindell, R. B. Skeie, T. Takemura, and S Tsyro	Multi-model simulations of aerosol and ozone radiative forcing for the period 1990-2015	10.5194/acp-17-2709-2017 Atmos. Chem. Phys., 17, 2709-2720
Patel,	Piyshkumar	J. Quaas, and R. Kumar	A new statistical approach to improve the satellite based estimation of the radiative forcing by aerosol- cloud interactions	10.5194/acp-17-3687-2017 Atmos. Chem. Phys., 17, 3687-3698

Quaas	Martin	J. Quaas, W. Rickels, and O. Boucher	Are there good reasons against research into solar radiation management? - A model of intergenerational decision-making under uncertainty	10.1016/j.jeem.2017.02.002 J. Environ. Econ. Manage., 84, 1-17
Redelstein	**Johanna**	**A. Raabe:**	Statistische Analyse zur Güte der Niederschlagprognose für Wassereinzugsgebiete sächsischer Talsperren	Wiss. Mitteil. Inst. f. Meteorol., 55, S. 71-84
Rösch	Carolin	D. K. Wissenbach, U. Franck, M. Wendisch, and U. Schlink	Degradation of indoor limonene by outdoor ozone: A cascade of secondary organic aerosols	doi:10.1016/j.envpol.2017.04.030 Environ. Pollut., 226 (2017), 463-472
Salzmann	Marc		The polar amplification asymmetry: Role of antarctic surface height	10.5194/esd-8-323-2017 Earth Syst. Dynam., 8, 323--336
Schäfer	Michael	Bierwirth, E., Ehrlich, A., Jäkel, E., Werner, F., and Wendisch, M.	Directional, horizontal inhomogeneities of cloud optical thickness fields retrieved from ground-based and airbornespectral imaging	doi:10.5194/acp-17-2359-2017 Atmos. Chem. Phys. 17 (2017), 2359-2372
Schnitt	Sabrina	E. Orlandi, M. Mech, A. Ehrlich, and S. Crewell	Characterization of water vapor and clouds during the Next-generation Aircraft Remote-sensing for VALidation (NARVAL)-south studies	doi:10.1109/JSTARS.2017.2687943 IEEE JSTARS, 99 (2017), 1-11
Stober	Gunter	V. Matthias, Ch. Jacobi, S. Wilhelm, J. Höffner, J.L. Chau	Exceptionally strong summer-like zonal wind reversal in the upper mesosphere during winter 2015/16	https://doi.org/10.5194/angeo-35-711-2017 Ann. Geophys., 35, 785-798
Smith	Steve	G. Stober, Ch. Jacobi, J.L. Chau, M. Gerding, M.G. Mlynczak, J.M. Russell, J.L. Baumgardner, M. Mendillo, M. Lazzarin, U. Gabriel	Characterization of a double mesospheric bore over Europe	https://doi.org/10.1002/2017JA024225 J. Geophys. Res.: Space Physics, 122, 9738–9750

Tshushima	**Yoko**	**F. Brient, S. A. Klein, D. Konsta, C. Nam, X. Qu, K. D. Williams, S. C. Sherwood, K. Suzuki, and M. D. Zelinka**	**The Cloud Feedback Model Intercomparison Project (CFMIP) Diagnostic Codes Catalogue - metrics, diagnostics and methodologies to evaluate, understand and improve the representation of clouds and cloud feedbacks in climate models**	**10.5194/gmd-2017-69 Geosci. Model Dev., 10**
Voigt	Christiane	U. Schumann, A. Minikin, A. Abdelmonem, A. Afchine, S. Borrmann, M. Boettcher, B. Buchholz, L. Bugliaro, A. Costa, J. Curtius, M. Dollner, A. Dörnbrack, V. Dreiling, V. Ebert, A. Ehrlich, A. Fix, L. Forster, F. Frank, D. Fütterer, A. Giez, K. Graf, J.-U. Grooß, S. Groß, K. Heimerl, B. Heinold, T. Hüneke, E. Järvinen, T. Jurkat, S. Kaufmann, M. Kenntner, M. Klingebiel, T. Klimach, R. Kohl, M. Krämer, T. C. Krisna, A. Luebke, B. Mayer, S. Mertes, S. Molleker, A. Petzold, K. Pfeilsticker, M. Port, M. Rapp, P. Reutter, C. Rolf, D. Rose, D. Sauer, A. Schäfler, R. Schlage, M. Schnaiter, J. Schneider, N. Spelten, P. Spichtinger, P. Stock, A. Walser, R. Weigel, B. Weinzierl, M. Wendisch, F. Werner, H. Wernli, M. Wirth, A. Zahn, H. Ziereis, and M. Zöger	ML-CIRRUS - The airborne experiment on natural cirrus and contrail cirrus with the high-altitude long-range research aircraft HALO	doi:10.1175/BAMS-D-15-00213.1 Bull. Am. Meteorol. Soc., 98 (2017),271-288
Wendisch	Manfred	M. Brückner, J. P. Burrows, S. Crewell, K. Dethloff, K. Ebell, Ch. Lüpkes, A. Macke, J. Notholt, J. Quaas, A. Rinke, and I. Tegen	ArctiC Amplification: Climate Relevant Atmospheric and SurfaCe Processes, and Feedback Mechanisms: (AC)3	doi:10.1029/2017EO064803 Eos, 98 (2017)
Wendich	Manfred	Marlen Brückner, John Burrows, Susanne Crewell, Klaus Dethloff, Kerstin Ebell, Christof Lüpkes, Andreas Macke, Justus Notholt, J. Quaas, Annette Rinke, and Ina Tegen	The Arctic Amplifier - Novel Science Planned in a New German Research Initiative	10.1029/2017EO064803 EOS, 98

Wendisch	Manfred,	Raabe A.,	Turbulent Diffusion in the Atmosphere	in: *A. Bunde, J. Caro, J. Kärger, G. Vogl (Eds.):* Diffusive Spreading in Nature, Technology and Society, Springer Vlg. 115-125
Wolf	Kevin	A. Ehrlich, T. Hüneke, K. Pfeilsticker, F. Werner, M. Wirth, and, M. Wendisch	Potential of remote sensing of cirrus optical thickness by airborne spectral radiance measurements at different sideward viewing angles	doi:10.5194/acp-17-4283-2017 Atmos. Chem. Phys., 17 (2017), 4283-4303

4. Mitarbeiter am LIM 2017

Name	E-Mail-Adresse
Block, Karoline	karoline.block@uni-leipzig.de
Brückner, Marlen	m.brueckner@uni-leipzig.de
Can, Özge	oezge.can@tropos.de
Carlsen, Tim	tim.carlsen@uni-leipzig.de
Cherian, Ribu	ribu.cherian@uni-leipzig.de
Donth, Tobias	tobias.donth@uni-leipzig.de
Ehrlich, André	a.ehrlich@uni-leipzig.de
Feck-Yao, Wolfgang	feckyao@uni-leipzig.de
Foth, Andreas	andreas.foth@uni-leipzig.de
Geißler, Christoph	christoph.geissler@uni-leipzig.de
Goren, Tom	tom.goren@uni-leipzig.de
Gottschalk, Matthias	matthias.gottschalk@uni-leipzig.de
Hirsch, Kerstin	khirsch@uni-leipzig.de
Jacobi, Christoph	jacobi@rz.uni-leipzig.de
Jäkel, Evelyn	evi.jaekel@uni-leipzig.de
Kaiser, Falk	fkaiser@rz.uni-leipzig.de
Krisna, Trismono Candra	trismono_candra.krisna@uni-leipzig.de
Kretzschmar, Jan	jan.kretzschmar@uni-leipzig.de
Lauermann, Felix	felix.lauermann@uni-leipzig.de
Lindemann, Simone	simone.lindemann@uni-leipzig.de
Mendes de Barros, Kátja	katia.mendes_de_barros@uni-leipzig.de
Mewes, Daniel	daniel.mewes@uni-leipzig.de
Mülmenstädt, Johannes	johannes.muelmenstaedt@uni-leipzig.de
Nam, Christine	christine.nam@uni-leipzig.de
Nitzsche, Gunda	gunda.nitzsche@uni-leipzig.de
Quaas, Johannes	johannes.quaas@uni-leipzig.de
Quaas, Johannes	johannes.quaas@uni-leipzig.de
Raabe, Armin	raabe@uni-leipzig.de
Redelstein, Johanna	johanna.redelstein@uni-leipzig.de
Rehnert, Jutta	rehnert@uni-leipzig.de
Ruiz Donoso, Elena	elena.ruiz_donoso@uni-leipzig.de
Salzmann, Marc	marc.salzmann@uni-leipzig.de
Samtleben, Nadja	nadja.samtleben@uni-leipzig.de
Schäfer, Michael	michael.schaefer@uni-leipzig.de
Schmidt, Jörg	joerg.schmidt@uni-leipzig.de
Seydel, Birgit	birgit.seydel@uni-leipzig.de
Sourdeval, Odran	odran.sourdeval@uni-leipzig.de
Sudhakar, Dipu	dipu.sudhakar@uni-leipzig.de
Sun, Bin	bin.sun@uni-leipzig.de
Stapf, Johannes	johannes.stapf@uni-leipzig.de
Vaishnav, Rajesh Ishwardas	rajesh_ishwardas.vaishnav@uni-leipzig.de
Weiße, Frank	weisse@uni-leipzig.de
Wendisch, Manfred	m.wendisch@uni-leipzig.de
Wendisch, Manfred	m.wendisch@uni-leipzig.de
Wilsdorf, Michael	mwils@uni-leipzig.de
Wolf, Kevin	kevin.wolf@uni-leipzig.de

5. Immatrikulationen am Institut f. Meteorologie

BSC Meteorologie

Datum	Semester	1.FS	2. FS	3.FS	4.FS	5.FS	6. FS	7.FS	8.FS	9. FS	10.FS	>10.FS	Meteo_BSC
Datum	Semester	BSC_FS1	BSC_FS2	BSC_FS3	BSC_FS4	BSC_FS5	BSC_FS6	BSC_FS7	BSC_FS8	BSC_FS9			Meteo_BSC
15.10.2017	WS 17/18	37		17		7		5					66
15.10.2016	WS 16/17	48		7		5		3					63
15.10.2015	WS 15/16	35		5		9		3					52
15.10.2014	WS 14/15	35		14		15		3		3		1	71
15.10.2013	WS 13/14	39		23		21		13		4			100
15.10.2012	WS 12/13	60		29	1	22	2	16	1	2			133
15.10.2011	WS 11/12	60		27		26	1	19		1			134
15.10.2010	WS 10/11	64		34		20							118
15.10.2009	WS 09/10	67	0	21	0	20	0						108
15.10.2008	WS 08/09	71	0	28	0	12							111
15.10.2007	WS 07/08	98	0	15									113
13.12.2006	WS 06/07	31											31

MSC Meteorologie

Datum	Semester	1.FS	2. FS	3.FS	4.FS	5.FS	6. FS
Datum	Semester	MSC_FS1	MSC_FS2	MSC_FS3	MSC_FS4	>MSC_FS5	Meteo_MSC
15.10.2017	WS 17/18	5		9		10	24
15.10.2016	WS 16/17	9		13		17	39
15.10.2015	WS 15/16	13		19		18	50
15.10.2014	WS 14/15	19		18		16	53
15.10.2013	Ws 13/14	18		16		20	54
15.10.2012	WS 12/13	18		20	1	15	54
15.10.2011	WS 11/12	21		17		10	48
15.10.2010	WS 10/11	20		9		5	34
15.10.2009	WS 09/10	11					11

Ausbildung Diplom-Meteorologie beendet

Diplom Meteorologie

Datum	Semester	1.FS	2. FS	3.FS	4.FS	5.FS	6. FS	7.FS	8.FS	9. FS	10.FS	>10.FS	Meteo_Diplom
15.10.2013	WS 13/14											2	2
17.10.2012	WS 12/13											3	3
16.10.2011	WS 11/12											3	3
15.10.2010	WS 10/11											14	14
15.10.2009	WS 09/10								0	14	0	7	21
15.10.2008	WS 08/09						0	14	0	23	1	25	63
15.10.2007	WS 07/08				0	22	0	26	1	18	2	19	88
13.12.2006	WS 06/07		0	40	0	36	0	24	2	14	1	17	175
15.10.2005	WS 05/06	109	0	49	0	30	2	16	1	17	1	13	237
08.12.2004	WS 04/05	97	0	35	1	20	0	19	0	12	1	15	200
03.12.2003	WS 03/04	68	1	25	0	20	1	13	1	12	1	13	155
14.10.2002	WS 02/03	45	0	19	0	16	0	15	1	12	1	9	118
06.12.2001	WS 01/02	43	0	21	0	16	0	13	0	7	0	5	105
07.12.2000	WS 00/01	41	1	27	0	22	0	8	0	6	1	6	112
01.12.1999	WS 99/00	40	0	24	0	9	0	9	0	6	1	6	95
16.12.1998	WS 98/99	36	0	11	0	17	1	9	1	5	0	8	88
10.11.1997	WS 97/98	29	0	17	0	10	1	8	0	7	0	4	76

6. Abschlussarbeiten Institut für Meteorologie 2017

Promotionen

Ying Chen
Abschluss: 10.07.2017
Evaluation and Improvement of Particle Number/Mass Size Distribution Modelling in WRF-Chem over Europe

Andreas Foth
Abschluss: 10.07.2017
Optimal Estimation of Water Vapour Profiles using a Combination of Raman Lidar and Microwave Radiometer

Daniel Merk
Abschluss: 24.04.2017
Uncertainties in the Quantification of Aerosol-Cloud Interactions

Stefanie Bauditz
Abschluss: 27.11.2017
Immersion freezing experiments of biological, mineral dust and dust-bio-mixed particles with the Leipzig Aerosol Cloud Interaction Simulator

Sebastian Bley
Abschluss: 23.10.2017
Investigation of warm convective cloud fields with Meteosat observations and high resolution models

Bachelor- Abschlussarbeiten:

Name / Vorname	Thema
Becker, Sebastian	Räumliche Variabilität der Schneekorngröße in der Antarktis und Vergleich mit Satellitenmessungen
Fauer, Felix	Influence of aerosols and greenhouse gases on time emergence of climate change signal in mean and extreme regional surface temperature
Linke, Olivia	Cloud Condensation Nuclei From Satellite Lidar Observations
Ohneiser, Kevin	Calibration of an Infrared, Multispectral All-Sky Camera and Verification of the Influence of Clouds on Thermal Radiation
Schreiner, Yannik	Simulation von Trends in der mittleren Atmosphäre
Wollschläger, Niels	Optimales Design von Monitoring-Netzen in der urbanen Atmosphäre

Master-Abschlussarbeiten

Bohlmann, Stephanie	Studying aerosol profiles with LIDAR over the Atlantic Ocean
Böhm, Christoph	Cloud-base height retrieval from multi-angle satellite data
Cheng, Hanmi	Simulation and Evaluation of the cloudd ice number concentration in global atmospheric model ECHAM6-HAM2
Cremer, Roxana	Covariance between large scale meteorology and cloud properties over the North East Atlantic Ocean
Doktorowski, Tobias	Improvement of the algorithmus for determining temperature profiles over the Atlantic
Faust, Matthias	Entwicklung eines Lagrangeschen Partikel Dispersions Modells zur Identifizierung von Geruchsquellen im Erzgebirge
Hörnig, Sabine	Evaluation and improvement of the Wegner-Bergeron-Findeisen Process in the ECHAMG
Jungandreas, Leonore	Radioactive-Convective equlibrium and organized convection - an observational perspective
Kaduk, Clara	Characterization of the optical properties of complex aerosol mixtures observed with a multiwavelenght-Raman-polarization lidar during the 6-weeks BACCHUS campaign in Cyprus in spring 2015
Kanngießer, Franz	Beobachtungen von Glorien über arktischen Grenzschichtwolken zur Identifikation der Wolkenphase und Ableitung deren Häufigkeit
Krug, Amelie	6h-Tides in the Mesosphere and Lower Thermosphere
Küchler, Tobias	Flüssigwasserwolken über dem Atlantischen Ozean, Kombination von satellitengetragener und schiffsgebundener Fernerkundung
Luttkus, Marie	Einfluss biogener Emissionen auf die Bildung von sekundärem organischem Aerosol (SOA)
Osterloh, Victoria	Analyzing temporal variability of meteorological and air quality records of Medellin, Colombia
Radenz, Martin	Observation of in-cloud vertical air motion with a combination of Doppler lidar, cloud radar and radar wind profiler - Results of the COLRAWI campaign
Redelstein, Johanna	Statistische Analyse zur Korrelation zwischen Warnzeitraum und Wetterprognose im Rahmen von Vorbeugemaßnahmen der Landestalsperrenverwaltung des Freistaates Sachsen
Rörup, Birte	Analysis of airborne Black Carbon measurements with the micro-Aethalometer AE51
Schubert, Jan	Multi-model-analysis of Artic climate trends
Tatzelt, Christian	Characterization of weather states over Germany using cloud-typing and textural features from satellite remote sensing
Ulrich, Max	Interactions of mineral Dust and tropical Storms on the North Atlantic
Villanueva Ortiz, Diego Santiago	Luftgetragene Ausbreitung von Infektionskrankheiten
Zimmer, Stefan	Variabilität des Niederschlags im Großraum Leipzig für den Zeitraum 1998 - 2015. Statistische Analyse stündlicher Stationsdaten unter Beachtung der Landnutzungsänderung sowie der RADOLAN-Daten des Deutschen Wetterdienstes

Wissenschaftliche Mitteilungen aus dem Institut für Meteorologie der Universität Leipzig

Band 1	*A. Raabe, G. Tetzlaff* und *W. Metz* (Edn.), 1995: Meteorologische Arbeiten aus Leipzig I
Band 2	*R. Devantier*, 1995: Wolkenbildungsprozesse über der südwestlichen Ostsee - Anwendungen eines neuen Wolkenschemas in einem mesoskaligen Modell
Band 3	*J. Laubach*, 1996: Charakterisierung des turbulenten Austausches von Wärme, Wasserdampf und Kohlendioxid über niedriger Vegetation anhand von Eddy-Korrelations-Messungen
Band 4	*A. Raabe* und *J. Heintzenberg* (Edn.), 1996: Meteorologische Arbeiten aus Leipzig II
Band 5	Wind- und Seegangsatlas für das Gebiet um Darß und Zingst *D. Hinneburg, A. Raabe* und *G. Tetzlaff*, 1997: Teil I: Windatlas
Band 6	*W. von Hoyningen-Huene* und *G. Tetzlaff* (Edn.), 1997: Sediment and Aerosol Teil I: Beiträge zur Alfred-Wegener-Konferenz, Leipzig 1997 Teil II: Aktuelle Beiträge aus dem Institut für Meteorologie
Band 7	*B.-R. Beckmann*, 1997: Veränderungen in der Windklimatologie und in der Häufigkeit von Sturmhochwassern an der Ostseeküste Mecklenburg-Vorpommerns
Band 8	*P. Posse*, 1997: Bestimmung klimarelevanter Parameter des maritimen Aerosols unter besonderer Berücksichtigung der Nichtkugelform realer Aerosolteilchen
Band 9	*A. Raabe, K. Arnold* und *J. Heintzenberg* (Edn.),1998: Meteorologische Arbeiten aus Leipzig III
Band 10	Wind- und Seegangsatlas für das Gebiet um Darß und Zingst, Teil II, 1998: *D. Hinneburg, A. Raabe* und *G. Tetzlaff*: Vergleich Windatlas –Beobachtungsdaten; *M. Börngen, H.-J. Schönfeldt, F. Riechmann, G. Panin* und *G. Tetzlaff:* Seegangsatlas; *M. Stephan* und *H.-J. Schönfeldt*: Sedimenttransportatlas
Band 11	*J. Rissmann, 1998*: Der Einfluss langwelliger Strahlungsprozesse auf das bodennahe Temperaturprofil
Band 12	*A. Raabe, K. Arnold* und *J. Heintzenberg* (Edn.), 1999*:*Meteorologische Arbeiten aus Leipzig IV
Band 13	*U. Müller, W. Kuttler und G. Tetzlaff (Edn.)*, 1999: Workshop Stadtklima 17. / 18. 02. 1999 in Leipzig
Band 14	*R. Surkow, 1999*: Optimierung der Leistungsverfügbarkeit von Windenergie durch ihre Integration in Wind-Biogas-Hybridanlagen
Band 15	*N. Mölders,* 1999: Einfache und akkumulierte Landnutzungsänderungen und ihre Auswirkungen auf Evapotranspiration, Wolken- und Niederschlagsbildung
Band 16	G. Tetzlaff und U. Grünewald (Edn.), 1999:2. Tagung des Fachausschusses Hydrometeorologie 15./16. 11. 1999 in Leipzig
Band 17	A. Raabe und K. Arnold (Edn.), 2000: Meteorologische Arbeiten aus Leipzig V
Band 18	K. Arnold, 2000: Ein experimentelles Verfahren zur Akustischen Tomographie im Bereich der atmosphärischen Grenzschicht
Band 19	*A. Ziemann*, 2000: Eine theoretische Studie zur akustischen Tomographie in der atmosphärischen Grenzschicht
Band 20	*Ch. Jacobi*, 2000: Midlatitude mesopause region dynamics and its coupling with lower and middle atmospheric processes
Band 21	*M. Klingspohn*, 2000: Interdekadische Klimavariabilität über dem Nordatlantik – Statistische Analysen und Modellstudien –
Band 22	*A. Raabe* und *K. Arnold* (Edn.), 2001: Meteorologische Arbeiten aus Leipzig VI
Band 23	*K. Arnold, A. Ziemann, G. Tetzlaff, V. Mellert* und *A. Raabe* (Edn.), 2001: International Workshop Tomography and Acoustics: Recent developments and methods 06. - 07.03.2001 in Leipzig
Band 24	*O. Fanenbruck*, 2001: Ein thermophysiologisches Bewertungsmodell mit Anwendung auf das Leipziger Stadtgebiet
Band 25	*M. Lange*, 2001: Modellstudien zum CO_2-Anstieg und O_3-Abbau in der mittleren Atmosphäre und Einfluss des Polarwirbels auf die zonale Symmetrie des Windfeldes in der Mesopausenregion
Band 26	*A. Raabe* und *K. Arnold* (Edn.), 2002: Meteorologische Arbeiten aus Leipzig VII
Band 27	*M. Simmel*, 2002: Ein Modul zur spektralen Beschreibung von Wolken und Niederschlag in einem Mesoskalenmodell zur Verwendung auf Parallelrechnern
Band 28	*H. Siebert*, 2002: Tethered-Balloon Borne Turbulence Measurements in the Cloudy Boundary Layer
Sonderband	*G. Tetzlaff* (Hrsg.), 2002:- Atmosphäre - Aktuelle Beiträge zu Luft, Ozon, Sturm, Starkregen und Klima
Band 29	*U. Harlander*, 2003: On Rossby wave propagation in atmosphere and ocean
Band 30	*A. Raabe* und *K. Arnold* (Edn.), 2003: Meteorologische Arbeiten aus Leipzig VIII
Band 31	*M. Wendisch*, 2003: Absorption of Solar Radiation in the Cloudless and Cloudy Atmosphere
Band 32	*U. Schlink*, 2003: Longitudinal Models in Biometeorology: Effect Assessment and Forecasting of Ground-level Ozone
Band 33	*H. Heinrich*, 2004: Finite barotrope Instabilität unter synoptischem Antrieb

Band 34 *A. Raabe* und *K. Arnold* (Edn.), 2004: Meteorologische Arbeiten aus Leipzig IX

Band 35 *C. Stolle*, 2004: Three-dimensional imaging of ionospheric electron density fields using GPS observations at the ground and on board the CHAMP satellite

Band 36 *A. Raabe* und *K. Arnold* (Edn.), 2005: Meteorologische Arbeiten (X) und Jahresbericht 2004 des Institutes für Meteorologie der Universität Leipzig

Band 37 *A. Raabe* und *K. Arnold* (Edn.), 2006: Meteorologische Arbeiten (XI) und Jahresbericht 2005 des Institutes für Meteorologie der Universität Leipzig

Band 38 *K. Fröhlich*, 2006: The Quasi Two-Day Wave – its impact on zonal mean circulation and wave-wave interactions in the middle atmosphere

Band 39 *K. Radtke*, 2006: Zur Sensitivität von Starkwindfeldern gegenüber verschiedenen meteorologischen Parametern im Mesoskalenmodell LM

Band 40 *K. Hungershöfer*, 2007: Optical Properties of Aerosol Particles and Radiative Transfer in Connection with Biomass Burning

Band 41 *A. Raabe* (Hrsg.), 2007: Meteorologische Arbeiten (XII) und Jahresbericht 2006 des Institutes für Meteorologie der Universität Leipzig

Band 42 *A. Raabe* (Hrsg.), 2008: Meteorologische Arbeiten (XIII) und Jahresbericht 2007 des Institutes für Meteorologie der Universität Leipzig

Band 43 *A. Kniffka, 2008*: Einfluss der Inhomogenitäten von Aerosol, Bodenalbedo und Wolken auf das aktinische Strahlungsfeld der Atmosphäre

Band 44 *M. Barth, 2009*: Akustische Tomographie zur zeitgleichen Erfassung von Temperatur- und Strömungsfeldern

Band 45 *A. Raabe* (Hrsg.), 2009: Meteorologische Arbeiten (XIV) und Jahresbericht 2008 des Institutes für Meteorologie der Universität Leipzig

Band 46 *G. Stober, 2009:* Astrophysical Studies on Meteors using a SKiYMET All-Sky Meteor Radar

Band 47 *A. Raabe* (Hrsg.), 2010: Meteorologische Arbeiten (XV) und Jahresbericht 2009 des Institutes für Meteorologie der Universität Leipzig

Band 48 *A. Raabe* (Hrsg.), 2011: Meteorologische Arbeiten (XVI) und Jahresbericht 2010 des Institutes für Meteorologie der Universität Leipzig

Band 49 *A. Raabe* (Hrsg.), 2012: METTOOLS_VIII Tagungsband

Band 50 *A. Raabe* (Hrsg.), 2012: Meteorologische Arbeiten (XVII) und Jahresbericht 2011 des Institutes für Meteorologie der Universität Leipzig

Band 51 *A. Raabe* (Hrsg.), 2013: Meteorologische Arbeiten (XVIII) und Jahresbericht 2012 des Institutes für Meteorologie der Universität Leipzig

Band 52 *A. Raabe* (Hrsg.), 2014: Meteorologische Arbeiten (XIX) und Jahresbericht 2013 des Institutes für Meteorologie der Universität Leipzig

Band 53 *A. Raabe* (Hrsg.), 2015: Meteorologische Arbeiten (XX) und Jahresbericht 2014 des Institutes für Meteorologie der Universität Leipzig

Band 54 *A. Raabe* (Hrsg.), 2016: Meteorologische Arbeiten (XXI) und Jahresbericht 2015 des Institutes für Meteorologie der Universität Leipzig

Band 55 *A. Raabe, M.Wendisch* (Hrsg.), 2017: Meteorologische Arbeiten (XXII) und Jahresbericht 2016 des Institutes für Meteorologie der Universität Leipzig

Band 56 *A. Raabe, M.Wendisch* (Hrsg.), 2018: Meteorologische Arbeiten (XXIII) und Jahresbericht 2017 des Institutes für Meteorologie der Universität Leipzig